UNIVERSITY OF THESSALY

SCHOOL OF ENGINEERING

DEPARTMENT OF MECHANICAL ENGINEERING

Doctor of Philosophy Dissertation

NUMERICAL SIMULATION OF STEEL MEMBER RESPONSE

UNDER STRONG CYCLIC LOADING

by

GEORGIOS E. VARELIS

Diploma of Civil Engineering, University of Thessaly, 2007

Master of Science (M.Sc.), Department of Mechanical Engineering,

University of Thessaly, 2010

Supervisor: Dr. Spyros A. Karamanos, Associate Professor

Submitted in partial fulfillment

of the requirements for the degree

of Doctor of Philosophy

Volos 2013

ΠΑΝΕΠΙΣΤΗΜΙΟ ΘΕΣΣΑΛΙΑΣ

ΠΟΛΥΤΕΧΝΙΚΗ ΣΧΟΛΗ

ΤΜΗΜΑ ΜΗΧΑΝΟΛΟΓΩΝ ΜΗΧΑΝΙΚΩΝ

Διδακτορική Διατριβή

ΑΡΙΘΜΗΤΙΚΗ ΠΡΟΣΟΜΟΙΩΣΗ ΤΗΣ ΔΟΜΙΚΗΣ ΣΥΜΠΕΡΙΦΟΡΑΣ

ΜΕΤΑΛΛΙΚΩΝ ΣΤΟΙΧΕΙΩΝ ΣΕ ΙΣΧΥΡΗ ΚΥΚΛΙΚΗ ΦΟΡΤΙΣΗ

υπό

ΓΕΩΡΓΙΟΥ Ε. ΒΑΡΕΛΗ

Διπλωματούχου Πολιτικού Μηχανικού, Πανεπιστήμιο Θεσσαλίας, 2007

ΜΔΕ, Τμήμα Μηχανολόγων Μηχανικών, Πανεπιστήμιο Θεσσαλίας, 2010

Επιβλέπων: Δρ. Σπύρος Α. Καραμάνος, Αναπληρωτής Καθηγητής

Υπεβλήθη για την εκπλήρωση μέρους των

απαιτήσεων για την απόκτηση του

Διδακτορικού Διπλώματος

Βόλος 2013

Examination Committee:

Dr. Spyros A. Karamanos (Supervisor), Associate Professor,
Mechanical Engineering Department, University of Thessaly

Dr. Antonios E. Giannakopoulos, Professor,
Civil Engineering Department, University of Thessaly

Dr. Nikolaos Makris, Professor,
Civil Engineering Department, University of Patras

Dr. Alexis Th. Kermanidis, Assistant Professor,
Mechanical Engineering Department, University of Thessaly

Dr. Oreste S. Bursi, Professor, Department of Mechanical and Structural Engineering,
University of Trento, Italy

Dr. Tasnim Hassan, Professor, Department of Civil, Construction & Environmental
Engineering, NC State University, USA

Dr. Philip Perdikaris, Professor,
Civil Engineering Department, University of Thessaly

Εξεταστική Επιτροπή:

Δρ. Σπύρος Α. Καραμάνος (Επιβλέπων), Αναπληρωτής Καθηγητής, Τμήμα
Μηχανολόγων Μηχανικών, Πανεπιστήμιο Θεσσαλίας

Δρ. Αντώνιος Ε. Γιαννακόπουλος (Μέλος Τριμελούς), Καθηγητής, Τμήμα
Πολιτικών Μηχανικών, Πανεπιστήμιο Θεσσαλίας

Δρ. Νικόλαος Μακρής, Καθηγητής (Μέλος Τριμελούς), Τμήμα Πολιτικών
Μηχανικών, Πανεπιστήμιο Πατρών

Δρ. Αλέξης Θ. Κερμανίδης, Επίκουρος Καθηγητής, Τμήμα Μηχανολόγων
Μηχανικών, Πανεπιστήμιο Θεσσαλίας

Dr. Oreste S. Bursi, Καθηγητής, Department of Mechanical and Structural
Engineering, University of Trento, Italy

Dr. Tasnim Hassan, Καθηγητής, Department of Civil, Construction &
Environmental Engineering, NC State University, USA

Δρ. Φίλιππος Περδικάρης, Καθηγητής, Τμήμα Πολιτικών Μηχανικών,
Πανεπιστήμιο Θεσσαλίας

Acknowledgements

Georgios E. Varelis

Ευχαριστίες

Είμαι ιδιαίτερα ευγνώμων στον επιβλέποντα της διατριβής μου, Αναπληρωτή Καθηγητή κ. Σπύρο Καραμάνο, για τις πολύτιμες συμβουλές, τη βοήθεια και τη καθοδήγησή του κατά τη διάρκεια εκπόνησης της διατριβής μου. Η συνεργασία μαζί του μου έδωσε πολύτιμες γνώσεις και έθεσε τα θεμέλια για τη μετέπειτα επαγγελματική μου πορεία. Επίσης, θα ήθελα να ευχαριστήσω ιδιαιτέρως τον Καθηγητή κ. Αντώνιο Ε. Γιαννακόπουλο και τον Καθηγητή κ. Νικόλαο Μακρή, καθώς και τα υπόλοιπα μέλη της εξεταστικής επιτροπής για την προσεκτική ανάγνωση της διατριβής μου και για τις πολύτιμες υποδείξεις τους.

Μέρος της παρούσας έρευνας χρηματοδοτήθηκε από την Ευρωπαϊκή Επιτροπή στα πλαίσια των ερευνητικών προγραμμάτων HITUBES - Grant No. RFSR-CT-2008-00035 και INDUSE - Grant No. RFSR-CT-2009-00022. Θα ήθελα επίσης να ευχαριστήσω την εταιρεία SHELTER ABEE και προσωπικά τον κ. Προκόπη Τσίντζο για την εμπιστοσύνη που μου έδειξε και την χρηματοδότηση που μου προσέφερε κατά τη διάρκεια της έρευνας μου.

Οφείλω να εκφράσω επίσης τις ιδιαίτερες ευχαριστίες μου στον J. Ferino (Centro Sviluppo Materiali S.p.A.), στον Αναπληρωτή Καθηγητή A.M. (Nol) Gresnigt (Delft University of Technology), στον Καθηγητή κ. Φίλιππο Περδικάρη και στον κ. Θεοχάρη Παπαθεοχάρη για τη συμβολή τους στο πειραματικό μέρος της έρευνας που παρουσιάζεται στα Κεφάλαια 3, 4 και 5 καθώς και για την άψογη συνεργασία μας.

Τέλος, ευχαριστώ τους συναδέλφους και φίλους μου Δανιήλ Βασιλική, Πατρίτσια Παππά, Αγλαΐα Πουρνάρα, Μαρία Βάθη, Γιαννούλα Χατζοπούλου και Θεοχάρη Παπαθεοχάρη για την πολύτιμη βοήθεια, τη φιλία και την ηθική υποστήριξή τους. Επίσης, θέλω να ευχαριστήσω όλους τους φίλους μου στο Βόλο που μου συμπαραστάθηκαν σε όλη μου την πορεία.

Αφιερώνω αυτή την διατριβή στην οικογένεια μου και τους ευχαριστώ για την αγάπη και υποστήριξη που μου έδωσαν σε κάθε μου βήμα.

Γεώργιος Ε. Βαρέλης

NUMERICAL SIMULATION OF STEEL MEMBER RESPONSE

UNDER STRONG CYCLIC LOADING

by

GEORGIOS E. VARELIS

University of Thessaly, Department of Mechanical Engineering, 2013

Abstract

The present study examines the behavior of steel structures subjected to strong cyclic loading, associated with severe plastic deformations at critical locations. In particular, it aims at the detailed examination of mechanical behavior of tubular members and welded tubular joints, using numerical simulation tools, with emphasis on the constitutive model. It should be noted though that the numerical models described within this study can be applied to any type of steel members, regardless the geometry.

A key feature of this study is the theoretical formulation and the numerical implementation of the Tseng-Lee model (Tseng & Lee, 1983). This model is considered as an advanced plasticity model, representative of the models adopting the "bounding surface" concept. The theoretical formulation and the numerical integration scheme are described in detail. The material model is implemented in ABAQUS, developing a user-material subroutine UMAT. Finally, modifications of the model that enhance its predicting capabilities are presented. The capabilities of this model are also presented through the use of illustrative examples.

In the first part of the study, the mechanical behavior of tubular members subjected to cyclic bending is examined. A set of experiments conducted on high-strength steel tubular members conducted in Centro Sviluppo Materiali (CSM) is presented and numerical models are developed for the simulation of the tests. Emphasis is given on the buckling phenomena that take place due to the accumulation of local plastic deformations (ratcheting effect) in combination with the evolution of initial geometrical imperfections in the form of wrinkles.

The behavior of steel elbows subjected to strong in-plane cyclic loading is also examined. Cyclic loading pressurized and non-pressurized tests have been conducted in the laboratories of TU Delft and CSM in order to evaluate the elbows capacity of undergoing severe bending loading associated with extensive plastic deformations and cross-sectional distortion in terms of flattening. Advanced numerical models have been developed for the simulation of this behavior adopting both the nonlinear kinematic hardening and the bounding

surface cyclic plasticity material models. Based on the analysis results, low-cycle fatigue design curves are also developed and an integrated fatigue design methodology accounting for the pressure effects is introduced. Finally, issues related to relevant design code provisions are discussed.

The behavior of tubular joints made of high-strength steel and subjected to severe in-plane, out-of-plane bending and axial loading is studied in the last chapter of the present study. A set of experiments has been conducted in the Laboratory of Concrete Technology and Reinforced Concrete Structures of the Civil Engineering Department of the University of Thessaly on welded tubular X-connections and the experimental results are compared with the corresponding numerical results provided by detailed numerical models. The overall structural behavior of the joints under monotonic and cyclic loading conditions, as well as stress and strain concentrations at the weld toe area of the joint, are studied thoroughly through a parametric analysis. An attempt to extend the currently available fatigue curves from the high-cycle fatigue range to the low-cycle fatigue regime is also presented.

ΑΡΙΘΜΗΤΙΚΗ ΠΡΟΣΟΜΟΙΩΣΗ ΤΗΣ ΔΟΜΙΚΗΣ ΣΥΜΠΕΡΙΦΟΡΑΣ ΜΕΤΑΛΛΙΚΩΝ ΣΤΟΙΧΕΙΩΝ ΣΕ ΙΣΧΥΣΡΗ ΚΥΚΛΙΚΗ ΦΟΡΤΙΣΗ

υπό

ΓΕΩΡΓΙΟΥ Ε. ΒΑΡΕΛΗ

Πανεπιστήμιο Θεσσαλίας, Τμήμα Μηχανολόγων Μηχανικών, 2013

Περίληψη

Ο σκοπός της παρούσας εργασίας είναι η λεπτομερής εξέταση της δομικής συμπεριφοράς και η εκτίμηση της οριακής αντοχής (σχετικά λεπτότοιχων) επιμηκών μεταλλικών κελυφών (π.χ. δομικών στοιχείων ή τμημάτων αγωγών) που υπόκεινται σε έντονη κυκλική φόρτιση συσχετισμένη με ανελαστική συμπεριφορά του υλικού. Η έρευνα διεξάγεται με αριθμητικά εργαλεία που βασίζονται στη μη-γραμμική ανάλυση των κατασκευών με τη χρήση πεπερασμένων στοιχείων. Ο κύριος στόχος της εργασίας είναι η ανάπτυξη ενός καταστατικού μοντέλου κυκλικής πλαστικότητας που περιγράφει επαρκώς τη συμπεριφορά του υλικού στην ανελαστική περιοχή, καθώς και η ενσωμάτωση του μοντέλου αυτού σε έναν μη-γραμμικό κώδικα πεπερασμένων στοιχείων.

Στη συνέχεια, τα αριθμητικά εργαλεία που έχουν αναπτυχθεί χρησιμοποιούνται για την επίλυση τυπικών προβλημάτων που σχετίζονται με τη δομική συμπεριφορά και αστοχία μεταλλικών στοιχείων υπό κυκλική φόρτιση. Παρά το γεγονός ότι η μεθοδολογία αντιμετώπισης των προβλημάτων κυκλικής καταπόνησης μεταλλικών στοιχείων που εξετάζεται μπορεί να εφαρμοστεί σε δομικά στοιχεία τυχαίας γεωμετρίας, στην παρούσα εργασία δίνεται έμφαση στη μελέτη επιμηκών κυλινδρικών στοιχείων κυκλικής διατομής. Τέτοια στοιχεία χρησιμοποιούνται ευρέως σε δικτυωτές κατασκευές που χρησιμοποιούν σωληνωτά στοιχεία (θαλάσσιες πλατφόρμες, ιστοί κ.τ.λ.), σε κτηριακές κατασκευές όπου χρησιμοποιούνται κυκλικά υποστυλώματα ή κυκλικοί σύνδεσμοι δυσκαμψίας, σε βιομηχανικά στοιχεία σωληνώσεων καθώς και χαλύβδινα στοιχεία αγωγών (επίγειων και υποθαλάσσιων).

Κομβικό σημείο της παρούσας διατριβής αποτελεί η αναλυτική εξέταση του καταστατικού μοντέλου κυκλικής πλαστικότητας Tseng-Lee. Το συγκεκριμένο μοντέλο αποτελεί χαρακτηριστικό δείγμα των καταστατικών μοντέλων που υιοθετούν την έννοια της «οριακής επιφάνειας». Οι καταστατικές σχέσεις με βάση τις οποίες περιγράφεται η συμπεριφορά του υλικού υπό συνθήκες έντονης κυκλικής φόρτισης στην πλαστική περιοχή παρουσιάζονται

λεπτομερώς. Ακολούθως παρουσιάζεται αναλυτικά η διαδικασία ενσωμάτωσης του μοντέλου σε πηγαίο κώδικα πεπερασμένων στοιχείων και στο πρόγραμμα ABAQUS. Τέλος, προτείνεται μια σειρά τροποποιήσεων που ενισχύουν την ικανότητα του μοντέλου να προβλέπει με ακρίβεια την συμπεριφορά του υλικού υπό τις παραπάνω συνθήκες. Με βάση το παραπάνω καταστατικό μοντέλο διεξάγεται η μελέτη μιας σειράς προβλημάτων που σχετίζονται με φαινόμενα κυκλικής πλαστικότητας μεταλλικών στοιχείων έχοντας ως βάση προγενέστερα πειραματικά και αριθμητικά αποτελέσματα.

Αναλυτικότερα, το πρώτο πρόβλημα υπό εξέταση αφορά τη δομική συμπεριφορά σωληνωτών στοιχείων από χάλυβα υψηλής αντοχής σε συνθήκες κυκλικής φόρτισης. Η έρευνα βασίζεται σε μια σειρά πειραμάτων που διεξήχθησαν στα εργαστήρια του CSM σε σωληνωτά στοιχεία από χάλυβα υψηλής αντοχής. Λεπτομερή μοντέλα πεπερασμένων στοιχείων που υιοθετούν το καταστατικό μοντέλο υλικού που αναπτύχθηκε χρησιμοποιούνται για την αριθμητική προσομοίωση των πειραματικών αποτελεσμάτων. Ακολούθως πραγματοποιείται περαιτέρω αριθμητική ανάλυση της συμπεριφοράς των παραπάνω στοιχείων υπό συνθήκες κυκλικής κάμψης. Έμφαση δίνεται στο φαινόμενο του τοπικού λυγισμού υπό την παρουσία σημαντικών πλαστικών παραμορφώσεων και στην επιρροή των αρχικών γεωμετρικών ατελειών στο φαινόμενο του κυκλικού λυγισμού.

Μελετάται επίσης η συμπεριφορά καμπύλων στοιχείων σωληνώσεων (elbows) υπό την επίδραση κυκλικής κάμψης με ή χωρίς την παρουσία εσωτερικής πίεσης. Η μελέτη διεξάγεται με τη χρήση λεπτομερών μοντέλων πεπερασμένων στοιχείων στα οποία υιοθετείται το μοντέλο κυκλικής πλαστικότητας με μη-γραμμική κινηματική κράτυνση καθώς και το μοντέλο υλικού που αναπτύχθηκε στα πλαίσια της παρούσας διατριβής. Τα αριθμητικά αποτελέσματα συγκρίνονται με αντίστοιχες πειραματικές μετρήσεις από πειράματα που διεξήχθησαν στα εργαστήρια του Πανεπσιτημίου Delft και του CSM, στα οποία εξετάστηκε η συμπεριφορά των στοιχείων αυτών σε συνθήκες έντονης κυκλικής κάμψης που έχει ως συνέπεια σημαντικές πλαστικές παραμορφώσεις. Ακολούθως, με βάση τα πειραματικά και αριθμητικά αποτελέσματα, προτείνεται μια ολοκληρωμένη μεθοδολογία πρόβλεψης αστοχίας των εν λόγω στοιχείων από ολιγοκυκλική κόπωση.

Στο τελευταίο μέρος της παρούσας διατριβής εξετάζεται η δομική συμπεριφορά σωληνωτών κόμβων από χάλυβα υψηλής αντοχής υπό την επίδραση ισχυρών κυκλικών φορτίων κάμψης εντός και εκτός επιπέδου, καθώς και αξονικής φόρτισης. Η συγκεκριμένη μελέτη βασίζεται σε μια σειρά πειραμάτων σε σωληνωτούς κόμβους μορφής Χ (X-joints) που διεξήχθησαν στο Εργαστήριο Τεχνολογίας και Κατασκευών Οπλισμένου Σκυροδέματος του Τμήματος Πολιτικών Μηχανικών του Πανεπιστημίου Θεσσαλίας. Για την αριθμητική προσομοίωση των πειραμάτων δημιουργήθηκαν λεπτομερή μοντέλα πεπερασμένων στοιχείων στο πρόγραμμα ABAQUS. Το καταστατικό μοντέλο που αναπτύχθηκε στα πλαίσια της παρούσας διατριβής χρησιμοποιείται στις

προσομοιώσεις και τα αποτελέσματά του συγκρίνονται με τα αντίστοιχα πειραματικά. Έμφαση δίνεται στη συνολική συμπεριφορά των κόμβων, στα φαινόμενα τοπικής συγκέντρωσης τάσεων και παραμορφώσεων καθώς και στα φαινόμενα ολιγοκυκλικής κόπωσης στις περιοχές συγκέντρωσης τάσεων. Επίσης, χρησιμοποιώντας λεπτομερή αριθμητικά μοντέλα πεπερασμένων στοιχείων, πραγματοποιείται μια παραμετρική μελέτη της επιρροής των γεωμετρικών χαρακτηριστικών των σωληνωτών κόμβων στη δομική τους συμπεριφορά. Τέλος, επιχειρείται η επέκταση των διαθέσιμων καμπύλων κόπωσης από την πολυκυκλική στην ολιγοκυκλική περιοχή.

Table of Contents

Chapter 1

Introduction

1.1 Severe cyclic loading of steel tubular members and pipe components

A wide range of applications from the structural and mechanical engineering field involve cyclic loading of metal structures and components well beyond the elastic regime. Even in structures that are designed to perform elastically, cyclic plastic actions often occur due to local discontinuities. This necessitates the prediction of metal cyclic behavior in the inelastic range through simple and robust cyclic plasticity models. Some indicative engineering problems associated with cyclic plasticity will be briefly discussed in the following paragraphs, to provide a framework for the present study.

In particular, applications where steel tubular members and pipes are subjected to severe cyclic loads are quite common in engineering practice. Severe cyclic loading induces repeated yielding of the steel material in the most strained locations. Typical examples are the response of tubular structures under strong earthquake action [Zayas et al. (1982)], offshore tubular platforms in extreme weather conditions [Bea & Young (1993), Schmucker and Cornell (1994)], nuclear reactor piping components under shut-down conditions [Shmnomura et al. (2002),] or hot hydrocarbon pipelines under significant variations of pressure and temperature [Klever et al. (2002)]. Those cyclic excursions into the inelastic range can lead to degradation and failure of structures due to accumulation of deformations and fatigue fracture, especially when they are combined with the presence of geometrical imperfections.

Failure due to cyclic loading, in the form of fatigue cracking is a well-known engineering problem related to the important issue of structural integrity. Many engineering failures of metal structures have been attributed to this phenomenon over the years. Depending on the number of cycles, fatigue is categorized into high or low-cycle fatigue. For loading cycles up to about 10^4, the structural problem is in the range of low-cycle fatigue, while for loading cycles exceeding this nominal limit, the problem is referred to as high-cycle fatigue problem.

High-cycle fatigue is associated with varying loads significantly lower than the elastic limit. Of course, due to material defects, geometrical discontinuities (e.g. sharp edges and cuts, welds or cracks) the material may be plasticized locally. The local cyclic loading induces material deterioration which causes crack initiation and propagation until total failure. However, the stresses in high-

1

cycle fatigue are generally low and below the yield limit of the material. On the contrary, low and ultra-low cycle fatigue is associated with a small number of cycles of intense loading and repeated excursions of stresses and strains in the inelastic range. The maximum number of cycles that a structure can sustain is related directly to the ability of the material to maintain its strength and ductility under strong cyclic loading conditions. For understanding low-cycle fatigue, the accurate description of metal behavior in the inelastic range under repeated loading is necessary, motivating the development of efficient cyclic plasticity constitutive models.

In addition to low-cycle fatigue problems, a significant motivation for developing cyclic plasticity models is the simulation of metal forming. In the mechanical engineering field, simulation of metal forming has significant applications in the oil & gas, pipeline, aerospace and automobile industry. In particular, numerous metal components such as industrial pressure vessels and pipeline components used to transmit or distribute hydrocarbon or other energy/water resources, widely used in the chemical, petrochemical and power plant facilities, are the outcome of similar forming processes. The cyclic loading of the material of these products during their fabrication process causes geometric imperfections, as well as fields of residual stresses and strains. As a consequence, the structural behavior of the final product is highly influenced by the manufacturing procedure and should be taken into account for the accurate assessment of their structural strength and integrity. Towards this purpose, the development and use of plasticity models, capable of describing metal behavior in the inelastic range under repeated loading is a key issue.

1.1.1 The mechanical behavior of steel pipe elbows

The behavior of steel pipe elbows which constitute key components of industrial piping systems is an important issue for understanding the structural response of industrial facilities under strong cyclic loading. Pipe elbows, sometimes referred to as "bends", are curved tubular elements that facilitate the change of the piping route direction, but because of their flexible structural response, they are capable of accommodating expansions and contractions of the piping system assembly due to severe variations of pressure and temperature. On the other hand, their initial curvature, the ensuing large ovalization of their cross-section and the presence of significant internal (or sometimes external) pressure significantly are responsible for their unique structural behavior. Failure of the elbows may occur in many different forms, with local or global buckling and fracture being the most critical ones. Their performance under monotonic and cyclic loading due to operational and seismic actions has attracted the scientific interest.

Significant contributions on the experimental investigation of the behavior and strength of steel elbows under monotonic loading conditions have

been reported by Sobel and Newman (1980, 1986), Dhalla (1987), Gresnigt et al. (1986, 1995), Greenstreet (1978) and more recently by Hilsenkopf et al.(1988), Suzuki and Nasu (1989) and Tan et al. (2002). In addition, notable numerical works on steel elbows have been reported by Shaleby and Younan (1998), Mourad and Younan (2001), and Chattopadhyay et al. (2000). More recent works by the research group of the University of Thessaly [Karamanos et al. (2003, 2006)] reported extensive numerical studies of steel elbow response under in-plane and out-of-plane bending, which were extended by Pappa et al. (2008), to include the effects of external pressure.

The above works have focused on monotonic loading. In the course of a strong loading event (e.g. a strong earthquake), the elbows are subjected to strong repeated cyclic structural loading, associated with deformation of the steel material in the inelastic range, so that the elbow exhibits significant accumulation of plastic strain (often referred to as "ratcheting"), which eventually may lead to failure. Extensive experimental work on the ratcheting behavior of pressurized 2-inch carbon and stainless steel pipe elbows has been reported by Yahiaoui et al. (1996a), under an "increasing input displacement amplitude" loading. This work was continued in the study of Yahiaoui et al. (1996b) for out-of-plane bending, whereas Moreton et al. (1996) attempted to predict analytically the ratcheting rate and ratcheting initiation. Slagis (1998) reported an EPRI/NRC experimental testing program on carbon/stainless steel pipe elbows, through a shaking-table apparatus, for both component tests and piping system tests. Extensive experimental work was presented by Fujiwaka et al. (1999), through a series of material tests, pipe component tests and piping system tests (bent pipes, tees, and straight pipes).

Notable works on the analytical investigation of elbows under cyclic loading have been reported by Degrassi et al. (2003) and Balan & Redektop (2004). More recently, Rahman and Hassan (2009) presented an extensive analytical work on cyclic behavior of steel elbows, supported by small-scale experiments, focusing at the capabilities of several cyclic plasticity models in predicting ratcheting. All the above works demonstrated that when steel elbows are subjected to strong repeated loading, they exhibit failure associated with material degradation and eventually fatigue cracking. In many instances, the elbow cross-section distorted or bulged with increasing number of cycles. The analysis of steel elbows constitutes a significant application, to be examined in the present study.

1.1.2 Tubular steel members under cyclic loading

In tubular steel structures, such as offshore platforms, mast, towers or cranes, the individual tubular members can be often subjected to strong cyclic loading and it is required that they have adequate resilience and a significant absorption capacity. At large deformations, the capacity of tubular members is

3

significantly affected by the ovalization of their cross-section and, eventually, the formation of a localized deformation pattern in the form of a "kink" or "local buckle". Previous attempts to analyze this phenomenon for structural tubular steel members have been reported by a series of papers by Popov and his associates describing experimental work on scaled tubular structural systems under cyclic loading [Popov et al. (1980), Mahin et al. (1980), Zayas et al. (1982)] and by Sohal & Chen (1988), using a simplified beam-type model, enhanced for taking into account the effects of cross-sectional distortion and buckling. More recent research on the cyclic bending performance of tubular structural members under cyclic loading has been reported by Gao et al. (1998) and by Elchalakani et al. (2004), describing an experimental programs aimed at re-examining bending ductility or slenderness limits for the case of cyclic loading.

In the energy related industry, apart from the behavior of steel elbows, understanding the behavior of straight tubular members such as piping systems and pipelines is also considered very important. These members, when subjected to strong loading conditions, may undergo repeated yielding of the steel material in the most strained locations. The structural behavior of tubes under cyclic bending loading has been examined experimentally by Shaw & Kyriakides (1985) and Kyriakides & Shaw (1987), and this work has been extended by Corona & Kyriakides (1991) to include the effects of external pressure. Notable works on the cyclic bending response of tubular members and pipes have been also reported in Lee et al. (2001), Chang & Pan (2009) using an experimental set-up very similar to the one in Corona & Kyriakides (1991), supported by analytical predictions based on a visco-plastic material model.

In addition to bending loading, described above, most recently, Jiao & Kyriakides (2009, 2010) have investigated meticulously the cyclic behaviour of steel pipes with respect to initial wrinkle imperfection. These studies indicated that there exist a strong interaction between the elastic-plastic behavior of the steel material and the geometric nonlinearities induced by initial wrinkles and the ovalization phenomenon, resulting in an accumulation of deformation at the critical region which leads to the formation of local buckling after a number of loading cycles. This is a situation that implies failure of the pipe; moment capacity is decreased abruptly and under continuing cyclic loading, the buckled area of the pipe may exhibit low-cycle fatigue due to strain concentration and, eventually, fracture [Dama et al. (2007)]. Nevertheless, the interaction between initial wrinkles and cyclic bending loading is still an open issue that requires further rigorous investigation.

1.1.3 Cyclic loading of welded tubular connections
In the case of steel tubular structures, separate tubular members are welded together forming tubular joints, often with complex multi-planar geometries. Even in the simplest tubular joints, due to the particular local joint

4

geometry, the developing local stress fields are significantly complex. The presence of welds introduces local stress risers, which are responsible for the development of very high local stresses even for moderate levels of externally applied loading, the so-called "hot spot" stresses. Under cyclic loading conditions, excessive plastic deformations appear at these regions constituting the tubular joints prone to fatigue failure.

The research on the performance of tubular joints has initiated back from the late 1960s, as described in Beale & Torpac (1967) or in the paper by Marshall (1974). Many empirical equations were developed for the design of tubular joints subjected to monotonic and cyclic loading and analytical model methods have also been developed [Wardenier (1982), Hoadley & Yura (1983), Swenson & Yura (1987), Romeijn (1994)] offering a rather simplified approach to the complicated design problem of tubular joints for static loading and fatigue. On the other hand, the vast majority of reported studies on fatigue loading of welded tubular connections refer to high-cycle fatigue, i.e. cyclic loading associated with relative low nominal stresses and a large number of loading cycles. On the other hand, under extreme cyclic loading conditions, stresses are quite high, usually beyond the yield limit of the steel material and fatigue failure occurs with a relatively small number of cycles, referred to as "low-cycle fatigue". This type of failure has received much less attention. To the author's knowledge, the only works on this issue have been published by Baba et al. (1981) and by van der Vegte et al. (1989), requiring further investigation, both experimentally and numerically.

1.1.4 High-strength steel in tubular members

In the recent years the advances in the available metallurgical techniques resulted to high-strength steel alloys which gained an important part in the everyday design practice, also in the field of tubular steel structures. The enhanced material properties are expected to result into higher load resistance of the members and their joints, as well as into more economical design in terms of steel weight consumption. In addition, new welding technologies were developed allowing for the development of more time-effective welded joint production with highly accurate local weld geometries.

The benefits of using high-strength steel on the static strength of welded tubular structures have been reported by Noordhoek & Verheul (1998) and in a relatively recent HSE report (HSE, 1999), which describes the results of a Joint Industry Program. Recently, in a series of papers, Choi et al (2012a, 2012b) the static performance of tubular T and K-joints has also been investigated. On the other hand, the fatigue performance of high-strength steel tubular joints has not been extensively examined, especially in terms of low-cycle fatigue.

In current design practice, from all existing design standards and guidelines for the design of welded tubular connections, the only standard the

can used for high-strength steel tubular members and joints is EN 1993-1-12, but its relevant provisions are rather conservative for static loading (requiring a reduction factor equal to 0.8 with respect to steel grades up to 460 MPa), whereas the fatigue provisions simply extent the corresponding rules for steel grades up to 460 MPa. In any case, low-cycle fatigue performance of welded tubular joints is still an open research issue and constitutes a primary motivation for the present study.

1.2. Scope of the present dissertation

The present study refers to the structural performance of steel structures subjected to strong cyclic loading, associated with severe plastic deformations at critical locations. In particular, it aims at the detailed examination of mechanical behavior of tubular members and welded tubular joints, using numerical simulation tools, with emphasis on the constitutive model. It sould be noted though that the numerical models described within this study can be applied to any type of steel member, regardless its geometry.

The study starts with the presentation of cyclic plasticity issues and the related phenomena in Chapter 2. The most popular plasticity models are briefly presented. A key feature of this study is the theoretical formulation and the numerical implementation of the Tseng-Lee model (Tseng & Lee, 1983). This model is considered as an advanced plasticity model, representative of the models adopting the "bounding surface" concept. The theoretical formulation and the numerical integration scheme are described in detail in Chapter 2. The material model is implemented in ABAQUS, developing a user-material subroutine UMAT. In the same chapter, the capabilities of this model are also presented through the use of illustrative examples. Finally, modifications of the model that enhance its predicting capabilities are presented. In addition to the Tseng-Lee model, the nonlinear kinematic hardening cyclic plasticity model, proposed by Armstrong & Frederick (1966) is presented, and its formulation and implementation are described in the Appendix. It is a popular plasticity model that constitutes the basis for the development of other more elaborate models with multiple back stresses, proposed during the last years.

The mechanical behavior of tubular members subjected to cyclic bending is examined in Chapter 3. A set of experiments conducted on high-strength steel tubular members is presented and numerical models are developed for the simulation of the tests. Emphasis is given on the buckling phenomena that take place due to the accumulation of local plastic deformations (ratcheting effect) in combination with the evolution of initial geometrical imperfections in the form of wrinkles.

In Chapter 4, the behavior of steel elbows subjected to strong in-plane cyclic loading is examined. Cyclic loading pressurized and non-pressurized tests have been conducted in order to evaluate the elbows capacity of undergoing

6

severe bending loading associated with extensive plastic deformations and cross-sectional distortion in terms of flattening. Advanced numerical models have been developed for the simulation of these experiments adopting both the nonlinear kinematic hardening and the bounding surface cyclic plasticity material models. Based on the analysis results, low-cycle fatigue design curves are also developed and an integrated fatigue design methodology accounting for the pressure effects is introduced. Finally, issues related to relevant design code provisions are discussed.

The behavior of tubular joints made of high-strength steel and subjected to severe in-plane, out-of-plane bending and axial loading is studied in Chapter 5 of the present study. A set of experiments has been conducted in the Laboratory of Concrete Technology and Reinforced Concrete Structures of the Civil Engineering Department of the University of Thessaly and the experimental results are compared with the corresponding numerical results provided by detailed numerical models. The overall structural behavior of the joints under monotonic and cyclic loading conditions, as well as stress and strain concentrations at the weld toe area of the joint, are studied thoroughly. An attempt to extend the currently available fatigue curves from the high-cycle fatigue range to the low-cycle fatigue regime is also presented. The experimental and numerical findings in terms of ultimate strength capacity and fatigue resistance of the welded tubular joints are compared with the corresponding provisions of the relevant design codes.

7

Chapter 2

Constitutive modeling and implementation

2.1 Introduction to cyclic plasticity

Metal cyclic plasticity is a unique area of constitutive equations, which describes metal material behavior in the plastic range under cyclic (reverse or repeated) loading conditions. Several interesting phenomena related to alternate plasticity take place under repeated loading in the plastic regime and their understanding is of crucial importance for the safe design of metal structures. In the following paragraphs the behavior of metal materials under cyclic loading is briefly discussed.

The behavior of metals when subjected to loading cycles exceeding the elastic range depends on the micro-structural characteristics of the material. Experimental studies have shown that the yield surface of the metal material, defining the limit of the elastic regime, may translate, change size and possibly change shape during plastic loading. Each stress state is history-dependent; this implies that the stress path followed to reach the current state is needed for the accurate prediction of any subsequent change in the stress state. Several important phenomena are strictly related to the plastic behavior of the metal material under cyclic loading, and are briefly presented below:

(a) A well-known phenomenon related to cyclic loading is the Bauschinger effect (Bauschinger, 1881). This effect occurs when a metal is loaded past its elastic limit followed by plastic loading in the opposite direction. During reverse loading, plastic deformation begins at a significantly lower stress level, with a gradual reduction of the post-yielding or hardening modulus.

(b) Cyclic hardening or cyclic softening may also take place under symmetric strain-controlled loading. In general, initially soft or annealed metals tend to harden toward a stable limit, whereas initially hard metals tend to soften.

(c) When a metal is subjected to unsymmetrical stress-controlled cycles, this causes progressive "creep" in the direction of the mean stress, a phenomenon often reported as "ratcheting". As with repeated, each consecutive hysteresis loop translates in this direction in a varying rate due to the fact that the cycles do not have complete closure of each loop. This phenomenon will be extensively discussed in the following Chapters of the present study.

2.2 Brief overview of cyclic plasticity models

Significant research effort has been devoted in the formulation of phenomenological plasticity models to predict the behavior of materials subjected to cyclic loading. These models have a different performance for a specific material and their efficiency in predicting cyclic loading effects has been extensively analyzed in previous publications [Corona et al.(1996), Bari and Hassan (2000)]. The models are based on the same basic principles, which stem from the classical theory of plasticity. In particular these characteristics are:

(a) the additive decomposition of total strain in an elastic and a plastic part

(b) the existence of a yield criterion in the form of a yield surface in the stress space

(c) the flow rule that determines the increment of plastic deformation

(d) the hardening rule which defines the post elastic increase of the stresses due to increasing strains

(i) The total strain decomposition

When loading takes place elastically, then the total strain is elastic and fully recoverable. When the elastic limit is exceeded, then the loading is elastoplastic. In this case we assume that the total strain has an elastic and a plastic part:

$$\boldsymbol{\varepsilon} = \boldsymbol{\varepsilon}^e + \boldsymbol{\varepsilon}^p \tag{2.1}$$

The elastic part is recoverable when the loading is removed, while the plastic part is permanent. The above equation is also used in its rate form.

(ii) The yield criterion

The yield criterion defines whether at every stress increment the material behavior is elastic or inelastic and for classical metal plasticity it has the following general form $F\left(\boldsymbol{\sigma}, \boldsymbol{\alpha}, \varepsilon_q\right) = 0$, where $\boldsymbol{\sigma}$ is the stress tensor, $\boldsymbol{\alpha}$ is the tensor that describes the position of the center of the yield surface sometimes referred to as "backstress" and ε_q is the equivalent plastic strain.

For metal materials, it has been proven that the plastic deformation is not affected by the hydrostatic part of the stress tensor. Therefore, the initial yield criterion function depends only on the second and third deviatoric stress tensor invariants. $F\left(J_2, J_3\right) = 0$. The most popular initial yield criterion for metal plasticity is the von Mises yield criterion described by the following equation:

9

$$F = 3J_2 - k^2 = 0$$

also written as

$$F = \frac{1}{2}\mathbf{s} \cdot \mathbf{s} - \frac{k^2}{3} = 0 \tag{2.2}$$

where k is the size of the yield surface which can be assumed to be constant or a general function of the equivalent plastic strain e_q, so that $k = k(e_q)$.

(iii) The flow rule

The flow rule governs the plastic strain rate increment through the use of a plastic multiplier $\dot{\lambda}$. In general, it is assumed that the increment of plastic strain can be written as follows

$$\dot{\boldsymbol{\varepsilon}}^p = \dot{\lambda}\frac{\partial Q}{\partial \boldsymbol{\sigma}} \tag{2.3}$$

where Q is the so-called plastic potential function that depends on $(\boldsymbol{\sigma}, \boldsymbol{\alpha}, \varepsilon_q)$. In the case of associated plasticity for metals $Q \equiv F$, therefore:

$$\dot{\boldsymbol{\varepsilon}}^p = \dot{\lambda}\frac{\partial F}{\partial \boldsymbol{\sigma}} \tag{2.4}$$

For the case of J_2-plasticity, with a yield surface of equation (2.2), the flow rule takes the following form:

$$\dot{\boldsymbol{\varepsilon}}^p = \dot{\lambda}\mathbf{s} \tag{2.5}$$

(iv) The hardening rule

The hardening rule describes the evolution of the "backstress" tensor $\boldsymbol{\alpha}$ in the stress space, which defines the center of the yield surface. Hardening rule can take several forms. In the following paragraphs the cases of Linear, Multilinear and Nonlinear hardening rules for cyclic plasticity are briefly discussed.

2.2.1 Models using kinematic hardening rules

The simplest way to describe plasticity is the Perfect Plasticity model (sometimes refer to as Prandt- Reuss model). According to this model, the center of the yield surface is fixed in the origin of the stress space and its size is constant. An advancement of the above model is the plasticity model that uses the isotropic hardening rule. In that case, the yield surface is assumed to remain

10

fixed in the stress space and change size according to the magnitude of the equivalent plastic strain ε_q defined as

$$\dot{\varepsilon}_q = \sqrt{\frac{2}{3}\dot{\boldsymbol{\varepsilon}}^P \cdot \dot{\boldsymbol{\varepsilon}}^P} \tag{2.6}$$

so that the size of the yield surface k is a function of ε_q. These models can be used for cyclic plasticity problems, not providing though reliable simulation results in many cases.

In cyclic plasticity, the use of kinematic hardening rule constitutes a starting point for the development of the constitutive model. In particular, it can take the form of Linear, Multilinear or Nonlinear kinematic hardening. According to this concept, the yield surface size can be assumed constant while its position described by the "backstress" tensor $\boldsymbol{\alpha}$ (defined at the center of the surface) varies within the stress space. Moreover, some changes of size of the yield surface can be also taken into consideration combined with the kinematic hardening rule in any of the aforementioned forms. In the following paragraph the general features of von Mises plasticity model with the kinematic hardening rule are discussed.

<u>Von Mises plasticity with kinematic hardening</u>

The von Mises (J_2) plasticity models employing the kinematic hardening rule have the following characteristics:

(a) The von Mises yield criterion:

$$F(\boldsymbol{\sigma} - \boldsymbol{\alpha}) = \frac{1}{2}(\mathbf{s} - \mathbf{a}) \cdot (\mathbf{s} - \mathbf{a}) - \frac{k^2}{3} = 0 \tag{2.7}$$

(b) The flow rule, written in a more general form:

$$\dot{\varepsilon}^p = \frac{1}{H}\left\langle \frac{\partial F}{\partial \boldsymbol{\sigma}} \cdot \dot{\boldsymbol{\sigma}} \right\rangle \frac{\partial F}{\partial \boldsymbol{\sigma}} \tag{2.8}$$

which is equivalent to Eq. (2.4) for associated plasticity.

(c) The kinematic hardening rule, which is a function of the state parameters and the plastic strain:

$$\dot{\mathbf{a}} = g(\boldsymbol{\sigma}, \boldsymbol{\varepsilon}^p, \mathbf{a}, \dot{\boldsymbol{\sigma}}, \dot{\boldsymbol{\varepsilon}}^p, etc) \tag{2.9}$$

In the above equations (2.7), (2.8) and (2.9), $\boldsymbol{\sigma}$ is the stress tensor, $\boldsymbol{\varepsilon}^p$ is the plastic strain tensor, $\mathbf{s}$ is the deviatoric stress tensor defined as $\mathbf{s} = \boldsymbol{\sigma} - p\mathbf{I}$ (p is

11

the equivalent pressure stress and $\mathbf{I}$ is the identity tensor), $\boldsymbol{\alpha}$ is the back stress tensor (current center of the yield surface), $\mathbf{a}$ is the current center of the yield surface in the deviatoric space, k is the size of the yield surface (constant for a cyclically stable material), and H is the hardening modulus. Also, $\langle \ \rangle$ indicates the MacCauley bracket and the dot express the inner product of two tensors.

The models discussed in the following paragraphs are distinguished in two groups, based on the way that the hardening modulus H is defined. This affects the translation of the yield surface in the stress space in each plastic stress increment. More specifically, the hardening modulus H can be defined in two different ways. The first way is through the consistency condition $\dot{F} = 0$, which couples the hardening modulus with the kinematic hardening rule, as described in the classical model proposed by Prager (1956). The models falling into this category are called "coupled models". The second category comprises the so-called "uncoupled" models.

In the uncoupled models the plastic modulus is defined directly and it is influenced only indirectly by the kinematic hardening rule. For a given hardening rule, the movement of the yield surface along the specified direction of the rule is determined using the consistency condition. Examples of plasticity models that belong to this class are the so-called "two-surface" models proposed by Dafalias and Popov (1976), Drucker and Palgen (1981) and Tseng and Lee (1983).

2.3 Coupled models for cyclic plasticity

In those models the kinematic hardening rule can take several forms. A short description for some characteristic coupled models is given in the following paragraphs.

2.3.1 Linear and multilinear kinematic hardening rule

The linear kinematic hardening rule is the simplest model for cyclic plasticity modeling. Prager (1956) was the first to introduce the linear kinematic hardening model which employs a linear form of the kinematic hardening rule:

$$\dot{\mathbf{a}} = C\dot{\boldsymbol{\varepsilon}}^p \qquad (2.10)$$

where C is a constant. The development of such a model is rather standard and it is described in several textbooks [e.g. Dunne and Petrinic (2005)].

Improvement to the linear kinematic hardening model was proposed by Mroz (1967) as a multi-surface model, where each surface represents a constant work hardening modulus in the stress space.

2.3.2 The nonlinear kinematic hardening rules

From the large number of models that fall into this category, only the most representative ones are reported in the following paragraphs starting from the Armstrong - Frederic model.

i. <u>The Armstrong and Frederic model</u>

The first nonlinear kinematic hardening model has been proposed by Armstrong and Frederick (1966), who introduced a kinematic hardening rule for the "backstress" containing a "recall" term, which incorporates the fading memory effect of the strain path and essentially makes the rule nonlinear in nature. The kinematic hardening rule in this model is given in the form:

$$\dot{\mathbf{a}} = C\dot{\boldsymbol{\varepsilon}}^p - \gamma_i \boldsymbol{\alpha} \dot{\varepsilon}_q \tag{2.11}$$

where C, γ are parameters calibrated from cyclic test data. More specifically, C is the initial kinematic hardening modulus, and γ determines the rate at which the kinematic hardening modulus decreases with increasing plastic deformation. More details about this model, as well as its numerical integration and implementation scheme in finite element codes are presented in the Appendix.

The Armstrong - Frederick nonlinear kinematic hardening model was a breakthrough at the time it was introduced. Its advantages and capabilities were well appreciated by other researchers. Several of them applied improvements on its original form in order to improve its deficiencies and introduced new advanced models based on the same nonlinear hardening rule.

Other models that employ the nonlinear kinematic hardening rule concept have also been proposed. They have some important similarities with the Armstrong – Frederick model, which are obvious through the equations formulation. The most characteristic models of this type are briefly presented and discussed in the following.

ii. <u>The Chaboche model</u>

Chaboche and his co-workers in their relevant publications [Chaboche et al. (1979), Chaboche (1986)] proposed a model based on the decomposition of the nonlinear kinematic hardening rule proposed by Armstrong and Frederick in the form:

13

$$\dot{\mathbf{a}} = \sum_{i=1}^{M} \dot{\mathbf{a}}_i,$$

$$\dot{\mathbf{a}}_i = C_i \dot{\boldsymbol{\varepsilon}}^p - \gamma_i \mathbf{a}_i \dot{\varepsilon}_q \qquad\qquad (2.12)$$

Compared to the original basic Armstrong-Frederick model, the main advantage of the Chaboche model is that the hysteresis curve can be divided into i segments, where each segment can described quite efficiently adopting an appropriate pair of C_i, γ_i.

iii. <u>The Ohno and Wang model</u>

The Ohno-Wang (1993) model is also a superposition of several kinematic hardening rules. It was introduced in the form:

$$\dot{\mathbf{a}} = \sum_{i=1}^{M} \dot{\mathbf{a}}_i,$$

$$\dot{\mathbf{a}}_i = C_i \dot{\boldsymbol{\varepsilon}}^p - \gamma_i \mathbf{a}_i \left\langle \dot{\boldsymbol{\varepsilon}}^p \cdot \frac{\mathbf{a}_i}{f(a_i)} \right\rangle H \left\{ \mathbf{a}_i^2 - \left(\frac{C_i}{\gamma_t} \right)^2 \right\} \qquad (2.13)$$

and H here stands for the Heaviside step function. This modification allows for better simulation of the ratcheting (accumulation of plastic deformations) response of the material under uniaxial or multiaxial stress-controlled cyclic loading conditions.

iv. <u>The Guionnet model</u>

Guionnet (1992) proposed a model which uses some parameters, determined from biaxial ratcheting experiments. The Guionnet model basically modifies the original Armstrong - Frederick hardening rule by incorporating the effect of accumulated plastic strain in it. For cyclically stabilized material, the kinematic hardening rule in this model is reduced to the form:

$$\dot{\mathbf{a}} = m p_1^{m-1} \left[\left\{ \frac{2}{3} C - \gamma_1 (\mathbf{a} \cdot \mathbf{n}) \right\} \dot{\boldsymbol{\varepsilon}}^p - (\gamma_2 a) \mathbf{a} \, dp \right],$$

$$\mathbf{n} = \frac{2}{3} \left(\frac{d\boldsymbol{\varepsilon}^p}{dp} \right) \qquad\qquad (2.14)$$

where the coefficient a takes the following form:

14

$$a = p_1^n = p_{1M}^n, \, for \, p_1 = p_{1M},$$

$$a = p_{1M}^n \left(\frac{p_{1M}}{p_{1M} + p_1} \right)^{\beta}, \, for \, p_1 \leq p_{1M}, \qquad (2.15)$$

$$p_1 = \int_{I_k}^{Q} dp \, \, and \, \, p_{1M} = \int_{I_{k-1}}^{I_k} dp$$

Here, p_1 is the accumulated plastic strain between the last reversal (I_k and the current loading point (Q), and p_{1M} is the accumulated plastic strain between the last two reversals (I_{k-1} and I_k). The parameters C and γ are similar to those in the Armstrong and Frederick model and are determined from a uniaxial stable hysteresis curve. Two ratcheting parameters, γ_2 and β are determined using a biaxial ratcheting response. No clear guidelines are provided by Guionnet (1992) to determine m and n.

2.4 Uncoupled models for cyclic plasticity

In the case of the uncoupled models, the plastic modulus is defined directly by an expression and it is only indirectly influenced by the kinematic hardening rule. Three representative models of this category will be presented briefly in the following paragraphs.

i. The Drucker - Palgen model

According to the Drucker – Palgen (1982) model, the plastic modulus H is assumed to be strictly a function of the second invariant of the deviatoric stress tensor J₂ of the following form:

$$H = \left(A J_2^N \right)^{-1} \qquad (2.16)$$

where A and N are material constants evaluated from a segment of a stable hysteresis loop.

ii. The Dafalias - Popov model

The Dafalias & Popov (1976) model constitutes one of the most effective models to describe complex loading histories including cyclic plasticity. In this model, in addition to the yield surface the concept of a "Bounding Surface" is introduced, which obeys kinematic hardening. The yield surface is free to translate within the bounding surface describing any possible stress state. During excessive loading these two surfaces may come in contact at a unique point that describes the current stress state. If loading continuous into the plastic

15

regime, then the two surfaces translate together, so that an intersection may not occur.

Special attention is also paid on the definition of the plastic modulus in order to achieve a smooth transition from the elastic to the fully-plastic state which is also compatible with experimental observations. The model accounts for the gradual decrease of the value of H as hardening proceeds, and this evolution is of great importance for the successful modeling of a complex loading history associated with reverse plastic loading, especially in cases where Bauschinger effects are important.

The basic idea of this model is that the current tangent modulus depends on the "distance" δ in stress space of the current stress state and of that representing the immediately previous elastic stress state from a *bounding surface*. The plastic modulus H is described as follows:

$$H(\delta, \delta_{in}) = E_0^p + h(\delta_{in})\left(\frac{\delta}{\delta_{in} - \delta}\right) \tag{2.17}$$

where E_0^p is the (final) constant value of the plastic modulus tends to after sufficient plastic strain, δ_{in} is the distance of the last elastic state point from the bound and $h(\delta_{in})$ is a model parameter function of δ_{in} which controls the "steepness" of the stress-strain curve and is defined as follows:

$$h(\delta_{in}) = \frac{\alpha}{1 + b\left(\frac{\delta_{in}}{2\sigma_b}\right)^m} \tag{2.18}$$

In the above equation α, b and m are model constants and σ_b is the size of the Bounding Surface. Function h is calibrated through an experimental stress-strain curve.

iii. The Tseng – Lee model

The model proposed by Tseng & Lee (1983) is similar to the model outlined above, except that the bounding surface is replaced by the so-called *"memory surface"*. This surface is centered at the origin and hardens isotropically every time its stress level is exceeded. Thus, it represents the biggest state of stress developed in the loading history. During initial loading, since the two surfaces are in contact, the flow rule is based on the memory surface. During the loading phase the yield surface stays attached to the memory surface at the current stress point. It detaches on the first reverse loading that includes plastic deformation. Then the plastic modulus is described as follows:

16

$$H(\delta, \delta_{in}) = \hat{H}\left[1 + h\left(\frac{\delta}{\delta_{in} - \delta}\right)\right] \qquad (2.19)$$

where $\hat{H}$ is the plastic modulus of the memory surface after sufficient plastic strain. Similarly δ_{in} is the value of δ at the last elastic state. This is a model that combines simplicity of formulation with the features of bounding surface plasticity, and will be used in the present dissertation as a basis for the description of cyclic behavior of steel material in the inelastic range. In the following paragraphs of this chapter, a detailed presentation of this model ad its numerical implementation is offered.

2.5 Description of the Tseng - Lee model

In the plasticity models where the so-called "*Bounding Surface*" concept is adopted, the hardening modulus is defined by a given expression, not through the consistency condition. The Tseng – Lee (1983) model is an effective model to describe loading histories including cyclic plasticity adopting the "*Bounding Surface*" concept. In this model, in addition to the yield surface, a "*memory surface*" is introduced, which plays the role of a bound and obeys isotropic hardening (Figure 2.1). The yield (inner) surface (Y.S.) is free to translate and change shape within the memory surface (M.S.) through a mixed (combined) hardening rule. The memory surface is centered at the origin and hardens only isotropically every time its stress level is exceeded. Thus, it represents the highest level of stress developed in the loading history.
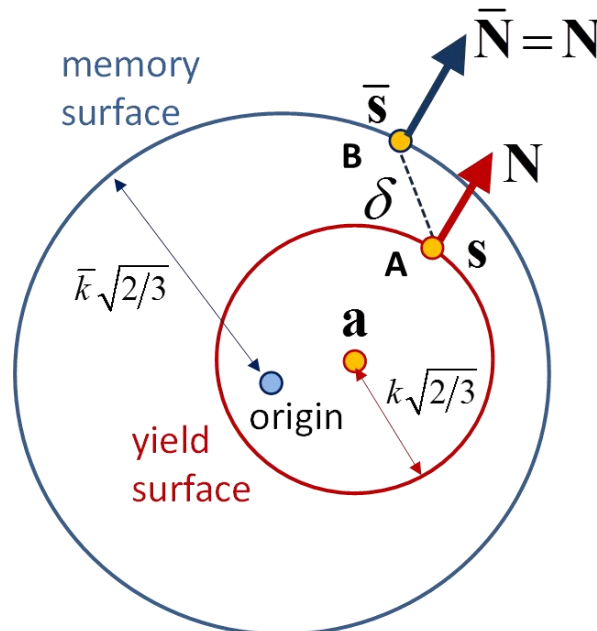

Figure 2.1: A schematic view of the two-surface model

17

During initial plastic loading, the flow rule is based on the yield surface and the hardening modulus depends on the relative distance of the current stress on the yield surface and an appropriately chosen stress point on the memory surface. When the yield surface reaches the memory surface during further loading, it stays attached to the memory surface at the specific stress point. The two surfaces lose contact when the first reverse loading occurs associated with plastic deformation. The expressions describing the yield surface $F=0$ and the memory surface $\bar{F}=0$ are respectively:

$$F = \frac{1}{2}(\mathbf{s}-\mathbf{a})(\mathbf{s}-\mathbf{a}) - \frac{K^2(\varepsilon_q)}{3} = 0 \tag{2.20}$$

$$\bar{F} = \frac{1}{2}(\bar{\mathbf{s}}\cdot\bar{\mathbf{s}}) - \frac{\bar{K}^2(\varepsilon_q)}{3} = 0 \tag{2.21}$$

where $\mathbf{s}$ is the deviatoric part of the stress tensor $\boldsymbol{\sigma}$, $\mathbf{a}$ is the deviatoric part of backstress tensor $\boldsymbol{\alpha}$, $\bar{\mathbf{s}}$ is the deviatoric stress on the memory surface and $K(\varepsilon_q), \bar{K}(\varepsilon_q)$ are functions of equivalent plastic strain ε_q, representing the size of the yield and the memory surfaces respectively. The rate of equivalent plastic strain is defined as follows:

$$\dot{\varepsilon}_q = \sqrt{\frac{2}{3}\dot{\boldsymbol{\varepsilon}}^P \cdot \dot{\boldsymbol{\varepsilon}}^P} \tag{2.22}$$

The flow rule is generally expressed as:

$$\dot{\boldsymbol{\varepsilon}}^p = \frac{1}{H}(\mathbf{N}\cdot\dot{\mathbf{s}})\mathbf{N} \tag{2.23}$$

where $\mathbf{N}$ is normal to the yield surface. If the two surfaces are not in contact, the normal vector $\mathbf{N}$ is the outward normal on the yield surface expressed as follows:

$$\mathbf{N} = \sqrt{\frac{3}{2}}\frac{1}{\|\mathbf{s}-\mathbf{a}\|}(\mathbf{s}-\mathbf{a}) \tag{2.24}$$

If the two surfaces are in contact, the normal vector $\mathbf{N}$ is common for both surfaces and has the following form:

$$\bar{\mathbf{N}} = \sqrt{\frac{3}{2}}\frac{1}{\|\bar{\mathbf{s}}\|}\bar{\mathbf{s}} \tag{2.25}$$

18

Note that $\mathbf{N}$ and $\bar{\mathbf{N}}$ are not unit vectors; their magnitude is equal to $\sqrt{3/2}$.

In this model, similar to all uncoupled models, the hardening modulus H is defined directly through an appropriate function. Motivated by experimental observations this definition of plastic modulus should account for the smooth transition from the elastic to the inelastic stage. The model accounts for the gradual decrease of the value of H as hardening proceeds, which is of particular importance for the successful modeling of strong low-cycle loading conditions associated with reverse plastic loading, the Bauschinger effect and subsequent inelastic loops.

The basic concept of this model is that the value of the hardening modulus H depends on the "distance" δ in stress space between the points A and B (Figure 2.1). Point A represents the current stress state on the yield surface, while point B is its "congruent point", defined as the point on the memory surface which has the same outward normal unit vector $\mathbf{N}$, as shown in Figure 2.1 ($\mathbf{N} = \bar{\mathbf{N}}$). More specifically H is described as follows:

$$H(\delta, \delta_{in}) = \hat{H}\left(1 + h\frac{\delta}{\delta_{in} - \delta}\right) \tag{2.26}$$

where $\hat{H}$ is the hardening modulus of the memory surface when the two surfaces get in contact. As a first approximation, the value of $\hat{H}$ can be considered as constant, but $\hat{H}$ could also be a function of equivalent plastic strain, as discussed in the following paragraphs. Parameter h affects the steepness of the strain-strain curve during plastic deformation. In the initial formulation of the Tseng – Lee model, h is assumed to be constant. Nevertheless, h can be also a function of plastic deformation, to be discussed next.

The evolution of backstress tensor is described using the Mroz (1967) rule and has the following rate form:

$$\dot{\mathbf{a}} = \dot{\mu}\,\mathbf{v} \tag{2.27}$$

where $\mathbf{v}$ is the unit vector along the direction of segment AB shown in Figure 2.1, written as follows:

$$\mathbf{v} = \frac{1}{\|\bar{\mathbf{s}} - \mathbf{s}\|}\left(\bar{\mathbf{s}} - \mathbf{s}\right) \tag{2.28}$$

where $\mathbf{s}$ is the deviatoric stress tensor and $\bar{\mathbf{s}}$ is the congruent point on the memory surface, and $\dot{\mu}$ is a multiplier defined by the consistency condition. It should be noted that the adopted rule for the evolution of the yield surface is not the same as the one originally proposed by Tseng –Lee, but the assumption of the

19

Mroz rule results to a more robust numerical implementation of the model [Kyriakides and Corona (2008)].

2.6 Numerical integration of the constitutive model

A numerical integration scheme of the Tseng-Lee model is proposed based on an "Elastic predictor – Plastic–corrector" method. The fundamental problem that needs to be solved at each iteration cycle can be briefly stated as follows:

"At a given stress state, denoted as state n, the stress tensor $\boldsymbol{\sigma}_n$, the backstress tensor $\mathbf{a}_n$, the equivalent plastic strain ε_{qn}, the sizes of the yield and memory surface $K_n, \bar{K}_n$ respectively, the distance δ_n between the two surfaces, and the initial distance between the two surfaces δ_{in} are known. Given the strain increment $\Delta\boldsymbol{\varepsilon}$, evaluate the state parameters at $n+1$. "

This problem is tackled by integrating numerically the constitutive equations of the Tseng-Lee model and it is described in the following paragraphs.

The numerical integration procedure starts with the computation of an elastic trial step, so that

$$\boldsymbol{\sigma}^e = \boldsymbol{\sigma}_n + \mathbf{D}\,\Delta\boldsymbol{\varepsilon} \tag{2.29}$$

where $\mathbf{D}$ is the fourth-order elastic rigidity tensor and $\boldsymbol{\sigma}^e$ is the trial elastic stress. If the trial stress $\boldsymbol{\sigma}^e$ falls within the yield surface, i.e.

$$F = \frac{1}{2}\left(\mathbf{s}^e - \mathbf{a}_n\right)\cdot\left(\mathbf{s}^e - \mathbf{a}_n\right) - \frac{K_n^2}{3} \leq 0 \tag{2.30}$$

where $\mathbf{s}^e$ is the deviatoric part of $\boldsymbol{\sigma}^e$, then the assumption of elastic behavior is correct and the final stress is equal to the trial stress $\boldsymbol{\sigma}_{n+1} = \boldsymbol{\sigma}^e$. If the above criterion is violated, then elastic-plastic behavior occurs, and the corresponding equations are considered.

The plastic correction step starts with the calculation of factor γ, defined as the elastic fraction of the total strain increment which, upon application, it will result to the maximum possible elastic stresses. This stress state corresponds to a point on the yield surface and it is achieved by applying a strain increment equal to $\gamma\Delta\boldsymbol{\varepsilon}$. In detail:

$$\mathbf{s}_n^{YS} = \mathbf{s}_n + \mathbf{D}\left(\gamma\Delta\boldsymbol{\varepsilon}\right) \tag{2.31}$$

The factor γ is calculated as follows:

20

$$\gamma = \frac{-3\left(\boldsymbol{\xi}_n \cdot \Delta \mathbf{s}\right) + \sqrt{9\left(\boldsymbol{\xi}_n \cdot \Delta \mathbf{s}\right)^2 + 3\left(\Delta \mathbf{s} \cdot \Delta \mathbf{s}\right) \cdot \left(2k^2 - 3\left(\boldsymbol{\xi}_n \cdot \boldsymbol{\xi}_n\right)\right)}}{3\left(\Delta \mathbf{s} \cdot \Delta \mathbf{s}\right)} \qquad (2.32)$$

where

$$\boldsymbol{\xi}_n = \mathbf{s}_n - \mathbf{a}_n \qquad (2.33)$$

and

$$\Delta \mathbf{s} = \mathbf{s}^e - \mathbf{s}_n . \qquad (2.34)$$

The definition of this stress state is necessary for the evaluation of the distance δ as it is described in the following paragraphs. The remaining strain increment is equal to $\left(1-\gamma\right)\Delta \boldsymbol{\varepsilon}$ and should be applied in order to complete the step. Considering the decomposition of the strain increment in an elastic and a plastic component, the new stress state can be described by the following equation:

$$\boldsymbol{\sigma}_{n+1} = \boldsymbol{\sigma}^e - \mathbf{D}\,\Delta \boldsymbol{\varepsilon}^p = \boldsymbol{\sigma}_n + \mathbf{D}\left(1-\gamma\right)\Delta \boldsymbol{\varepsilon} - \mathbf{D}\,\Delta \boldsymbol{\varepsilon}^p \qquad (2.35)$$

The above equation, assuming isotropic material behavior, can be written in the deviatoric form as follows:

$$\mathbf{s}_{n+1} = \mathbf{s}^e - 2G\,\Delta \boldsymbol{\varepsilon}^p \qquad (2.36)$$

During plastic strain increments, the hardening modulus $H\left(\delta\right)$ is defined as in Eq. (2.26), according to the relative distance in the stress space of the current stress point on the YS to its congruent point on the memory surface. The congruent point is defined as the point on the MS having the same outward unit vector as the point that represents the current stress state and lays on the YS. Using this definition and considering that the two surfaces are geometrically similar (Figure 2.1), the congruent point is uniquely defined as:

$$\overline{\boldsymbol{\sigma}} = \frac{\overline{K}}{K}\left(\boldsymbol{\sigma} - \boldsymbol{\alpha}\right) \Rightarrow \overline{\mathbf{s}} = \frac{\overline{K}}{K}\left(\mathbf{s} - \mathbf{a}\right) \qquad (2.37)$$

The distance between the current stress point and its congruent point is then calculated as follows:

$$\delta = \left[\left(\overline{\mathbf{s}}_n - \mathbf{s}_n\right) \cdot \left(\overline{\mathbf{s}}_n - \mathbf{s}_n\right)\right]^{1/2} \qquad (2.38)$$

21

The hardening modulus $H(\delta)$ is also a function of δ_{in} calculated through Eq. (2.26) as the initial distance of the two surfaces at the beginning of the loading sequence. The correct definition and update of the δ_{in} value is a critical procedure for obtaining accurate predictions from this model. More details for this issue are presented in the following paragraph.

The relative distance of the two surfaces indicated by the value of δ defines the way that the plastic loading will take place. Two cases are considered:

<u>Case 1</u>: If the distance between the two surfaces is zero ($\delta_n = 0$), then $H = \hat{H}$ and the increment of plastic strain $\Delta\boldsymbol{\varepsilon}^p$ is calculated from the integration of Eq. (2.23). Using a Forward-Euler scheme,

$$\Delta\boldsymbol{\varepsilon}^p = \frac{1}{\hat{H}}\left[\bar{\mathbf{N}}_n \cdot \left(\mathbf{s}_{n+1} - \mathbf{s}_n\right)\right]\bar{\mathbf{N}}_n \tag{2.39}$$

$$\bar{\mathbf{N}}_n = \sqrt{\frac{3}{2}}\frac{1}{\|\bar{\mathbf{s}}_n\|}\bar{\mathbf{s}}_n \tag{2.40}$$

Inserting equation (2.40) into equation (2.36), one obtains the following explicit expression for the deviatoric stress at the final state $n+1$:

$$\mathbf{s}_{n+1} = \mathbf{A}^{-1}\,\mathbf{b} \tag{2.41}$$

where

$$\mathbf{A} = \left[\mathbf{I} + \frac{2G}{\hat{H}}\left(\bar{\mathbf{N}}_n \otimes \bar{\mathbf{N}}_n\right)\right] \tag{2.42}$$

and

$$\mathbf{b} = \mathbf{s}^e - \frac{2G}{\hat{H}}\left(\bar{\mathbf{N}}_n \otimes \bar{\mathbf{N}}_n\right)\mathbf{s}_n \tag{2.43}$$

The new size of the memory surface at state $n+1$ is

$$\bar{K}_{n+1} = \sqrt{\frac{3}{2}\mathbf{s}_{n+1} \cdot \mathbf{s}_{n+1}} \tag{2.44}$$

and the new size of the yield surface is given by the corresponding function as follows:

$$K_{n+1} = K\left(\varepsilon_{qn+1}\right) \tag{2.45}$$

The equivalent plastic strain is updated as follows:

$$\varepsilon_{qn+1} = \varepsilon_{qn} + \Delta\varepsilon_q \tag{2.46}$$

where

$$\Delta\varepsilon_q = \sqrt{\frac{2}{3}\Delta\boldsymbol{\varepsilon}^p \cdot \Delta\boldsymbol{\varepsilon}^p} \tag{2.47}$$

and finally, the backstress tensor at $n+1$ is given by the following expression:

$$\mathbf{a}_{n+1} = \left(1 - \frac{K_{n+1}}{\bar{K}_{n+1}}\right)\mathbf{s}_{n+1} \tag{2.48}$$

<u>Case 2</u>: If the distance between the two surfaces is nonzero ($\delta_n > 0$), then

$$H = H(\delta_n) = \hat{H}\left(1 + h\frac{\delta}{\delta_{in} - \delta}\right) \tag{2.49}$$

and the increment of plastic strain $\Delta\boldsymbol{\varepsilon}^p$ is calculated from the integration of equation (2.23). Using a Forward-Euler scheme,

$$\Delta\boldsymbol{\varepsilon}^p = \frac{1}{H}\left[\mathbf{N}_n \cdot (\mathbf{s}_{n+1} - \mathbf{s}_n)\right]\mathbf{N}_n \tag{2.50}$$

where

$$\mathbf{N}_n = \sqrt{\frac{3}{2}}\frac{1}{\|\mathbf{s}_n - \mathbf{a}_n\|}(\mathbf{s}_n - \mathbf{a}_n) \tag{2.51}$$

Inserting Eq. (2.50) into Eq. (2.36), one obtains the following equation for the final deviatoric stress

$$\mathbf{s}_{n+1} = \mathbf{A}^{-1}\mathbf{b} \tag{2.52}$$

where

$$\mathbf{A} = \left[\mathbf{I} + \frac{2G}{H}(\mathbf{N}_n \otimes \mathbf{N}_n)\right] \tag{2.53}$$

and

$$\mathbf{b} = \mathbf{s}^e - \frac{2G}{H}(\mathbf{N}_n \otimes \mathbf{N}_n)\mathbf{s}_n \tag{2.54}$$

At this point the size of the MS should be checked. If the application of the strain increment results to a stress point inside the MS, then the MS size should be unchanged. However, if the resulting stress state falls outside the MS, then the MS should expand in order to coincide with the YS at the point that refers to the current stress state. In this case the new size of the yield surface is given by Eq.

23

(2.45). In addition, the increment of plastic strain and the equivalent plastic strain at state $n+1$ are given by Eq. (2.46) and (2.47). Finally, the backstress tensor (position of the yield surface center) at $n+1$ is given by the integration of expression (2.27) with an Euler-forward scheme:

$$\mathbf{a}_{n+1} = \mathbf{a}_n + \Delta\mu\,\mathbf{v}_n \tag{2.55}$$

where

$$\mathbf{v}_n = \frac{1}{\left\| \overline{\mathbf{s}}_n - \mathbf{s}_n \right\|} \left(\overline{\mathbf{s}}_n - \mathbf{s}_n \right) \tag{2.56}$$

The quantity $\Delta\mu$ is calculated from the consistency condition:

$$F = \frac{1}{2} \left(\mathbf{s}_{n+1} - \mathbf{a}_{n+1} \right) \cdot \left(\mathbf{s}_{n+1} - \mathbf{a}_{n+1} \right) - \frac{K_{n+1}^2}{3} \le 0 \tag{2.57}$$

Inserting Eq. (2.55) into Eq. (2.57), one obtains

$$\Delta\mu = \mathbf{c} \cdot \mathbf{v}_n - \sqrt{\left(\mathbf{c} \cdot \mathbf{v}_n \right)^2 - \left(\mathbf{c} \cdot \mathbf{c} \right) + \frac{2}{3} K_{n+1}^2} \tag{2.58}$$

where

$$\mathbf{c} = \mathbf{s}_{n+1} - \mathbf{a}_n \tag{2.59}$$

Finally, the new congruent point is computed

$$\overline{\mathbf{s}}_{n+1} = \frac{\overline{K}}{K} \left(\mathbf{s}_{n+1} - \mathbf{a}_{n+1} \right) \tag{2.60}$$

and distance between the two surfaces in the stress space is calculated:

$$\delta_{n+1} = \left[\left(\overline{\mathbf{s}}_{n+1} - \mathbf{s}_{n+1} \right) \cdot \left(\overline{\mathbf{s}}_{n+1} - \mathbf{s}_{n+1} \right) \right]^{1/2} \tag{2.61}$$

The calculated distance δ_{n+1} is compared with the initial distance δ_{in} which is defined as the distance in the stress space of the current and the congruent point measured at the initiation of plastic deformation of the material, either under monotonic loading or after a load reversal. The correct update procedure of δ_{in} plays a significant role in the accuracy of the model, especially in the case of arbitrary changing loading directions. More details on this are

24

reported in the following section. It is important to note that this parameter has to be stored along with other key parameters during the numerical analysis.

Once the new stresses, backstress and sizes of YS and MS are calculated, the elastoplastic rigidity tensor has to be defined. The formulation adopted is using the "tangent stiffness" tensor defined as:

$$\mathbf{D}^{ep} = \mathbf{D} - \frac{9G^2 \left(\boldsymbol{\xi}_{n+1} \otimes \boldsymbol{\xi}_{n+1} \right)}{K^2 \left(H + 3G \right)} \qquad (2.62)$$

The integration scheme described above is used for the numerical implementation of the constitutive plasticity model into a finite element code for the general 3D case and for the plane-strain case. Towards this purpose, two user-subroutines (UMAT) for the commercial finite element code ABAQUS have been developed and implemented into the code for the plane-strain case and the general 3D case respectively.

2.7 Prediction of ratcheting rate

The performance of the Tseng-Lee model for predicting uniaxial ratcheting behavior is examined. A complete stress-controlled cycle of a metal material is considered under uniaxial loading conditions between two stress levels denoted as σ_{max} and σ_{min} with $\sigma_{max} > 0$, and $\sigma_{min} < 0$. Furthermore σ_{max} exceeds the initial yield stress. The stress variation is non-symmetric with positive mean stress $(\sigma_{max} + \sigma_{min} > 0)$ as illustrated in Figure 2.2. It is further assumed that σ_{max} is on the memory surface and that the size of the yield (inner) surface is assumed constant, representing a stabilized material. An analytical solution for the residual strain $\Delta\varepsilon_r$ accumulated in this cycle is sought.

Institutional Repository - Library & Information Centre - University of Thessaly
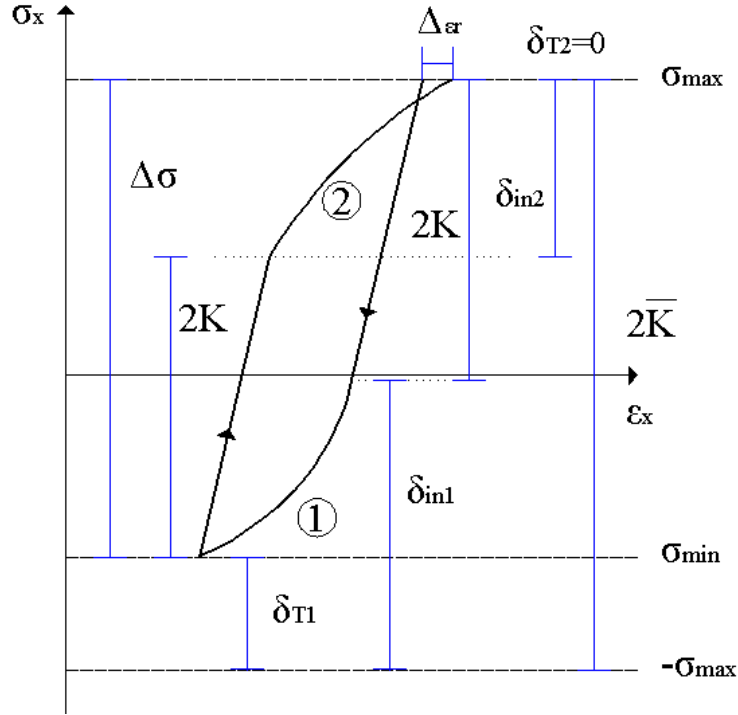18/05/2024 09:43:48 EEST - 3.145.36.43

Figure 2.2: Stress-controlled cyclic loading

The stress cycle assumed for this example consists of two plastic loading steps of opposite signs under uniaxial loading conditions. Starting from a stress level equal to σ_{max}, the first plastic deformation occurs during the unloading phase, at region (1). The second phase consists of reloading the material from σ_{min} until the σ_{max} stress is reached again to complete the load cycle. In this phase, plastic deformation occurs at region (2). For uniaxial loading conditions the plastic strain increment in regions (1) and (2) is equal to:

$$\dot{\varepsilon}_x^p = \frac{1}{H(\delta)}\dot{\sigma}_x = -\frac{1}{H(\delta)}\dot{\delta} \tag{2.63}$$

where $H(\delta)$ is defined in Eq. (2.26). Equation (2.63) is a function of the stress distance δ and can be integrated from an initial stress distance δ_{in} to a final stress distance δ_T, resulting in the plastic strain $\Delta\varepsilon_j^p$ associated with each plastic loading region (1) or (2):

$$\Delta\varepsilon_j^p = \frac{1}{\hat{H}(h-1)^2}\left[-\left(\delta_{inj} - \delta_{Tj}\right)(h-1) + \delta_{inj}h\left(\ln\left[\delta_{inj}h\right] - \ln\left[\delta_{inj} + \delta_{Tj}(h-1)\right]\right)\right], j=1,2 \tag{2.64}$$

26

where the value $j{=}1$ corresponds to unloading/reverse loading in region (1) and the value $j{=}2$ corresponds to re-loading in region (2). Parameters $\delta_{in1}, \delta_{in2}, \delta_{T1}, \delta_{T2}$ can be expressed with the use of Figure 2.2 as follows:

$$
\begin{aligned}
\delta_{in1} &= \sigma_{max} - \sigma_{min} - 2K \\
\delta_{in2} &= 2\left(\sigma_{max} - K\right) \\
\delta_{T1} &= -\left(\sigma_{max} + \sigma_{min}\right) \\
\delta_{T2} &= 0
\end{aligned}
\tag{2.65}
$$

Moreover, the following expressions are also valid from Figure 2.2:

$$
\delta_{in1} - \delta_{T1} = \delta_{in2} - \delta_{T2} = \sigma_{min} - \sigma_{max} - 2K
\tag{2.66}
$$

The accumulated plastic strain at the end of the cycle $\Delta\varepsilon_r$ is equal to the difference of plastic strain during unloading $\Delta\varepsilon_1^p$ and reloading $\Delta\varepsilon_2^p$. Using equations(2.64), (2.65) and(2.66), and denoting $\Delta\sigma = \sigma_{max} - \sigma_{min}$ the following expression for the accumulated plastic strain can $\Delta\varepsilon_r$ can be derived:

$$
\Delta\varepsilon_r = -\frac{h\left(\Delta\sigma - 2K\right)\left(\ln\left[h\left(\Delta\sigma - 2K\right)\right] + \ln\left[\Delta\sigma - 2K\right]\right) + \left(h-1\right)\left(2\bar{K} - \Delta\sigma\right)}{\hat{H}\left(h-1\right)^2} +
$$

$$
+\frac{2h\left(\ln\left[2h\left(\bar{K}-K\right)\right] - \ln\left[2\left(\bar{K}-K\right) + \left(h-1\right)\left(2\bar{K}-\Delta\sigma\right)\right]\right)\left(\bar{K}-K\right) + \left(h-1\right)\left(2\bar{K} - \Delta\sigma - 2\left(\bar{K}-K\right)\right)}{\hat{H}\left(h-1\right)^2}
$$

$$
\tag{2.67}
$$

From Eq. (2.67), one readily obtains that $\Delta\varepsilon_r{=}0$ for $h=0$. Furthermore the limit value of $\Delta\varepsilon_r$ in Eq. (2.67) when $h\rightarrow1$ is:

$$
\Delta\varepsilon_r = \frac{\left(2K - \Delta\sigma\right)\left(\Delta\sigma - 2\bar{K}\right)}{4\hat{H}\left(K - \bar{K}\right)},\ h\rightarrow1
\tag{2.68}
$$

It is interesting to note that for the type of problems considered in this case, the ratcheting rate predicted by the Tseng – Lee model depends on the applied stress range and the relevant sizes of the yield and memory surfaces. Moreover, for given values of $\sigma_{max}, \sigma_{min}$, K, $\bar{K}$ and h, the predicted ratcheting rate is constant. Note that for $h{=}0$, the model has a constant hardening modulus equal to $\hat{H}$ and predicts zero ratcheting $(\Delta\varepsilon_r{=}0)$, since it becomes identical to the linear kinematic hardening model.

27

Introducing the non-dimensional parameters $\Sigma = \Delta\sigma/2K$, $\Phi = \bar{K}/K$, $\Lambda = \hat{H}/2K$, a parametric analysis is conducted to examine the ratcheting predictions of the constitutive model. In Figure 2.3 the ratcheting rate prediction of the model for $h \to 1$ is shown in terms of the normalized stress amplitude. The ratcheting rate is zero when $\Sigma = 1$, which corresponds to elastic cyclic loading ($\Sigma = 2K$), or when $\Sigma = \Phi$, where the stress variation $\Delta\sigma$ is equal to the size of the memory surface $2\bar{K}$. This corresponds to symmetric loading, which has been experimentally shown not to cause ratcheting. It is also worth mentioning that the ratcheting rate increases as the Φ parameter increases. Moreover, for a given value of Φ, the ratcheting rate in terms of Σ maximizes when $\Sigma = (\Phi+1)/2$.

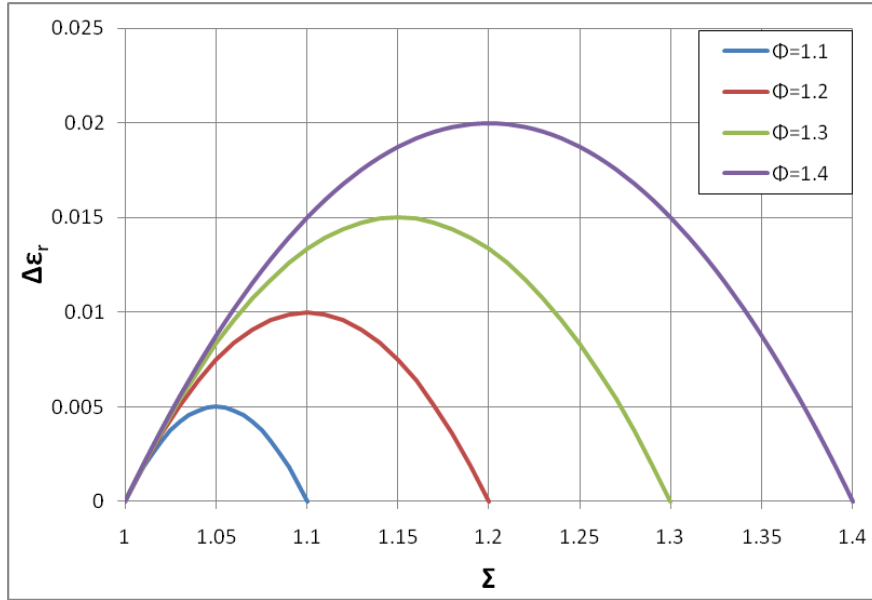Figure 2.3: Parametric ratcheting predictions for $h=1$, $\Lambda=2.5$

If $h > 0$, Eq. (2.67) can be rewritten with the use of the non-dimensional parameters Σ, Φ and Λ as follows:

$$\Delta\varepsilon_r = -\frac{h\big(-(1+\Sigma)\ln[h]\big)+(\Phi-1)\ln\left[\dfrac{h(\Phi-1)}{\Sigma(1-h)+h\,\Phi-1}\right]}{\Lambda(h-1)^2} \qquad (2.69)$$

This form is used for a parametric study that shows the effect of parameter h on the ratcheting rate, as illustrated in Figure 2.4. In this graph there is a general increase of ratcheting rate due to an increase of the parameter h. This increase is more significant for values of h up to 0.2, especially for lower values of Σ [Figure 2.4(b)]. As Σ increases and approaches the value of Φ, the effect of parameter h becomes less significant.

28

The effect of parameter Λ on the ratcheting predictions of the model for the loading case under consideration is presented in Figure 2.5. It is observed that lower Λ values, (i.e. lower constant values of the hardening parameter $\hat{H}$), result in higher ratcheting rates. As the value of Λ increases, the predicted ratcheting rates decrease drastically. Finally, for the specific values of Φ and Σ, the ratcheting rate maximizes when $h = 0.5$ as shown in Figure 2.5(b).
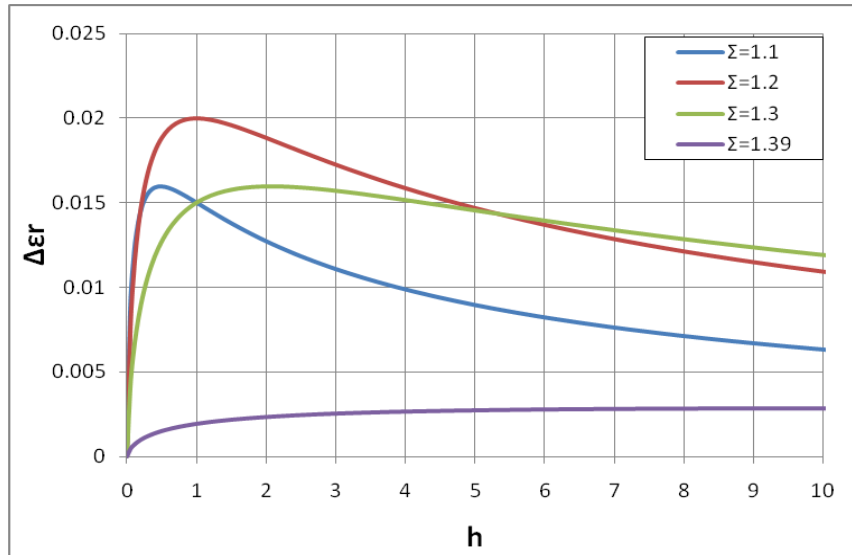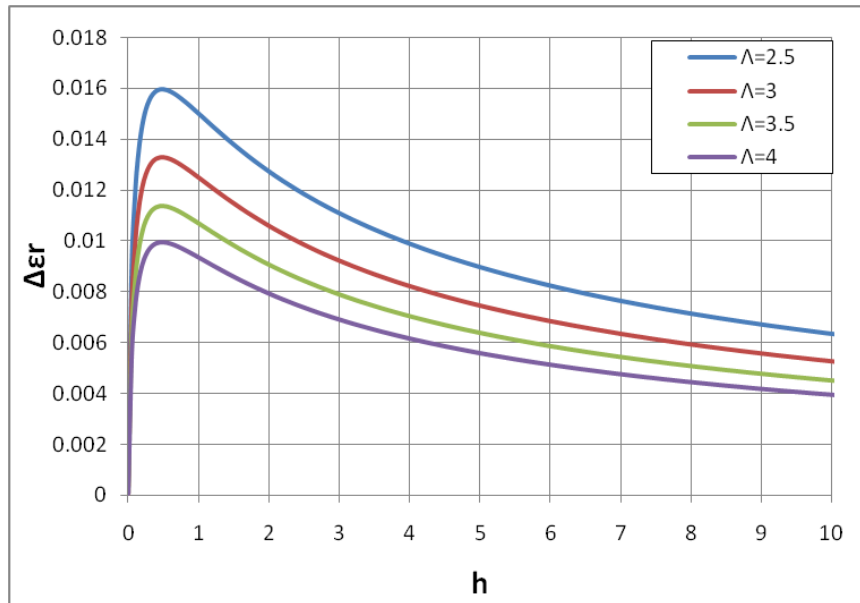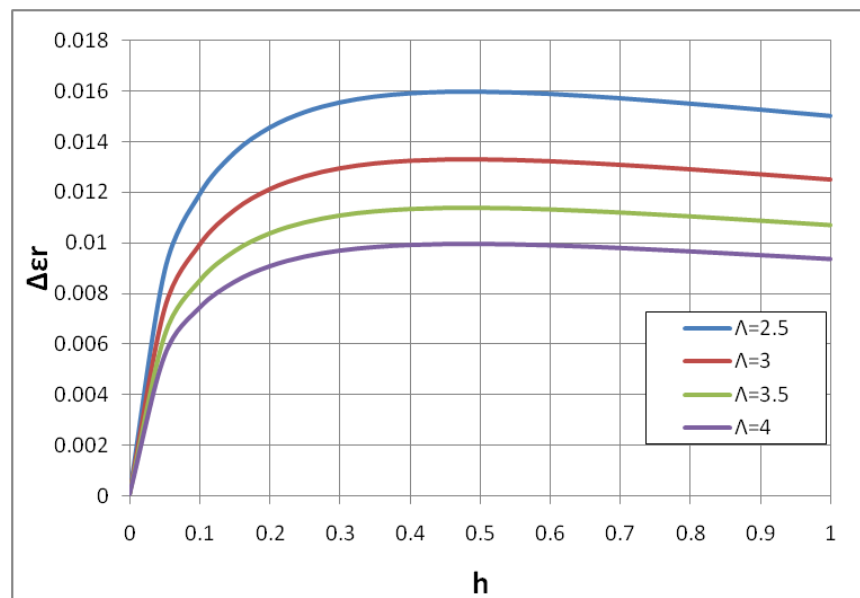

(a)
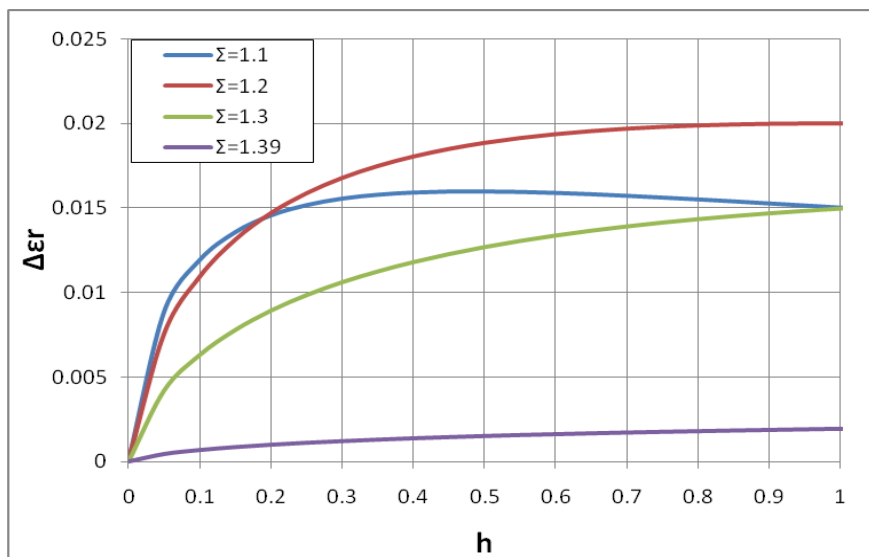
(b)

Figure 2.4: The effect of the parameter h on the ratcheting rate, $\Phi = 1.4$, $\Lambda = 2.5$: (a) General behavior, (b) Graph detail.

29

(a)

(b)

Figure 2.5: The effect of the parameter h on the ratcheting rate, $\Phi = 1.4$, $\Sigma = 1.1$: (a) General behavior, (b) Graph detail.

In the following paragraphs, the ratcheting capabilities of the Tseng-Lee model are compared with the corresponding capabilities of other plasticity models where only one surface is used. The ratcheting rate according to these models can be zero if the linear kinematic hardening rule is used or constant if the nonlinear kinematic hardening rule is used. It can only vary if an isotropic term is combined with the nonlinear kinematic hardening rule [Varelis (2010)].

The Tseng-Lee model allows for varying ratcheting rate simulations as shown in the example presented in Figure 2.6(a) and (b). In Figure 2.6(a), the

30

unsymmetrical cyclic stress-strain curves resulting using the Tseng-Lee model are presented. In these simulations the material is loaded up to a maximum stress level and then unloaded until the minimum stress level is achieved. Moreover, the size of the yield surface is assumed as constant, shrinking or expanding.

As presented in Figure 2.6(b), depending on the assumption adopted, the ratcheting rate can be constant but nonzero if the yield surface is assumed to be stable, it can increase if the yield surface shrinks with increasing plastic deformation or it can decrease if the yield surface expands with increasing plastic deformation. In addition, when the yield surface stabilizes after a few plastic loading cycles, the ratcheting rate becomes constant, as the material follows the same stress-strain curve as shown in Figure 2.2.

The increasing ratcheting rate when the yield surface shrinks as plastic deformation increases is attributed to the fact that, upon several loading reversals in the plastic regime, the plastic deformation will initiate at stress levels having greater distance from the maximum/minimum value, therefore the final stress level will be reached at increased strain value. On the contrary, when the yield surface expands as plastic deformation increases, upon several loading reversals, plastic deformation will initiate at a stress level which is closer to the maximum stress of the load cycle. This will result to reduced plastic deformations for each subsequent cycle and consequently to a decreasing ratcheting rate. The proper calibration of the model parameters allows for precise ratcheting simulations.

(a)

31
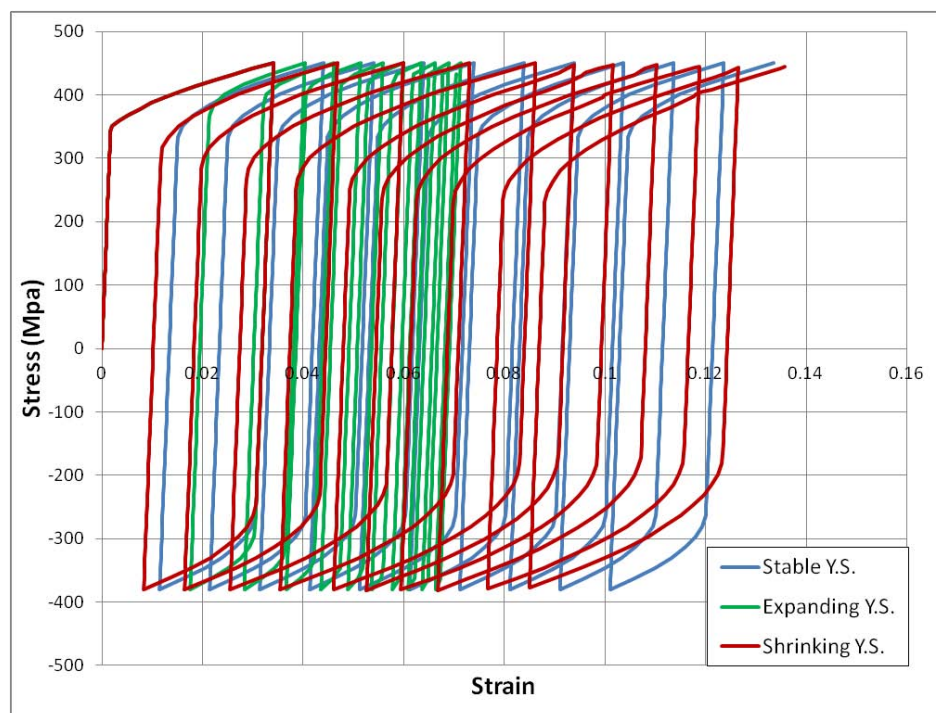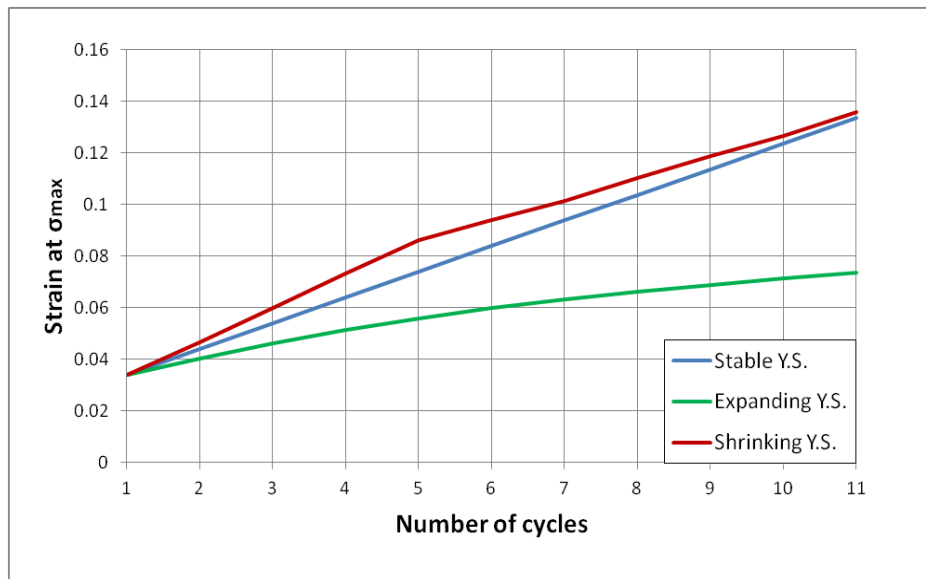
(b)

Figure 2.6: (a) Stress-strain loops, (b) Ratcheting evolution

The ratcheting performance of the Tseng-Lee model under biaxial loading is also examined through an illustrative example. Biaxial ratcheting can take place when the material is stressed in one direction while plastic deformation takes place in the orthogonal direction. A characteristic example of such loading scenario is the application of internal pressure to a pipe which is also subjected to cyclic bending in the plastic regime. To simulate the biaxial ratcheting effect, a "one element" model is assumed that is first subjected to a constant stress load in the y-direction. Subsequently the element is subjected to symmetric strain-controlled cyclic loading which results to plastic deformation, keeping the stress in the y-direction constantly applied. This load pattern will result to accumulation of plastic deformation in the y-direction, even if the load at this direction does not change. The Tseng-Lee model predicts a constant ratcheting rate in the y-direction if the yield surface is assumed to be constant, also verified by Hassan et al. (1994). If the yield surface is assumed to expand or shrink, the ratcheting rate remains constant but its absolute value is smaller or higher that the corresponding value predicted when the yield surface is constant as shown in Figure 2. **7**.
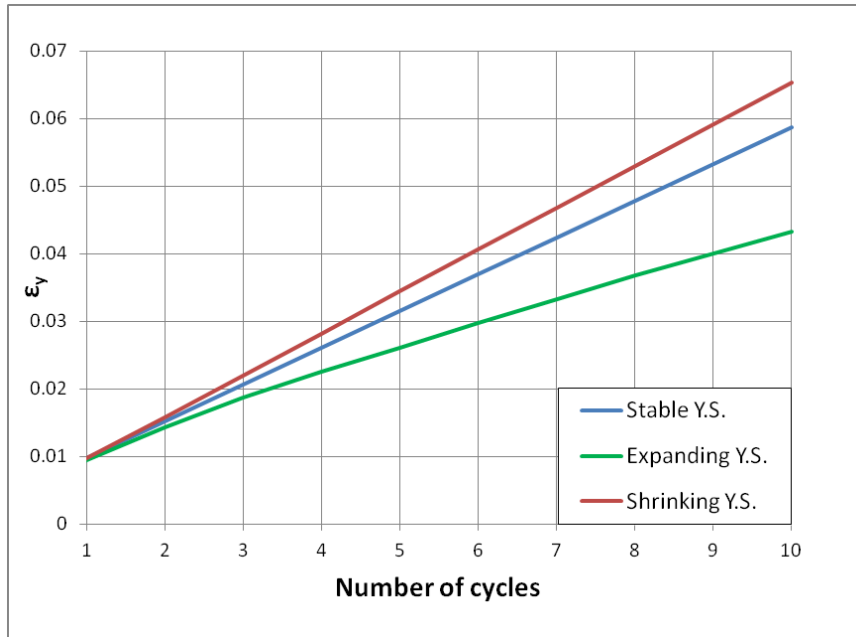
32

Figure 2. 7: Biaxial ratcheting evolution

2.8 Proposed modifications of the Tseng–Lee constitutive model

2.8.1 Criteria for the update of the δ_{in} value

In the original formulation of the Tseng-Lee model described in Tseng and Lee (1983), it is stated that during uniaxial cyclic loading the length of the elastic unloading chord between the current load point on the YS and the previous position at which the elastic unloading initialized can be used as a criterion of updating the value of δ_{in}. Furthermore, sudden directional change of $\dot{s}$ during the loading process may result in a distance between the two surfaces δ greater than the initial distance δ_{in} which means that under these circumstances the value of δ_{in} should be updated by δ. However, no additional information has been provided by Tseng & Lee (1983) on this matter.

A systematic approach on the update procedure of δ_{in} was presented recently by Lee et al. (2007) where the "overshooting" behavior of the model is discussed. This problem was first addressed by Khan and Huang (1995) and it is observed when the material is elastically unloaded with limited plastic deformation before it is reloaded to the original stress state (the last state before the unloading) following plastic deformation, as illustrated in the following figure.
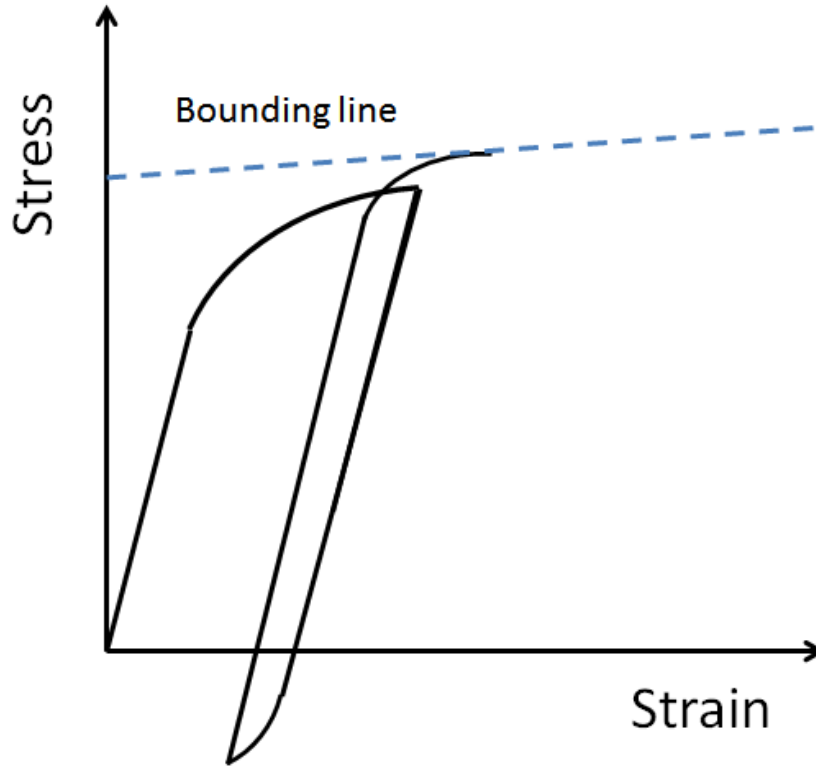
33

Figure 2. 8: The overshooting problem in the two-surface model.

The early work by Tseng and Lee (1983) and Dafalias and Popov (1976) suggested the use of the previously defined value of δ_{in} without any update to overcome this problem, but this is in contradiction with the updating procedure used in the model. Lee et al. (2007) suggested that the value of δ_{in} should be only updated for loading scenarios whose stress directions are different for more than 180 degrees. The change of loading direction is monitored using the angle between the stresses on the loading surface for two subsequent steps. In this case, the new δ_{in} should be a linear combination of the newly evaluated stress distance and the former value of δ_{in}.

In the integration scheme presented in the previous section, the "angle-change" update criterion is adopted: at each loading step, the loading direction in the previous and the new load step is monitored using the $\mathbf{v}_{old}$, $\mathbf{v}_{new}$ tensors respectively, defined as:

$$\mathbf{v}_{old} = \frac{\mathbf{s}_n - \mathbf{a}_n}{|\mathbf{s}_n - \mathbf{a}_n|}, \ \mathbf{v}_{new} = \frac{\mathbf{s}_{n+1} - \mathbf{a}_{n+1}}{|\mathbf{s}_{n+1} - \mathbf{a}_{n+1}|} \tag{2.70}$$

The angle θ between $\mathbf{v}_{old}$, $\mathbf{v}_{new}$ is defined using the inner product rule:

$$\theta = \cos^{-1}(\mathbf{v}_{old} \cdot \mathbf{v}_{new}) \tag{2.71}$$

34

and it is compared to a limit angle value $\theta_{\lim}$. The limit angle does not have to be 180 degrees as suggested by Lee et. al. (2007). If a smaller value is adopted, the results improve considerably, especially in the case of abrupt change of loading directions, as for example when buckling takes place.

2.8.2 Treatment of the yield plateau and the strain hardening region

Most structural steels exhibit a plastic plateau region on the stress-strain curve for structural steels after the initial material yielding. This region, also known as the Lüders region, is extended up to a certain strain level until the material stress-strain curve enters the strain hardening region. The most commonly used classical plasticity models are not able to capture this behavior. For example, the perfect plasticity model assumes that the hardening value is equal to zero. Nonlinear kinematic models cannot describe the abrupt change of the stress-strain curve after the initial yielding, nor can it describe the yield plateau regions. This deficiency has been well recognized by many researchers and modifications of the aforementioned plasticity models have been proposed.

For the case of nonlinear kinematic hardening models, Ucak and Tsopelas (2011) have proposed a modified model defining a critical plastic strain level is defined as the point where the plastic plateau region ends. For the models using more than one surface, the equivalent plastic strain limit and the plastic work are used to define the end of the plateau region as in the works of Shen et al. (1992) and Usami et al. (2000).

In the original description of the Tseng-Lee model, the plastic plateau is treated by assuming that the yield and the memory surface coincide before loading and by adopting a function to describe the hardening modulus for the memory surface. The proposed function depends on the equivalent plastic strain and it is calibrated accordingly based on experimental monotonic curves. In the present study this formulation is adopted. More specifically, the parameter $\hat{H}$ found in the general description of the hardening modulus as given in Eq. (2.26) is substituted by a function of the equivalent plastic strain $\bar{H}(\varepsilon_q)$, described in Eq. (2.72). This function can take the value of zero (or a very small value to avoid possible numerical convergence problems) if the equivalent plastic strain is less than a critical value ε_{qcr} defined as the equivalent plastic strain at the end of the plastic plateau (Figure 2. **9**). At this range the model reduces to a perfect plasticity model. When the critical value ε_{qcr} is exceeded, the function $\bar{H}(\varepsilon_q)$ can take a linear or a nonlinear form, allowing for better simulation of the material behavior in the strain hardening region.

Such a nonlinear form has been also adopted by Usami et al. (2000) where the plastic work is used instead of the equivalent plastic strain. In this study, the

plastic work is replaced by the equivalent plastic strain for simplicity and the adopted formula is presented in Eq. (2.72):

$$\bar{H}(\varepsilon_q) = 0, \ \varepsilon_q \leq \varepsilon_{qcr}$$

$$\bar{H}(\varepsilon_q) = \frac{\hat{H}}{1 + \omega\varepsilon_q}, \ \varepsilon_q > \varepsilon_{qcr} \tag{2.72}$$

In this equation, ω is a material parameter that can be calibrated using a monotonic loading material stress-strain curve, as for example the curve resulting from a tensile test. Note that by varying the value of the parameter ω, the stress-strain curve can simulate linear or nonlinear hardening after the yield plateau, as well as the reduction of the hardening modulus near the area of the ultimate stress.
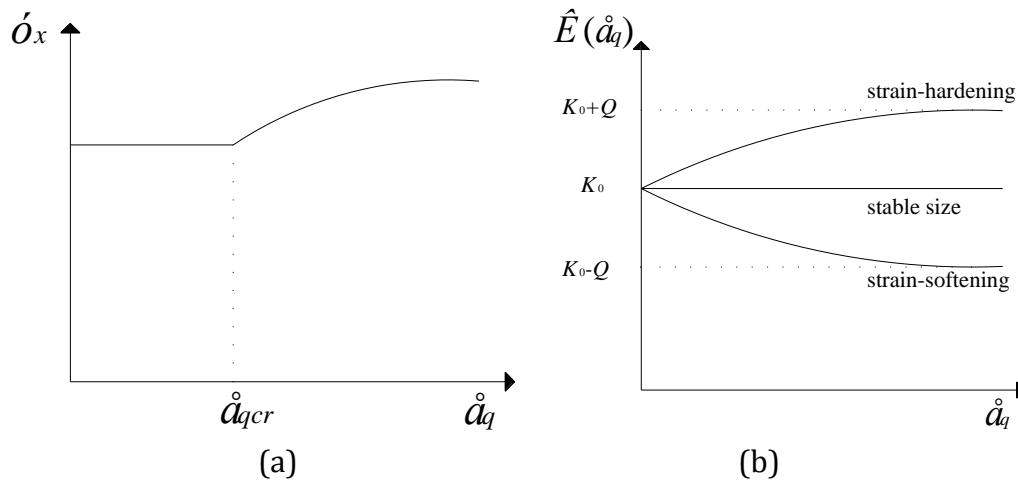

Figure 2. 9: (a) Plastic plateau, (b) Yield surface size variation

Moreover, the size of the yield surface can be assumed as a function of the equivalent plastic strain, introducing mixed (isotropic and kinematic) hardening. This formulation allows for simulating accurately cyclic hardening or softening of the material inside or outside the plateau region. An exponential function for determining the size of the yield surface of the following form is adopted:

$$K(\varepsilon_q) = K_0 + Q\left(1 - e^{b\varepsilon_q}\right) \tag{2.73}$$

The function enables the control of the yield surface change rate, as well the prediction of stabilization phenomena. In Eq. (2.73) K_0 is the initial yield stress, Q is the total change of the initial yield stress until a saturation value K_s is reached ($K_s = Q + K_0$) and b is a term that defines the rate at which the saturated values are reached. Positive values of the parameter Q refer to cyclic

36

hardening conditions, while negative values of Q refer to cyclic softening conditions [Figure 2. 9(b)]. The calibration of the parameters K_0, Q and b is performed with the use of experimental material curves. Including this function in the model to describe the changing size of the yield surface does not modify the methodology described in a previous section for its numerical integration.

An example is presented in Figure 2.10 concerning the precise simulation of plastic plateau in the material stress-strain curve of many structural steels, as well as the Bauschinger effect that appears at load reversals. In particular, a characteristic uniaxial cyclic loading test example from a coupon test on a TS590 high-strength steel specimen is presented, reported in Bursi (2012). The predictions of the Armstrong-Frederick (1966) model denoted as "A-F", as well as the predictions of a simple linear kinematic hardening model denoted as "LKH" are compared with the predictions provided by the Tseng-Lee model. The efficient description of initial yielding and the Bauschinger effect is a basic advantage of bounding surface models, with the respect to nonlinear kinematic hardening models.
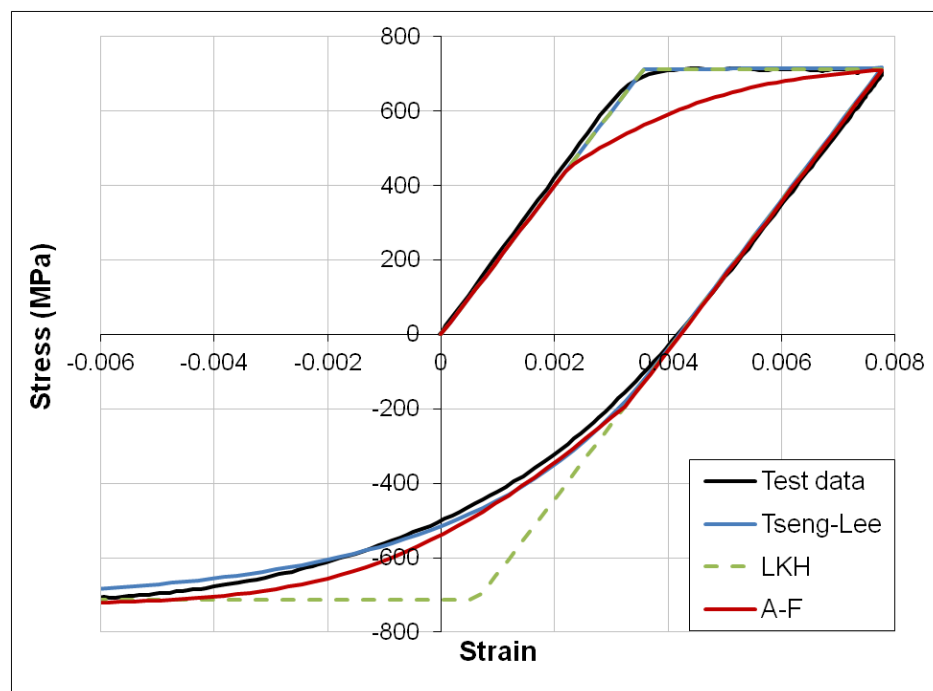

Figure 2.10: Plastic plateau and Bauschinger effect simulation.

2.8.3 Modifications for improved ratcheting performance

2.8.3.1 The hardening modulus function formulation

The form of hardening modulus expression in Eq. (2.26) may result to unrealistic ratcheting predictions, especially when the actual stress-strain

37

material curve under stress-controlled cyclic loading presents sharp edges near the location of the maximum stress level. The reason is that Eq. (2.26) implies a hardening modulus equal to $\hat{H}$ when the two surfaces get in contact ($\delta = 0$). Note that $\hat{H}$ is the hardening modulus of the outer surface and its value is rather small. Experimental results from cyclic material testing, have demonstrated that this smooth transition is not encountered in actual material curves, as for example in high-strength steel specimens presented in Figure 2.11.

To account for this phenomenon, an additional term is added to the expression of the hardening modulus, so that the hardening modulus when the two surfaces get in contact ($\delta \to 0$) is greater than $\hat{H}$. Taking into consideration the modification for $\bar{H}$ introduced in Eq. (2.72) and Eq.(2.26), the following equation is proposed for the hardening modulus:

$$H(\delta) = \bar{H}\left[1 + h^* \frac{\delta + c}{\delta_{in} - \delta}\right] \qquad (2.74)$$

where c is a constant affecting the hardening modulus for $\delta \to 0$ and h^* is a parameter to be discussed in the next section.

2.8.3.2 The effect of parameter "h" on ratcheting performance

In the initial formulation of the Tseng – Lee model, parameter h is assumed constant. Nevertheless, in various ratcheting simulation problems presented in the literature [e.g. Shen et al. (1992)], it has been demonstrated that this assumption may not be necessarily true. Several expressions have been proposed for this parameter in order to overcome the inaccuracies observed in the simulation results.

In the work of Shen et al. (1992), a linear function of the parameter h is introduced, that employs the distance δ of the two surfaces to describe the evolution of the parameter h in the form:

$$h = a\delta + b \qquad (2.75)$$

where the material parameters a,b are calibrated from appropriate experimental stress-strain curves, like the one presented in Figure 2.11(a).

Another approach to define an equation for parameter h is to adopt the nonlinear equation available in the work of Dafalias & Popov (1976). Equation (2.26) is the original equation that defines the hardening modulus and is quite similar to the corresponding equation proposed by Dafalias & Popov (1976). More specifically, in the Dafalias & Popov model, parameter h is a function of the ratio of the initial distance between the yield and memory surfaces at the current stress state and it is given by the following nonlinear equation:

38

$$h = \frac{a}{1 + b\left(\dfrac{\delta_{in}}{K\left(\varepsilon_q\right)}\right)^m} \qquad (2.76)$$

where a, b, m are material parameters calibrated from the experimental stress-strain curve.

The ratcheting rate predicted by the aforementioned expressions of h is compared with material test data derived for TS590 high-strength steel grade. A cyclic stress-controlled test on this material between two stress levels with non-zero mean stress ($\sigma_{max} = 739\,\text{MPa}$, $\sigma_{min} = -587\,\text{MPa}$), presented in Figure 2.11. The test has been conducted by CSM, Italy, and it is reported in Bursi (2012). In Figure 2.11(a) the first cycles of this test are presented, where the ratcheting rate observed is almost linear for the first 30 cycles, as shown in Figure 2.11(b).


(a)

39
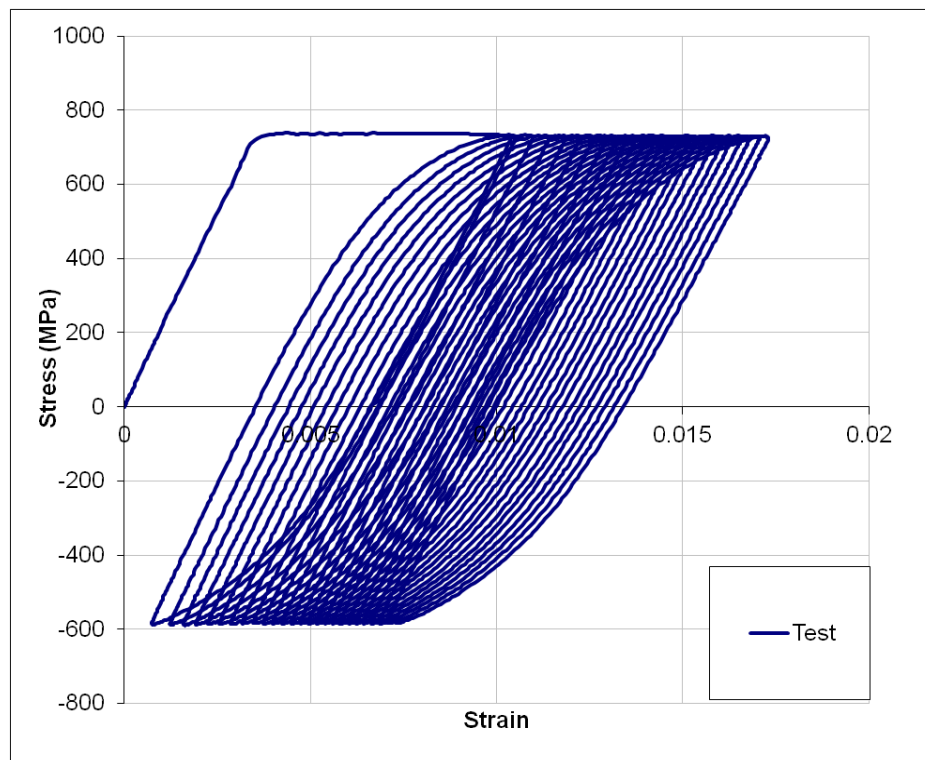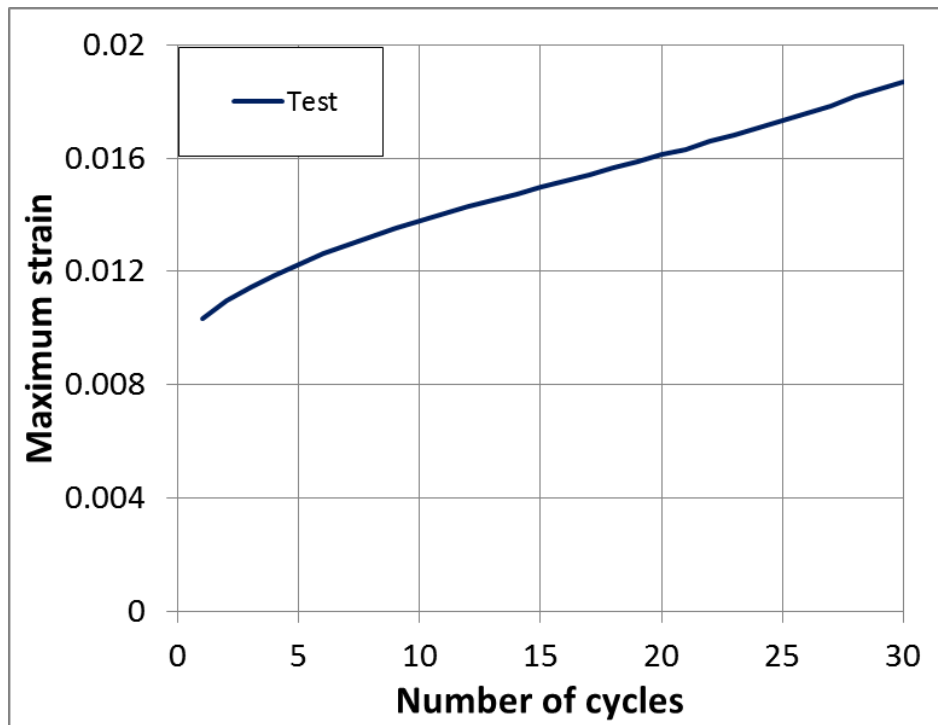
(b)

Figure 2.11: Cyclic stress-controlled material test; (a) Stress-strain curve, (b) Evolution of maximum strain

The two expressions of parameter h have been implemented in the developed UMAT. Since the specific material test presented in Figure 2.11(a) does not result into strain levels outside the limit of the yield plateau in the strain hardening region, initially it is assumed that the initial size of the Y.S. coincides with the size of the M.S., both equal to 738 MPa. The almost horizontal part of the stress-strain curve before the first unloading takes place is captured assuming a small value for the hardening modulus $\hat{H}$ equal to 100 MPa. Furthermore, the size of the Y.S. is assumed to decrease as plastic deformation takes place until it reaches the value of 430 MPa, in order to simulate accurately the Bauschinger effect observed in the first load reversal, and the closed loops in the subsequent loading cycles.
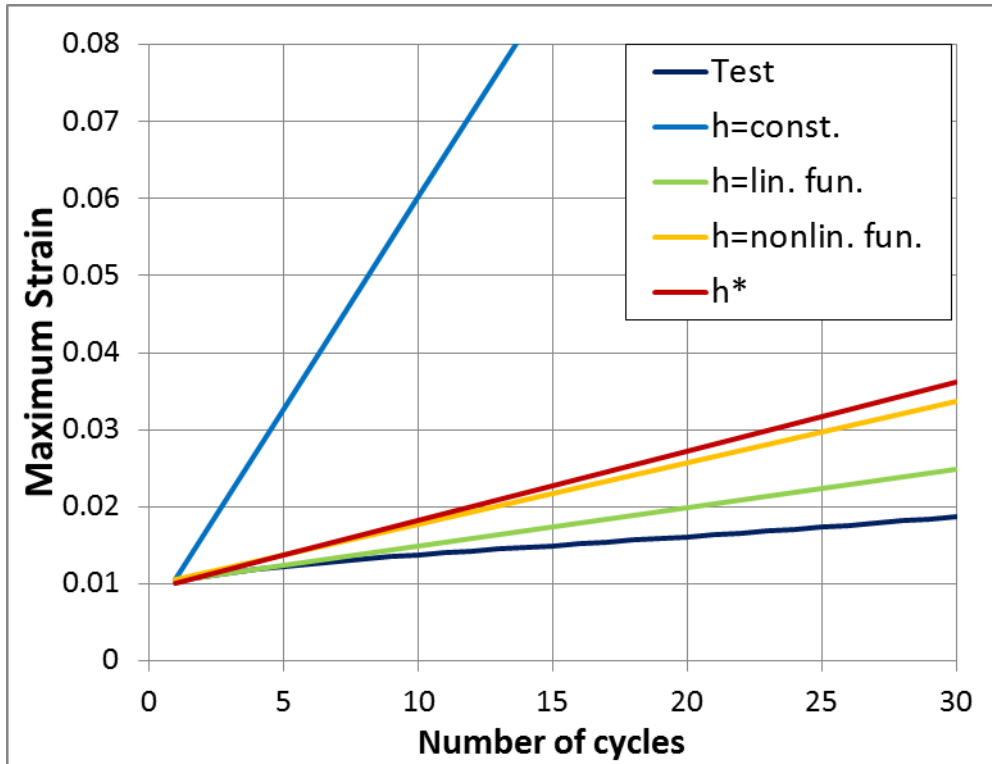
The parameters described in Eq. (2.75) and Eq. (2.76) are properly calibrated to provide the best possible description of the predicted stress-strain curve to the test data and acceptable ratcheting rate predictions. The predicted stress-strain curve and the corresponding ratcheting evolution are presented in Figure 2.12.

40

(a)

(b)

41
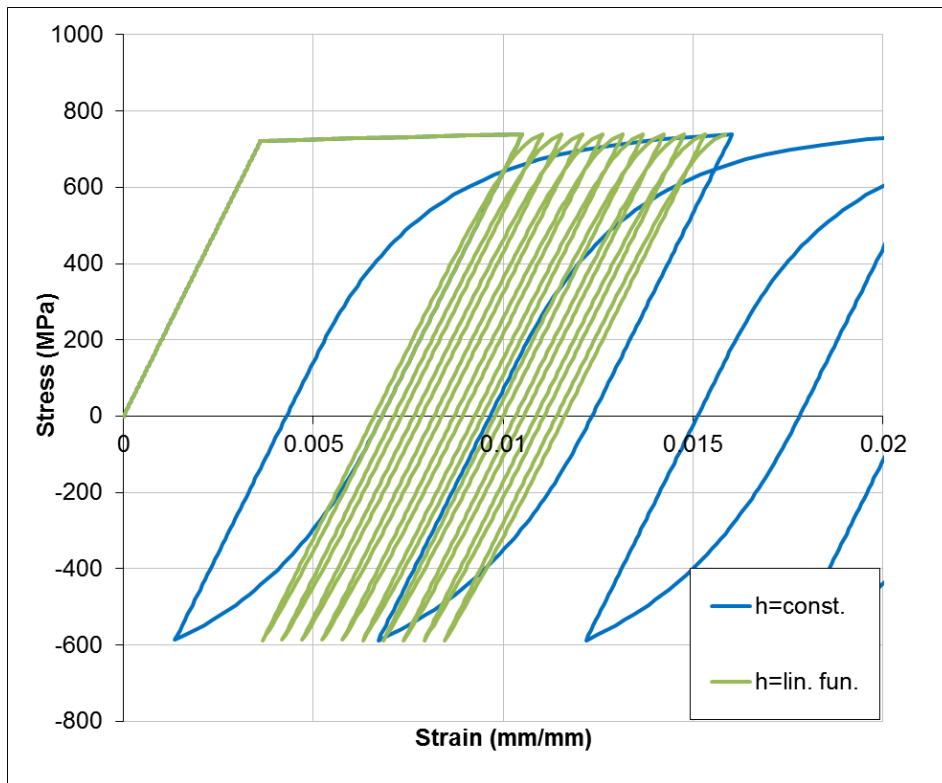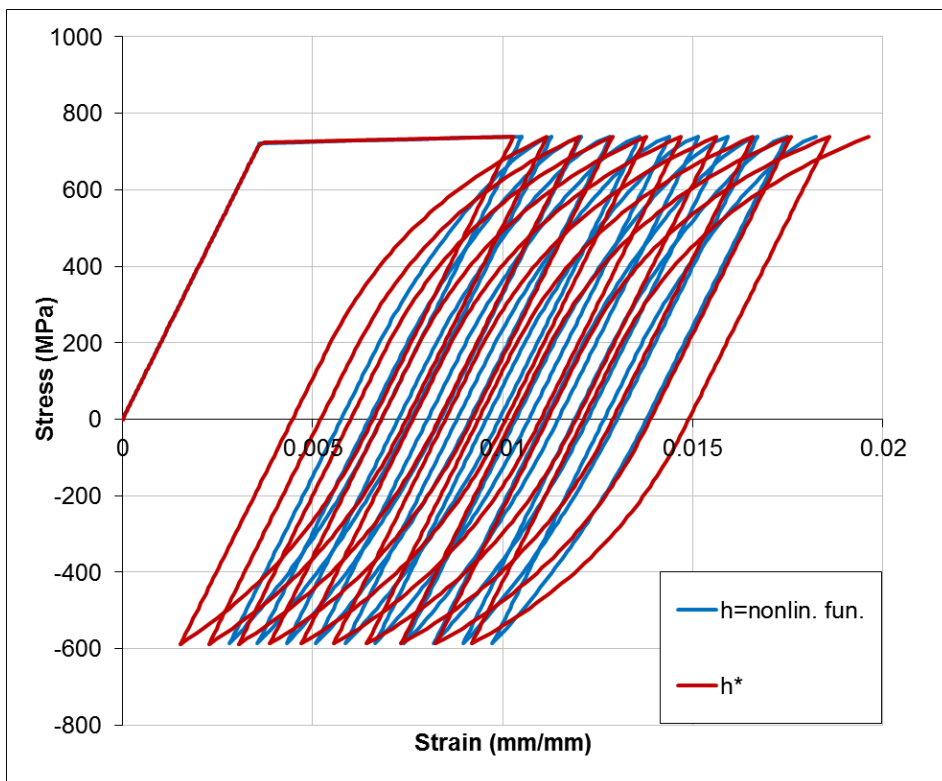
(c)

Figure 2.12: Numerical simulation of the cyclic stress-controlled material test. (a) Stress-strain curve for constant value and linear function for h, (b) Stress-strain curve for nonlinear and proposed function for h, (c) Evolution of maximum strain.

Figure 2.12 shows that the three assumptions made for the parameter h, namely constant value, linear function and nonlinear function, fail to describe accurately both the experimental stress-strain curve and the ratcheting rate. When h is assumed to be constant, denoted as "$h = \text{const.}$", the resulting ratcheting rate is extremely over estimated. Similar results are obtained assuming a linear function for h, as described in Eq.(2.75), denoted as "$h = \text{lin.}$ fun.", while the ratcheting rate predicted is much closer to the experimental rate. Adopting the nonlinear function of Eq.(2.76) for h, denoted as "$h = \text{nonlin.}$ fun.", one results to slightly improved predictions in terms of the stress-strain curve and satisfactory ratcheting rate predictions.

In summary, poor fitting is obtained by all of the above expressions; one should notice that, upon the stabilization of the Y.S. size in this stress-controlled test, the values of δ, δ_{in} are the same at each load cycle. This results to a constant value of h throughout the simulation. When unloading takes place and plastic deformation occurs toward the unloading stress direction until $\sigma_{\min}$ is reached, the Y.S. detaches from the bound of the M.S. and moves within the M.S. covering a

42

distance δ which is less than the initial distance defined at the initiation of the plastic deformation (initial loading phase). When reloading takes place, the two surfaces finally get in contact again at $\sigma_{\max}$. Following the loading path described above and especially in the case where the hardening modulus of the M.S. is small enough, in order the transition to be smooth, the slope of the stress-strain curve decreases significantly and reaches the almost horizontal part of the curve in an almost asymptotic manner at increased strain levels.

This response is not matching the response observed experimentally; the steepness of the plastic part of the stress-strain curve is almost the same during loading or reverse loading, which implies that a constantly changing value of h has to be used, regardless the size of the yield surface or the distances δ and δ_{in} accounted on their own.

In order to account for the aforementioned observations, a new function is introduced for parameter h expressed by the following equation:

$$h^* = A + B \left(\frac{\delta}{\delta_{in}} \right)^m \qquad (2.77)$$

The new value of h is denoted as h^*, and depends of the ratio of δ and δ_{in}. At the beginning of plastic loading ($\delta/\delta_{in} = 1$), h^* is equal to $A+B$. The benefit of this expression is that the ratio δ/δ_{in} becomes less than unity with increasing plastic loading, and this results to a constantly varying value of h^* between the $A+B$ and A, i.e. for $\delta/\delta_{in} = 1$ and $\delta/\delta_{in} = 0$ respectively. The exponent "m" controls the effect of the ratio on the h^* value.

The proposed expression for h^* has been implemented in the developed UMAT and the resulting stress-strain curve and ratcheting evolution curve after the proper selection of the parameters A, B are presented in the same graphs Figure 2.12(b) and (c). The shape of the predicted stress-strain curve is in better agreement to the experimental material curve. In addition, the ratcheting rate predictions are sufficiently close to the experimentally measured values.

2.9 Numerical example: buckling of thick-walled cylinder under external pressure

In the present section, the present constitutive model is employed for the simulation of a specific numerical example concerning buckling of pressurized cylindrical steel shells (pipes). In this example, the capabilities of the model are compared with the capabilities of other plasticity models and its specific benefits are highlighted.

More specifically, the structural behavior of relatively thick-walled pipes subjected to external pressure loading is presented. The prediction of the collapse or ultimate pressure is of great interest for the off-shore pipeline industry. The pipes used in deep-water pipeline applications are thick-walled in order to withstand high levels of external pressure. The collapse pressure is significantly affected by the presence of residual stresses and initial imperfections. For such pipes, a common manufacturing method for line pipe fabrication is the UOE process. Previous publications [e.g. Herynk et al. (2007) and Varelis et al. (2009)] have shown that the UOE process introduces significant plastic deformations in the pipe-wall, resulting in residual stresses, as well as geometrical imperfections (out-of-roundness, thickness variations). In particular, the final expansion phase of the UOE process affects significantly the final distribution of residual stresses and initial geometrical imperfections [Varelis et al. (2009)].

Herein, a thick-walled pipe is considered, with outer diameter of 609.4 mm (24 inches) and thickness equal to 32.3 mm ($D/t = 18.87$). Motivated by the UOE pipe forming process, a generic problem is considered. The pipe is subjected first to internal pressure that causes plastic deformation on the pipe wall, resulting in pipe expansion. Then the internal pressure load is removed so that the pipe undergoes elastic unloading, causing a residual stress/plastic deformation field in the pipe. Subsequently, at the final unloading phase, uniform hydrostatic external pressure is gradually increased until buckling of the pipe takes place. The first two loading steps (internal pressure and unloading) refer to the expansion phase of the UEO process, whereas the third loading step refers to deep water conditions.

The finite element model developed is shown in Figure 2.13 in its original and deformed (buckled) configuration. Taking advantage of the double symmetry of the problem, only the one quarter of the pipe is modeled. The appropriate boundary conditions are introduced into the model and a sufficient number of eight-node reduced integration solid elements (C3D8R) are employed along the circumference and the thickness of the pipe. A very small geometrical imperfection is introduced as a small thickness reduction equal to 1% of the nominal thickness located at the upper part of the pipe.

Institutional Repository - Library & Information Centre - University of Thessaly
18/05/2024 09:43:48 EEST - 3.145.36.43

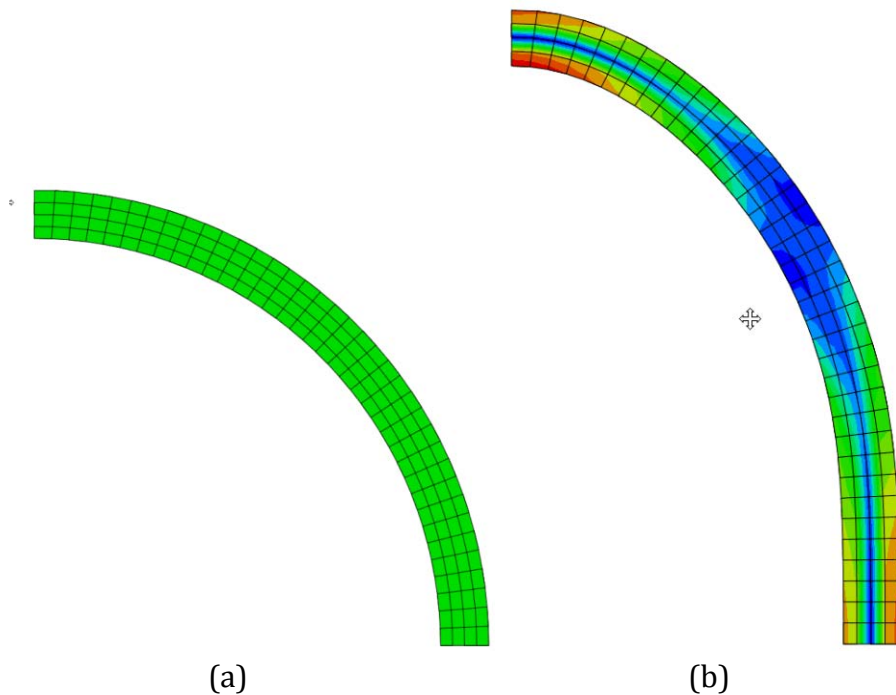(a)   (b)

Figure 2.13: The numerical model: (a) original configuration, (b) deformed
configuration

The steel pipe material is P355 grade, which is equivalent to API 5L X52 grade. In Figure 2.14 the uniaxial material stress-strain curve obtained experimentally is shown for monotonic loading up to about 500 MPa stress and, subsequently reverse loading well into the plastic range. The material exhibits an abrupt transition from the elastic to the plastic region at initial plastic loading at about 400 MPa, and Bauschinger effect upon reverse plastic loading at a stress of about -100 MPa.

In the present simulation, several von Mises plasticity models have been adopted, namely the isotropic hardening rule (ISO), the linear kinematic hardening rule (LKH) and the nonlinear kinematic hardening rule (NLKH). All these models are already implemented in the ABAQUS FE code. In addition, the present constitutive model, denoted as "TL" (Tseng-Lee) model has been also used through the developed material user-subroutine (UMAT) described in the previous section.

In Figure 2.14, the fitting of the test data using the plasticity models reported above is also presented. The abrupt change of the curve slope at the initiation of the plastic deformations part of the curve can be predicted by the ISO and LKH models. It is evident that this part of the curve cannot be simulated precisely by the NLKH model. On the contrary, the Bauschinger effect upon load reversal can be captured by the NLKH model, which is not possible using the ISO and the LKH models. This is because the ISO model assumes a constantly increasing yield surface size as the equivalent plastic strain increases, therefore it overestimates the elastic range of the stress-strain curve when reverse loading

45

takes place, and the LKH model assumes a constant size of the yield surface, therefore it predicts the initiation of plastic deformations at a lower stress level upon reverse loading.

The key benefit of the TL constitutive model is that it is capable of predicting accurately the material behavior in all parts of the displayed curve. In more detail, the predictions of the TL model coincide with those of the ISO and the LKH models up to the point where the maximum stress level is achieved. Upon load reversal, the Bauschinger effect can be predicted accurately and the results are very close to the reciprocal results of the NLKH.
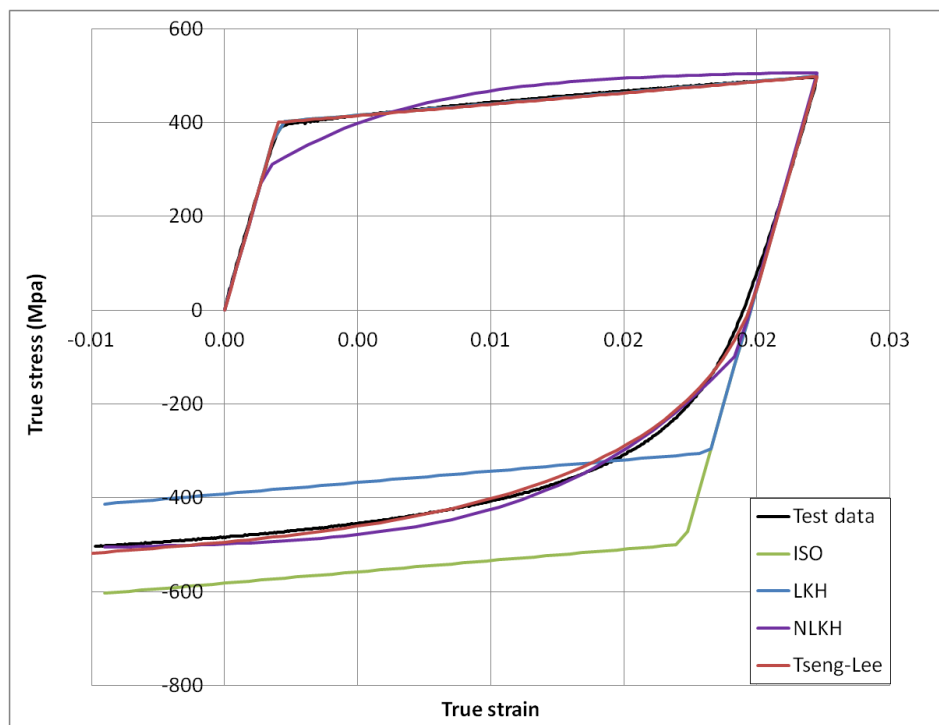

Figure 2.14: P355 steel material curve and predictions of constitutive models.

Following the three-step loading pattern described above, a parametric analysis is conducted aiming at the examination of the effect of pipe expansion due to internal pressure, on the maximum external pressure the pipe can withstand. A characteristic value of internal pressure is the one causing yielding of the pipe wall material. This "yield pressure", denoted as p_y, is defined as:

$$p_y = 2\sigma_y \frac{t}{D}$$

(2.78)

where σ_y is the yield stress of the material used and t, D are the thickness and diameter of the pipe respectively. Using the actual yield stress of the steel material (401.2 MPa), the corresponding value of yield pressure p_y is equal to

46

42.53 MPa. For the purposes of the present parametric study, the internal pressure varies from p_y up to $1.35 p_y$.

In Figure 2.15 and Table 2. 1 the parametric analysis results are presented. The maximum external pressure values are also normalized by the value of p_y. The ISO, LKH, NLKH and TL models have all been used in the numerical simulations. The graph in Figure 2.15 can be divided in three regions. The first part corresponds to low internal pressure levels up to $1.125 p_y$, the second part contains the intermediate internal pressure levels (between $1.125 p_y$ and $1.25 p_y$) and the final part corresponds to high pressure levels from $1.25 p_y$ up to $1.35 p_y$. The main observation from the numerical results in Figure 2.15 and Table 2. 1 is the remarkably different predictions of the TL model with respect to the other models. The different predictions of the other three models are due to their inadequacy in describing accurately the cyclic stress-strain curve (loading and reverse loading) of the steel material. A more detailed discussion of those differences is offered below.

Table 2. 1: Parametric analysis results.

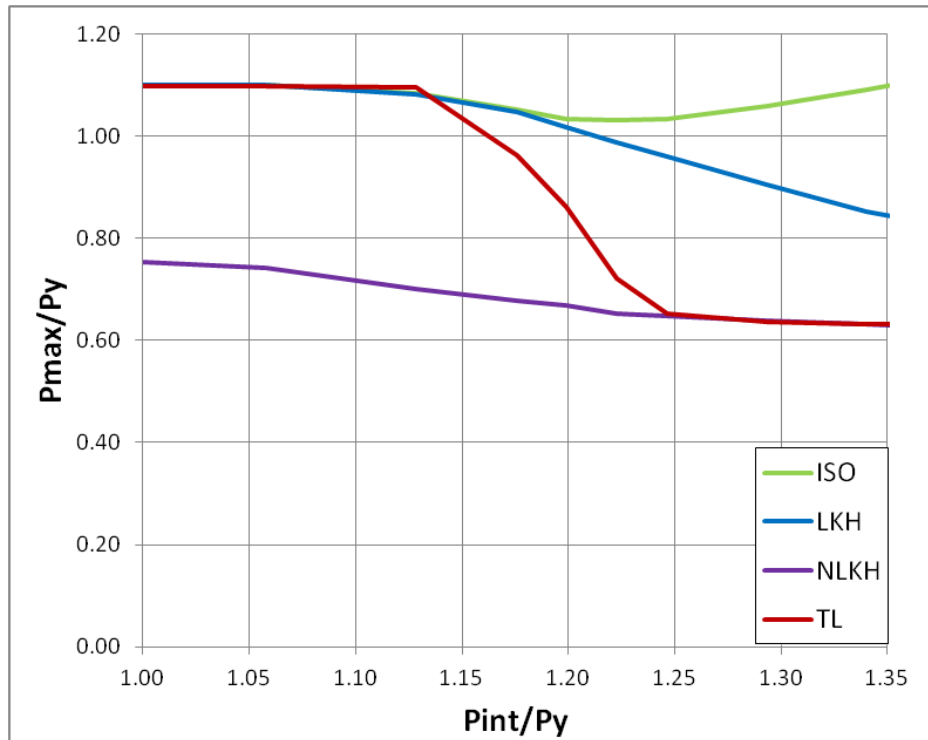| p_{int}/p_y	p_{max}/p_y			
	ISO	LKH	NLKH	TL
1.00	1.10	1.10	0.75	1.10
1.06	1.10	1.10	0.74	1.10
1.13	1.08	1.08	0.70	1.10
1.18	1.05	1.05	0.68	0.96
1.20	1.03	1.02	0.67	0.86
1.22	1.03	0.99	0.65	0.72
1.25	1.03	0.96	0.65	0.65
1.29	1.06	0.91	0.64	0.64
1.34	1.09	0.85	0.63	0.63
1.35	1.10	0.84	0.63	0.63

47

Figure 2.15: The effect of internal pressure on the maximum collapse pressure.

In the first part of the graph for internal pressure levels up to about $1.25 p_y$, the collapse pressure p_{max} predicted by the ISO, LKH and the TL model is almost constant and equal to $1.10 p_y$. The NLKH model is not capable of predicting the abrupt change of the material stress-strain curve at the yield stress level as depicted in Figure 2.14. This results to significantly lower collapse pressure predictions of the NLKH model for this range. The predictions of this model are also low for the whole range of the parametric study due to the increased plastic deformation this model predicts, even for low levels of internal pressure.

For internal pressure levels above $1.25 p_y$, i.e. for the second and third part of the graph, all kinematic hardening models (LKH, MLKH, TL) predict a significant reduction of the collapse pressure p_{max} with respect to the one in the first part of the graph. On the contrary, the ISO model predicts substantially higher values of the collapse pressure p_{max}. The high predictions of the ISO model are due to the uniform size increase of the yield surface size due to internal pressure expansion, resulting in a higher value of yield stress in both tension and compression. Consequently, upon load reversal and buckling, the material has an increased elastic stress region in both tension and compression, which increases the predicted collapse pressure.

48

For low levels of initial expansion, the TL model predictions for the collapse pressure are very close to the predictions of the ISO and LKH models. In this range, the initial plastic deformations are rather small, and pipe behavior is governed mainly by the yield stress level predicted accurately by those three models. On the contrary, at higher levels of initial expansion, i.e. for internal pressure values greater than $1.25p_y$, the pipe material exhibits significant plastic deformation, and its structural behavior under external pressure is governed by the Bauschinger effect. Therefore the predictions of the TL model are identical to the predictions of the NLKH model. In the intermediate range of internal pressure (i.e. from $1.125p_y$ to $1.25p_y$) the TL model predicts a transition from the first part of the graph (where the behavior is dominated by initial yield stress) to the third part of the graph (where the Bauschinger effect is more dominant).

Detailed numerical results are presented for applied internal pressure equal to 51 MPa ($1.20p_y$). Throughout the loading sequence, ovalization (out-of-roundness) of pipe cross-section is monitored. Cross-sectional ovalization is defined as the ratio of the difference between the maximum and minimum pipe diameter over their sum. In Figure 2.16 the equilibrium path of external pressure with respect to cross-sectional ovalization is plotted for all the plasticity models adopted. A summary of the analysis results is provided in Table 2.2. The ISO, LKH, NLKH and the Tseng-Lee model provide different predictions for the maximum pressure and for the corresponding values of ovalization (i.e. where the maximum pressure occurs in the diagram). The pressure-ovalization curves predicted by the ISO, LKH and the TL model have a similar form; after the pipe reaches the maximum (collapse) pressure, it exhibits a rather smooth post-buckling load path. On the other hand, the NLKH model predictions are significantly different. Due to the increased plastic deformations predicted by the model throughout the loading steps, the maximum pressure capacity is reached gradually within a region of almost equal pressure levels which extends throughout the ovalization range considered (Figure 2.16).
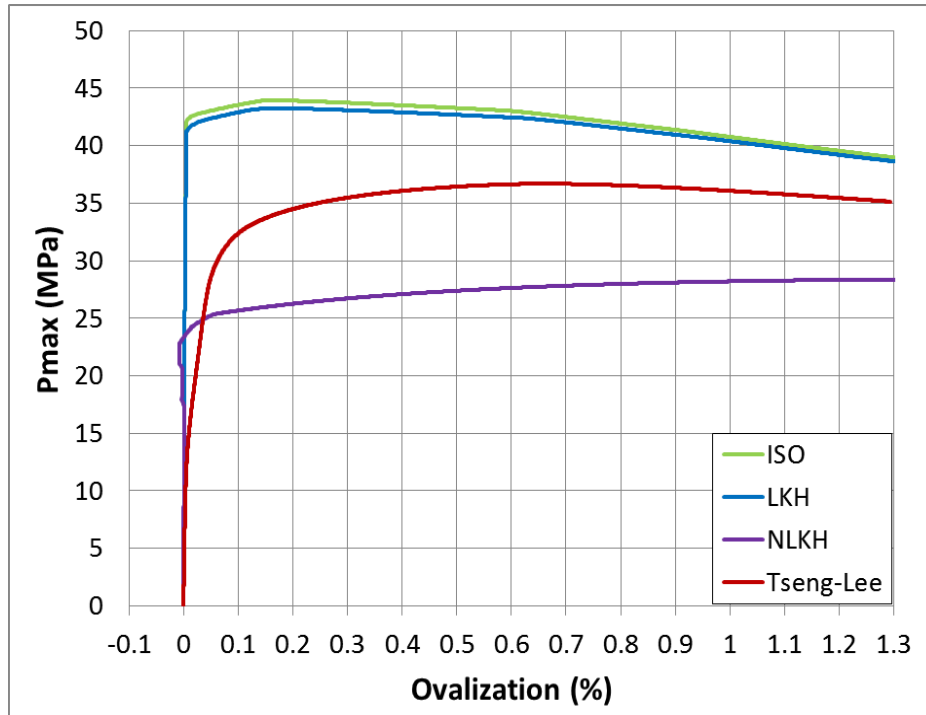
49

Figure 2.16: Collapse pressure versus ovalization curves

Table 2.2: Collapse pressure and ovalization values for internal pressure equal to 51 MPa ($1.20 p_y$).

Model	P_{max} (MPa)	Ov(%) at P_{max}
ISO	43.95	0.153
LKH	43.26	0.165
NLKH	28.39	1.514
TL	36.68	0.662

Four check points (C.P.) have been introduced at the plastic hinge locations of the buckling shape, as shown in Figure 2.17. At these points the evolution of stress and strain at the pipe hoop direction is monitored and the corresponding stress-strain curves are plotted in Figure 2.18. The corresponding curves from the ISO, LKH and the TL model are almost identical for the initial loading phase. Differences are observed upon the load direction reversal caused due to the geometry change of the pipe during buckling. It can be also observed that according to the NLKH model, plastic deformations initiate at lower stress levels. This is in accordance with the predicted material curve shown in Figure 2.14. Due to the increased plastic deformations predicted by this model, the maximum pressure resistance is reached at a lower external pressure loading level (Figure 2.16). In all cases, the TL model is able to provide smooth transition zones from elastic to plastic deformations (Bauschinger effect) and thus more realistic stress-strain curves compared to the rest models considered.
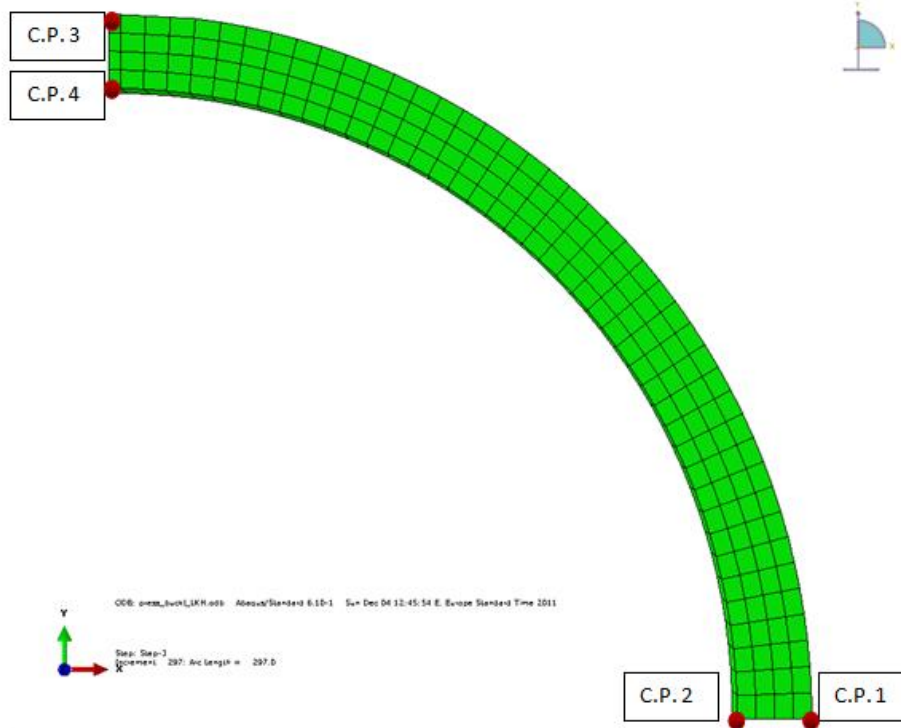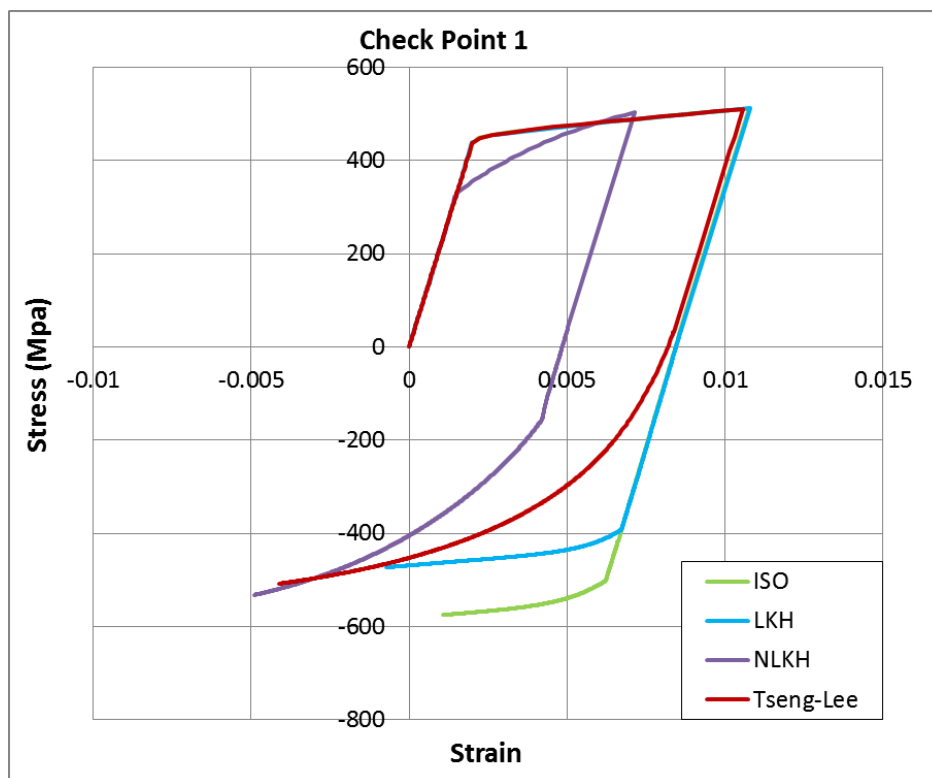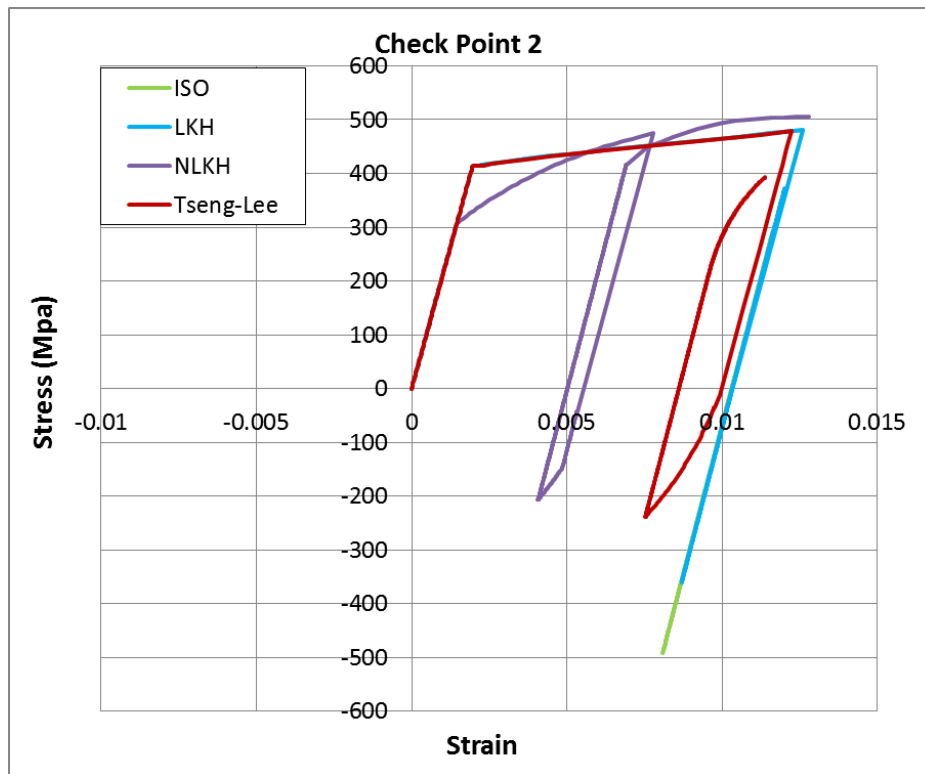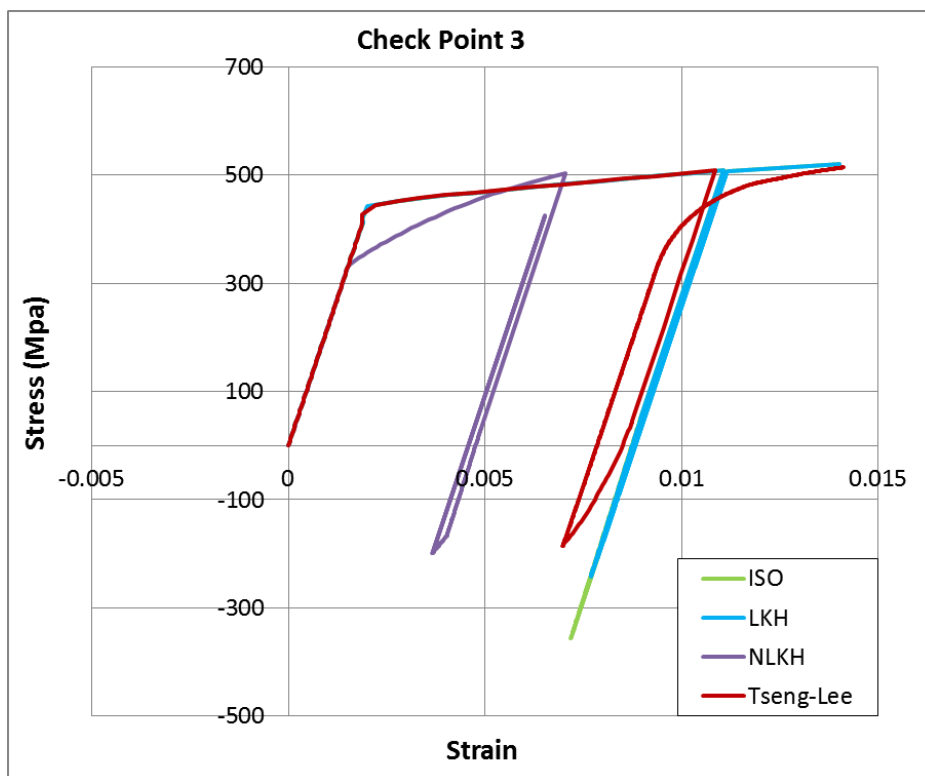
50

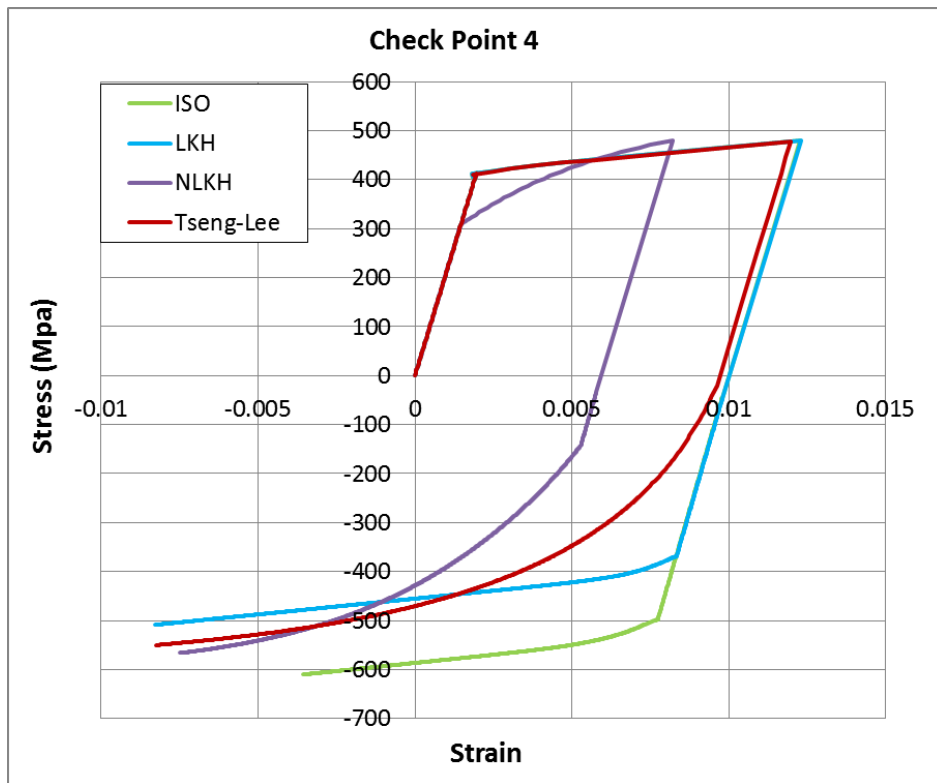Figure 2.17: Introduction of check points for stress and strain monitoring.

(a)

51

(b)

(c)

52

(d)

Figure 2.18: Stress-strain curves: (a) Check point 1, (b) Check point 2,
(c) Check point 3, (d) Check point 4.

53

Chapter 3

Buckling of high-strength steel cylinders under cyclic bending in the inelastic range

3.1. Introduction

Steel tubes and pipes subjected to monotonically-increasing longitudinal bending, exhibit a moment-curvature response, primarily governed by the elastic-plastic characteristics of the steel material. It is also influenced by the ovalization phenomenon referred to as "Brazier effect", induced to the pipe cross-section by the bending loading, resulting to a limit moment instability [Corona & Kyriakides (1998), Karamanos & Tassoulas (1991), Kyriakides & Corona (2007)]. For relatively-thick tubes and pipes, with diameter-to-thickness ratio less than 50, the cross-sectional ovalization is rather small with insignificant effect on the value of the maximum moment sustained by the member. However, with increasing bending into the inelastic regime, the elastic-plastic behavior assisted by cross-sectional ovalization leads to the development of wrinkles on the flattened compression side of the tube wall, which very soon localize and the tube eventually fails catastrophically in the form of a sharp wrinkle, also referred to as "kink" or "local buckle" [Karamanos & Tassoulas (1996), Kyriakides & Ju (1992)]. In the case of thick tubes, with diameter-to-thickness ratio less than 30, local buckling occurs at a late stage, after a limit moment is reached on the moment-curvature diagram [Ju & Kyriakides (1992)]. On the other hand, thinner tubes, with diameter-to-thickness ratio between 30 and 50, exhibit local buckling more suddenly, sometime prior to attainment of the theoretical limit moment, due to ovalization [Houliara & Karamanos (2011)].

Initial wrinkles are always present in tubes and pipes and may affect their bending response. Nevertheless, in steel pipes with diameter-to-thickness ratio less than 50 the effect of initial wrinkling may not be very important in terms of the ultimate moment sustained by the tubular member. On the other hand, their presence may affect the value of the curvature at which local buckling occurs [Kyriakides & Ju (1992), Ju & Kyriakides (1992), Houliara & Karamanos (2011)].

In many practical applications, steel tubular structures, piping systems and pipelines are subjected to severe cyclic loads, which induce repeated yielding of the steel material in the most strained locations. Typical examples are the response of tubular structures under strong earthquake action [Zayas et al. (1982)], offshore tubular platforms in extreme weather conditions [Bea & Young (1993), Schmucker and Cornell (1994)], or nuclear reactor piping components and hot hydrocarbon pipelines under shut-down conditions [Shmnomura et al. (2002), Klever et al. (2002)]. Those cyclic excursions into the inelastic range can

54

lead to degradation and failure of structures due to accumulation of deformation. The structural behavior of tubes under cyclic bending loading has been examined experimentally by Shaw & Kyriakides (1985)and Kyriakides & Shaw (1987), and this work has been extended by Corona & Kyriakides (1991) to include the effects of external pressure. Notable works on the cyclic bending response of tubular members and pipes have been also reported in Lee et al. (2001), Chang & Pan (2009) using an experimental set-up very similar to the one in Corona & Kyriakides (1991), supported by analytical predictions based on a visco-plastic material model. Finally, cyclic loading of tubular members has also been examined with reference to structural applications and seismic structural design [Chang & Pan (2009), Elchalakani et al. (2004), Gao et al. (2004)].

The above works indicated that there exist a strong interaction between the elastic-plastic behavior of the steel material and the geometric nonlinearities induced by initial wrinkles and the ovalization phenomenon, resulting in an accumulation of deformation at the critical region which leads to the formation of local buckling after a number of loading cycles. This is a situation that implies failure of the pipe; moment capacity is decreased abruptly and under continuing cyclic loading, the buckled area of the pipe may exhibit low-cycle fatigue due to strain concentration and, eventually, fracture [Dama et al. (2007)].

Herein, motivated by experimental evidence, the cyclic bending response of tubes and pipes is examined, with special emphasis on the effects of initial wrinkles on tube wall. Previous experimental and analytical works on axially-loaded tubular members have indicated that initial wrinkles may grow under repeated axial loading within the inelastic range of the material, leading to instability followed by member collapse [Jiao & Kyriakides (2009), Jiao & Kyriakides (2010)]. Those works have been extended in Jiao & Kyriakides (2011a) and Jiao & Kyriakides (2011b) to examine the effects of internal pressure on the structural behavior of axially-loaded tubular members and the growth of wrinkles.

The present work focuses on seamless tubular members, made of high-strength steel, subjected to cyclic bending and the formation of a local buckling pattern. The tubes have constant thickness, and are initially imperfect, with very small wrinkles, The amplitude of those wrinkles is in accordance with reported measurements on high-strength steel seamless tubes, which are well below the allowable limits of EN 10216. The analysis monitors wrinkle evolution with respect to the number of loading cycles and the determination of local buckling formation. Towards this purpose, a numerical simulation is employed, modeling the tube with nonlinear finite elements. Particular emphasis is given on the material model. A cyclic plasticity model introduced elsewhere is employed and is enhanced and calibrated for the purposes of describing accurately the mechanical behavior of the high-strength steel material. The results are reported in "buckling-life" diagrams, which indicate the sensitivity of buckling on the amplitude of initial wrinkles.

3.2 Experimental data on tubular members

In the course of the HITUBES project [Bursi (2012)], sponsored by the European Commission, large-scale axial and bending tests on seamless CHS tubular members have been conducted in the facilities of CSM in Sardinia, Italy. The tubular specimens made of TS590 high-strength steel have been provided by Tenaris Dalmine SpA, Italy. A heavy-frame loading device shown in Figure 3. 1 and presented in Pournara et al. (2012) was used to apply the required loads to the specimens. In most of the tests, loading has been applied monotonically, to determine the strength of high-strength steel tubular beam-columns [Bursi (2012), Pournara et al. (2012), Pappa & Karamanos (2012)].

In the present study, reference is made to two specimens that have been tested under cyclic bending loading in the absence of axial force. They are 12-inch diameter CHS sections of nominal dimensions $\varnothing 323.9 \times 10$, subjected to constant-amplitude (rotation-controlled) cyclic bending loads until buckling. The first specimen has been subjected to symmetric loading, whereas the second specimen has been subjected to non-symmetric loading. The tubular specimen length is equal to 4.77 meters, capped with thick end plates, which are bolted on two rigid parts that connect to the two hinges of the bending apparatus. The entire specimen length (hinge-to-hinge) is equal to 7.93 meters. The test set-up is shown in Figure 3. 1and the experimental results are briefly reported in Table 3. 1.

56

Figure 3. 1: Experimental set-up for tube bending [Bursi (2012)].

Table 3. 1: Summary of cyclic loading tests

Test	Actual Cross-section (mm)	Load type	Hinge rotation range (degrees)	N_f
1	323.36×10.89	Symm.	±8.50	10
2	324.75×10.88	Non Symm.	+8.40/-6.10	11

Material testing has been conducted in the laboratories of CSM on steel coupons extracted from the specimens. Monotonic loading of the coupons indicated a yield stress of 735 MPa, significantly higher than the nominal value. In addition, cyclic strain-controlled and stress-controlled tests on coupons have been performed to determine cyclic properties of the steel material, as shown in Figure 3. 2 and Figure 3. 3(a) respectively. The material specimens were manufactured according to the ASTM E466-07 standard and an anti-buckling device was used to allow the application of compressive loading, in the course of symmetric cyclic loading, as presented in Bursi (2012). Under cyclic plastic loading conditions the material exhibits slight softening which is soon followed by stabilization of its behaviour [Figure 3. 2.(a)], whereas under stress-

57

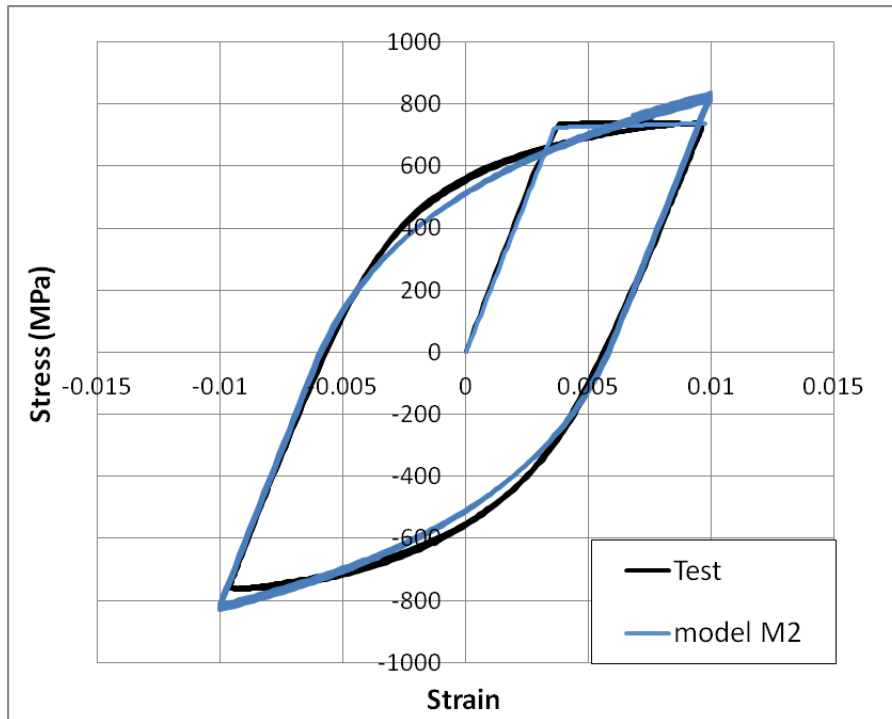controlled cyclic loading, the material exhibits ratcheting at a constant rate as shown in Figure 3. 3(a).

Before testing, measurements have been obtained to determine the actual geometry of the tubular specimens. The measured mean values of diameter and thickness are reported in Table 3. 1. Furthermore, initial wrinkle measurements have been performed, and the measured wrinkle amplitudes, expressed as a percentage of the tube wall thickness, were found less than 5%, with a representative value equal to about 0.8% [Pournara et al. (2012), Pappa & Karamanos (2012)]. Residual stress measurements have also been obtained and indicated very small residual stresses in the longitudinal direction and residual stresses less than 17% of the yield stress in the hoop direction [Pournara et al. (2012)]. Given the fact that, in the case of bending loading, the primary stresses are in the longitudinal direction, the small residual stresses in the hoop direction can be neglected for the purposes of the present analysis.

The results are depicted in Table 3. 1. During the first cycles, no tube wall wrinkling has been observed in the two specimens, but with continuing repeated loading the two specimens failed due to buckling after 10 and 11 loading cycles respectively. The buckled shapes are shown in Figure 3. 4. These two tests indicate clearly that repeated bending of a tubular member may cause buckling failure, despite the fact that the loading range is within the safety margins determined by the ultimate strength consideration. This is a key observation to be examined in detail in the following sections.
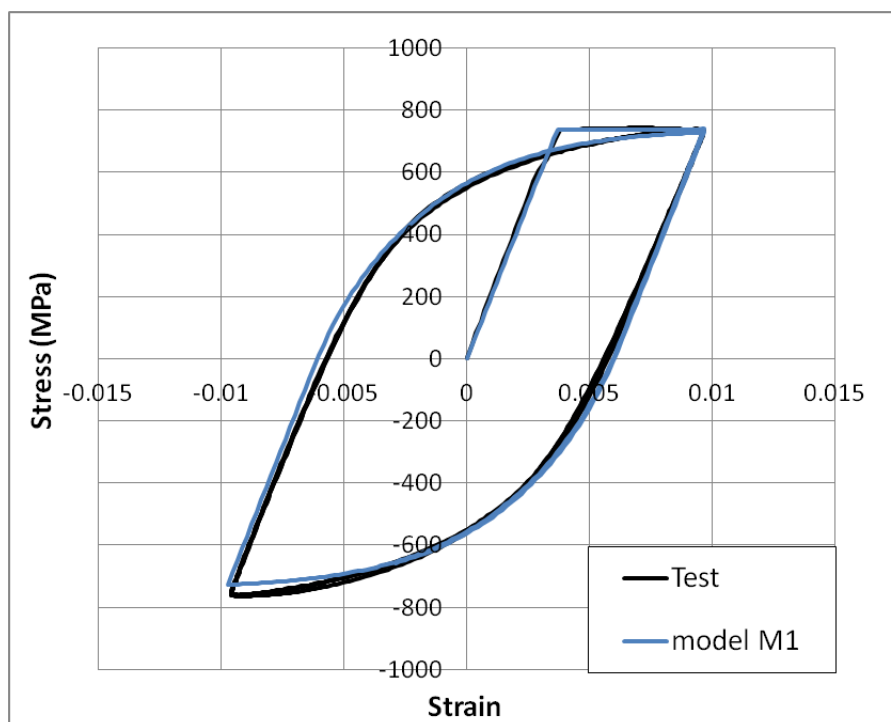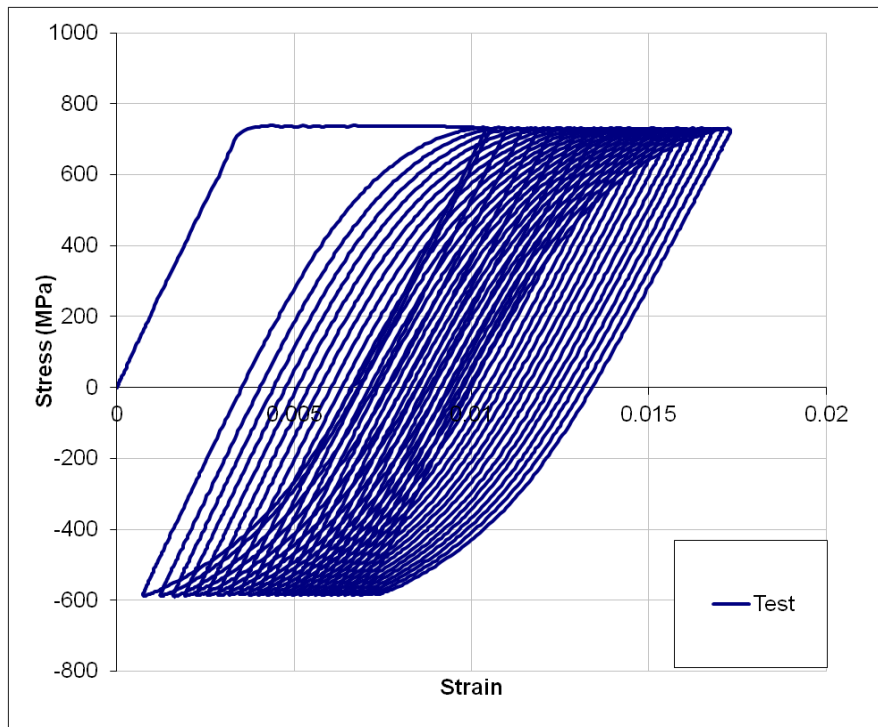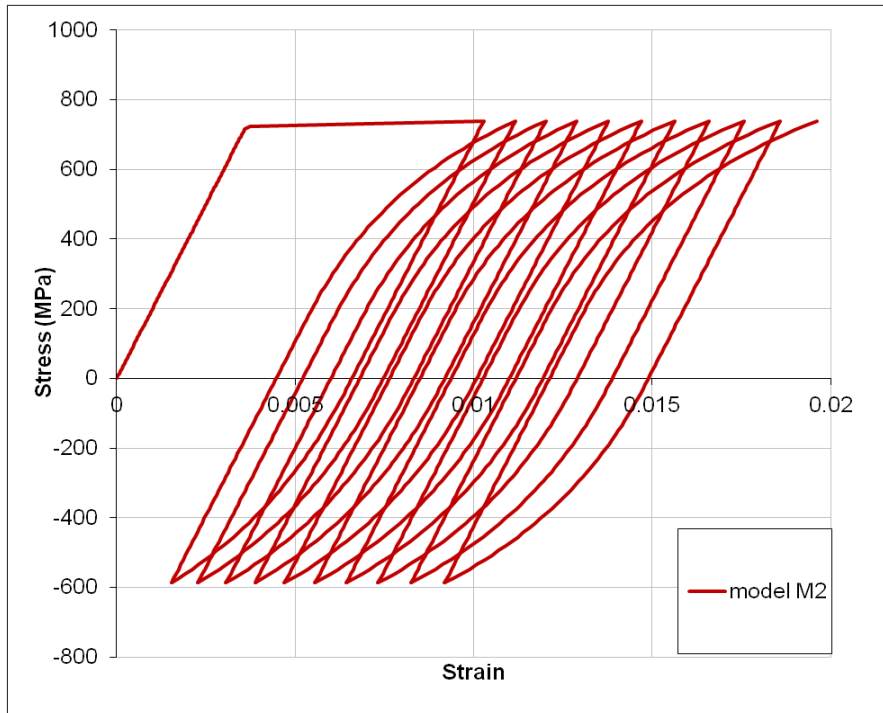

(a)

(b)

Figure 3. 2: Cyclic loading material curves for the T590 material and bounding-surface constitutive model predictions under strain-controlled conditions - $\Delta\varepsilon = \pm0.96\%$. (a) model with parameter set M1, (b) model with parameter set M2.

(a)

59

(b)

Figure 3. 3: Cyclic loading material curves for the T590 material; (a) test results and (b) bounding-surface constitutive model M2 predictions under stress-controlled conditions.


(a)

60

(b)
Figure 3. 4: Local buckling modes: (a) Specimen No. 1, (b) Specimen No. 2 [Bursi (2012)].

3.3 Finite element model

To simulate the cyclic behavior of tubular members, finite element models have been developed in the general-purpose program ABAQUS, using eight-node reduced integration solid elements (C3D8R). The tubular member is assumed to have uniform thickness distribution along its length. The finite element mesh is denser at the central part of the tube, where buckling occurs, as shown in Figure 3. 5. Three elements along the thickness of the tubular member were used. The use of more than three elements along the tube thickness did not affect the numerical results. To represent the actual conditions of the experiments, two rigid parts, modeled with very stiff beam elements (B31), are attached at both ends of the tubular member to simulate the rigid parts connected to the hinges of the testing apparatus (Figure 3. 5).

61
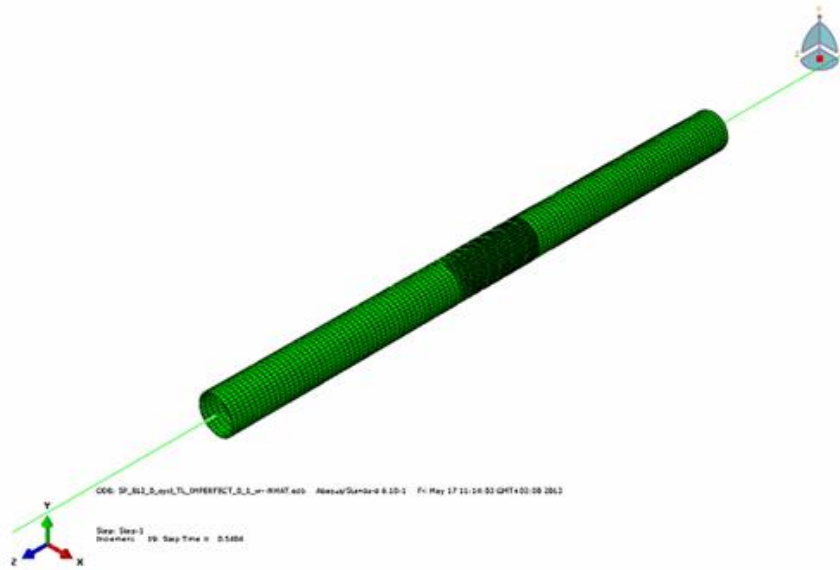
(a)
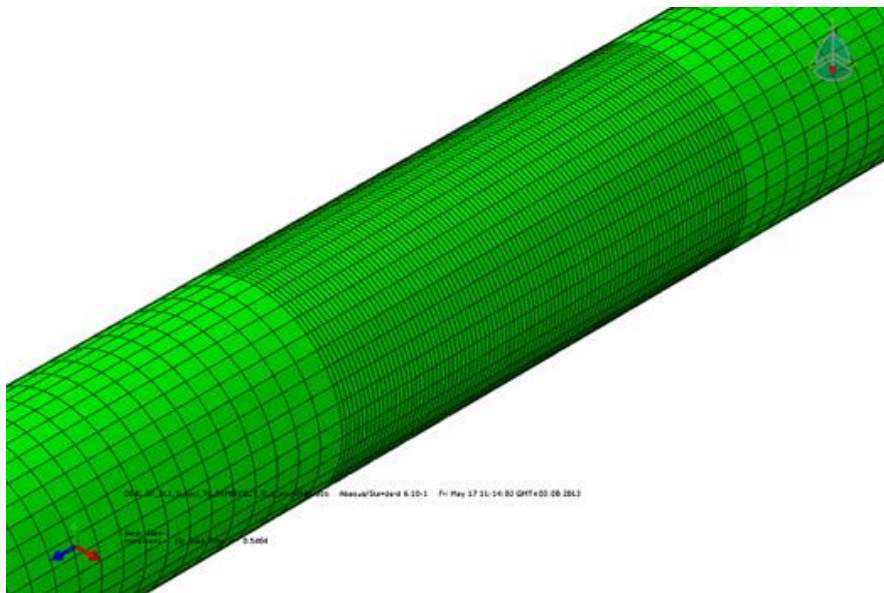
(b)

Figure 3. 5: Numerical model: (a) general view, (b) mesh detail.

An initial profile of tube wall wrinkles is also considered. Towards this purpose, a linearized buckling (eigenvalue) analysis of the specimen under bending loading has been conducted. The corresponding first buckling (wrinkling) mode of the tube is obtained, as shown in Figure 3. 6, amplified by a factor of 100 for visualization purposes. The half wavelength of the wrinkling mode is equal to 73.15 mm, or equivalently, in dimensionless form, equal to $1.23\sqrt{Dt}$, which is quite close to the buckling half wavelength values reported in Kyriakides & Ju (1992) and Ju & Kyriakides (1992) for aluminum pipes. This wrinkling mode, scaled appropriately to match the desired wrinkling amplitude, is used as the initial wrinkling pattern of the tubular member for the nonlinear bending analysis.
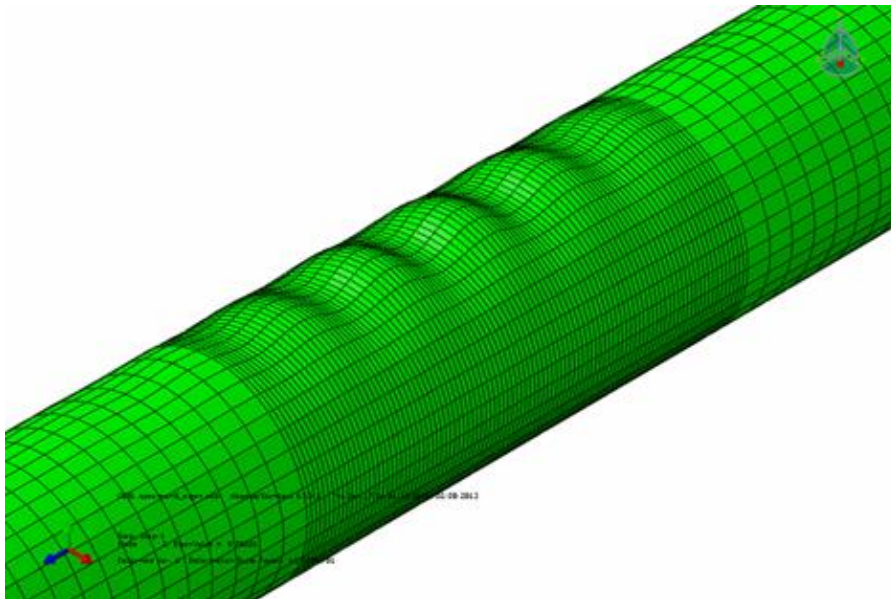
62

Figure 3. 6: Wrinkling imperfections (amplified).

## 3.4 Material modeling and implementation

The nonlinear behavior of the steel material is described through the cyclic plasticity constitutive model, introduced by Tseng & Lee (1983), which adopts the "bounding surface" concept. The reader is referred to Chapter 2, where more details about the numerical formulation of the model, as well as its numerical implementation, are reported.

In the present analysis the material model parameters have been properly defined based on the material testing data given in the report of Bursi (2012). Two sets of parameters, namely M1 and M2, have been defined in order to provide best fit to the strain-controlled and stress-controlled tests respectively. The values for each parameter set are reported in Table 3.2.

The first set (M1), considers a zero value of c , as in the original formulation of the model (see Chapter 2, Eq. 2.41). The values of the other parameters have been selected for simulating accurately the strain-controlled loop, as shown in Figure 3. 2 (a). Nevertheless, this model may not provide good predictions for the ratcheting rate, also noticed in the studies of Hassan & Kyriakides (1992) and Bari & Hassan (2001). In the second set (M2), assuming a value of c equal to 250 MPa, the ratcheting rate is significantly improved and is quite close to experimental results, as shown in Figure 3. 3, whereas the simulation of the strain-controlled loop is somewhat less accurate.

63

Table 3. 2: Summary of material parameter values

Parameter	M1	M2
$\hat{H}$	2300	2300
ω	5	5
c (MPa)	0	250
A	80	50
B	0	10
m	0	2
k_0 (MPa)	738	738
Q (MPa)	-350	-350
b	500	500

(a)

64
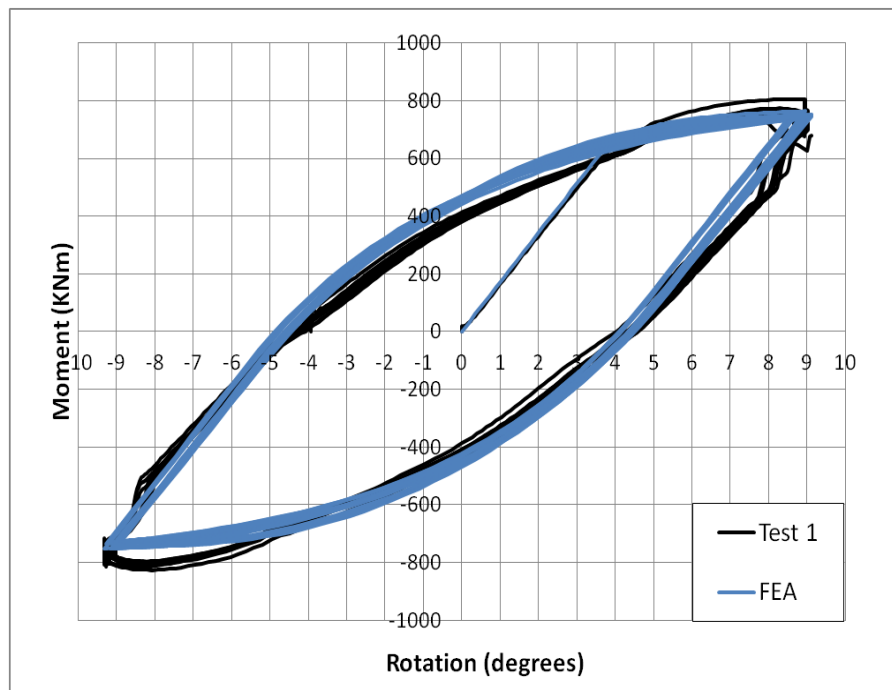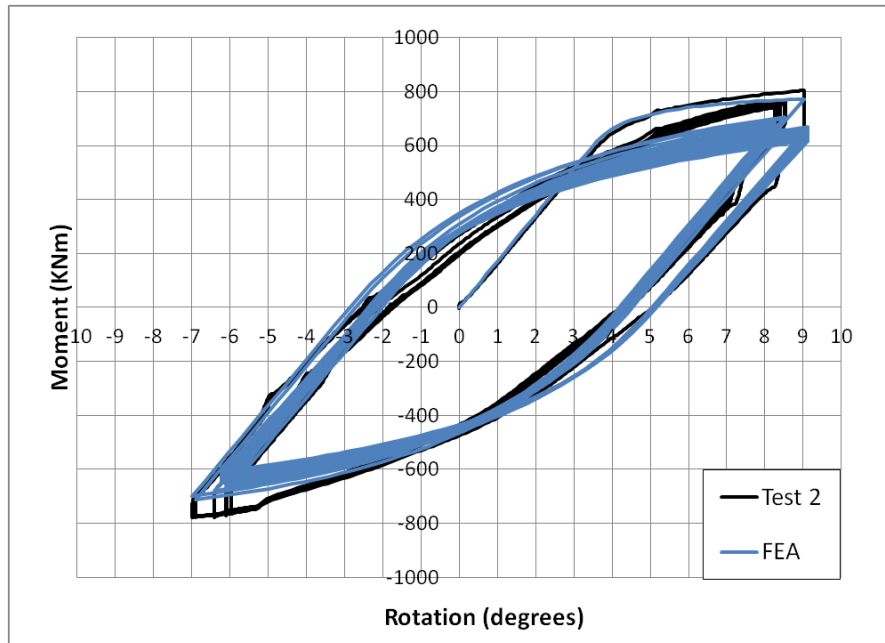
(b)

Figure 3. 7: Experimental results and numerical predictions for the moment-rotation loops for (a) Test 1 and (b) Test 2.

3.5 Numerical simulation of the experiments

The finite element model presented in the previous section is used to simulate the two tests reported in Table 3. 1. The numerical results for both parameter sets M1 and M2 coincide. The comparison of the predicted moment-rotation curves with the corresponding experimental curves shows that the adopted model is capable of providing good predictions. In Figure 3. 7 the simulation of Test 1 and Test 2 are presented assuming an initial wrinkle amplitude equal to 0.8% of the tube wall thickness, which is considered as a typical value observed in experiments. The first loading branch of the curves, the subsequent hysteretic loops and the number of cycles until buckling are predicted accurately, i.e. 10 and 11 cycles for test specimens No.1 and No.2 respectively. It is worth-noticing that no significant moment degradation is observed until buckling of the specimen occurs.

3.6 Numerical parametric study

Using the finite element model, with the steel material model properly calibrated, a numerical study is conducted aiming at examining the effects of applied rotation range and the influence of initial wrinkling imperfections on the "buckling life" of the tubular member, i.e. the number of bending cycles to buckling. It should be noted that the range of wrinkle amplitudes measured on the tubular specimens [Pournara et al. (2012), Pappa & Karamanos (2012)] are significantly lower than the corresponding limits specified in EN 10216.

65

3.6.1 Monotonic loading of tubular members

Figure 3. 8 shows the response of a high-strength steel tube subjected to monotonically increasing bending, with diameter and thickness equal to 324.75 mm and 10.88 mm respectively. Bending is applied through a set-up similar to the one used in the experiments, until local buckling occurs. Under these loading conditions, the predictions of both parameter sets M1 and M2 are identical, since the behavior is governed by the hardening modulus of the memory surface which is the same in both parameter sets. In this analysis, initial wrinkling amplitudes equal to 1%, 10% and 20% of the tube thickness are assumed. In the moment-rotation diagram of Figure 3. 8(a), the applied rotation is normalized by the value of the elastic limit rotation φ_y corresponding to the development of the yield moment M_y defined as $M_y = W_{el}\,\sigma_y$, where W_{el} is the elastic section modulus and σ_y is the yield strength of the material. Similarly, using the plastic section modulus W_{pl}, a reference plastic moment M_{pl} is defined as $M_{pl} = W_{pl}\,\sigma_y$, and the corresponding rotation is denoted as φ_p. Using the actual geometric and material properties of the tube, one readily obtains $M_y = 595.2$ kNm and $M_{pl} = 785.01$ kNm, and based on the finite element results, the corresponding values of rotation to reach these values are $\varphi_y = 3.45$ degrees and $\varphi_p = 11.73$ degrees respectively. It should be noted that the value of φ_p is not well-defined due to the almost flat part of the moment-rotation curve at the plastic moment level. Finally, the end rotation corresponding to the formation of local buckling φ_b is defined as the rotation that corresponds to a sudden drop in the moment-rotation diagram.

The above analysis under monotonic bending conditions has been repeated for several values of initial wrinkling amplitude, and the results are summarized in Figure 3. 9. The numerical results show that the presence of initial wrinkles does not affect the value of the ultimate moment. In particular, for wrinkling amplitude values less than 9%, the theoretical fully-plastic moment M_{pl} is reached for the members under examination while for a tube wall wrinkling amplitude of 30% of the tube thickness, the corresponding maximum moment is equal to 95% of the fully-plastic moment [Figure 3. 9(a)]. On the contrary, increasing the size of initial wrinkles, the value of the corresponding critical rotation φ_b is significantly reduced as presented in Figure 3. 9(b). The critical rotation φ_b for initial wrinkling amplitude of 1% is equal to $\varphi_b = 19.32$ degrees, a value 5.6 times larger than the value of the yield rotation, whereas for wrinkling amplitude equal to 20% the value of φ_b is only 7.91 degrees (equal to 2.29 times the value of the yield rotation). In terms of curvature, the numerical findings for the critical curvature defined as $k_b = 2\varphi_b/L$ are in good agreement

66

with experimental observations for tests on metal tubes in pure bending reported by Kyriakides and Ju (1992) for wrinkling amplitudes near the characteristic value and for the D/t very close to the range of interest.
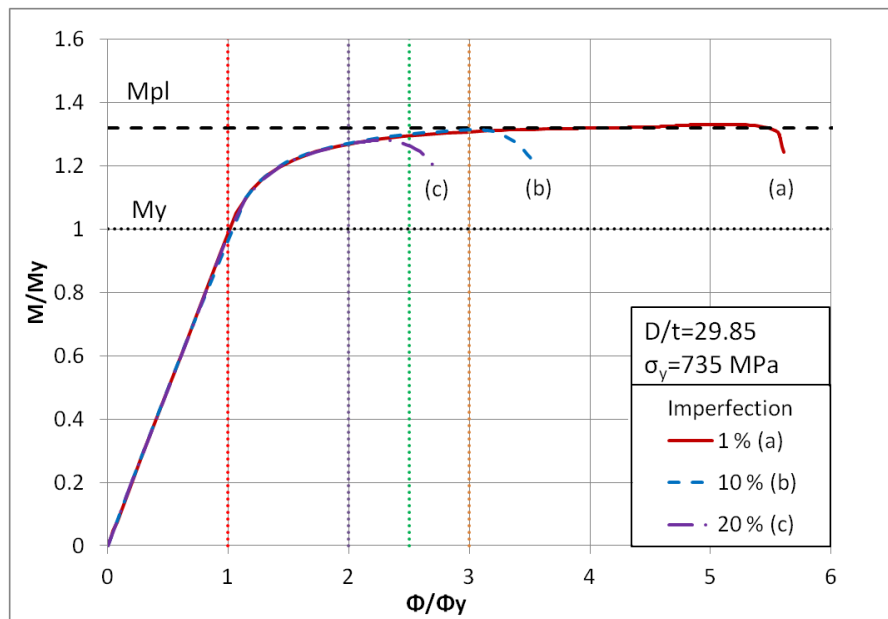
(a)
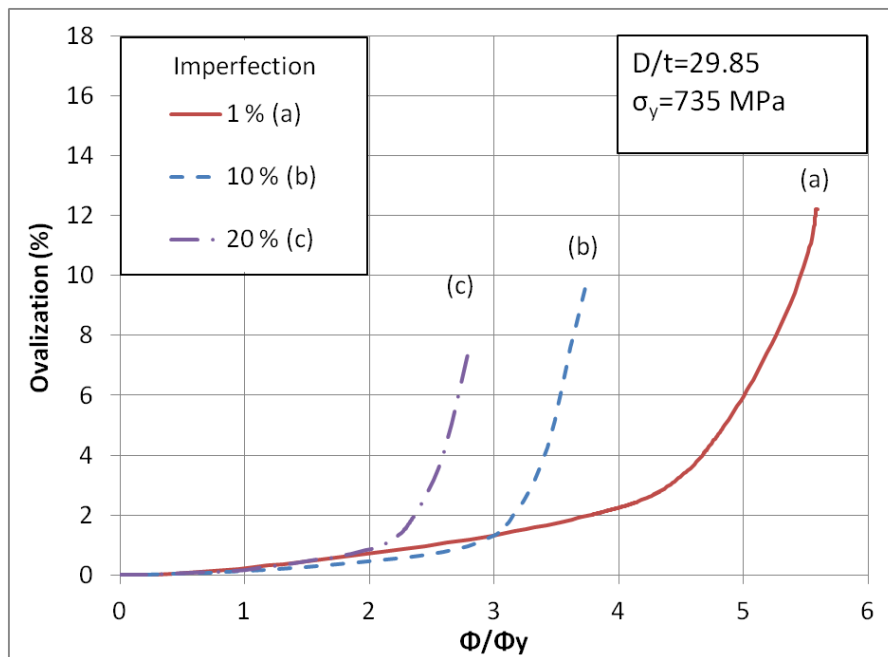
(b)

Figure 3. 8: Monotonic bending behavior, test No.2 geometry: (a) Moment – rotation curves, (b) Ovalization – rotation curves.

67
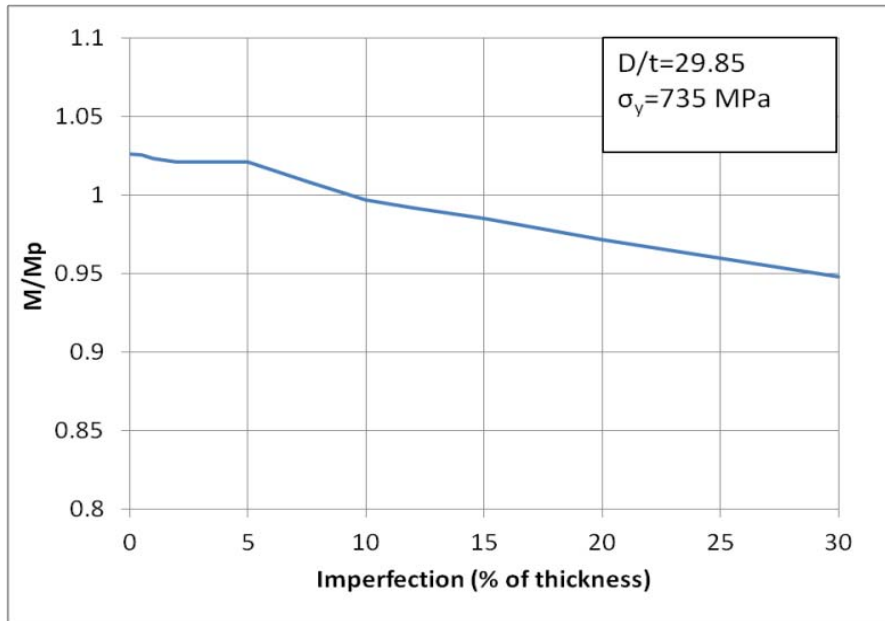
(a)
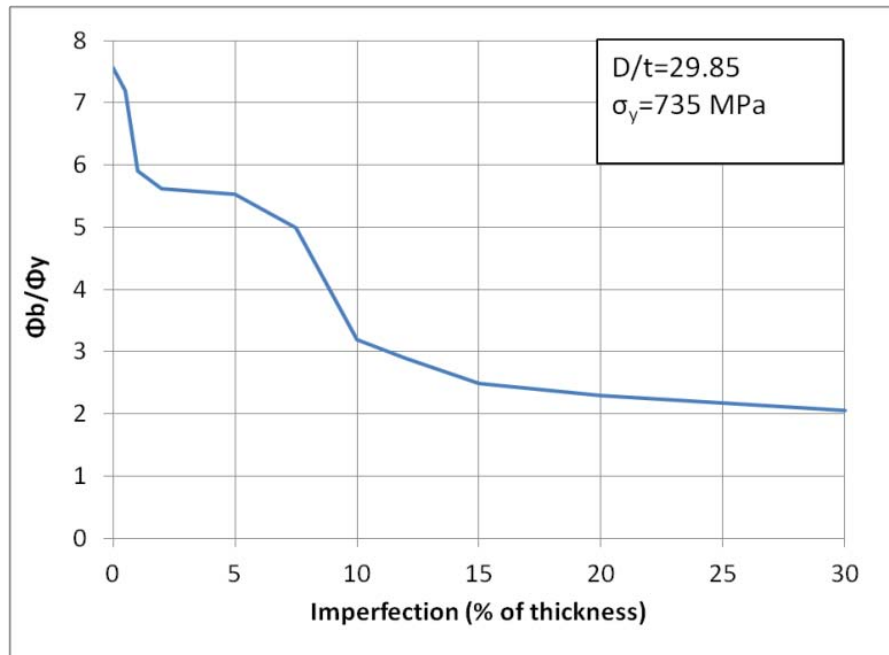
(b)

Figure 3. 9: Effect of the initial wrinkling amplitude on (a) on the maximum moment and (b) the critical rotation φ_b f or monotonic loading.

Monitoring the distortion of the tube cross-section may offer significant information on the structural behavior of the cyclically bent tubular member. As a measure of cross-sectional ovalization, the following non-dimensional "ovalization" parameter is defined as:

$$ov = \frac{D_{\max} - D_{\min}}{D_{\max} + D_{\min}} \qquad (3.1)$$

68

where $D_{\max}$ and $D_{\min}$ are the maximum and minimum tube diameters in the deformed configuration, located in two orthogonal directions, with the minimum diameter on the plane of bending. With increasing bending, the initially circular cross-section of the tube obtains an oval shape and prior to the development of local buckling, the rate of ovalization becomes significant, as presented in Figure 3. 8(b).

3.6.2 Cyclic loading of tubular members

A tubular specimen with the same geometric and material properties is subjected to cyclic bending loading under symmetric and non-symmetric rotation-controlled conditions. Considering a suitable scaling of the wrinkling mode of the tube shown in Figure 3. 6, initial wrinkling amplitudes of magnitude up to 5% of the tube thickness are considered.

The range of applied rotation $\Delta\varphi$ is such that the maximum absolute value does not exceed the buckling rotation φ_b in each direction of loading. This implies that the loading is within the safe (no-buckling) range $\pm\varphi_b$ determined from monotonic conditions, as defined in Figure 3. 8. In this analysis the gradual development of plastic deformation is monitored in terms of cross-sectional ovalization and wrinkle size with increasing number of loading cycles for different values of initial imperfections.

Numerical results for cyclic loading at $\Delta\varphi = \pm 2.5\varphi_y$ are shown in Figure 3. 10 considering material parameter set M1. The results indicate that the initial amplitude of the principal wrinkle is maintained almost constant for a certain number of cycles. Subsequently, the principal wrinkle located in the middle of the specimen, increases very rapidly. The other wrinkles also increase in size but at lower rate, as illustrated in Figure 3. 11 for the characteristic initial wrinkling amplitude of 0.8 %. This leads to localization of deformation in the principal wrinkle, resulting in buckling of the tubular member in the form presented in Figure 3. 13, also observed in the experiments (Figure 3. 4). In Figure 3. 12the evolution of the longitudinal tensile strains measured at the inner pipe wall at the main buckle location is presented. It is observed that the developing local strains increase because of the increasing size of the local wrinkle, and reach significantly high values when local buckling takes place.

Buckling of the tubular member can be expressed in a diagram form as in Figure 3. 14, referred to as "buckling-life" diagram. In this figure, each curve represents the relation between the wrinkling imperfection amplitude and the corresponding number of cycles N_f until buckling failure of the tube, for a specific loading range. In the present analysis the ranges $\Delta\varphi = \pm 2\varphi_y$, $\Delta\varphi = \pm 2.5\varphi_y$ and $\Delta\varphi = \pm 3\varphi_y$ have been examined. For increasing initial wrinkling amplitude, the number of cycles to buckling is reduced. It is also observed that the effect of the imposed wrinkling imperfection on the buckling

69

life is more significant for smaller end-rotation amplitudes, while it becomes less important as the rotation amplitudes increase. For greater values of imposed rotation the induced plastic deformations govern the structural behavior, and the effects of initial wrinkling become less important.

For the particular case of loading range equal to $\Delta\varphi = \pm\, 2.5\varphi_y$ (also used in test No.1) the results obtained from two material parameter sets M1 and M2 are also compared in Figure 3. 14. The effect of initial wrinkling imperfections is dominant in the range of amplitudes less than 2%. It is also worth noticing that the predicted number of cycles coincides with the cycles obtained experimentally, for wrinkling amplitude equal to about 0.8% for both material parameter sets M1 and M2.

In general, the resulting curves are very close for both material sets. Some differences are observed for wrinkling imperfection values less than 0.5%. For these small initial wrinkles, the resulting failure shape is slightly different. Using the M1 parameter set, a more localized buckling pattern is observed, which is similar to experimental observations. On the contrary, using the M2 parameter set, a wider spread of plastic deformations occurs around the main buckle resulting at local buckling at a higher value of cross-section ovalization, which dominates the deformation of the cylindrical member (Figure 3. 15). Overall, the two material parameter sets provide similar predictions in terms of the buckling life of the cylindrical member.
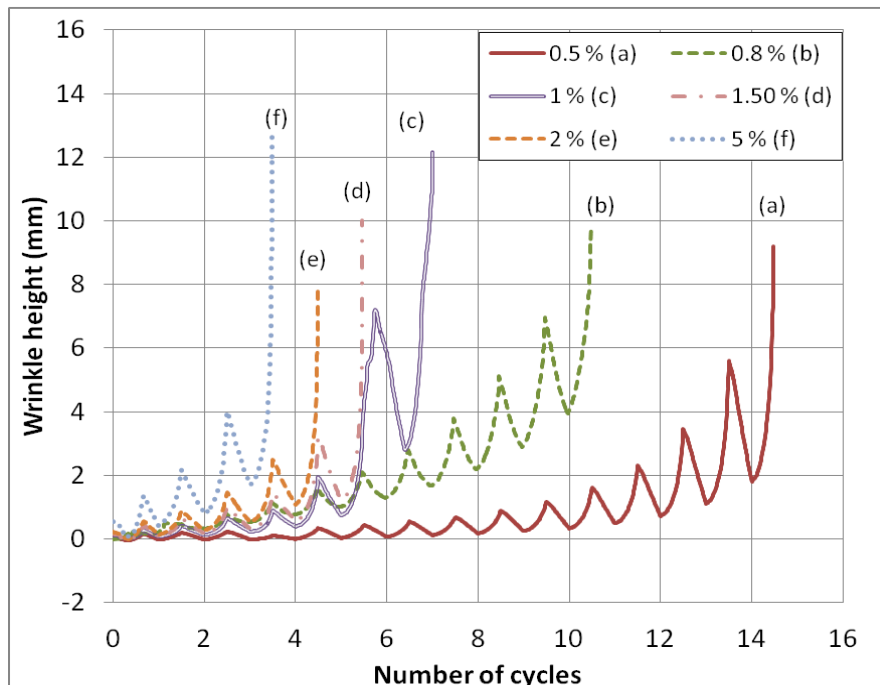

Figure 3. 10: Evolution of wrinkle height, $\Delta\varphi = \pm 2.5\varphi_y$, $D = 324.75\,\mathrm{mm}$, $t = 10.88$, $\sigma_y = 735$ MPa.

70
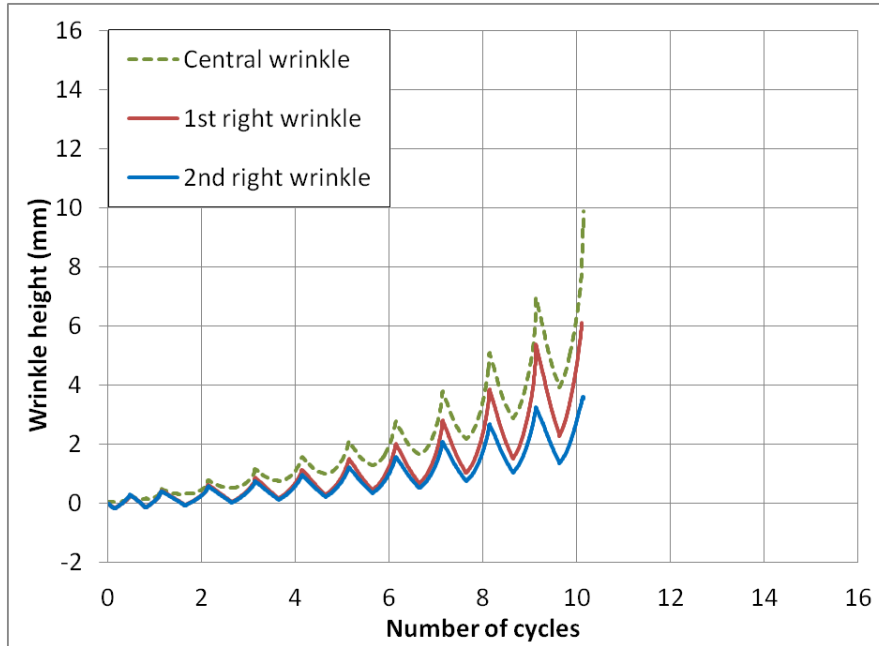
Figure 3. 11: Evolution of the central and the secondary wrinkles under cyclic loading; initial wrinkling imperfection 0.8%, $\Delta\varphi = \pm 2.5\varphi_y$, $D = 324.75$ mm, $t = 10.88$, $\sigma_y = 735$ MPa.
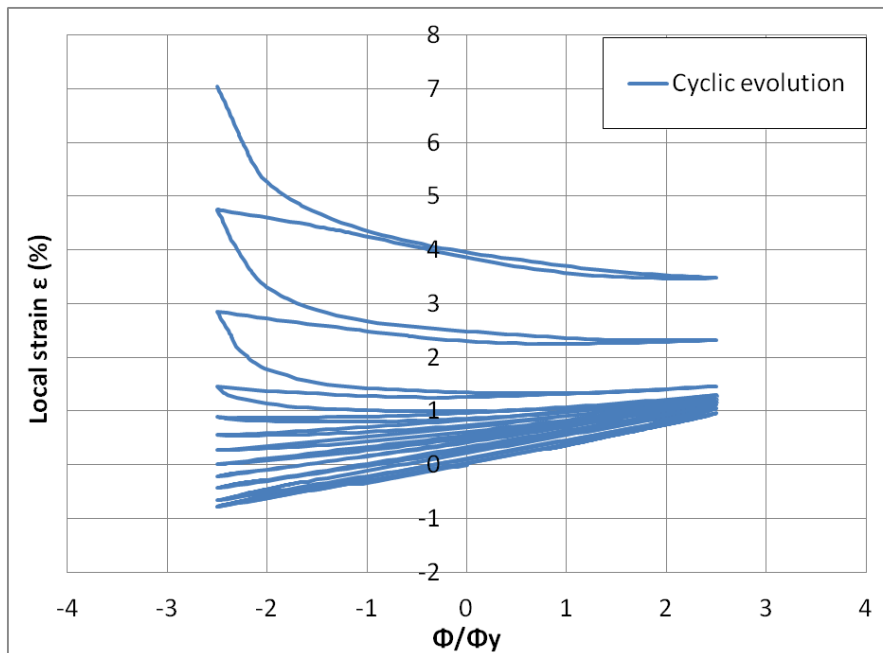
Figure 3. 12: Evolution of longitudinal tensile strains at central buckle – inner pipe side, initial wrinkling imperfection 0.8%, $\Delta\varphi = \pm 2.5\varphi_y$, $D = 324.75$ mm, $t = 10.88$, $\sigma_y = 735$ MPa.

The curves presented in Figure 3. 14, indicate that for initial wrinkling amplitude greater than about 2% of the tube wall-thickness, the number of cycles to buckling can be very small. In particular, for applied end-rotation

71

$\Delta\varphi = \pm 3\varphi_y$ and for initial wrinkling values at about 5% of the tube thickness, the tube is expected to buckle during the first 1-2 complete loading cycles. In addition to wrinkle height evolution, a significant increase of ovalization is also observed due to the development of plastic deformations on the tube, shown in Figure 3. 16 for $\Delta\varphi = \pm 2.5\varphi_y$.

Figure 3. 13: Local buckling of cyclically bent cylinder; 1% wrinkling imperfection.
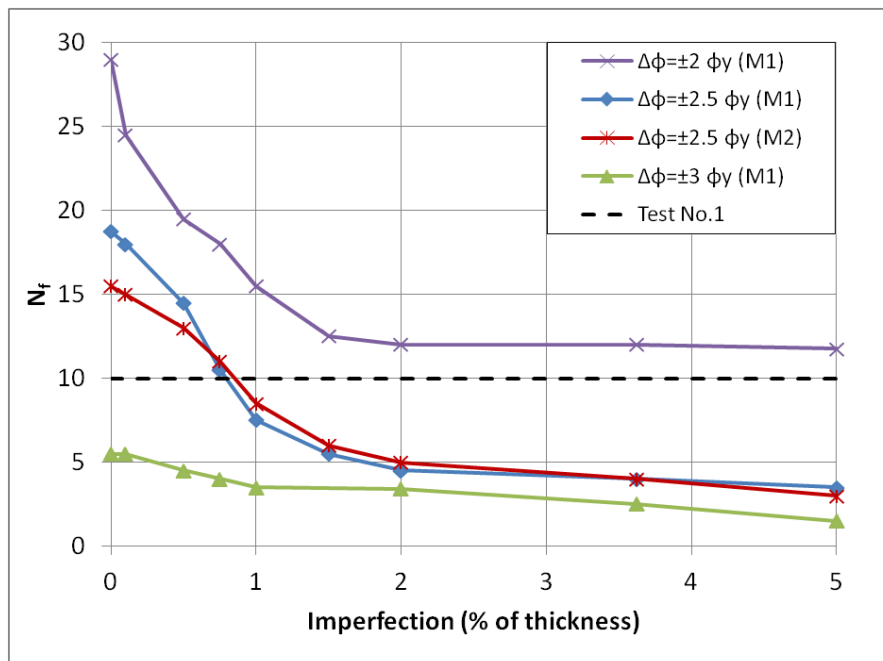
Figure 3. 14: Initial imperfection effects on the number of cycles to buckling, $\Delta\varphi = \pm 2.5\varphi_y$, $D = 324.75\,\text{mm}$, $t = 10.88$, $\sigma_y = 735$ MPa.

72

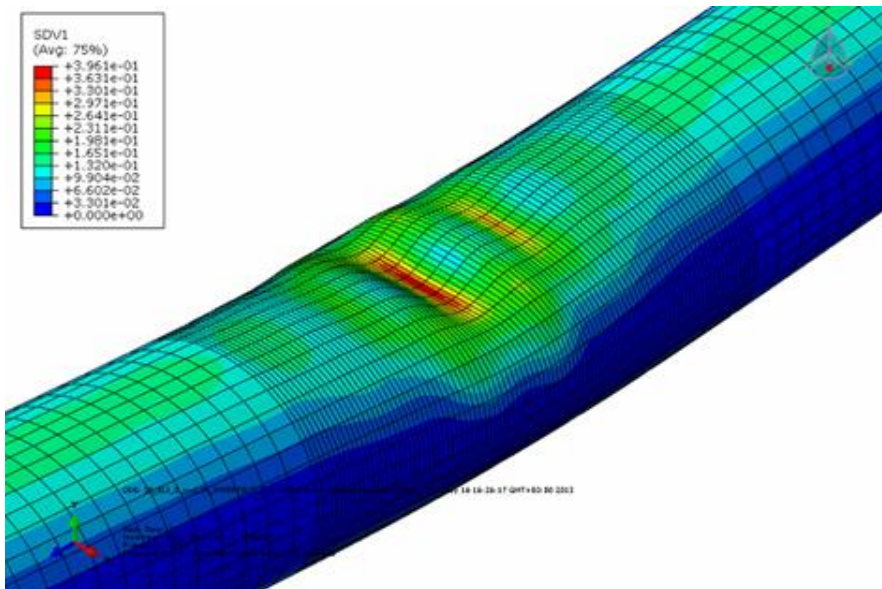Previous experimental works on cyclically bent tubes by Kyriakides & Shaw (1987) have reported that buckling occurs when the cross-sectional ovalization reaches approximately the corresponding critical ovalization for monotonic loading. The validity of this observation is examined in the present study. Figure 3. 16 shows the evolution of ovalization for a tubular member with the mechanical and geometric characteristics of specimen No.1, and initial imperfection equal to 1% of the tube wall-thickness, subjected to cyclic loading. In addition, the ovalization of this tubular member at local buckling under monotonic bending, is also depicted with a horizontal dashed line. This latter value is equal to 0.12, as shown in Figure 3. 8(b). The results show that, under cyclic loading conditions, buckling of the specimen occurs at a value of cross-sectional ovalization very close to this value as shown in Figure 3. 14, demonstrating the validity of this argument. Similar results have been observed in all cases examined in the present study.

(a)

73
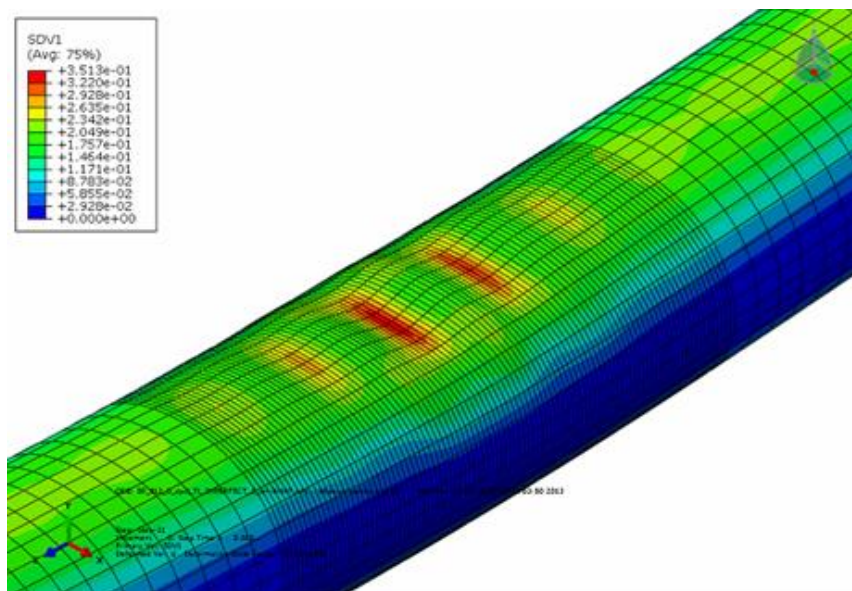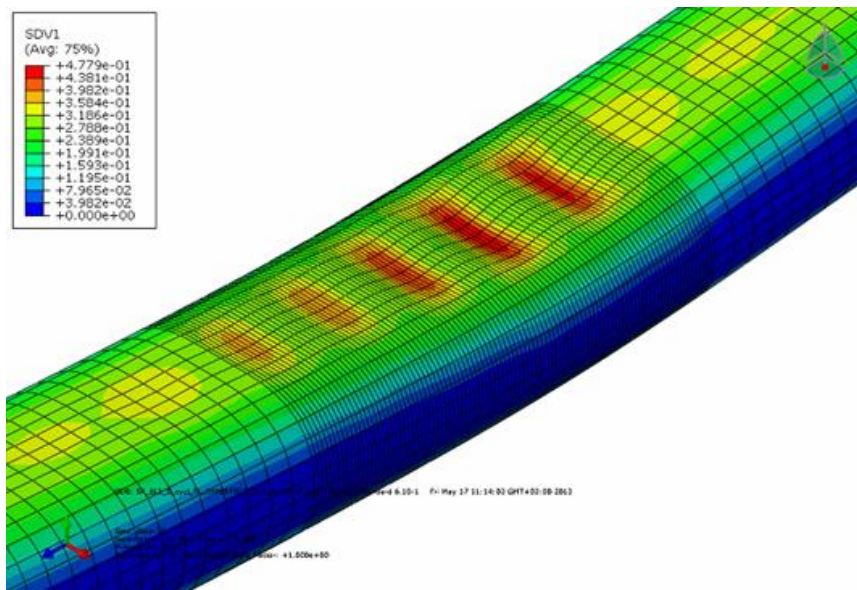
(b)

Figure 3. 15: Local buckling – FE results – 0.1% initial wrinkle amplitude: Distribution of plastic deformation (a) M1 set, (b) M2 set.
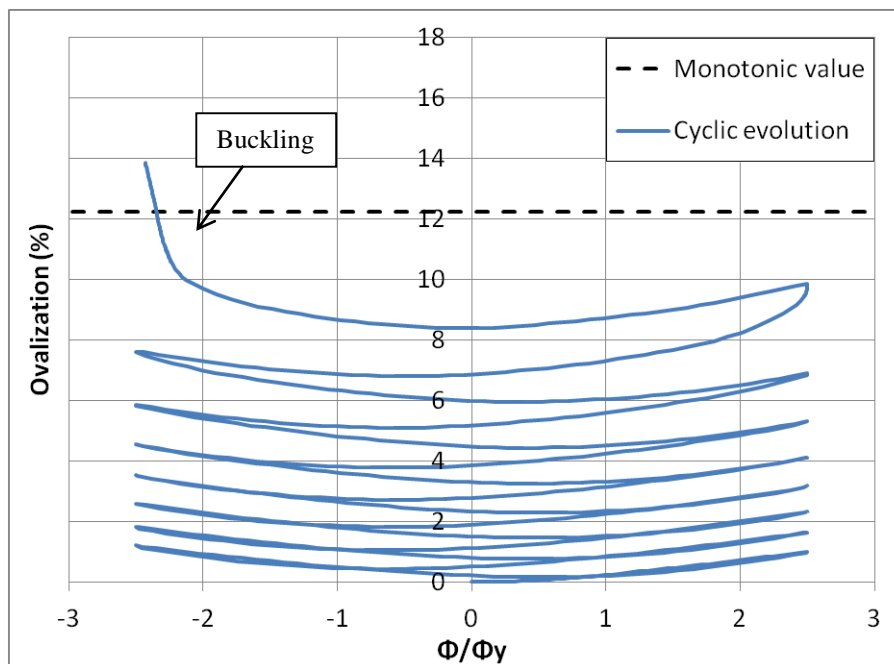
Figure 3. 16: Evolution of cross-sectional ovalization for symmetric cyclic bending; initial wrinkling imperfection 1%.

The effect of non-symmetric cyclic loading on the members under consideration has been also examined for the tube under consideration, using the M1 material parameter set. The selected loading pattern is $\Delta\varphi = \pm 2.5\varphi_y$ with $\varphi_{max} = 3.5\varphi_y$ and $\varphi_{min} = -1.5\varphi_y$. The rotation range is equal to $5\varphi_y$ similar to the one applied in test No.1, but with a non-zero mean rotation, equal to φ_y. For initial wrinkling amplitude equal to 0.8% the cylindrical member exhibits local

74

buckling after 11 load cycles, very close to the corresponding predicted number of cycles for symmetric loading ($N_f = 10$), as presented in Figure 3. 17, verifying the experimental results. The resulting curve for non-symmetric loading conditions is compared with the corresponding curve for symmetric loading conditions with the same total rotation amplitude. It can be observed that the non-symmetric loading conditions are more severe on the buckling life of the member for initial wrinkling amplitudes up to 0.5%. Nevertheless, for higher wrinkle amplitudes, the symmetric loading pattern results to somewhat fewer cycles until buckling. Results in terms of ovalization evolution under non-symmetric loading are presented in Figure 3. 18. It is worth noticing that under non-symmetric loading conditions local buckling appears when the total ovalization value reaches a value of somewhat higher than 0.12, the value corresponding to buckling under monotonic loading, a result very similar to the one observed in symmetric loading conditions.
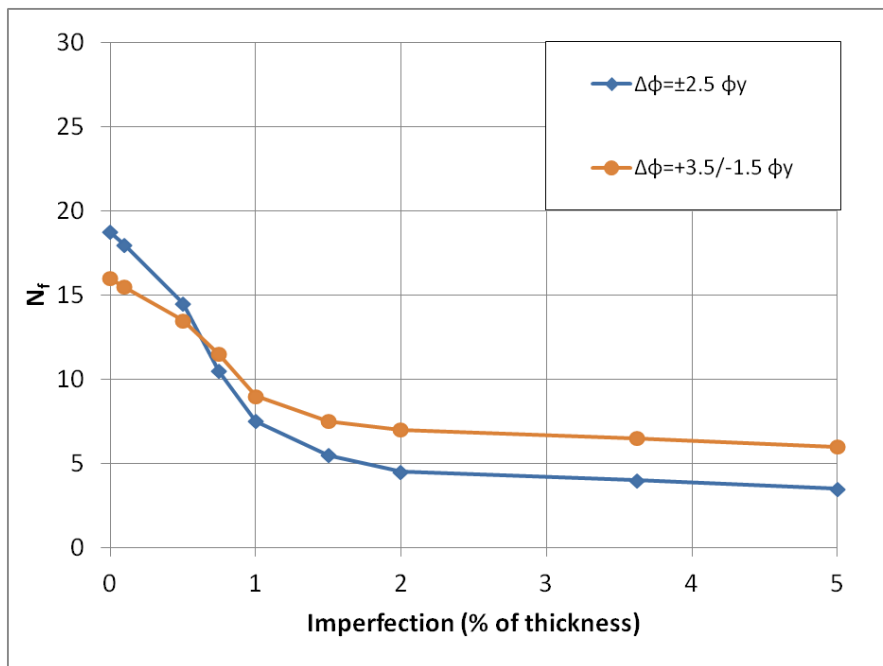
Figure 3. 17: Wrinkling imperfection effects on the "buckling life" for symmetric and non-symmetric loading.

75
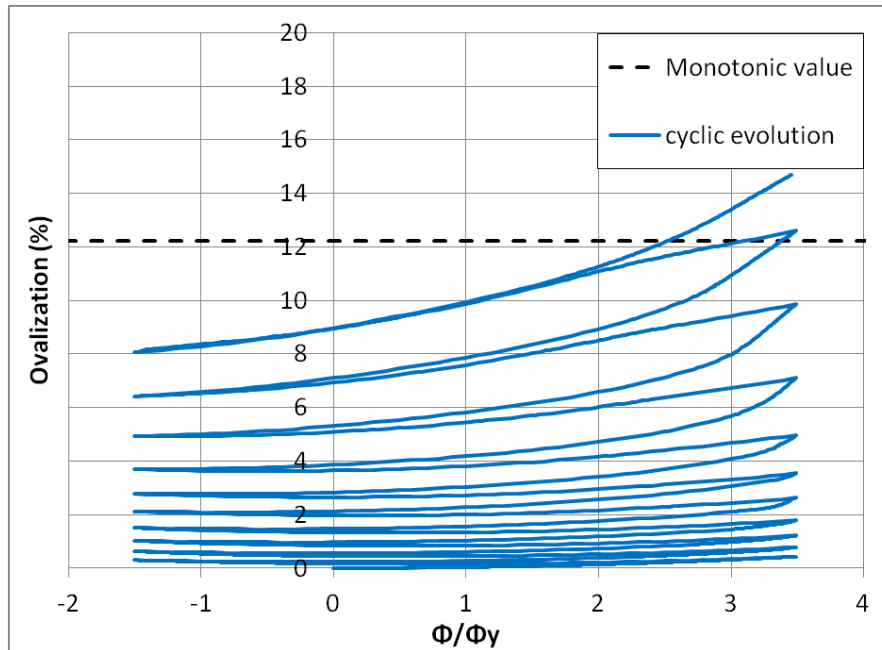
Figure 3. 18: Evolution of cross-sectional ovalization for non-symmetric cyclic bending; initial imperfection 1%.

3.7 Conclusions

A numerical investigation of the behavior of high-strength steel tubular members subjected to cyclic bending conditions beyond the elastic behavior limit is presented. The investigation is motivated by relevant experimental evidence, and employs rigorous finite element simulation tools, that adopt an appropriate constitutive cyclic plasticity model.

The parametric analysis results have demonstrated that under cyclic bending conditions, tubular members are susceptible to buckling, even for rotation amplitudes within the rotation limits imposed by monotonic loading conditions. The numerical results have also shown significant imperfection sensitivity on the "buckling life" of these members (i.e. the number of loading cycles to buckling), especially for relatively small rotation amplitudes. It has also been observed that for initial wrinkling values greater than 2% of the tube thickness, the corresponding number of cycles to buckling for a given value of imposed rotation is quite small, but not significantly affected by the amplitude of the initial wrinkles.

Under both symmetric and non-symmetric cyclic loading conditions, the evolution of the cross-sectional ovalization results to buckling of the cylindrical member. The numerical results show that buckling occurs at an ovalization value very close to the corresponding ovalization under monotonic loading conditions.

76

Chapter 4

Steel pipe elbows under strong cyclic loading

4.1 Introduction

Steel pipe elbows are essential components of industrial piping systems and steel pipelines, and their structural performance is critical for the integrity of the industrial facility or the pipeline (Suzuki (2006), Paolacci et al. (2011)). Under extreme loading conditions (e.g. earthquake), they may exhibit significant cross-sectional distortion (ovalization), associated with deformation well beyond the elastic limit of the material, which may cause failure of the piping component, in the form of excessive cross-sectional ovalization or local buckling.

Notable experimental data on the behavior and strength of steel elbows under monotonic loading conditions have been reported by Sobel and Newman (1980, 1986), Dhalla (1987), Gresnigt et al. (1986, 1995), Greenstreet (1978) and more recently by Hilsenkopf et al.(1988), Suzuki and Nasu (1989) and Tan et al. (2002). Notable numerical works on steel elbows have been reported by Shaleby and Younan (1998), Mourad and Younan (2001), and Chattopadhyay et al. (2000). Karamanos et al. (2003, 2006) carried out extensive numerical studies of steel elbow response under in-plane and out-of-plane bending, which were extended by Pappa et al.(2008), to include the effects of external pressure.

The above works focused on monotonic loading. However, in the course of a strong seismic event, the elbows are subjected to strong repeated cyclic structural loading, associated with deformation of the steel material in the inelastic range. Under those cyclic loading conditions, the elbow may exhibit significant accumulation of plastic strain (often referred to as "ratcheting"), which eventually may lead to failure. Extensive experimental work on the ratcheting behavior of pressurized 2-inch carbon and stainless steel pipe elbows has been reported by Yahiaoui et al. (1996a), under an "increasing input displacement amplitude" loading. This work was continued in the study of Yahiaoui et al. (1996b) for out-of-plane bending, whereas Moreton et al. (1996) attempted to predict analytically the ratcheting rate and ratcheting initiation. Slagis (1998) reported an EPRI/NRC experimental testing program on carbon/stainless steel pipe elbows, through a shaking-table apparatus, for both component tests and piping system tests. Extensive experimental work was presented by Fujiwaka et al. (1999), through a series of material tests, pipe component tests and piping system tests (bent pipes, tees, and straight pipes).

Degrassi et al. (2003) performed seismic time-history finite element analysis of piping system for simulating ratcheting, using the bilinear, multilinear and Chaboche models in ANSYS. Balan and Redektop (2004) simulated the response of elbow specimen under cyclic bending and internal pressure with bilinear plasticity model in the finite element code ADINA. More recently, Rahman and Hassan (2009) presented an extensive analytical work on cyclic

77

behavior of steel elbows, supported by 3 experiments on 2-inch SCH10 pipes, aiming at determining the capabilities of several cyclic plasticity models in predicting the ratcheting rate. All the above works demonstrated that when steel elbows are subjected to strong repeated loading, they present failure associated with material degradation or cyclic creep. In many instances, the elbow cross-section distorted or bulged with increasing number of cycles.

A joint effort of Delft University of Technology, Centro Sviluppo Materiali (CSM) and the University of Thessaly was recently conducted in the framework of a large European research program, aimed at investigating the structural safety of industrial equipment structures and components under seismic loading with emphasis on process piping and elbows. This research focused on the low-cycle fatigue of pipe elbows and their elastic-plastic behavior under strong cyclic bending, and had an experimental and a numerical part. In the followings emphasis is given on the numerical part, while the experimental part is briefly described herein for the sake of completeness

4.2 Experiments on steel pipe elbows

The elbow experiments conducted in the course of INDUSE project [Karamanos (2013)] are presented extensively in Varelis et al. (2013a , 2013b). In those experiments 8-inch SCH40 long-radius steel pipe hot bends have been tested with nominal diameter and thickness equal to $D = 219.1$ mm and $t = 8.18$ mm respectively, and bend radius $R = 305$ mm under strong cyclic in-plane bending. The material of the specimens is P355N, according to EN 10216 standard, which is the EN equivalent of API 5L X52 steel grade.
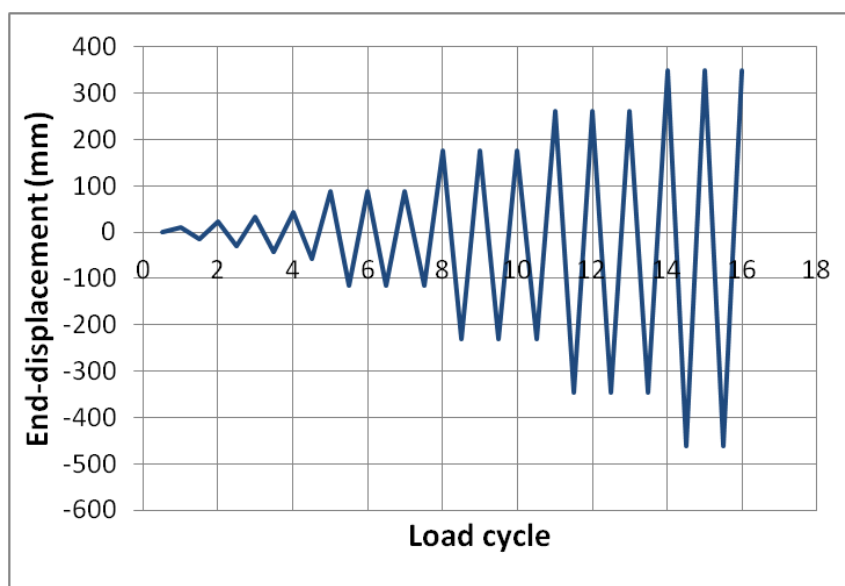
Figure 4. 1: Increasing amplitude loading pattern according to the ECCS No 45 recommendations.

The first set of experiments took place at Delft University of Technology, as presented in [Karamanos (2013), Varelis et al. (2013a)], and consisted of eight tests; the seven first tests followed a constant-amplitude end-displacement, whereas a constantly increasing-amplitude loading sequence according to the ECCS No 45 provisions has been applied to the eight specimen. All eight

78

specimens had a very small internal pressure (0.1 MPa) with negligible effects on the overall behavior, applied for the purpose of detecting through-thickness crack. In the following, these experiments are referred to as "non-pressurized" tests.
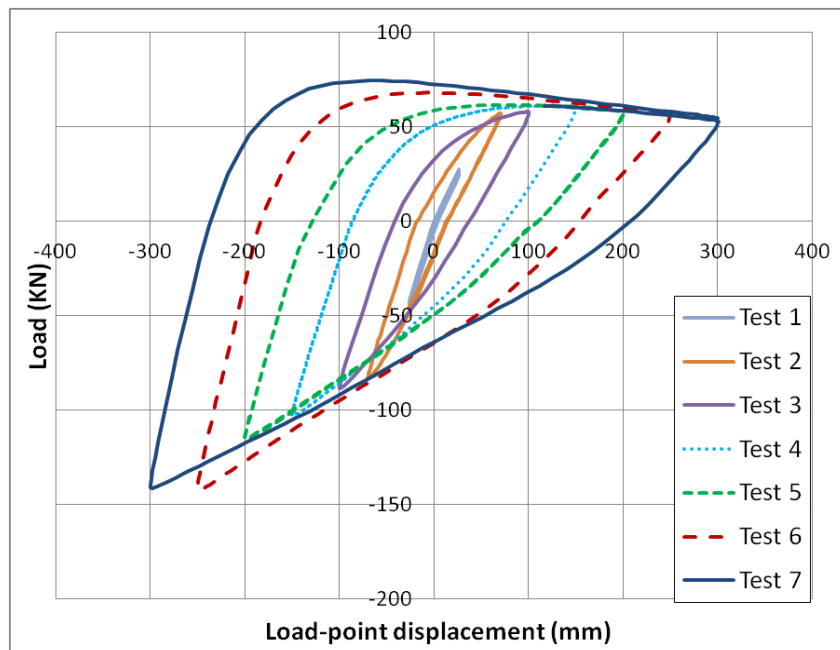
Figure 4. 2: First load cycle for Test 1 to Test 7
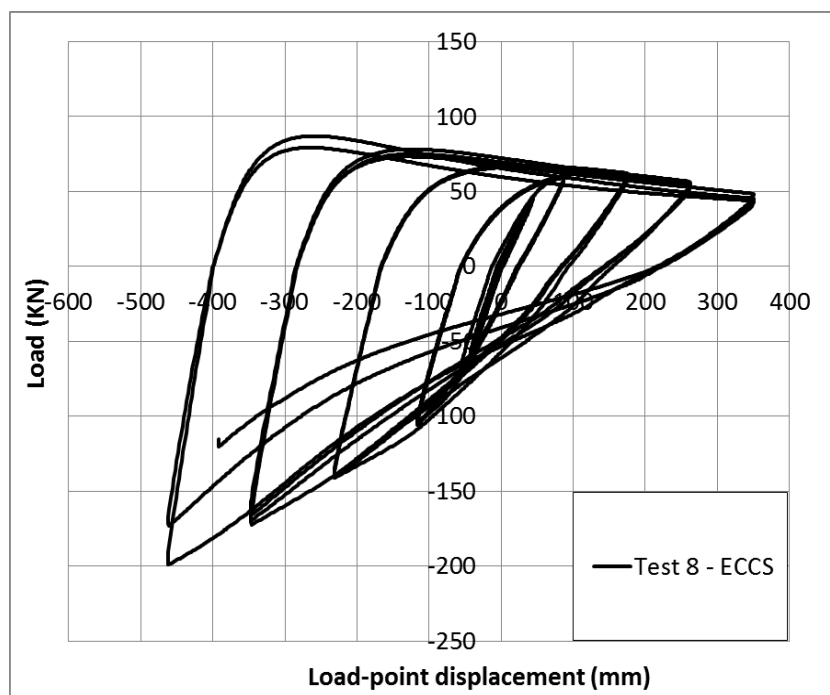
Figure 4. 3: The Test 8 – ECCS load cycles

The effect of the internal pressure was studied in the second set of experiments performed at CSM laboratories, Sardinia [Karamanos (2013), Varelis et al. (2013b)]; five pressurized elbows bending tests have been subjected to in-plane bending in the presence of various internal pressure load

79

levels. The specimens and the test configuration are identical to the corresponding ones employed in the "non-pressurized" elbows. Internal pressure has been applied at levels of 3.2MPa, 7MPa, and 12 MPa, corresponding to nominal hoop stress equal to 12%, 26% and 45% of the yield stress. Pressure has been applied first up to the desired level, then kept constant and cyclic loading been applied.

The experimental set-up of sets of tests is presented in Figure 4. 5. In both experimental series, the instrumentation was very similar; strain gauges were used to monitor the evolution of local strains at critical location (elbow "flank"), displacement transducers monitored accurately the opening or closing displacements of the elbow ends, whereas the change of the elbow vertical diameter (referred to as "flattening") was monitored at the middle cross-section of the elbow with the use of special-purpose frame devices attached on each specimen.
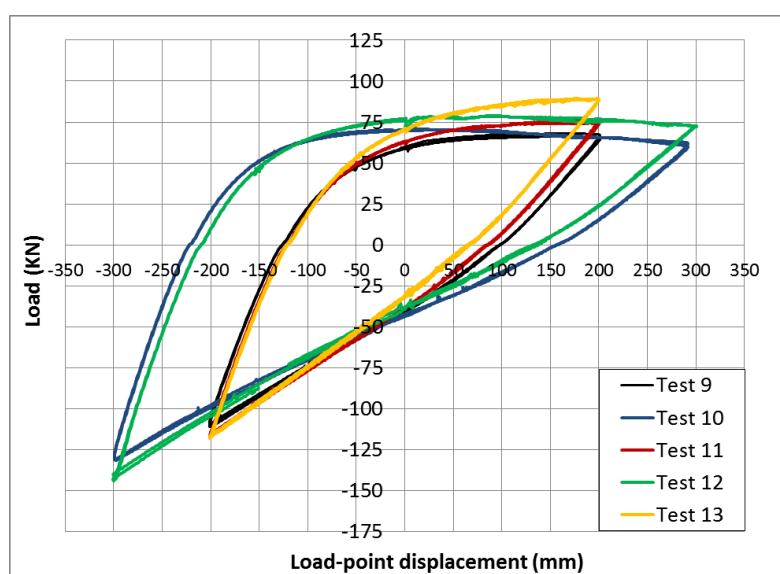
Figure 4. 4: First load cycle for Test 9 to Test 13

Before testing the specimens, thickness variation measurements on the elbow and the straight pipes have been obtained on each specimen at various cross-sections. The measured values differ significantly from the nominal thickness value (8.2 mm) up to 1.9 mm at the elbow mid-section with an average thickness value of 9.98 mm (21.7 % higher than the mean value), attributed to the manufacturing process of the elbows. This variation was taken into consideration in the development of the numerical models, as presented in the next section.

The mechanical properties of the P355N steel grade have been determined experimentally [CSM (2011)], conducting several uniaxial and cyclic material tests on strip specimens extracted from the longitudinal and hoop direction of the elbow. The material test results were employed for the calibration of the constitutive material model parameters, to be presented in a subsequent section.

A summary of the experimental results on the elbow specimens is

presented in Table 4. 1. The number of cycles until failure of each specimen N_f corresponds to the development of through-thickness crack and loss of piping containment. It is noted that the crack configuration presented in Figure 4. 6 is similar for all specimens.
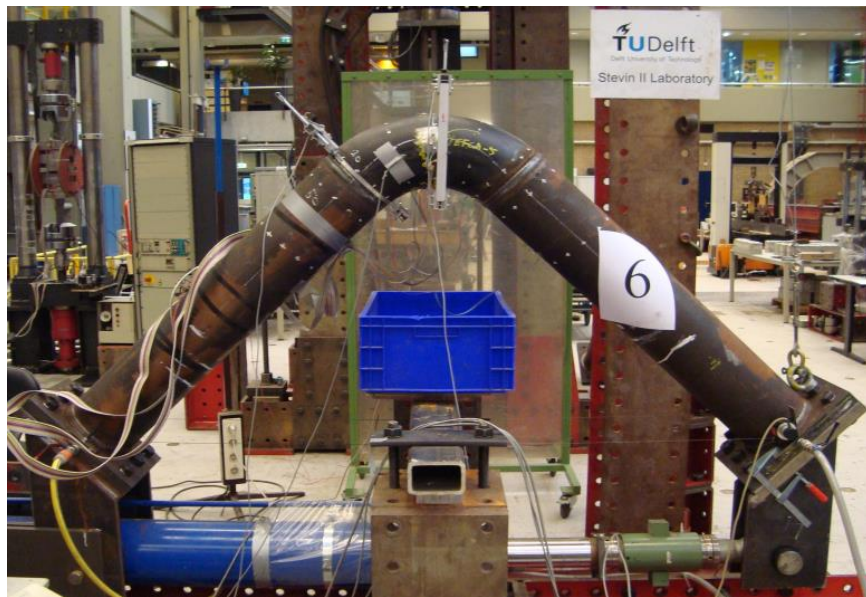
(a)

(b)

Figure 4. 5: Experimental set-up: (a) non-pressurized specimens tested at TU Delft, (b) pressurized specimens tested at CSM

81

Figure 4. 6: Crack location at the elbow "flank".

Table 4. 1: Summary of tests

Test No.	Δl (mm)	N_f	p (MPa)	$\Delta\varepsilon_{H,exp}$ (%)	$\Delta\varepsilon_H$ (%)	$\Delta\varepsilon_L$ (%)
1	±25	13160	0.0	0.33	0.33	0.04
2	±70	444	0.0	1.23	1.25	0.14
3	±100	171	0.0	-	1.59	0.14
4	±150	61	0.0	2.61	2.55	0.16
5	±200	28	0.0	-	2.77	0.16
6	±250	17	0.0	3.84	3.75	0.18
7	±300	10	0.0	4.02	4.03	0.30
8	ECCS	16	0.0	-	-	-
9	±200	26	3.2	3.01	2.89	0.23
10	±300	10	3.2	-	2.39	0.97
11	±200	27	7.0	-	2.69	0.39
12	±300	10	7.0	1.94	2.25	0.98
13	±200	22	12.0	-	0.63	1.49

4.3 Finite element modeling of steel pipe elbows

The experimental work described in the previous section motivated the development of rigorous finite element models for simulations. The models have been developed in finite element code ABAQUS and employ the dimensions of the specimen based on relevant measurements conducted prior to the test execution. The elbow part of the specimen and the two straight pipe segments have been modeled as three separate parts. Thickness variability of the elbow has been taken into account, adopting a uniform thickness equal to the local mean measured thickness value. A uniform thickness, equal to the measured average value, has also been used for the straight parts. In the weld regions, the

82

weld over-thickness is also modeled appropriately, allowing for a realistic and smooth thickness transition between the elbow and the adjacent straight parts.
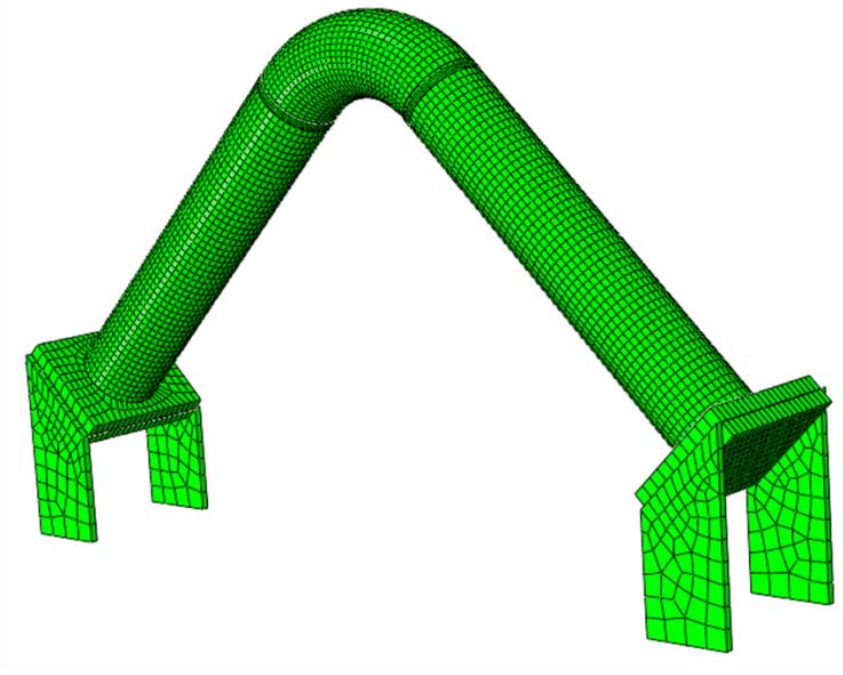
Figure 4. 7: General view of the finite element model.

Eight-node incompatible mode (C3D8I) solid elements are used for the numerical simulations. The specific type of elements was selected against the eight-node reduced integration elements (C3D8R) because of its ability to provide simulation results in better agreement with the experimental measurements, without the need of increasing the number of elements. Nevertheless, comparison of the simulation results adopting both types of elements shows only minor differences, less than 1.5%. The models take into account nonlinear geometry and material nonlinearities through a large-strain formulation and a von Mises yield surface. A short parametric study was conducted for the selection of this type of elements and mesh size in order the models to simulate accurately and efficiently the overall behavior of the specimen, as well as the local plasticity phenomena. The size of the element in the longitudinal direction at mid-height of the pipe section is equal to 12.23 mm, i.e. about 1/18 of the pipe diameter. In the hoop direction, it is equal to 17.2 mm which is about 1/13 of the pipe diameter. In Figure 4. 7, a general view of the numerical model is depicted.

Special attention is given on the accurate simulation of the material behavior under cyclic loading conditions. The nonlinear behavior of the steel material is described through the two advanced cyclic material models, namely the Armstrong – Frederic nonlinear kinematic/isotropic (combined) hardening model, denoted as "NLKH" hereafter, and the Tseng – Lee model, denoted as "TL", presented in the Appendix and Chapter 2 respectively.

83

Figure 4. 8: Material curve and model predictions

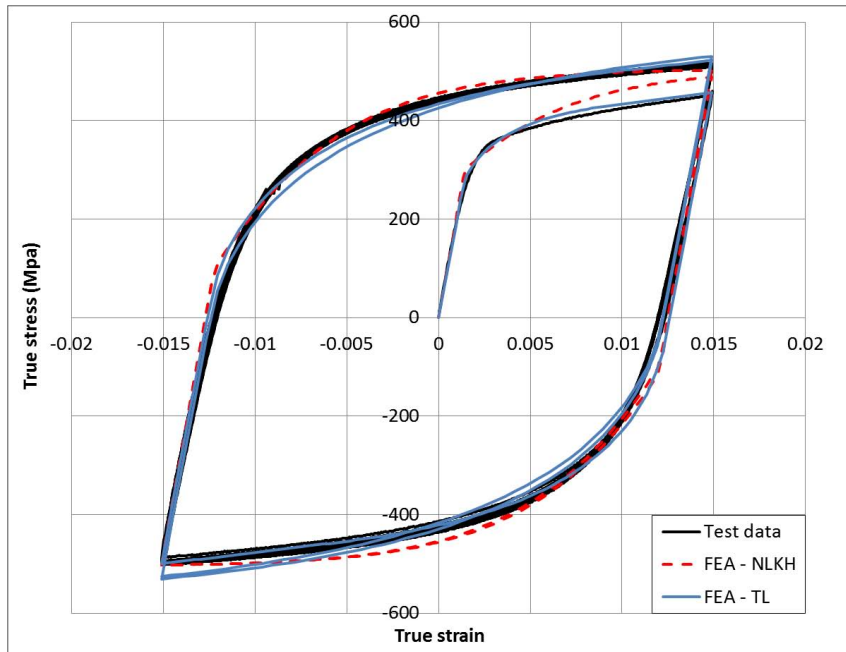Both models were calibrated to fit the material cyclic stress-strain curve, using the material test results from [CSM (2011)], and the corresponding values of k, C and γ are taken equal to 300 MPa, 46,000 MPa and 215 respectively. Based on the same material test results, the Tseng – Lee model was also calibrated. The resulting values of $\hat{H}$ and h are equal to 5,000 MPa, and 10. In addition, the initial size k_0 of the yield surface is equal to 280 MPa, Q is -50 MPa (cyclic softening) and b is equal to 100. The initial size of the memory surface is equal to 430 MPa, allowing for the simulation of the smooth transition from the elastic to the plastic regime observed in material testing. Adopting the aforementioned material model parameter values, the developed numerical model is able to predict accurately the material behavior under cyclic loading conditions, as presented in Figure 4. 8.

4.4 Numerical simulation of experiments

Based on the calibrated numerical model presented in the previous sections, the tests reported in Table 4. 1 have been simulated. The numerical results for the non-pressurized and the pressurized tests are compared with the corresponding experimental measurements in the following sections. The numerical simulation is aimed at demonstrating that the numerical models are capable of simulating accurately the test results in terms of the loading-displacement curves and flattening-displacement curves for non-pressurized and pressurized elbows for various end displacement ranges, even for complex loading schemes.

4.4.1 Numerical simulation of the non-pressurized tests

Using the numerical model presented in the previous paragraph, the non-pressurized tests (Test 1 to Test 9) have been simulated. For each specimen, a different finite element model has been developed taking into account the exact

84

geometry of each specimen part, as well as the weld region and the supports. Both cyclic plasticity models were employed for the simulations, providing similar results in the majority of the cases examined. Apart from the load-displacement curve, the numerical simulation is capable of predicting accurately cross-sectional flattening of each specimen. In all cases examined, the simulation results are in very good agreement with the experimental measurements, as presented in Figure 4. 9 to Figure 4. 13.
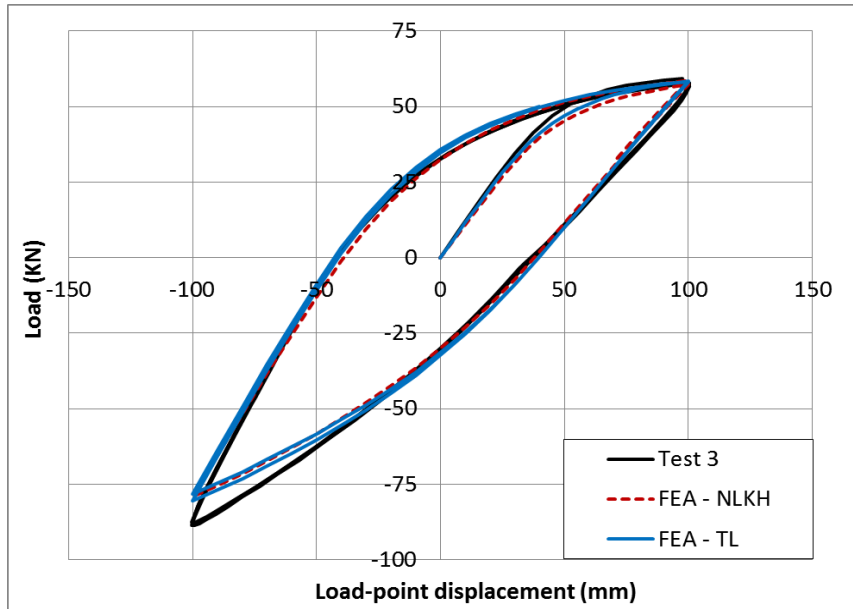
(a)
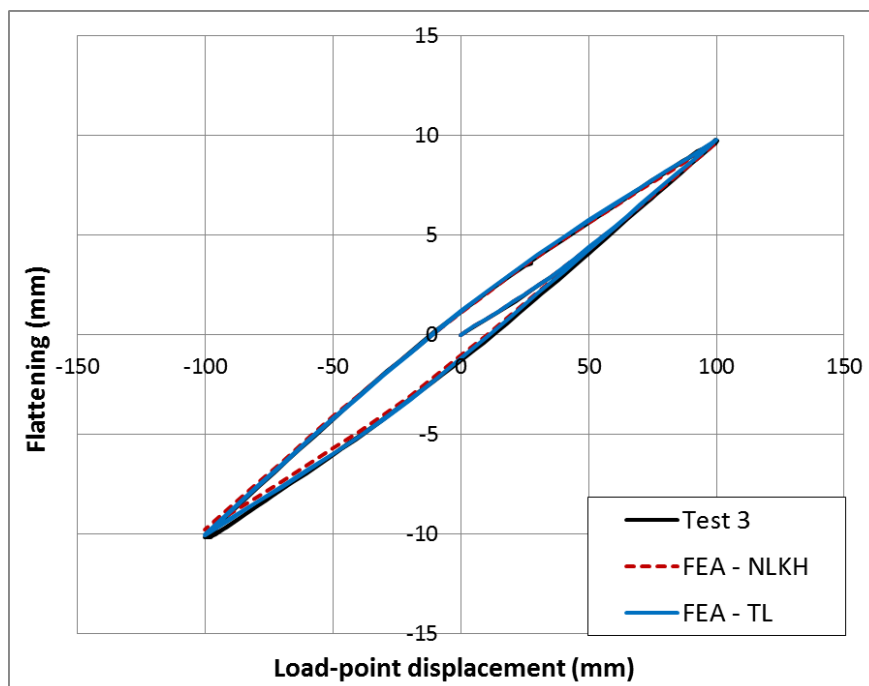
(b)

Figure 4. 9: Test 3 $\Delta l = \pm 100 \; mm, \; P = 0 \; MPa$: (a) Load-displacement curve, (b) Flattening-displacement curve

85
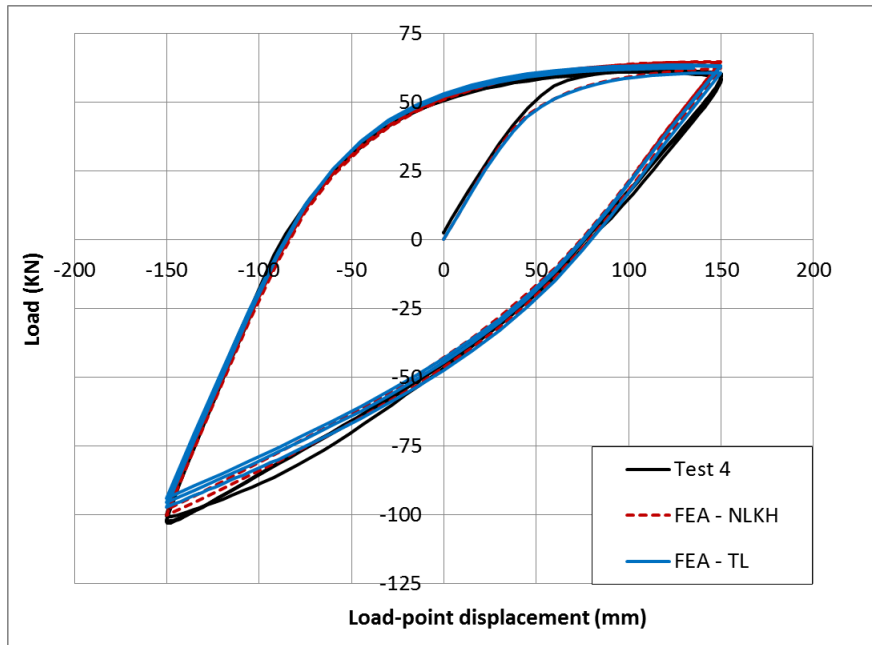
(a)
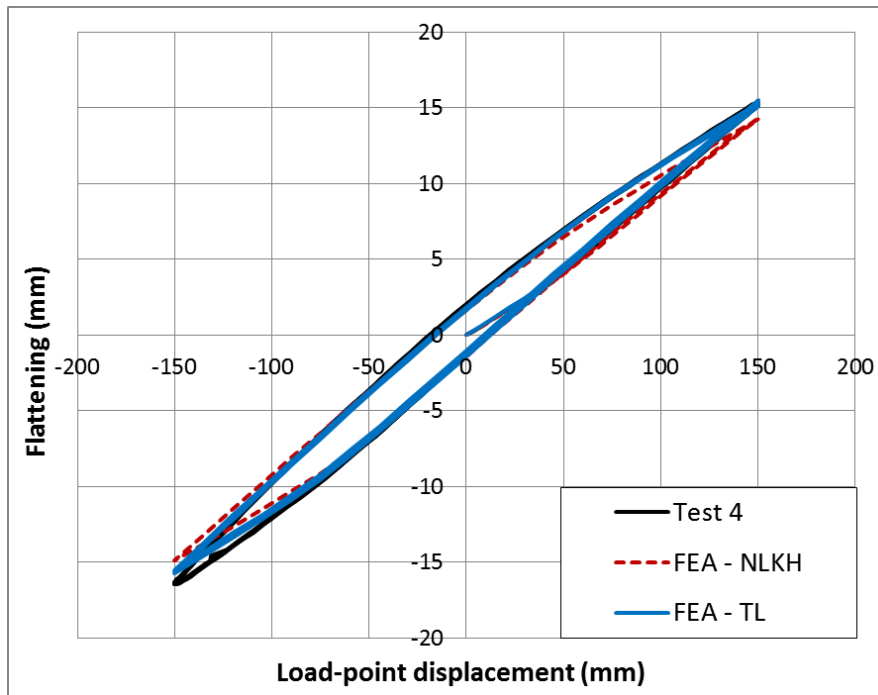
(b)

Figure 4. 10: Test 4 $\Delta l = \pm 150\ mm,\ P = 0\ MPa$: (a) Load-displacement curve, (b) Flattening-displacement curve

86
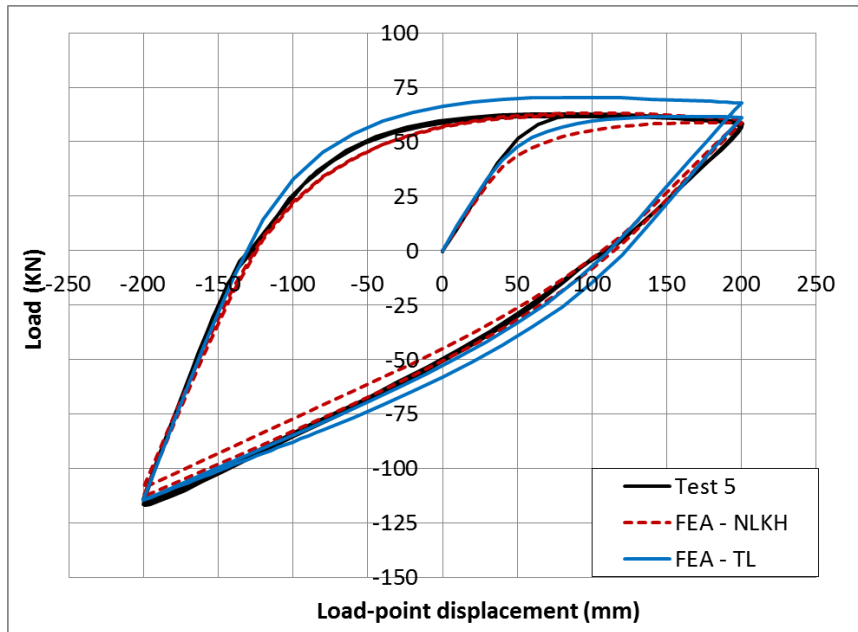
(a)
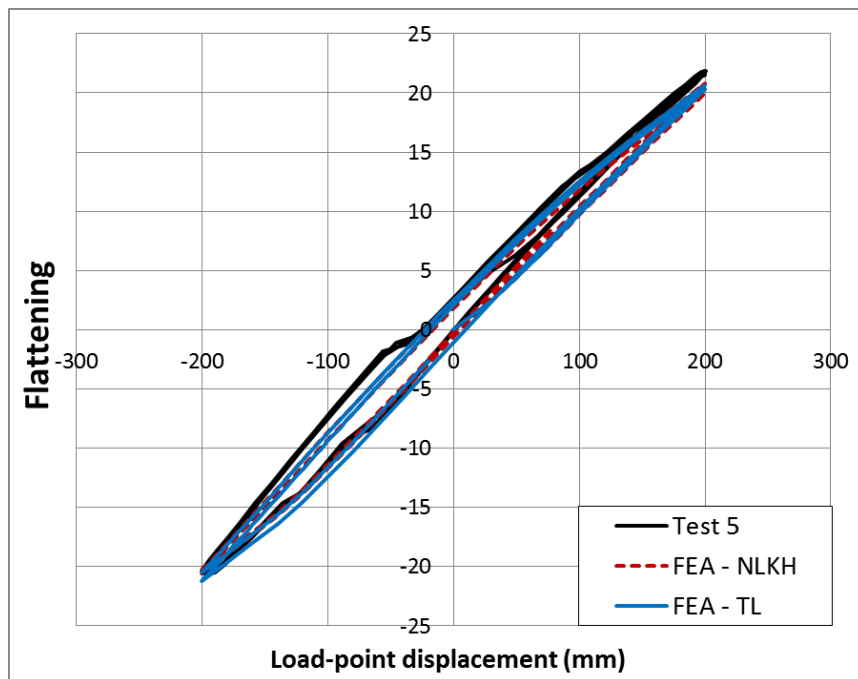
(b)

Figure 4. 11: Test 5 $\Delta l = \pm 200\ mm,\ P = 0\ MPa$: (a) Load-displacement curve, (b) Flattening-displacement curve
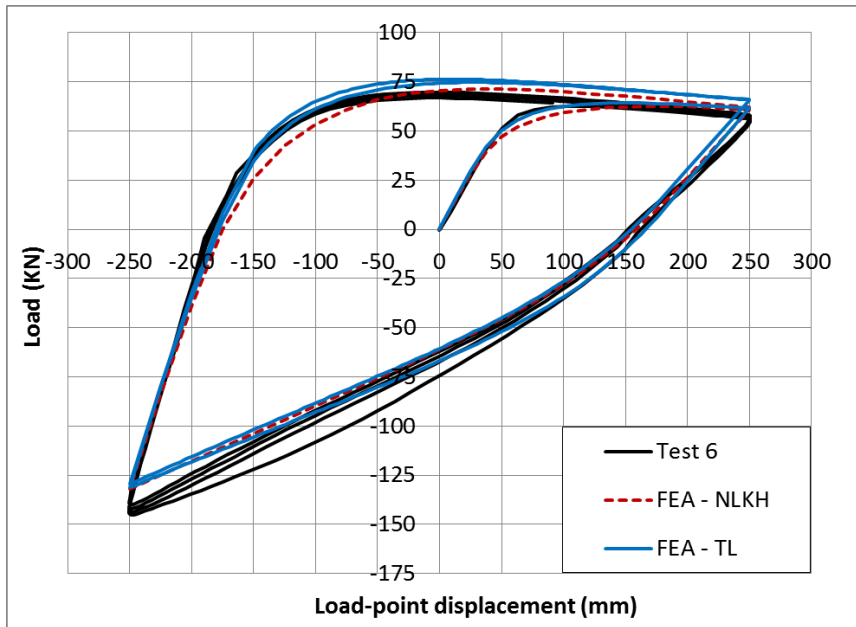
(a)
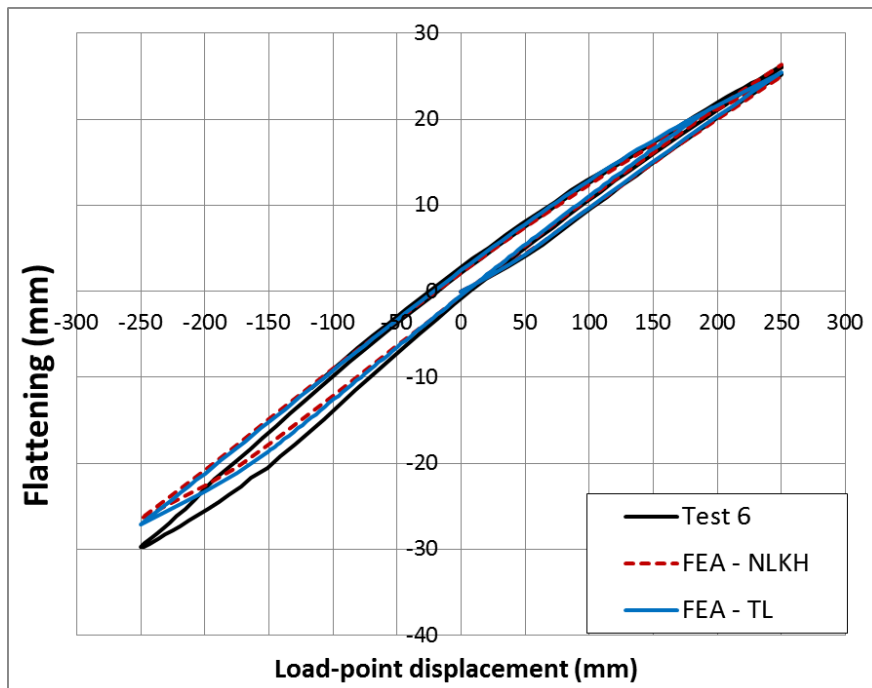
(b)

Figure 4. 12: Test 6 $\Delta l = \pm 250$ *mm*, $P = 0$ *MPa* : (a) Load-displacement curve,
(b) Flattening-displacement curve

88
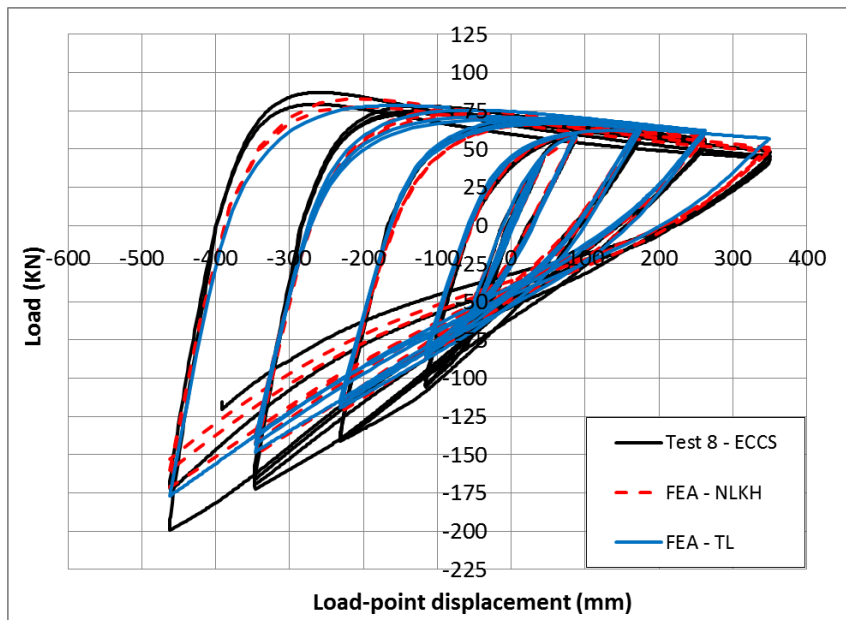
Figure 4. 13: Test 8 - ECCS $P = 0 \, MPa$: Load-displacement curve

The behavior of the elbow under opening and closing bending loads is not symmetric, as presented in the previous Figures. This is due to the different ovalization shape of the elbow section at its mid-plane, which results to different cross-sectional inertia characteristics, and thus different bending behavior under opening and closing bending. In Figure 4. 14, the aforementioned different ovalization shapes of the elbow are displayed. The depicted shapes indicate a severe flattening of the cross-section at opposite planes during the application of opening and closing bending loads.

The numerical results also verified the location of cracking; the concentration of plastic deformations reaches its highest value at about 20 mm below the elbow "flank" (at a distance equal to 2.5 times the pipe wall thickness), as illustrated in Figure 4. 15, exactly where the crack is developed, as shown in Figure 4. 6. Numerical results show that in this position the hoop stress reaches its maximum value. Furthermore, at this location, hoop strain is always greater than the corresponding longitudinal strain, and this verifies the direction of the crack in Figure 4. 6. Finally, it is interesting to note that an elastic analysis of the elbow shows a concentration of stresses in almost the same location where the cracks appear after excessive plastic deformation.

89

(a)   (b)
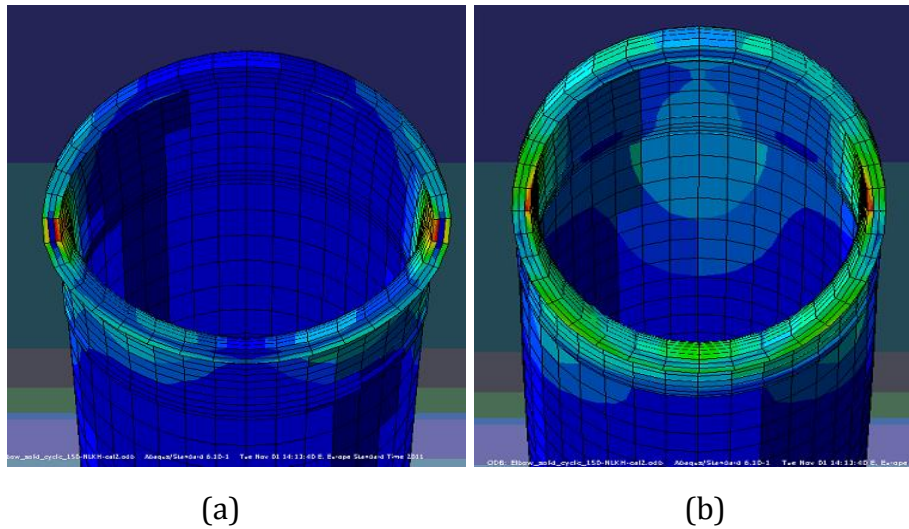
Figure 4. 14: Ovalization of middle section: (a) Closing and (b) Opening bending loads
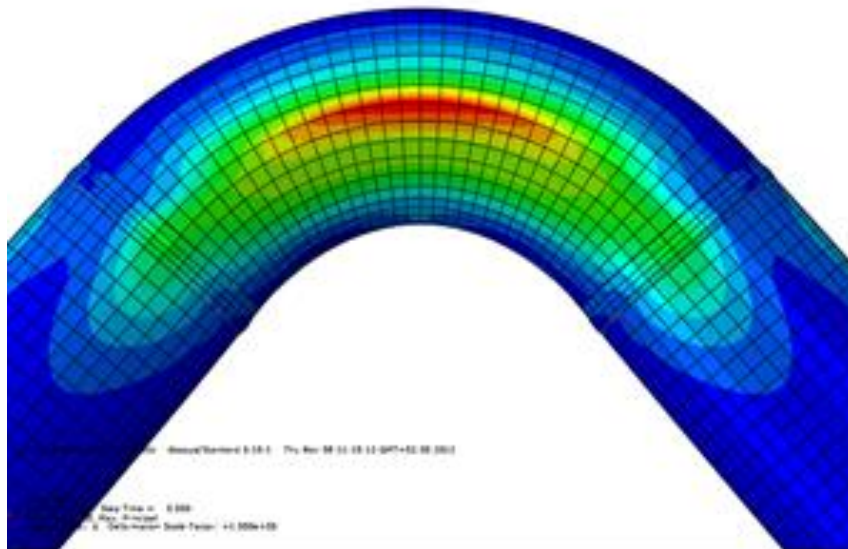
Figure 4. 15: Concentration of strain at the elbow critical region (elbow "flank").

Experimental results also show that the evolution of strains at the critical location with increasing number of loading cycles is characterized by accumulation of plastic strain at each cycle and an increase of the mean strain, while the total range is nearly constant. In Figure 4. 16 the evolution of hoop strain as measured in the non-pressurized case of Test No 4 is compared with the corresponding numerical predictions. Both experimental and numerical results show a significant accumulation of hoop strain, which leads to member failure due to fatigue. Nevertheless, the predictions of the TL model are much closer to the experimental measurements, while the NLKH model over predicts the local strain evolution rate.

90
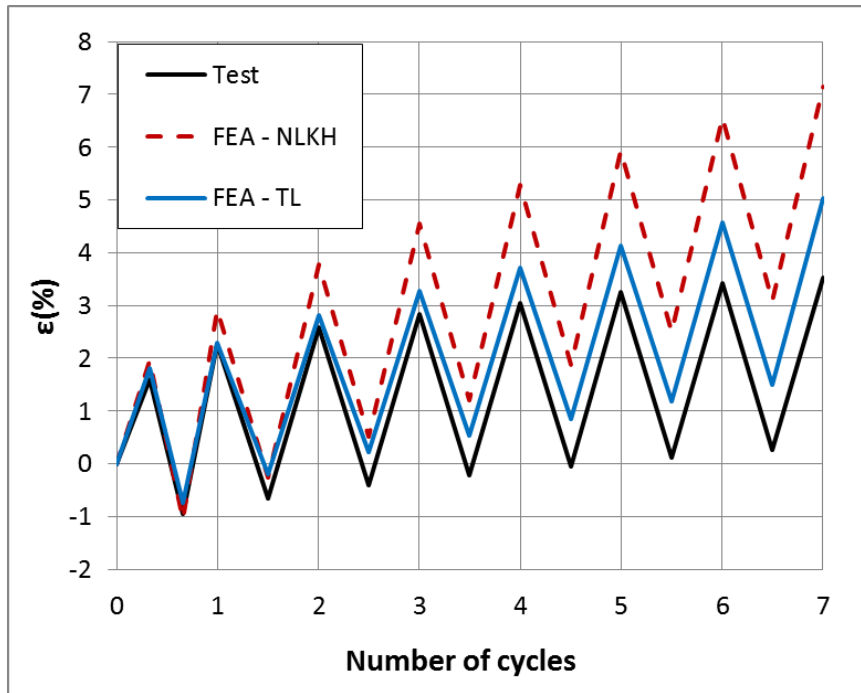
Figure 4. 16: Evolution of strains ranges at the critical region; end-displacement range $\Delta l = \pm 150\ mm$, hoop direction.

4.4.2 Numerical simulation of the pressurized tests

Using detailed numerical models, as those presented in the previous paragraph, the rest tests reported in Table 4. 1 on pressurized elbows have been simulated. In this set of tests only the TL constitutive material model was adopted for the simulations. Indicative simulation results for tests 9 to 13 are compared with the corresponding experimental measurements in Figure 4. 17 to Figure 4. 21. Apart from load-displacement curves, in some of the reported cases the numerically predicted flattening-displacement curves are compared with the corresponding experimental measurements. As in the experimental set of the non-pressurized elbows reported in the previous section, the developed numerical models are able to simulate accurately the tests on pressurized elbows as well.

The critical position where cracking took place in the experiments is also verified by the numerical model. Bellow the elbow mid-axis at the elbow flank region, there is a localization of strains mainly in the hoop direction, very similar to the one observed in the non-pressurized tests (Figure 4.15). This justifies the fact that all specimens exhibited cracks, which opened in the longitudinal direction of the elbow, regardless the pressure level applied.

The comparison between the flattening curves of the nine tests under consideration with the same end-displacement range for various pressure levels shows a small dependence of the cross-sectional deformation on the level of internal pressure. Figure 4. 22 presents the total cross-sectional flattening ΔD during an entire cycle, as obtained from numerical analysis for the tests with end-displacement ranges equal to $\Delta l = \pm 200\ mm$ and $\Delta l = \pm 300\ mm$. The flattening values are normalized by the elbow diameter D. It can be observed that as internal pressure increases, cross-sectional flattening decreases. In other words, in the case of pressurized elbows, the elbow cross-section at its mid-plane

91

maintains a more circular shape, and therefore it is capable of sustaining higher load level. Nevertheless, internal pressure induces additional stresses on the elbow that need to be added to the stress field of the deformed elbow for an accurate fatigue assessment. The effects of internal pressure on the fatigue life are discussed in a subsequent section.
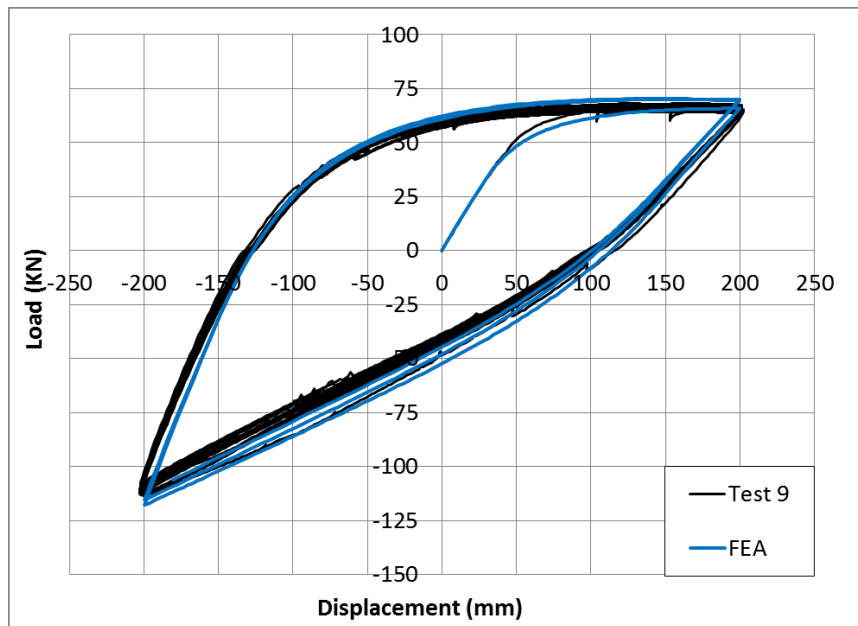
(a)
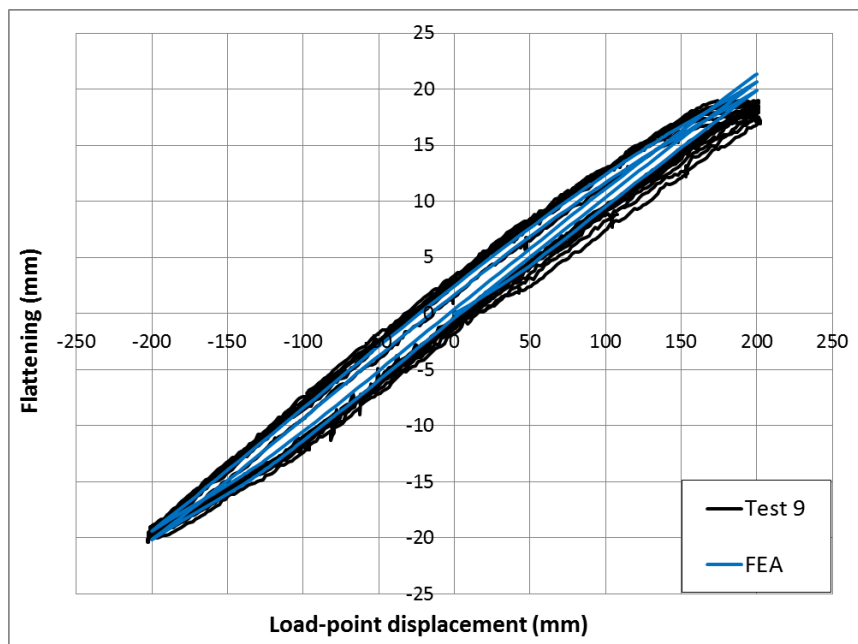
(b)

Figure 4. 17: Test 9, $P=3.2$ *MPa*, $\Delta l=\pm 200$ *mm* (a) Load - displacement, (b) Ovalization - displacement curve

92
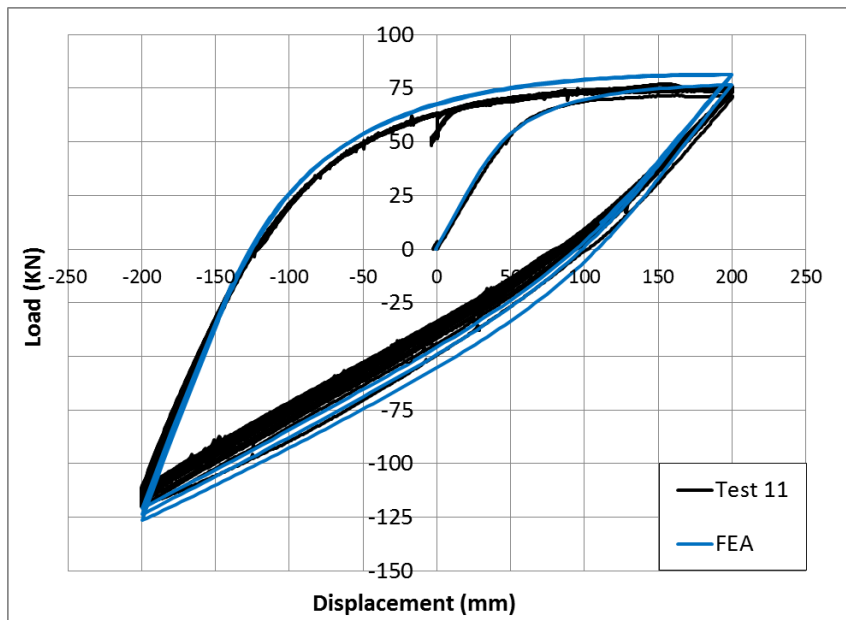
(a)
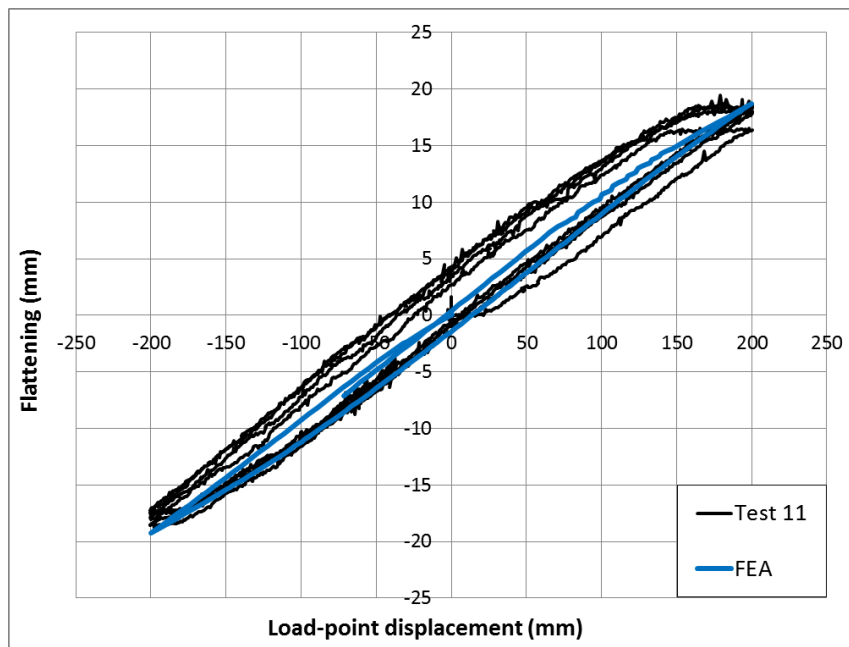
(b)

Figure 4. 18: Test 11, $P=7\ MPa$, $\Delta l=\pm 200\ mm$ (a) Load - displacement, (b) Ovalization - displacement curve

93
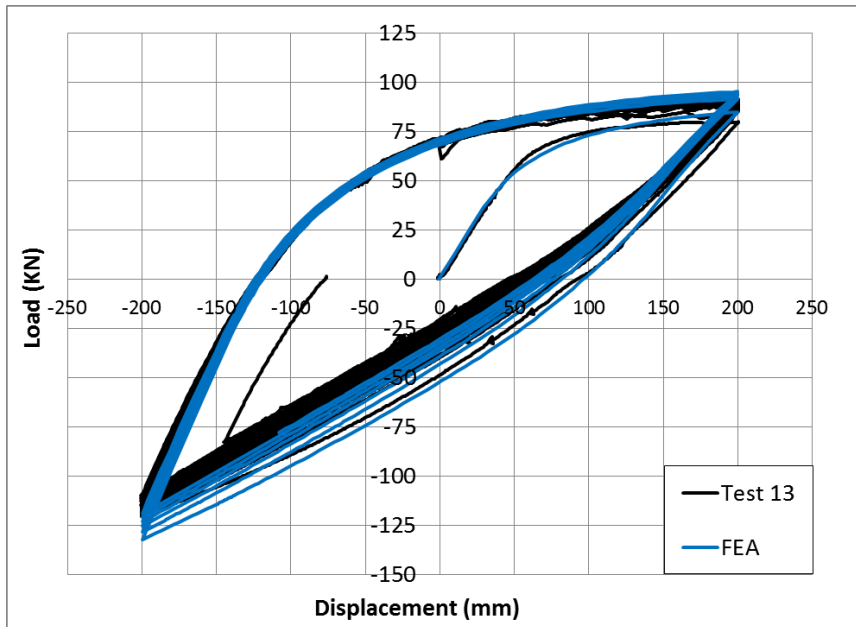
(a)
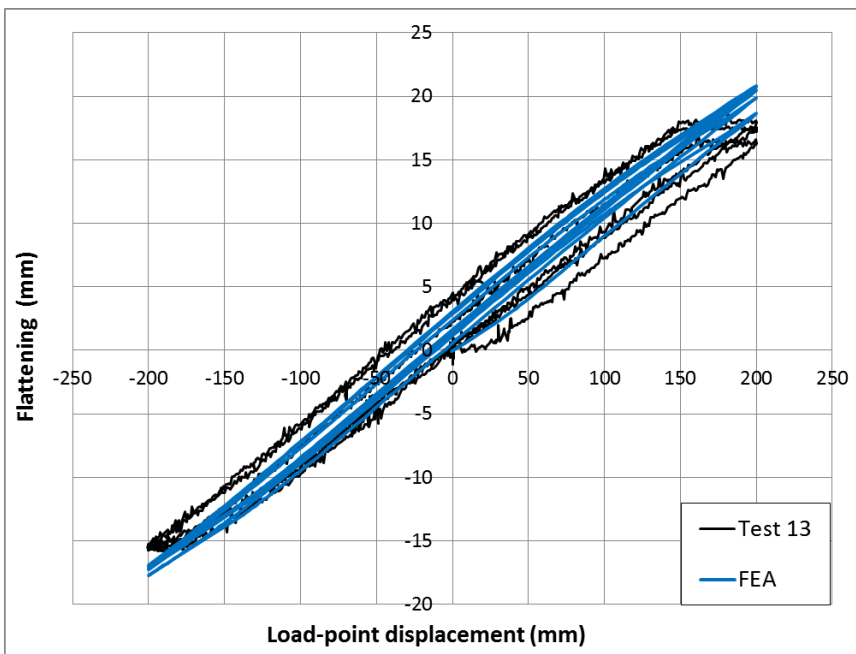
(b)

Figure 4. 19: Test 13, $P=12\ MPa$, $\Delta l=\pm200\ mm$ (a) Load - displacement, (b) Ovalization - displacement curve.

94
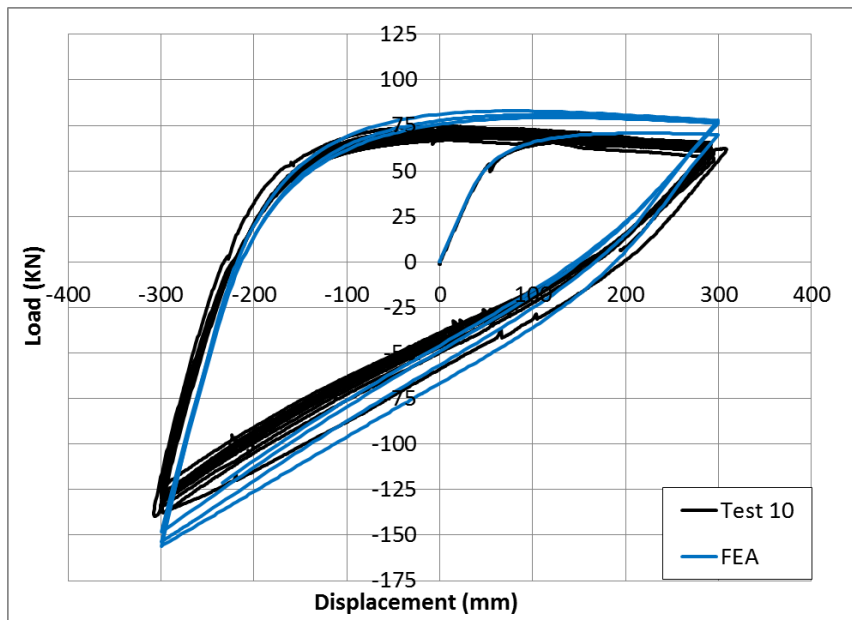
Figure 4. 20: Test 10, $P=3.2$ MPa, $\Delta l = \pm 300$ mm: Load – displacement curve
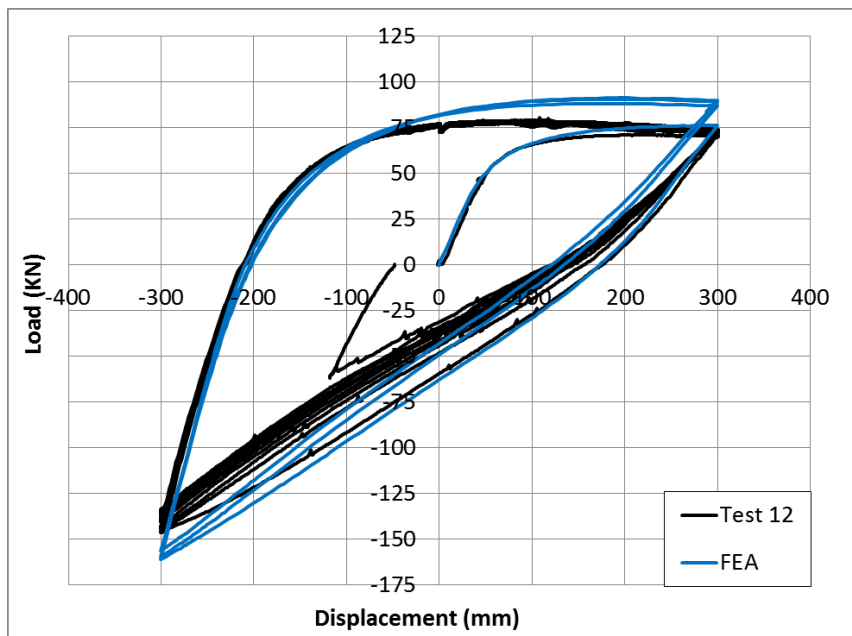
Figure 4. 21: Test 12, $P=7$ MPa, $\Delta l = \pm 300$ mm: Load – displacement curve

95
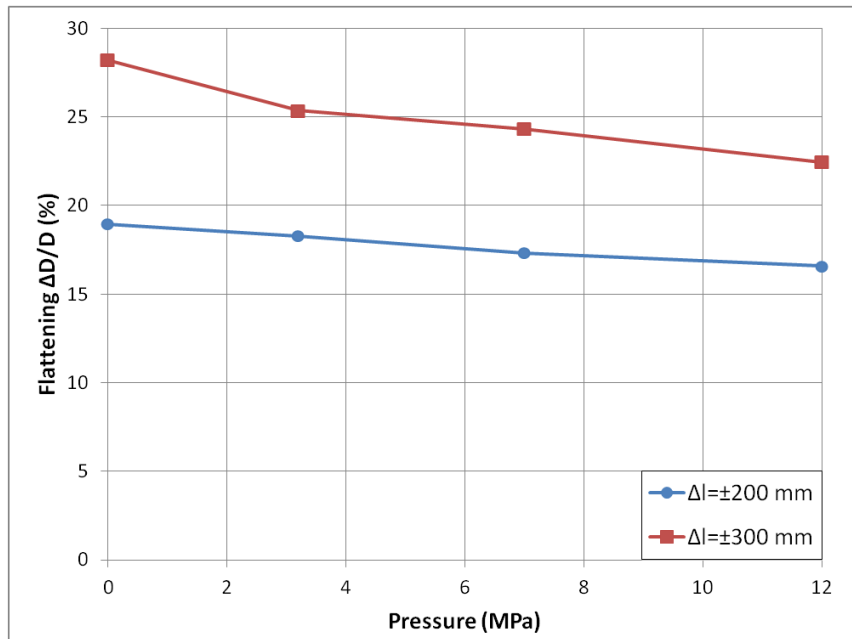
Figure 4. 22: Total cross-sectional flattening for tests with end-displacement range $\Delta l = \pm 200\ mm$ and $\Delta l = \pm 300\ mm$.

4.5 Fatigue analysis

The non-pressurized specimens Nos.2-7 have been subjected to constant amplitude end-displacement range and failed under a number of cycles below the 10^5 low-cycle-fatigue limit (Table 4. 1). The results from these six specimens are plotted in a log-log scale in Figure 4. 23, in terms of the number of cycles to failure N_f, with respect to the corresponding end-displacement amplitude Δl. The data points in Figure 4. 23 are fitted remarkably well with a straight line in the log-log scale, with a slope equal to 1 over 2.59, expressed by the following equation:

$$N_f = \left(\frac{1467.8}{\Delta l}\right)^{2.59} \tag{4.1}$$

The result of Test No.1 is also plotted on the same graph. The corresponding number of cycles ($N_f = 13{,}160$) can be considered at the transition region between low-cycle and high-cycle fatigue regimes. The extension of the straight line described by Eq.(4.1), passes close to the aforementioned point.

A more rational manner to examine the fatigue behavior of the elbows under consideration is to express the number of cycles until failure in terms of the hoop strain amplitude at the critical location where cracking takes place. The numerical results have been in good agreement with the available measured strains. For each test, the hoop strain range $\Delta \varepsilon$ at the critical location computed from the numerical simulations adopting the two plasticity models (NLKH, TL) is shown in the last columns of Table 4. 2. Using these values for the non-pressurized tests Nos. 2-7, the following equations correlate the number of cycles to failure N_f with the local hoop strain range $\Delta \varepsilon$:

96

➢ Experimental measured values

$$N_f = \left(\frac{9.124}{\Delta\varepsilon}\right)^{3.11} \qquad (4.2)$$

➢ Numerically predicted values - NLKH model

$$N_f = \left(\frac{9.057}{\Delta\varepsilon}\right)^{2.88} \qquad (4.3)$$

➢ Numerically predicted values - TL model

$$N_f = \left(\frac{8.693}{\Delta\varepsilon}\right)^{3.13} \qquad (4.4)$$

and the resulting fatigue curves are presented in Figure 4. 24.

Table 4. 2: Summary of results on non-pressurized elbows

Test No.	Displ. Range Δl (mm)	Number of cycles until failure N_f	Local strain range * (%) (Exp)	Local strain range * (%) (NLKH)	Local strain range * (%) (TL)
1	±25	13160	0.33	0.46	0.33
2	±70	444	1.23	1.07	1.25
3	±100	171	-	1.59	1.59
4	±150	61	2.61	2.21	2.55
5	±200	28	-	2.66	2.77
6	±250	17	3.84	3.30	3.75
7	±300	10	4.02	4.29	4.03
8	ECCS protocol	16	-	-	-

*: calculated in the elbow hoop direction at the critical location

It is interesting to note that the number of cycles until failure for the variable-amplitude loading test No.8 could be accurately predicted by Miner's rule applied to the fatigue curve (4.1) or (4.2) to (4.4). More specifically, using the strain-based fatigue curves (4.2) to (4.4), the number of cycles N_i at a specific loading range is recorded, and the corresponding number of cycles to failure N_{fi} is computed. Summation of the "damage indices" $D_i = N_i / N_{fi}$ indicates that a value of unity is reached at the end of the 16th cycle as reported in Table 4. 3 and Figure 4. 25, which is exactly equal to the number of cycles to failure observed in experiments. It should be noted that, despite the fact that fatigue curves (4.2) to (4.4) provide very similar predictions, equation (4.4) that resulted by using the TL model gives results more closer to unity in terms of the damage index.

Table 4. 3: Summary of damage indices using the Miner's rule

ECCS test	NLKH fit	TL fit	Test fit
Sum of D_i *	1.088	1.048	0.913

(*): at the 16th cycle
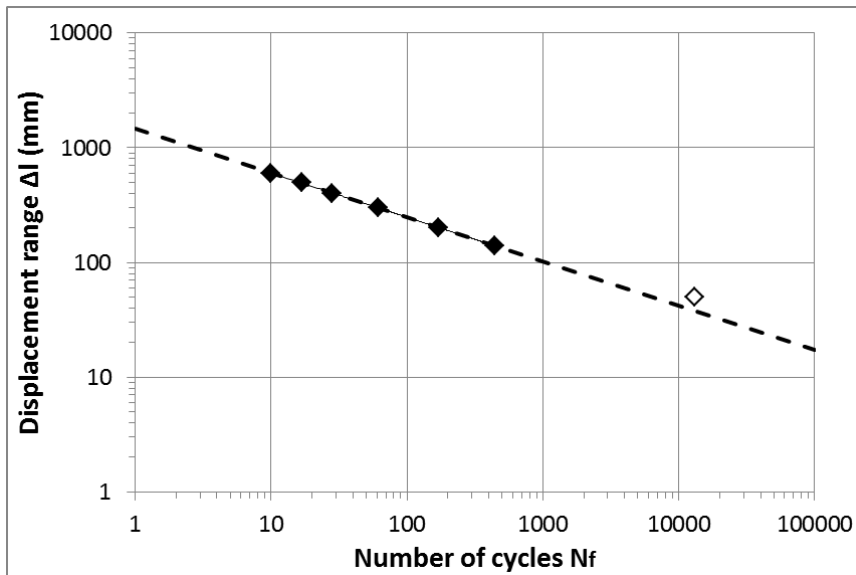
Figure 4. 23: Displacement range versus number of cycles to failure
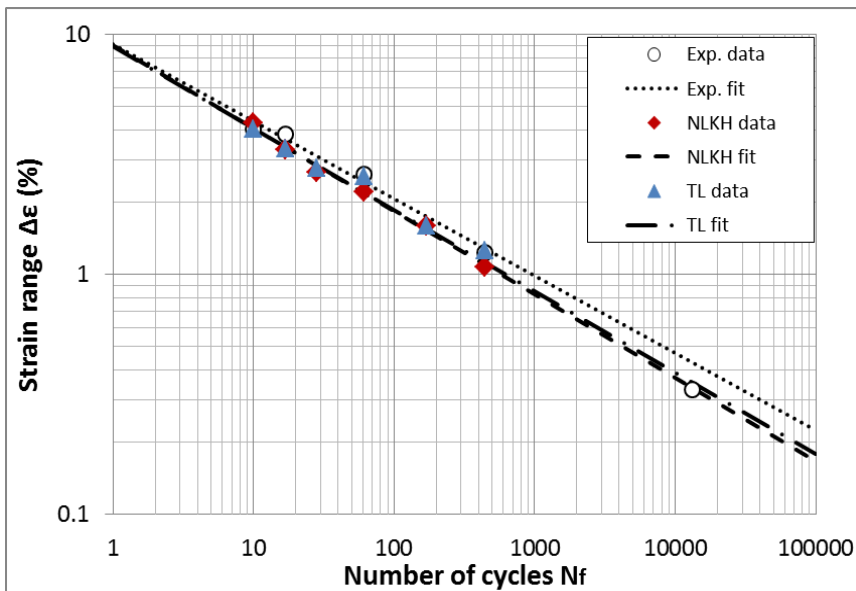
Figure 4. 24: Local hoop strain range vesus number of cycles to failure
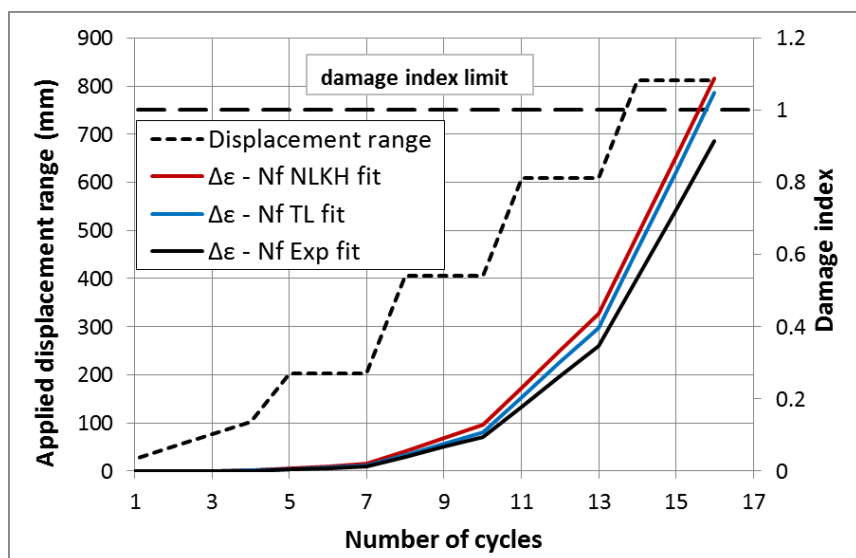
Figure 4. 25: Test 8 - failure prediction using the Miner's rule

98

In most tests, it was possible to measure the developing hoop strain range in the elbow circumferential direction at the critical region where cracking occurred. This strain range is reported in Table 4. 1 as $\Delta\varepsilon_{H,exp}$. The available values measured during testing are compared with the corresponding values predicted by the numerical models using the TL plasticity model (denoted as $\Delta\varepsilon_H$) and are found to be in good agreement for all specimens. In addition to the strain range values in the elbow hoop direction, the corresponding strain ranges in the longitudinal direction have been also reported in Table 4. 1 for the critical point of the elbow, denoted as $\Delta\varepsilon_L$. The longitudinal strain range values are obtained from the numerical analysis only, since no longitudinal strain measurements were taken during the experimental testing procedure. The results shown in Table 4. 1indicate that for the first set of tests (Test No. 1 to Test No. 7), the longitudinal strain range is small compared to the corresponding range in the hoop direction. On the contrary, as internal pressure increases (i.e. for Test No. 9 to Test No. 13), the longitudinal strain ranges become comparable or even greater than the corresponding hoop strain ranges.

Based on the data reported in Table 4. 1, it can be readily concluded that the local strain field developed at the critical region is biaxial, especially for the pressurized elbows. It is possible to take this biaxial strain field into consideration defining an equivalent strain range definition given as:

$$\Delta\varepsilon_{eq} = \sqrt{\Delta\varepsilon_H^2 + \Delta\varepsilon_L^2 + \Delta\varepsilon_H \Delta\varepsilon_L} \qquad (4.5)$$

where $\Delta\varepsilon_H$ and $\Delta\varepsilon_L$ are the corresponding strain ranges in the hoop and longitudinal direction respectively. A similar approach has been adopted in Dama et al. (2007). The results of this analysis are reported in the relevant column of Table 4. 2.

The presence of internal pressure results in a decrease of the corresponding strain range in the hoop direction $\Delta\varepsilon_H$, as shown in Figure 4.26, compared to the non-pressurized cases. This can be attributed to the reduced cross-sectional flattening associated with the presence of internal pressure, as demonstrated by the results reported in Figure 4. 22. On the other hand, internal pressure increases the strain range in the longitudinal direction. In addition, the increase of the internal pressure level results in higher rate of strain accumulation in both directions.

Furthermore, no significant bulging of the cross-section has been observed prior to fatigue failure, for the levels of internal pressure considered. In particular, the experimental measurements for Test No. 13 ($\Delta l = \pm 200\,mm$, $P = 12\,MPa$) show a change of the elbow mean-diameter in the range of only 1% after 22 load cycles, which is also verified numerically.

99
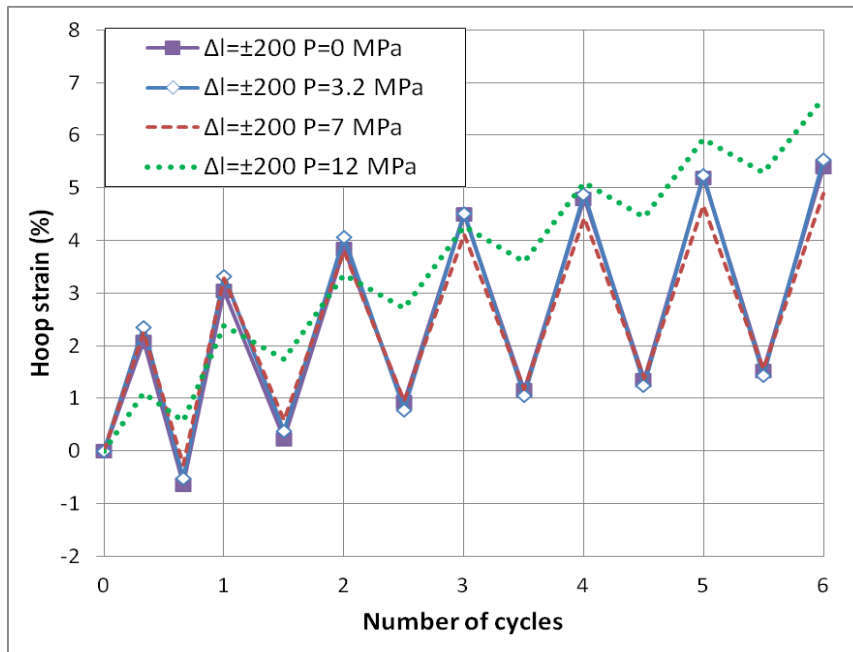
(a)
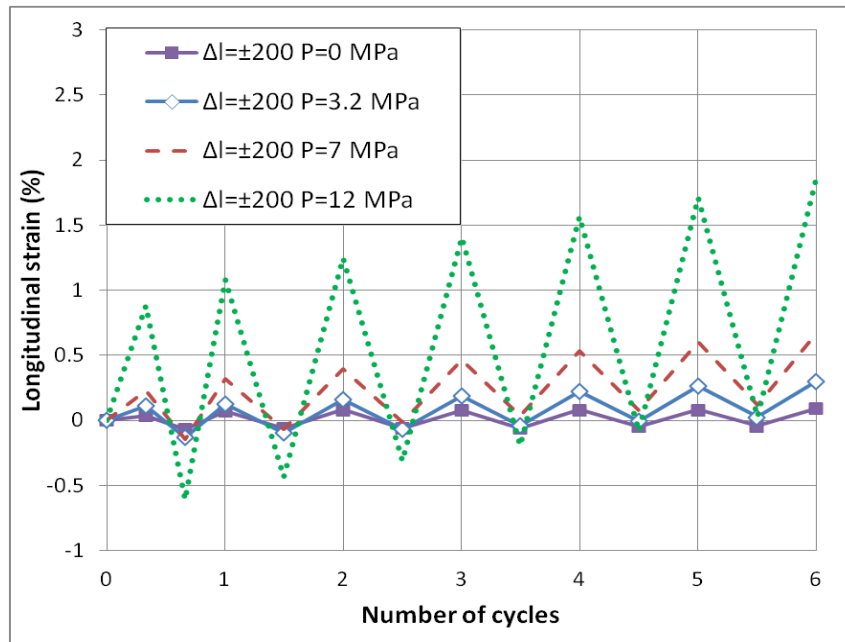
(b)

Figure 4. 26: Evolution of strains ranges at the critical region; end-displacement range $\Delta l = \pm 200$ mm: (a) hoop direction, (b) longitudinal direction; numerical results.

Regarding fatigue life, the fatigue results depicted in Table 4. 1 for tests 5, 9, 11 and 13 indicate a trend of decreasing number of cycles with increasing internal pressure level. This trend cannot be explained by the range of hoop strain at the critical location. To account for the effect of internal pressure on the cyclic response of elbows, an enhanced equivalent strain range $\Delta \varepsilon^*$ is suggested, as defined in Eq.(4.6).

100

$$\Delta\varepsilon^* = \frac{1}{1-\dfrac{p}{p_y}}\Delta\varepsilon_{eq} \qquad\qquad (4.6)$$

In this equation, the strain range $\Delta\varepsilon_{eq}$ is multiplied by a "pressure" factor, which accounts for the pressure level p with respect to the yield pressure p_y. In other words, this factor is used to account for the case that a specific strain range takes place at a mean non-zero stress value. This enhanced strain range for each experiment is presented in the last column of Table 4. 4, and the corresponding fatigue life points are presented in Figure 4. 27. Following a standard fitting procedure, the following equation is proposed that correlates the number of cycles until failure with the enhanced strain range as follows:

$$N_f = \left(\frac{8.198}{\Delta\varepsilon^*}\right)^{3.43} \qquad\qquad (4.7)$$

Furthermore, the fatigue curve expressed by Eq.(4.7) is quite similar to the fatigue curve given in Eq. (4.4) for the non-pressurized specimens, taking into account only the strain range in the hoop direction. Finally, it should be underlined that the above curve does not consider the variable amplitude test No.8, as well as tests No.1, which falls outside the low-cycle fatigue range.

Table 4. 4: Analysis of test results

Test No.	Δl (mm)	N_f	p/p_y	$\Delta\varepsilon_{eq}$ (%)	$\Delta\varepsilon^*$ (%)
1	±25	13160	0.00	0.35	0.35
2	±70	444	0.00	1.32	1.32
3	±100	171	0.00	1.66	1.66
4	±150	61	0.00	2.63	2.63
5	±200	28	0.00	2.85	2.85
6	±250	17	0.00	3.84	3.84
7	±300	10	0.00	4.19	4.19
8	ECCS	16	0.00	-	-
9	±200	26	0.12	3.01	3.42
10	±300	10	0.12	3.00	3.41
11	±200	27	0.26	2.90	3.94
12	±300	10	0.26	2.97	3.90
13	±200	22	0.45	1.89	3.45
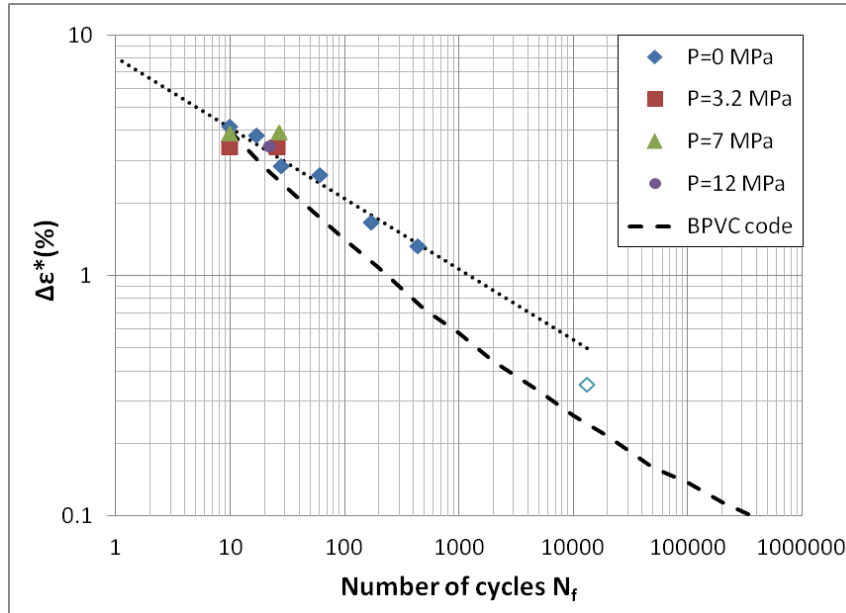
Figure 4. 27: Fatigue life curve and BPVC code predictions.

4.6 Fatigue life predictions

To predict the fatigue life of a cyclically loaded elbow, it is necessary to estimate the local strain at the critical location. This can be achieved using an appropriate finite element model that accounts for geometric and material nonlinearities, as described in the previous sections. Nevertheless, this may not always be feasible, especially for design purposes. In the present section, an efficient methodology is presented for estimating fatigue life of a cyclically loaded elbow, based on Neuber's equation [Neuber (1961), v.d Vegte et al. (1989)].

Neuber's equation correlates the theoretical elastic stress concentration factor SCF with the plastic stress concentration factor K_σ and the plastic strain concentration factor K_ε as follows:

$$SCF^2 = K_\sigma K_\varepsilon \qquad (4.8)$$

The value of SCF is obtained from the ratio of the local peak stress $\Delta\sigma^e$ obtained from elastic analysis, over the nominal stress range ΔS :

$$SCF = \frac{\Delta\sigma^e}{\Delta S} \qquad (4.9)$$

where superscript *e* refers to elastic analysis. Similarly, if $\Delta\sigma$ is the local peak stress range, $\Delta\varepsilon$ is the local peak strain range, both obtained from "elastic-plastic" analysis, and Δe is the nominal strain range, the values of K_σ and K_ε can be obtained as follows:

$$K_\sigma = \frac{\Delta\sigma}{\Delta S} \qquad (4.10)$$

and

$$K_\varepsilon = \frac{\Delta\varepsilon}{\Delta e} \qquad (4.11)$$

Combining the above equations(4.8), (4.10) and (4.11), one readily obtains

102

$$\Delta\sigma\,\Delta\varepsilon = SCF^2\,\Delta S\,\Delta e \qquad (4.12)$$

The value of $\Delta\sigma^e$ to calculate SCF may be obtained numerically, using an elastic finite element analysis. However, in lieu of such a finite element analysis, the stress intensification factor (SIF) proposed by available design standards can be used as an approximation of the stress concentration factor SCF. For in-plane bending conditions and 90-degree smooth elbows, the SIF value is equal to ASME B31.3, EN 13480-3:

$$SIF = \frac{0.9}{h^{2/3}} \qquad (4.13)$$

where h is the flexibility characteristic defined as $h = tR/r^2$, t is the elbow thickness, r is the elbow cross-sectional radius and R is the elbow bend radius. The nominal stress and strain ranges ΔS and strain Δe can be evaluated using elementary mechanics formulae:

$$\Delta S = \frac{\Delta M}{Z}, \quad \Delta e = \frac{\Delta S}{E} \qquad (4.14)$$

where ΔM is the total moment range $\Delta M = M_{max} - M_{min}$ applied on the elbow, Z is the section modulus and E is Young's modulus. It should be noted that the stress and strain ranges defined in Eq.(4.14) are the maximum stress and strain according to classical beam theory, located at the points with maximum distance from the neutral axis. In the case of elbows under in-plane bending, the most stressed location is the elbow flank where cracking takes place due to the cross-sectional flattening, as discussed previously. The local stress intensification factor given in Eq.(4.13) accounts for this effect and correlates the nominal stress and strain ranges with the corresponding ranges at the critical region.

To employ this methodology and compute the local strain range, the so-called "cyclic stress-strain curve" is necessary. Connecting the tips of the hysteresis loops, as shown in Figure 4. 28, an analytical expression of the cyclic material curve can be derived as follows:

$$\frac{\Delta\varepsilon}{2} = \frac{\Delta\sigma}{2E} + \left(\frac{\Delta\sigma}{2K}\right)^{1/n} \qquad (4.15)$$

where K, n are the cyclic stress coefficient and cyclic strain hardening exponent respectively, equal to 623.5 MPa and 0.169 respectively.

Under cyclic bending loading under moment range ΔM, the nominal stress range ΔS and strain range Δe are calculated from Eq.(4.14), the local peak ranges of stress and strain ($\Delta\sigma$, $\Delta\varepsilon$) are defined by the intersection of the cyclic material curve with Neuber's hyperbola expressed in Eq.(4.12), where SCF is obtained from Eq. (4.13). Subsequently, the local strain range $\Delta\varepsilon$ is used to calculate the number of cycles to failure N_f through an appropriate fatigue curve.

Figure 4. 29 shows graphically the definition of the ($\Delta\varepsilon$, $\Delta\sigma$) pair at the intersection of equations (4.12) and (4.15). Subsequently, the fatigue life of the elbow N_f can be readily calculated from the right vertical axis of the same graph, using Eq. (4.7).

This simplified fatigue prediction method has been applied for predicting the fatigue life of the tested specimens. For each test conducted, the predicted strain range values are presented in the third column of Table 4. 5 adopting the actual geometric characteristics of each elbow, denoted as $\Delta\varepsilon_N$. The resulting predictions are consistent with the corresponding strain range predictions obtained by the aforementioned methodology. The corresponding predictions of the fatigue life through Eq. (4.7) are shown in Table 4. 5 and in Figure 4. 30, and are in good agreement with the experimental data.
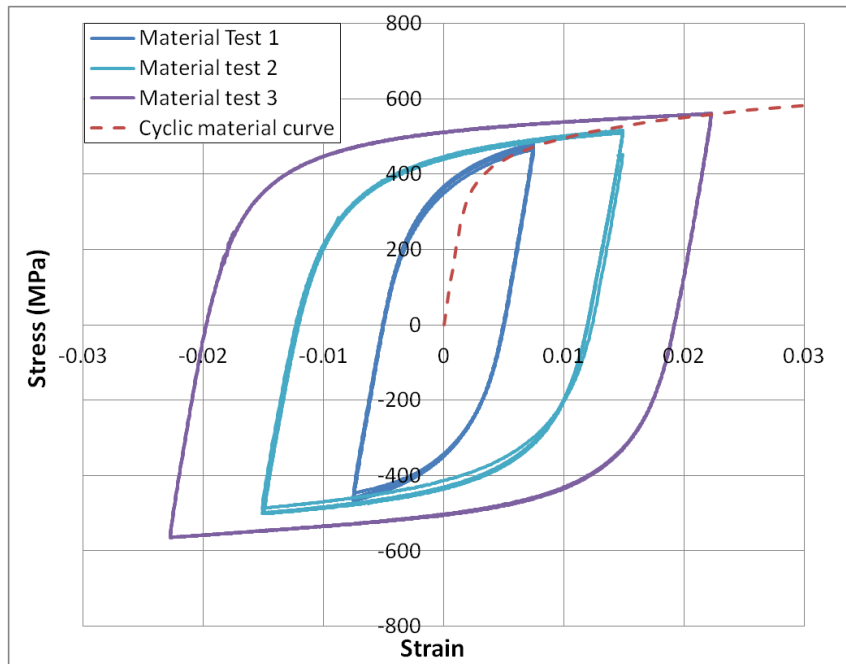
Figure 4. 28: Cyclic material stress-strain curve.
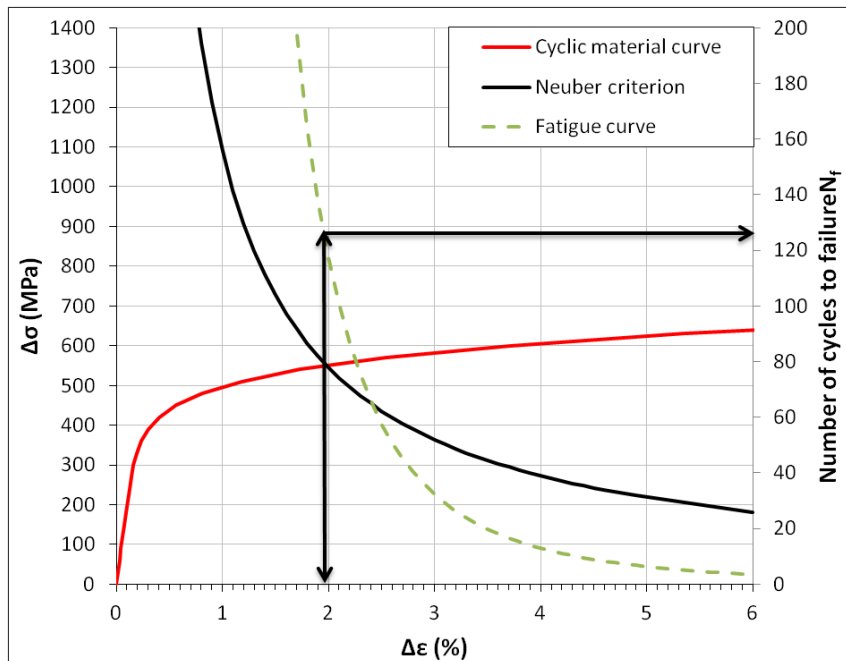
Figure 4. 29: Schematic representation of the fatigue life prediction using the simplified method.

Table 4. 5: Fatigue predictions using the Neuber's rule

Test No.	$\Delta\varepsilon^*$ (%)	$\Delta\varepsilon_N$ (%)	N_f	$N_{f,N}$
1	0.35	0.45	13160	20758
2	1.32	1.35	444	482
3	1.66	1.80	171	179
4	2.63	2.15	61	97
5	2.85	2.50	28	58
6	3.84	2.85	17	37
7	4.19	3.25	10	23
8	-	-	16	-
9	3.42	3.05	26	29
10	3.41	3.65	10	15
11	3.94	3.20	27	25
12	3.90	4.60	10	7
13	3.45	3.60	22	16
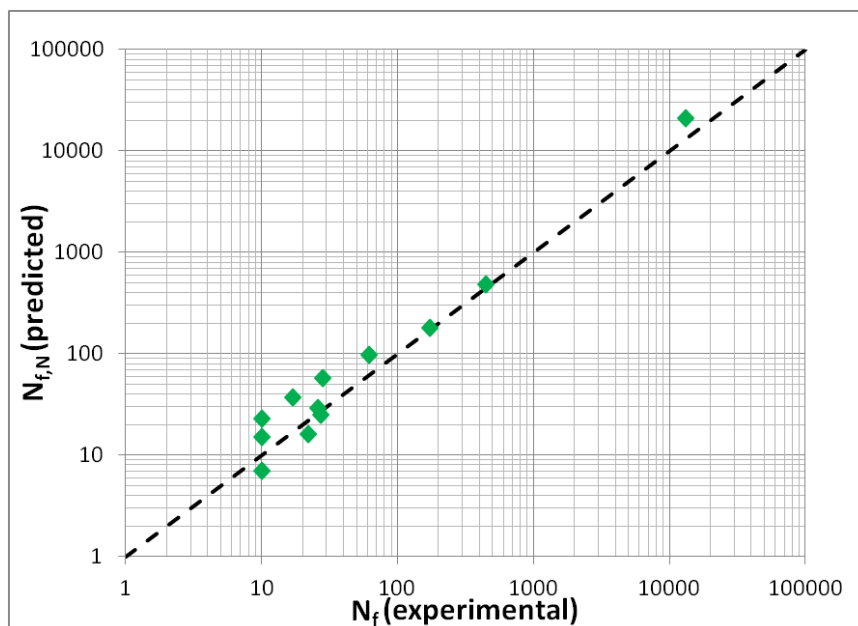
Figure 4. 30: Fatigue life predictions using the simplified method.

4.7 Parametric study

The aim of this study is to examine the effects of the variation of the elbow geometrical characteristics on its fatigue life. The developed numerical model has been modified accordingly in order to be used for the scope of a parametric study. The end-supports have been removed and the mesh density has been defined through a mesh sensitivity analysis using C3D8I solid elements as in the original model. The loading on the elbow is introduced as end-rotations at the

ends of its straight parts. A general view of the developed numerical model is presented in Figure 4. 31.
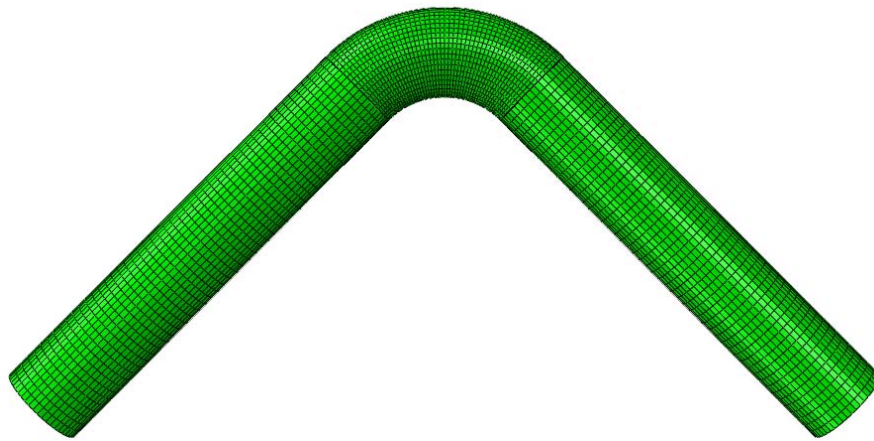
Figure 4. 31: Numerical model used for the parametric analysis

Table 4. 6: Parametric analysis – grid of cases examined

Rotation Amplitude	8-inch SCH20 Long radius	8-inch SCH40 Long radius	8-inch SCH80 Long radius	8-inch SCH40 Short radius
±0.02 rad	✓	✓	✓	✓
±0.04 rad	✓	✓	✓	✓
±0.08 rad	✓	✓	✓	✓
±0.12 rad	✓	✓	✓	✓

Table 4. 7: Geometrical characteristics of examined cases

Geometrical Characteristics	Diameter D (mm)	Thickness t (mm)	Bend radius R (mm)	R/D
8-inch SCH20 Long radius	219.1	6.4	304.8	1.391
8-inch SCH40 Long radius	219.1	8.2	304.8	1.391
8-inch SCH80 Long radius	219.1	12.7	304.8	1.391
8-inch SCH40 Short radius	219.1	8.2	203.2	0.927

A complete list of the cases examined is reported in Table 4. 6 and their geometrical characteristics are reported in Table 4. 7. Both the NLKH and the TL models have been adopted for the numerical analysis. For each case examined, moment-rotation curves where derived and the local strain ranges at the critical locations where monitored. Indicative analysis results for the case of case of 8-inch SCH40 long radius case are reported in Figure 4. 32.

106

In the monotonic loading cases where the elbow is subjected to opening or closing moment loading [Figure 4. 32 (a)], the two plasticity models predict similar behavior. The differences become evident in the rotation levels where significant plastic deformations are involved, due to the different constitutive equations formulation of the two models. The same trend is also observed in the cyclic loading at different end-rotation levels presented in Figure 4. 32 (b)-(e). Despite the fact that the moment-rotation curves from the two models are quite close, the measured local strain ranges differ significantly. Consequently, the predicted fatigue life for these cases differs as well. The reason for the above observations is that under increased plastic deformations, the hardening modulus predicted by the NLKH model tends to zero, while the TL model provides a more realistic value as shown in the experiments presented in Figure 2.10 (Chapter 2).

The results of the parametric analysis are reported in Table 4. 6(a) to (d) for the complete set of cases. The local strain ranges at the critical location of the elbow are reported for each case. The fatigue life predictions were based on Eq.(4.3) and Eq.(4.4) for the NLKH and the TL model respectively. A thorough examination of the results shows that increasing the elbow wall thickness results to longer fatigue life for the same end-rotation range due to the reduction of the strain field range developing locally. In addition, higher R/D ratio results to increased fatigue life for the same end-rotation amplitude and schedule.

(a)

107

(b)

(c)

(d)

108
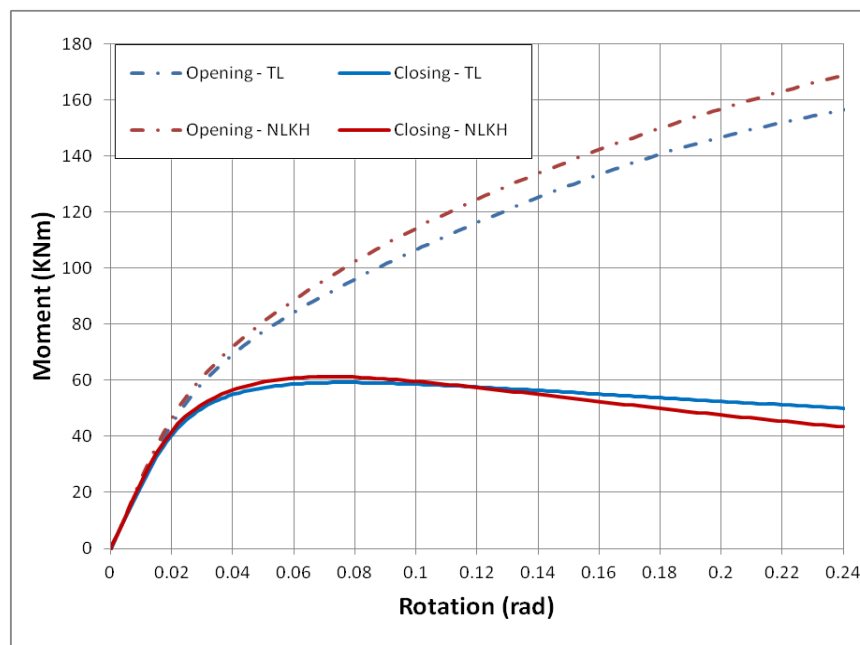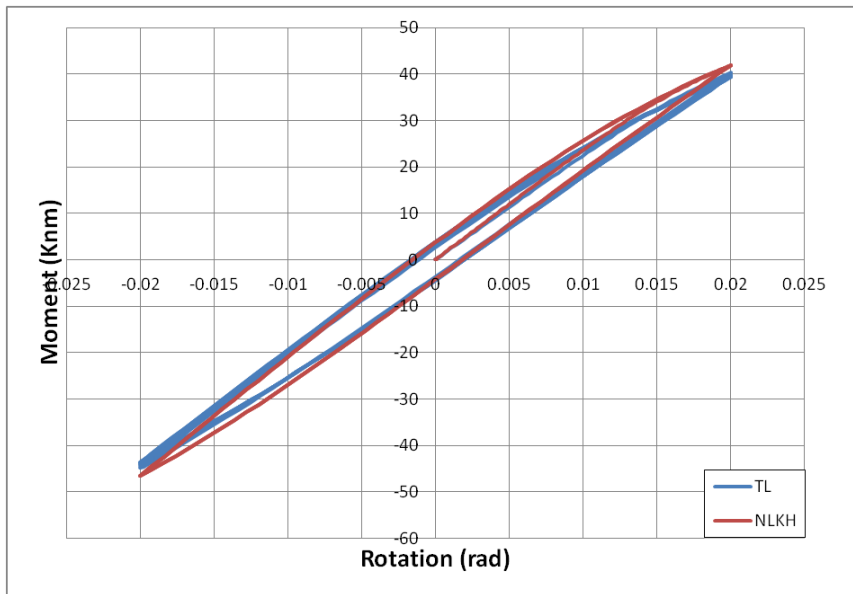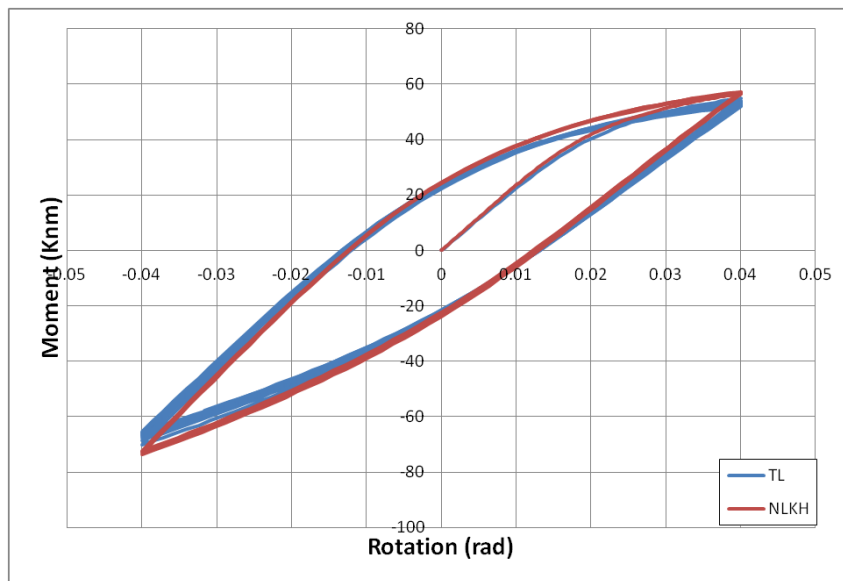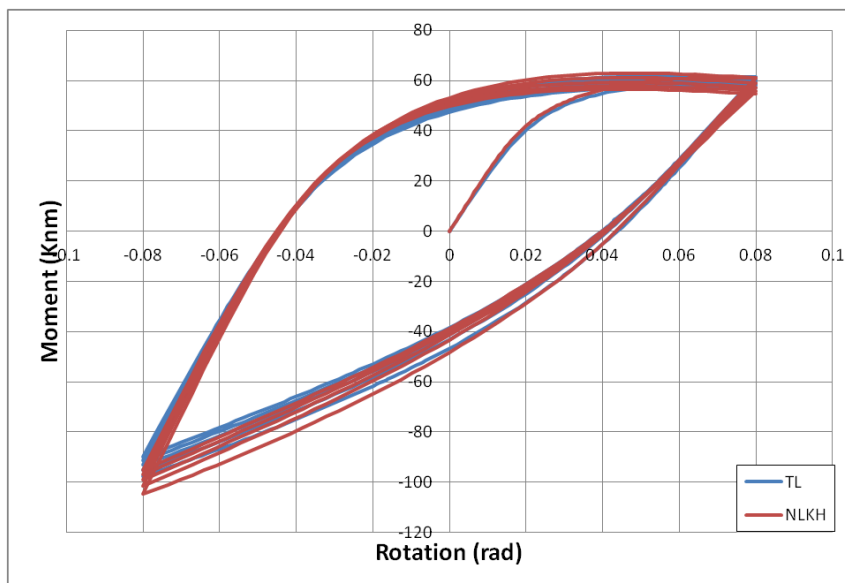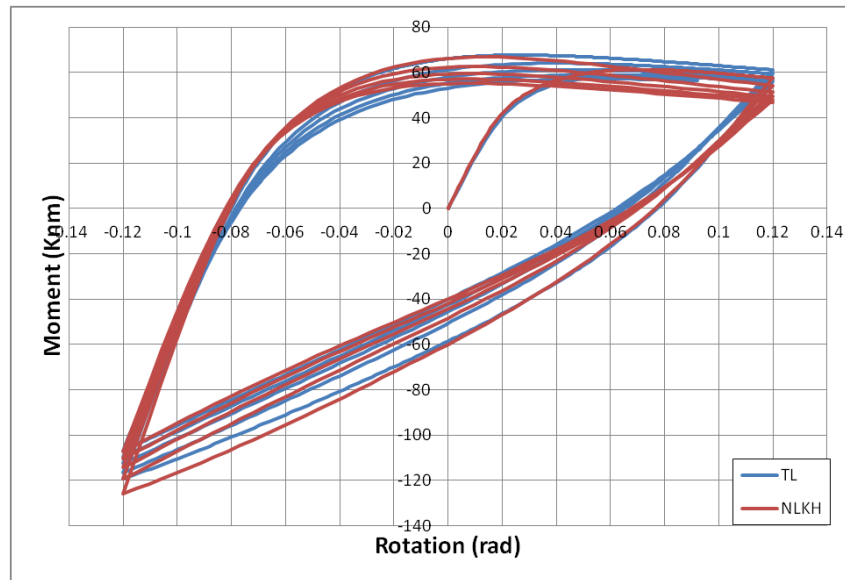
(e)

Figure 4. 32: Parametric analysis results – 8-inch SCH40 long radius: (a) Monotonic analysis, (b) $\Delta r = \pm 0.02\ rad$, (c) $\Delta r = \pm 0.04\ rad$, (d) $\Delta r = \pm 0.08\ rad$, (e) $\Delta r = \pm 0.12\ rad$

Table 4. 8: Parametric analysis results: a) 8-inch SCH20 long radius, b) 8-inch SCH40 long radius, c) 8-inch SCH80 long radius, d) 8-inch SCH40 short radius

8-inch SCH20 Long radius	$\Delta \varepsilon$ (%)		N_f	
Rotation Amplitude (rad)	NLKH	TL	NLKH	TL
± 0.02	0.69	0.76	1651	1263
± 0.04	1.66	1.70	133	123
± 0.08	4.87	3.18	5	20
± 0.12	7.88	4.47	1	7

(a)

8-inch SCH40 Long radius	$\Delta \varepsilon$ (%)		N_f	
Rotation Amplitude (rad)	NLKH	TL	NLKH	TL
± 0.02	0.67	0.68	1838	2848
± 0.04	1.61	1.58	143	207
± 0.08	6.00	2.95	5	29
± 0.12	6.70	3.12	2	24

(b)

109

8-inch SCH80 Long radius	$\Delta\varepsilon$ (%)		N_f	
Rotation Amplitude (rad)	NLKH	TL	NLKH	TL
±0.02	0.59	0.61	2630	2399
±0.04	1.46	1.56	193	157
±0.08	3.80	1.67	12	130
±0.12	6.99	2.46	2	42

(c)

8-inch SCH40 Short radius	$\Delta\varepsilon$ (%)		N_f	
Rotation Amplitude (rad)	NLKH	TL	NLKH	TL
±0.02	0.77	0.81	1215	1712
±0.04	2.01	1.79	76	141
±0.08	6.02	3.42	3	18
±0.12	9.78	6.42	0	2

(d)

A critical review of the parametric analysis results illustrates that increasing the rotation amplitude, the local strain ranges predicted using the NLKH model are quite large compared to the corresponding values derived using the TL model. This has been also observed during the simulation of elbow experiments presented in the previous sections, and is attributed to the very small hardening modulus considered by the NLKH model for large plastic deformations. On the contrary, the formulation of the TL model allows for better control this effect, leading to more accurate and reliable results.

Regarding the predicted fatigue life of the elbows, the numerical results show that increasing elbow wall thickness (higher schedule) results to increased fatigue life of the elbow for the same end-rotation range. In addition, long radius elbows (higher R/D ratio) showed lower local strain ranges, implying longer fatigue life compared to short radius elbows of the same schedule.

4.8 Design implications

The extreme loading conditions considered in the present study are motivated by earthquake loading and, therefore, they can be treated as occasional loading according to the provisions of both ASME B31.3 and EN 13480-3 standards for process piping. Both standards adopt the "allowable stress" concept based on elastic analysis. The present results exceed the limit of applicability of elastic analysis, so that an elastic-plastic analysis is necessary, and therefore, the predictions from those two standards are expected to be conservative.

Following the design methodology in ASME B31.3 for occasional loading acting on a piping component (paragraph 302.3.6), the sum of longitudinal stress S_L due to sustained loads (e.g. pressure, self-weight) and of longitudinal stress

110

$S_{L,Occ}$ produced by occasional loads (e.g. wind or earthquake), may be as much as 1.33 times the basic allowable stress, given in the relevant Table of material allowable stresses in Appendix A of B31.3. For API 5L X52 material, the allowable stress S_h at maximum metal temperature expected during the applied displacement cycle is equal to 151.68 MPa (22 ksi). This requirement can be expressed as:

$$S_L + S_{L,Occ} \leq 1.33\, S_h \tag{4.16}$$

If no pressure or other sustained loads are considered, as in the present experimental study, the value of S_L can be assumed equal to zero. Furthermore, $S_{L,Occ}$ for in-plane bending can be computed from ASME B31.3 paragraph 319.4.4 as follows

$$S_{L,Occ} = i_i M_i / Z \tag{4.17}$$

where i_i is the intensification factor given in Appendix D of ASME B31.3 (equal to 2.44 in our case), M_i is the bending moment and Z is the pipe cross-section modulus.

Similar provisions exist in EN 13480-3, where the stresses due to occasional loading conditions, given by Eq. (4.17), are limited by the product $k f_h$, where k is a coefficient equal to 1.2 for the design basis earthquake and 1.8 for the safe shut-down earthquake, and f_h is the allowable stress of the pipe material, equal to 163.3 MPa for the present case. It is noticeable that the EN 13480-3 code considers two seismic levels, allowing for a less conservative design under extreme earthquake action.

For the piping elbows under consideration, according to ASME B31.3, the maximum bending moment allowed for occasional loading according to Eq. (4.16)and Eq. (4.17) is limited to 24 kNm corresponding to an end-displacement equal to 14.8 mm. Furthermore, according to EN 13480-3, the maximum allowable moment is equal to 34.9 kNm for the safe shut-down earthquake, which corresponds to an end-displacement of the present elbow equal to 21.5 mm. Considering that the elbow specimen of Test 1 is able to withstand 13,160 load cycles before failure under an imposed displacement of ± 25mm, it can be concluded that the above provisions in both standards are very conservative for this type of loading. This conservativeness is attributed to the fact that both design standards follow an "allowable stress design" concept, not accounting for the ultimate capacity of the elbow component, which is associated with deformations well beyond the elastic limit of the steel material.

Regarding cyclic loading, both standards adopt a similar approach. The allowable local stress amplitude S_A is related to the number of loading cycles N_f according to the following equations (ASME B31.3, paragraph 302.3.5):

$$S_A = \left(6 N_f^{-0.2}\right)\left[1.25\left(S_C + S_h\right) - S_L\right] \tag{4.18}$$

or alternatively

$$S_A = \left(6 N_f^{-0.2}\right)\left[1.25 S_h + 0.25 S_C\right] \tag{4.19}$$

111

where the first term in the parenthesis of the right-hand-side is limited by the value of 1.2 for ferritic steel material, whereas S_C and S_h are the basic allowable stresses at minimum and maximum metal temperature respectively and S_L is the corresponding longitudinal stress due to sustained loading.

In both standards, equations (4.18) and (4.19) are valid for a number of cycles greater than 1,000 corresponding to high-cycle fatigue, and therefore, they do not cover the extreme loading conditions of Tests Nos.2-13, where failure occurs in the low-cycle fatigue regime with a number of cycles N_f less than 500. For the particular case of Test No.1, setting the number of cycles N equal to 13,160 and the value of S_L equal to zero, one readily obtains a corresponding allowable stress amplitude S_A equal to 204.8 MPa and 341.33 MPa, using equations (4.18) and (4.19) respectively. The resulting stress amplitude by Eq. (4.18) is significantly lower than the calculated maximum stress amplitude (350.8 MPa) that this elbow exhibits at the crack location under an imposed cyclic displacement of $\pm 25mm$, indicating the conservativeness of this equation. On the other hand, Eq. (4.19) provides a less conservative prediction for the stress amplitude, which is quite close to the calculated maximum amplitude at the crack location.

On the other hand, the ASME BPVC (2010) standard, oriented for the design of nuclear piping components, provides design fatigue curves for elbows in the low-cycle fatigue regime. The fatigue design curve for carbon steel piping components presented in section III of ASME BPVC (2010) and covers quite low values of fatigue life up to 10 cycles. In addition, according to BPVC, mean stress effects (e.g. internal pressure effects) have already been incorporated in the fatigue curve under consideration.

The BPVC stress-range fatigue curve can be transformed into a $\Delta\varepsilon - N_f$ curve, dividing the stress range by the Young's modulus E of the steel material. The transformed fatigue curve is plotted in Figure 4. 27, it offers reasonable, yet conservative, fatigue life predictions for cyclically loaded elbows in the low-cycle fatigue regime, and can be used for design purposes.

112

Chapter 5

High-strength steel tubular welded joints under extreme loading conditions

5.1 Introduction

Tubular members are widely used in structural engineering applications due to their attractive structural properties such as the high bending capacity to weight ratio, their increased stability and strength against compressive loading and the enhanced resistance under torsional loads. Moreover, their shape provides reduced drag forces when exposed to wind actions. In addition, tubular members are highly appreciated in modern architectural design because of their attractive from the aesthetical point of view.

For the formation of a structure using tubular members, the separate parts of the structure are usually welded together forming tubular joints, often with complex multi-planar geometries. Even in the simplest tubular joint configuration, due to the particular joint geometry, the developing local stress fields are significantly complex. In particular, the existence of welds introduces local effects responsible for the development of very high local stresses, the so-called "hot-spot" stresses.

The performance of tubular joints has attracted significant scientific interest back from the 1960s. Many empirical equations were developed for the design of tubular joints subjected to simple loading conditions and to examine the interaction between several loads acting on a joint, as presented for example in the work of Swenson & Yura (1987). In addition, analytical model methods were also developed offering a rather simplified approach to the complicated design problem of tubular joints. Along with the analytical approaches, the finite element method was also employed for the simulation of the tubular joint behavior.

In the recent years the advances in the available metallurgical techniques resulted to the production of high-strength steel alloys. In addition, new welding technologies were developed allowing for the development of more time-effective welding processes with increased accuracy with respect to the local weld geometries. There is a growing demand for the use of high-strength steel (yield strength higher than 500MPa) in tubular steel structures. Despite the lower ductility of high-strength steel with respect to lower-grade steel (yield strength up to 460MPa), this increasing demand is motivated mainly by the static strength improvement of both tubular connections and members. The benefits of using high-strength steel on the static strength of welded tubular connections have been reported in Noordhoek & Verheul (1998) and in a HSE report [HSE

(2007)], which describes the results of a joint industry project. Extensive experimental testing on steel welded tubular connections has been reported by van der Vegte et al. (1989). Recent studies on the static strength of welded tubular T-joints and K-joints made of X52 steel (i.e. members' yield stress up to 500 MPa) have been reported by Waalen & Berge (2005), Boge et al. (2007), Hochman et al. (2010). In more recent publications, Choi et al. (2012a, 2012b) reported tests on tubular joints made of HSB 600 steel (members' yield stress up to 590 MPa) and verified the superiority of the these joints on static strength capacity.

Those studies also aimed at examining the applicability of current design practice, in tubular joints made of high-strength steel. It is important to note that current design standards for tubular structures have been developed for steel grades with yield stress up to 460 MPa, and may not cover high-strength steel applications. In the studies of Choi et al. (2012a) and (2012b) it was found that the existing provisions in AISC (2005) could be used for predicting the ultimate strength of tubular connections, but a significant reduction of the safety margin was also noticed.

To account for the use of high-strength steel in structural applications, the new EN 1993-1-12 standard has been developed within the Eurocode 3 (EN 1993) design framework. The specific standard refers to high-strength structural steel and specifies some rules, additional to the existing EN 1993 provisions, for grades higher than 460; for the particular case of welded tubular connections made of high-strength steel, an additional reduction factor equal to 0.8 is specified in the static strength calculation.

On the other hand, the use of high-strength steel in structural applications associated with cyclic loading and fatigue damage has received less attention than static loading. In particular, despite the fact that fatigue of welded tubular connections has been extensively investigated for ordinary steel grades (up to 460) and there exist quite a few relevant design tools (e.g. CIDECT, EN 1993-1-9), there is a lack of information for the fatigue performance of high-strength steel tubular joints. Furthermore, EN 1993-1-12 standard does not contain any special rules for the fatigue of welded tubular connections, allowing for the use of EN 1993-1-9 provisions.

It is important to notice that most of the existing literature and the relevant fatigue design specifications and guidelines focus on high-cycle fatigue of tubular connections, whereas limited research efforts have been reported on the low-cycle fatigue performance of those joints. In an early publication, Baba et al (1984) static and low-cycle fatigue tests on stiffened tubular joints made of STK41 steel (ultimate material strength equal to 402 MPa) are reported aiming at the definition of an optimum stiffening geometry configuration. Furthermore, experimental tests on welded tubular connections have been reported by van der Vegte et al. (1989), focusing on the hot-spot stress ranges. In addition, it is found that an extrapolation of high-cycle fatigue design equations in the low-cycle

114

fatigue range may provide safe fatigue life predictions and that a fatigue curve with a slope equal to -3 in the log-log scale characterizes the low-cycle fatigue regime. More recently, in a series of papers, the low-cycle fatigue performance of tubular T-joints has been reported under repeated in-plane bending [Waalen et al. (2005)] out-of-plane bending [Boge et al. (2007)] and axial loading [Hochman et al. (2010)]. Nevertheless, all the above works on low-cycle fatigue of tubular joints refer to steel grades up to X52 (yield stress in the range of 500 MPa). To the author's knowledge, no experimental results are available for the low-cycle fatigue of tubular joints made of high-strength steel.

In the present chapter, the behavior of welded tubular connections made of high-strength steel and subjected to strong cyclic loading that leads to low-cycle fatigue is discussed. The analysis is part of the European research program HITUBES (2008-2011), which investigated the structural performance of tubular structures made of high-strength steel (grade equal or higher than 590 MPa). The work in this project consisted of a first experimental part with 10 tests on tubular joints made of high-strength steel, aiming at the examination of the behavior of these joints under extreme loading conditions. The second part of the research was numerical/analytical with the purpose at supporting the experiments, using advanced finite element models, and conducting a parametric study for the assessment of low-fatigue fatigue behavior of high-strength steel welded tubular connections.

The present chapter describes in detail the numerical/analytical work conducted in the course of the above research project. For completeness reasons, the test set-up and results are briefly described in the next section. Subsequently, the rigorous finite element models developed for the simulation of the welded tubular joints are described and extensive numerical results are obtained. The numerical results are compared with the experimental measurements, and special attention is given to the evaluation of the stress and strain fields at the so-called "hot spot" locations. Finally, an assessment of the low-cycle fatigue performance of welded tubular connections is conducted, using the numerical results and a simplified methodology based on Neuber's rule.

5.2 Experiments on tubular joints

In this paragraph, a short description of the experimental activity is offered. The experiments were conducted at the Laboratory of Concrete Technology and Reinforced Concrete Structures of the Civil Engineering Department of the University of Thessaly, as reported in Bursi (2012). The experimental investigation consisted of ten tests on welded tubular connections. Four tubular X-joint specimens were tested under in-plane bending (IPB), another four X-joints were tested under out-of-plane bending (OPB) and finally two X-joints were subjected to axial cyclic loading (AX). The tubular joint specimens and set-up configurations for each category of tests are shown in Figure 5.1.

115

The steel tubes for the welded tubular joint specimens, i.e. the chord and the two braces, were provided by Tenaris Dalmine SpA, Dalmine, Italy. The tubes were seamless, and made of high-strength steel (TS590 grade) with a nominal yield stress of 590 MPa. The two braces of each specimen were 7-inch-diameter CHS tubes (diameter equal to 7.625in or 193.7mm) with 10mm nominal wall thickness, whereas the chord was a 14-inch-diameter CHS tube (diameter equal to 355.6mm) with a nominal wall thickness of 12.5 mm.

The welded specimens were manufactured by Stahlbau Pichler SpA, Bolzano, Italy. The welds were performed according to the general provisions of AWS D1.1 and EN ISO 15609-1. Two different electrodes were used for the welds, corresponding to Classes 55 and 79 (i.e. nominal yield strength of 550 MPa and 790 MPa respectively). The two electrodes are referred to as "weld A" and "weld B" respectively in the following paragraphs.

5.2.1 Experimental set up

The IPB tests were carried out adopting a three-point-bending configuration. Both ends of the X-joint specimen braces were hinged, using a double-hinge "roller" system that allows for horizontal movement of the two ends without introducing axial loading, while keeping the symmetry of the specimen set-up at the deformed configuration. The hydraulic jack was connected to the top of the joint chord through a specially designed system of plates as shown in Figure 5.1(a). The moment lever-arm of by this test set-up was equal to 1307.5 mm, and it is used in all calculations thereafter.

The experimental set-up for the OPB tests consisted of a four-point-bending loading configuration applied to the joint braces through a steel cross-beam, and appropriate wooden grips. Two special ball-joint hinges were used for connecting the cross-beam with the grips. The joint braces were hinged using the same "roller" system as described above. The moment lever-arm created by this load-support set-up was equal to 830 mm. Details of the overall geometry, loading system for the OPB tests are shown in Figure 5.1 (b). Finally, the AX loading tests were conducted by connecting the hydraulic jack at the one brace-end of the joint and by supporting the joint at the other brace-end, as presented in Figure 5.1 (c).

116

SBJ: spherical ball joint
SH: spherical hinge
H: hinge

(a)

(b)

117

(c)
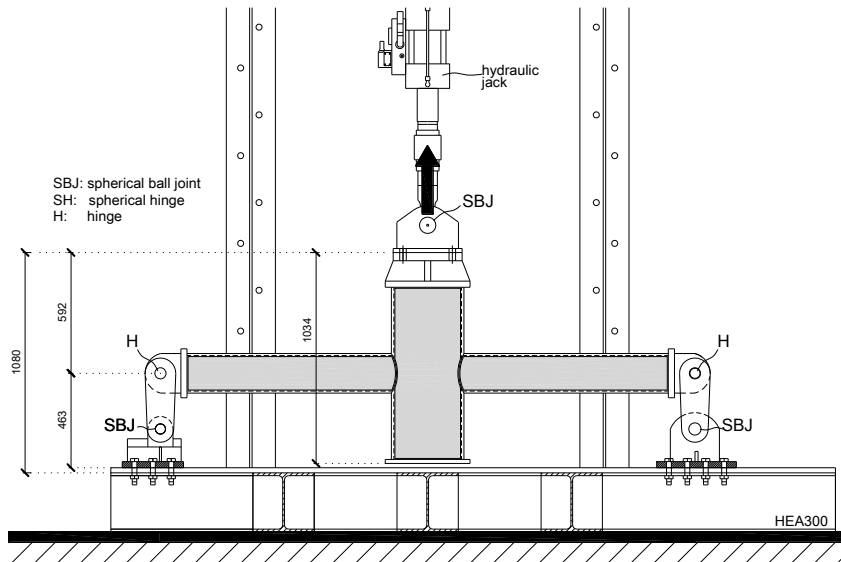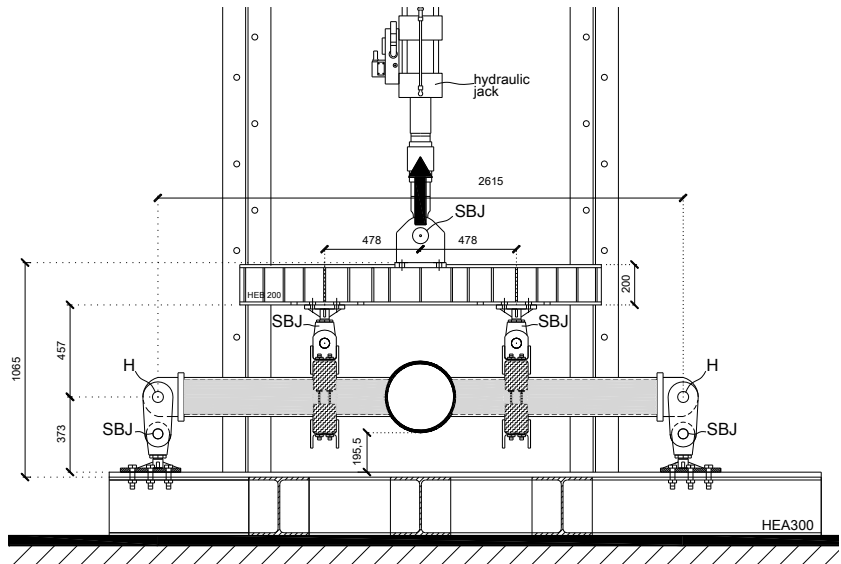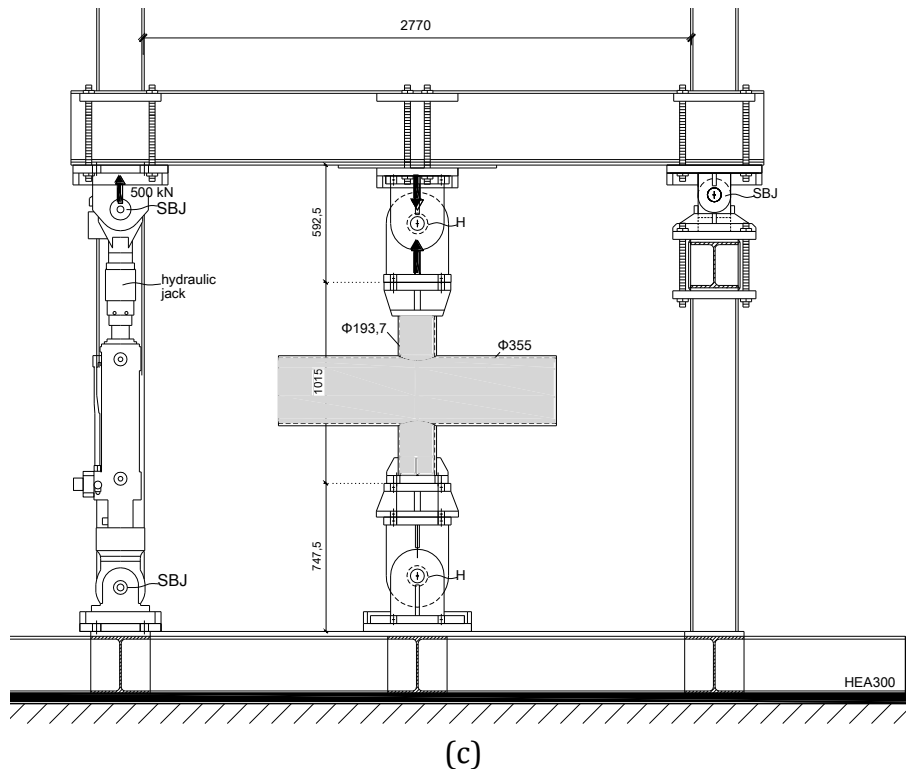
Figure 5.1: Schematic representation of the test setup (a) IPB, (b) OPB, (c) AX,

In all tests, the local strains at the critical parts of the joint were monitored through appropriate strain gauges at the top and bottom side of the joint. Finally, wire position transducers and DCDT's were used for recording the displacement at the location of load application, and the displacement of the support. More details are reported in Varelis et al. (2012) and in the HITUBES report [Bursi (2012)].

5.2.2 Thickness measurements and material characterization

Prior to test execution, thickness measurements were conducted in several cross-sections, on the chord and braces to detect possible deviations from the nominal values (12.5 mm and 10 mm respectively). It was found that, despite some small variations of the thickness value around the cross-section of the tubes, the mean value for the chord thickness was measured equal to 12.49 mm, practically equal to the nominal value, while the mean measured thickness for the brace was measured equal to 10.27 mm, slightly greater than the nominal value. The thickness measurements were adopted for the development of the numerical models used for the simulation of the experiments.

The mechanical properties of the steel material were determined through tensile tests on steel coupon specimens extracted from the tubes before the specimens are manufactured. The tests were conducted by CSM, Rome, Italy and are reported in detail in Bursi (2012). According to these tests, it was found that the actual yield stress of the TS590 steel material is 746 MPa, significantly higher (26.4%) than the nominal value. The stress-strain curve exhibits a small plastic

118

plateau up to 1.5% engineering strain, and the ultimate stress is equal to 821 MPa, reached at a strain of 7.5%. The corresponding material true stress-strain curves derived from cyclic tests on steel coupon specimens are presented in Chapter 3, and in particular in Figure 3.2 and in Figure 3.3.

The mechanical properties of welds A and B were also examined through tensile testing, by ITMA, Spain. It was found that the actual material properties of weld A material were 866 MPa and 900 MPa for the yield stress and the ultimate stress respectively, whereas the corresponding actual material properties of weld B material were 961 MPa and 1078 MPa. Both weld materials had values of yield and ultimate stress higher than those of the tube steel base material (746 MPa and 821 MPa), so that both welds can be considered as "overmatched". Moreover, fracture toughness tests were also conducted. The specimens examined using the weld A presented increased fracture toughness (136 KJ/m^2) compared to the specimens using the weld B (89 KJ/m^2).

In addition, in order to characterize the fatigue behavior of TS590 base material and of the welds A and B, fatigue tests on specimens made of the TS590 material as well as specimens containing both types of welds were conducted in the facilities of ITMA, Spain following the ASTM E466 standard, as presented in Bursi (2012). The specimens were extracted from two aligned and full-penetration butt-welded tubes with nominal dimensions of CHS355.6×12.5, same as those used for the chord members of the X joints under consideration. The strip specimens were subjected to fatigue loading with a load ratio $R=0.1$. The resulting fatigue endurance limit (referring to 2×10^6 cycles) for the base material was found equal to 693 MPa, while the corresponding limits for the specimens using the weld A and B were found equal to 135 MPa and 98 MPa respectively. Based on the above test results on small scale specimens, it became evident that weld A had lower yield and ultimate stress compared to weld B, but better fatigue behavior.

5.2.3 Monotonic and cyclic IPB tests of tubular joints

Two specimens were subjected to monotonic IPB loading, one for each weld type. The specimen with weld type A failed at a M_{max}=267.8 kNm corresponding to a load-point displacement (LPD) equal to 159.3 mm and the specimen with weld type B at M_{max}=251.5 kNm corresponding to a LPD equal to 111.5 mm. Failure occurred at the chord crown location of the weld toe of the joint in the form a sudden crack. This type of failure indicates a "punching shear" mode of failure, to be examined in subsequent paragraphs. The test configuration is presented in Figure 5.2. Another two specimens, one for each weld type, were tested under IPB low-cycle fatigue. These specimens were subjected to fatigue loading with a M_{min}=21.3 kNm and M_{max}=213.1 kNm (load ratio, $R=M_{min}/M_{max}$=0.1). The specimen with weld type A failed after 976 loading cycles and the specimen with weld type B after 669 cycles. Both specimens failed due to

fatigue at the chord crown region of the joint, at the same location as in the tests under monotonic loading.

Figure 5.2: Test configuration for IPB loading.

5.2.4 Monotonic and cyclic OPB tests on tubular joints

Two specimens were subjected to monotonic OPB loading, one for each weld type. The bending moment capacity M_{max} of the specimen with weld type A was equal to 121.4 kNm reached at a LPD of 107.5 mm. The corresponding values for the specimen with weld type B were 115.4 kNm and LPD=78.5 mm, respectively. Both specimens failed at the chord saddle region of the weld toe of the joint. The test configuration is presented in Figure 5.3. The remaining two OPB specimens were tested under low-cycle fatigue, one with weld type A and one with weld type B. After an initial applied bending moment of 100 kNm to both specimens, they were subjected to fatigue loading with a M_{min}=9.3 kNm and M_{max}=93.4 kNm (load ratio, R=0.1). The specimen with weld type A and that with weld type B failed after 240 and 200 cycles, respectively. Both failed due to low-cycle fatigue at the chord saddle location.

120

Figure 5.3: Test configuration for OPB loading.

5.2.5 Cyclic axial fatigue (AX) tests

Two X-joint specimens, one for each weld type, were subjected to low-cycle fatigue under cycling axial loading. The test set-up is presented in Figure 5.4(a). Both specimens were subjected to fatigue loading with a F_{min}=75 kN and F_{max}=750 kN (load ratio, R=F_{min}/F_{max}=0.1) and failed due to through-thickness fatigue cracking at the chord saddle, as shown in Figure 5.4(b). The specimens were able to sustain the applied load for more than 1,000 cycles. In the specimen with weld type B, after about 750 loading cycles the rate of increase of overall axial deformation (axial stiffness loss) became quite significant and this could be considered as "structural failure". The weld type A specimen had better performance in terms of maintaining its axial stiffness. All experimental results discussed in the previous sections for the three types of applied loading are summarized in Table 5.1.

(a)

121

(b)

Figure 5.4: Tested specimen under axial cyclic loading; (a) general set-up, (b) failed specimen with fatigue crack at weld toe (chord saddle location).

Table 5.1: Summary of test results.

Test No.	Type of specimen and loading type	Weld type	Type of loading	Applied moment M_{max} (kNm) and axial force F_{max} (kN)	R ratio	Loading cycles to failure, N_f
1		A	monotonic	267.8	-	-
2		B	monotonic	251.5	-	-
3	IPB	A	cyclic	21.3 to 213.1	0.1	976
4		B	cyclic	21.3 to 213.1	0.1	669
5		A	monotonic	121.4	-	-
6	OPB	B	monotonic	115.4	-	-
7		A	cyclic	9.3 to 93.4	0.1	240
8		B	cyclic	9.3 to 93.4	0.1	200
9	AX	A	cyclic	75 to 750	0.1	1,000 (*)
10		B	cyclic	75 to 750	0.1	750 (*)

(*) approximate values, corresponding to loss of axial stiffness

5.3 Static design provisions

5.3.1 Static strength design provisions

Design provisions for the ultimate resistance of the joints under examination have been proposed by EN 1993-1-8, which are identical to those proposed by CIDECT Guidelines No.1 for the static strength for welded tubular connections. The provisions are used herein for predicting the joint capacity

122

under IPB and OPB loading conditions and comparing with the experimental findings. For the joint configuration of interest, neglecting all safety factors and simplifying the formulae for the joint geometry under consideration (chord-to-brace angle equal to 90^0), the resistance against the aforementioned types of loading can be evaluated using Eq. (5.1):

$$M_{IPB} = 4.85\sigma_{y0}t_0^2 d_1\beta\sqrt{\gamma}$$
$$M_{OPB} = \sigma_{y0}t_0^2 d_1 \frac{2.7}{1-0.81\beta}$$

(5.1)

where σ_{y0} is the yield strength of the chord material, t_0 is the chord thickness, d_1 is the brace diameter and β is the ratio of the chord diameter d_0 over the brace diameter d_1. In addition, when the condition $d_1 \leq d_0 - 2t_0$ is satisfied, the joints should be checked against punching shear failure, which can be described by the following equations:

$$M_{IPB,PS} = M_{OPB,PS} = \frac{\sigma_{y0}t_0^2 d_1}{\sqrt{3}}$$

(5.2)

It should be noted that the EN 1993 design tools for welded tubular connections have been developed for ordinary steel grades up to 460 MPa.

Similar design formulae are available in the API RP 2A (2000) design standard for steel grades up to 500 MPa. According to this standard, the moment resistance of the tubular joints under consideration is defined as:

$$M_{IPB} = M_{OPB} = Q_u \sigma_{y0}t_0^2 d_1$$

(5.3)

where the parameter Q_u is defined differently for IPB and OPB as given below:

$$Q_u = (5+0.7\gamma)\beta^{1.2}$$
$$Q_u = 2.5+(4.5+0.2\gamma)\beta^{2.6}$$

(5.4)

The reported experimental results in in terms of maximum load capacity of the joints, are compared with the corresponding code predictions in Table 5.2 without taking into consideration any safety factors. The available design code predictions given in CIDECT No. 1/ EN 1993-1-8 are very close to the maximum loads that the joints can withstand, as recorded in the corresponding experiments. The predicted difference is up to 11.2%. On the contrary, in the case of IPB, there is a significant underestimation of the maximum load up to 32.7% between the predicted values and the experimental results. The provisions of API RP 2A are significantly more conservative compared to the experimental values and the CIDECT No. 1/ EN 1993-1-8 provisions both for IPB

and OPB. The comparison with the experimental data shows differences varying from +27% up to +64.6% for OPB and IPB respectively.

It should be noted that the EN 1993-1-12 provisions for the ultimate strength of high-strength-steel welded tubular connections introduces a reduction factor equal to 0.8. This factor has been introduced in EN 1993-1-12 because of the reduced ductility of the high-strength steel in comparison with ordinary carbon steel, in connection with the lack of adequate test data. This factor is not considered in the present comparison. More experimental data are required before reaching to a safe conclusion regarding the necessity of using the 0.8 reduction factor. Nevertheless, the experimental results reported in the present study indicate that, for the joints under consideration and the specific type of welds, the use of this reduction factor is not necessary. Based on the above comparisons, it can be concluded that the static strength equations provided by the aforementioned specifications can be also applied safely to the specific steel grade for design purposes.

As far as the deformation capacity of the joints is concerned, the present results indicate that – for welds of type A and B within the range considered in the present investigation – the increase of the weld metal grade results in a reduction of the deformation capacity of the tubular joints under monotonic loading conditions. More elaborate results and relevant deformation capacity criteria will be presented in a following section.

Table 5.2: Comparison of experimental results and predictions using the CIDECT No. 1/ EN 1993-1-8 and the API RP 2A provisions.

Type of loading	Weld type	Applied moment M_{max} (kNm)	CIDECT No. 1 /EN1993-1-8 * (kNm)	API RP 2A (kNm)	Difference	
					CIDECT No. 1 /EN1993-1-8	API RP 2A
IPB (monotonic)	A	267.80	201.84	162.7	+32.7%	+64.6%
	B	251.50	201.84	162.7	+25.1%	+54.6%
OPB (monotonic)	A	121.44	108.92	90.5	+11.2%	+34.2%
	B	115.42	108.92	90.5	+6.0%	+27.5%

*: Not accounting for the 0.8 factor (EN 1993-1-12)

5.4 Finite element modeling

Detailed numerical models have been developed for the simulation of the experiments, considering the actual dimensions of the welded joints for each case under examination. The weld geometry has been modeled in detail, according to the provisions of the American Structural Welding Code AWS D1.1. The models are developed in ABAQUS using 8-node, reduced integration solid elements (C3D8R) for the chord, the brace and the weld region of the joint. Only

124

half of the joint is modeled, taking advantage of symmetry and applying the appropriate symmetry conditions. The mesh size is denser near the weld region in order to provide accuracy in the simulation results and time-effective simulations.

A mesh sensitivity analysis was conducted in order to define an optimum mesh for the numerical model in terms of efficiency and accuracy of the results with respect to the value of the local stress at the weld toe, as well as the overall behavior. The resulting mesh configuration adopts 96 elements along the circumference of the brace and the chord parts of the joint, and is properly modified near their connection area. For the simulation of the IPB tests, following this parametric study, four elements along the thickness of the joint chord were sufficient to describe accurately the deformed shape; further increase of the element number resulted in non-significant changes of the numerical results. On the contrary, a finer mesh consisting of eight elements through the chord thickness has been necessary for the simulation of the OPB tests and AX tests. This result is in accordance with the predicted stress and strain concentration factors for these two types of loading. More specifically, the stress concentration factors due to OPB and AX loading schemes are considerably higher than the corresponding stress concentration factors for IPB loading, implying that the chord wall undergoes significant bending even for low externally applied loads. The difference in the number of elements through the chord thickness is the only one among all the models adopted for the analysis. Along with the above, it has been also decided that in all cases, four elements are used through the thickness of the brace. The developed model is shown in Figure 5.5.

(a)

125
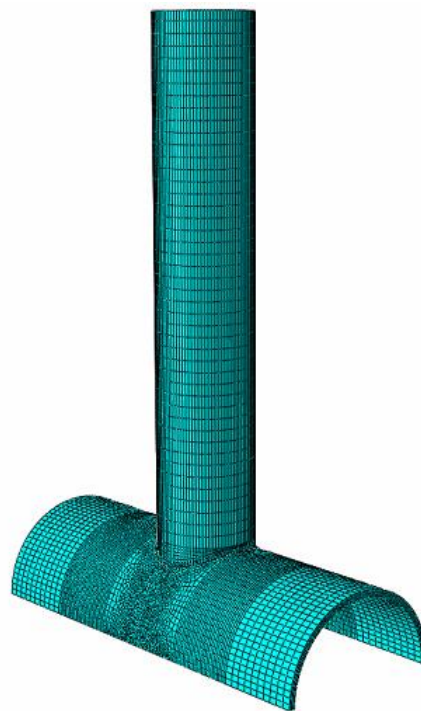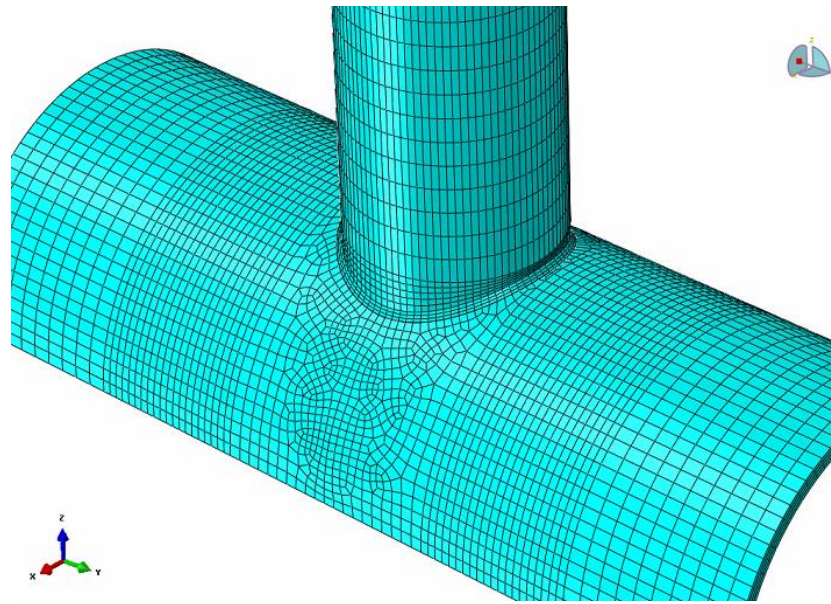
(b)

Figure 5.5: Numerical finite element model: (a) General view (b) Weld region.

For the description of the nonlinear material behavior, the constitutive bounding surface model presented in Chapter 2 has been employed. The material model parameters have been properly defined based on the material testing data given in the report by Bursi (2012). The parameter values reported in Table 5.3 have been defined in order to provide best fit to the strain-controlled and stress-controlled tests respectively, and are the same as those adopted for the analysis conducted in Chapter 3.

Table 5.3: Summary of material parameter values

Parameter	$\hat{H}$	ω	c (MPa)	A	B	m	k_0 (MPa)	Q (MPa)	b
Value	2300	5	250	50	10	2	746	-350	500

5.5 Numerical results and comparison with experimental data

The numerical models developed allow for the detail examination of the behavior of each joint. The global strength and deformation characteristics have been monitored and the simulation results are compared with the experimental measurements. In addition, several local strain measurements have been recorded at strain gauge locations, as described in a previous section.

More specifically, based on local strain measurements, the strain concentration factor ($SNCF$) for each test specimen has been evaluated. For each joint, an extrapolation zone normal to the weld toe has been defined near the weld-toe area according to the provisions of CIDECT Guidelines No. 8, as

126

presented in Figure 5.6. The limits of the extrapolation zone (L_{min}, L_{max}) have been defined based on the geometrical properties of the joint at the location of interest (chord, saddle). By limiting the extrapolation zone it is assured that the highly localized effects of the weld notch are alleviated while the size of the zone is such that the stress rise is described sufficiently.

Inside the extrapolation zone, strain values have been monitored in several points from experimental measurements and numerical calculations. The evaluation of the $SNCF$ has been conducted based on a linear extrapolation of those values. Apart from the specific locations of strain measurements, with the use of the developed models the local strain field along the circumference of the weld has been evaluated as well. Finally, using the numerical models, the corresponding stress concentration factor (SCF) has been also evaluated and compared with the predictions of CIDECT Guidelines No. 8 and the results according to the Wordsworth and Smedley (1978) formula. A quadratic extrapolation scheme has been adopted for the evaluation of the SCF, as suggested by CIDECT Guidelines No. 8, which is found to describe better the local stress gradient. More details are presented in the following sections for each loading scheme.
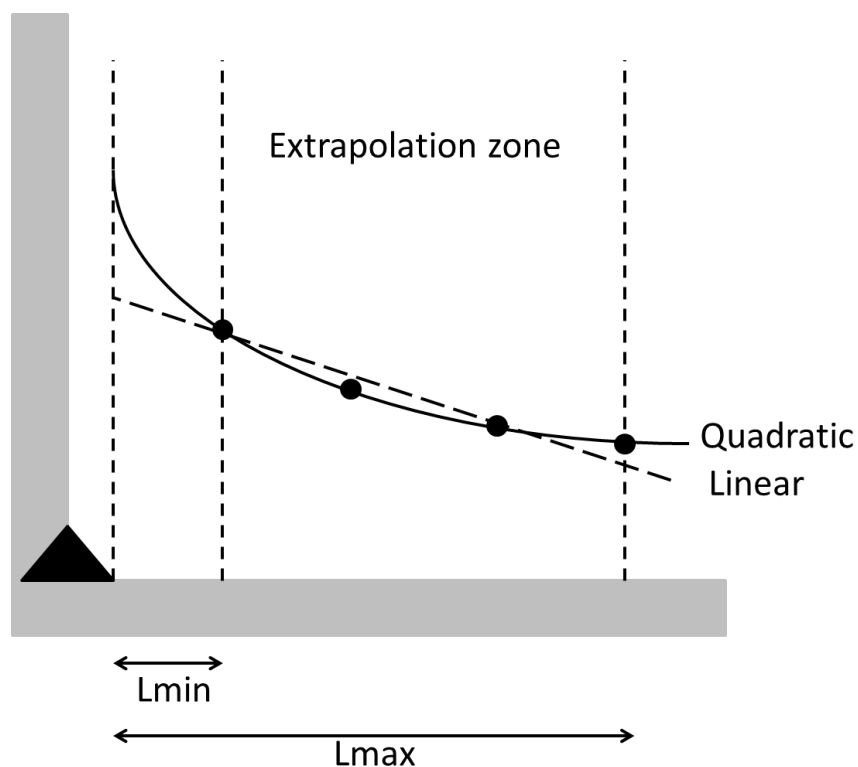

Figure 5.6: Extrapolation zone near the weld toe area.

5.5.1 Simulation of IPB tests

In the numerical models developed for the simulation of the IPB tests (monotonic and cyclic), the joint geometry was modeled according to the

measured dimensions of the tubular members, which are very close to the nominal ones, considering a uniform thickness of the chord and the brace. The predictions of the model are in good agreement with the experimental measurements for monotonic and cyclic loading in terms of the moment-displacement diagram, as shown in Figure 5.7. Based on experimental measurement, the strain concentration factor ($SNCF$) ranges from 2.70 to 3.68 for specimens T1 to T4, as reported in Table 5.4. The numerical model prediction for the strain concentration factor is very close to the corresponding experimental values and equal to 2.51. The stress concentration factor (SCF) has been evaluated equal to 3.48 using the CIDECT Guidelines No. 8 provisions, while it is equal to 3.22 according to W/S. The numerical model predicts a stress concentration factor equal to 3.57. Finally, based on the numerical model, the local strain values at the chord saddle weld toe position at the displacement where failure of the specimens was observed experimentally are equal to 6.9% and 5.1% for the weld A and the weld B specimens respectively.

The distribution of local tensile strains along the weld toe path on the joint chord ε_r, calculated perpendicular to the weld toe tangent in the brace radial direction (normal to the weld) are plotted in Figure 5.8 for several loading levels. The same linear extrapolation technique for the evaluation of the $SNCF$ has been adopted. The strain value is normalized by the yield strain ε_y. The chord saddles are positioned at 0 and 180 degrees, while the chord crown is positioned at 90 degrees. The results show that hot spot strain values maximize at the chord crown location and that for a range of ±45 degrees at both sides of the crown, relatively high strains extend over a significant part of the weld toe about the hot spot location. This results to a distribution of plastic deformations along a significant part of the circumference of the weld (Figure 5.9), which has a small gradient and justifies the shear dominant failure observed during the execution of the tests. It should be noted that according to the provisions of EN 1993-1-8 for this particular joint, the joint resistance under IPB is equal to 202 KNm and the predicted failure mode is punching shear, which is compatible with the calculated strain distribution around the hot spot location. The predicted resistance value is significantly lower than the experimentally measured resistance (32.6% and 24.5% for weld conditions A and B respectively), but lays on the safe side.
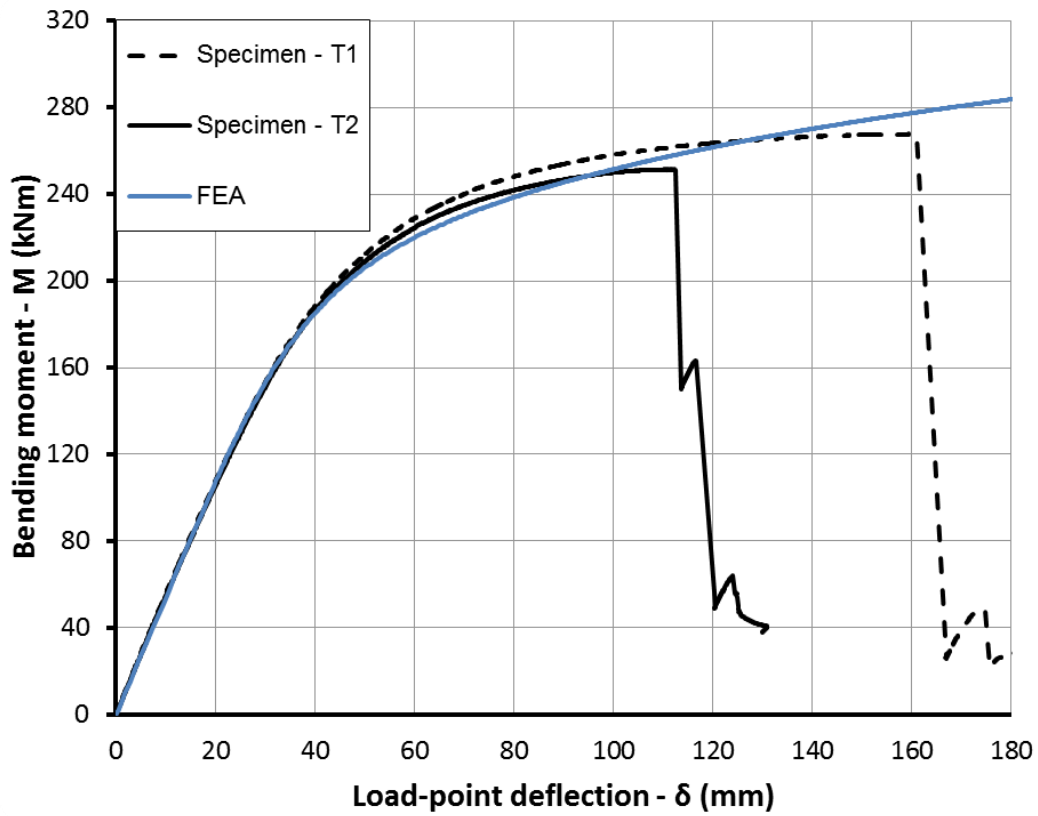
(a)
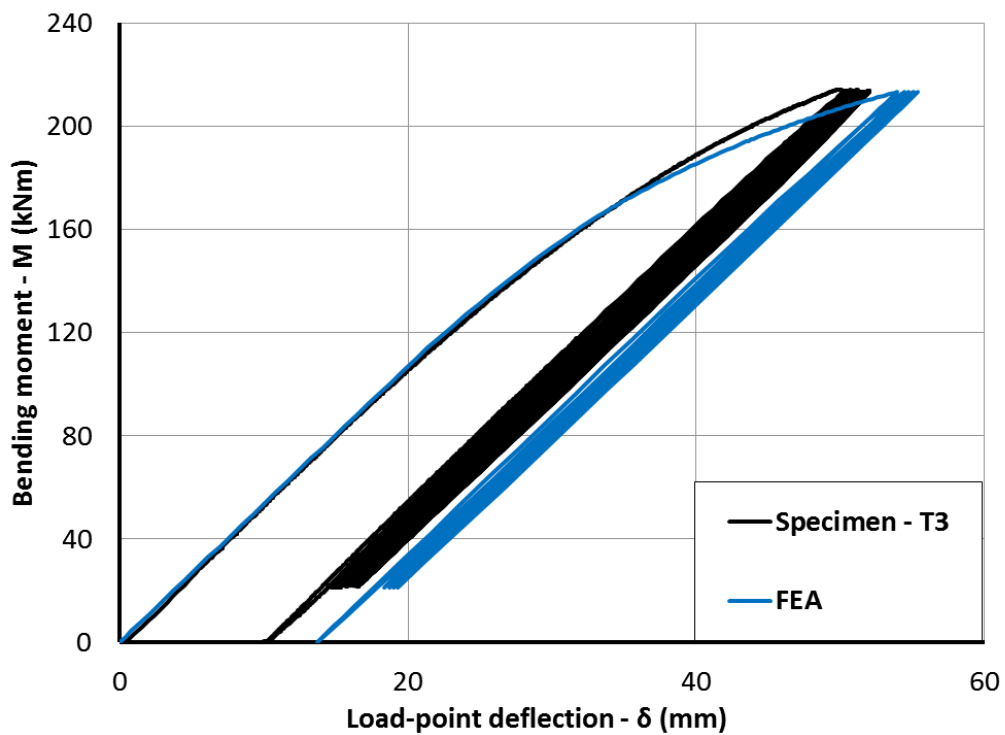
(b)

Figure 5.7: In-plane bending test and numerical simulation results: (a) Static loading, (b) Cyclic loading.
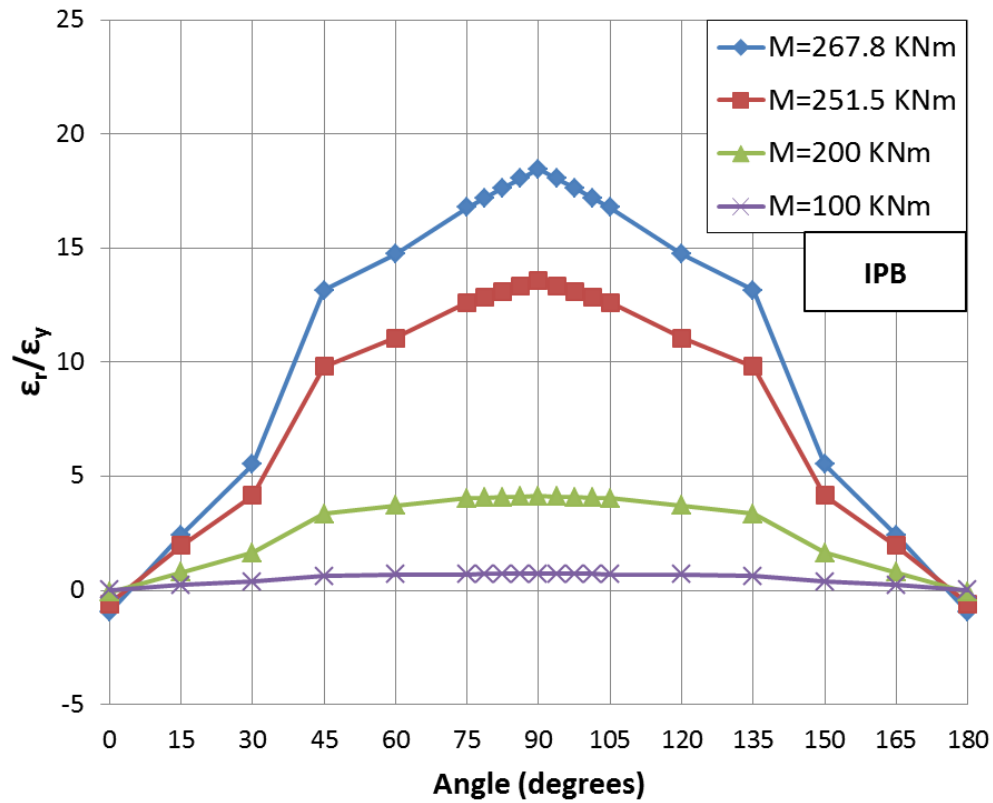
Figure 5.8: Distribution of local strain along the weld toe, on the joint chord along the weld toe (chord saddle at 0 and 180 degrees, chord crown at 90 degrees).

(a)

130
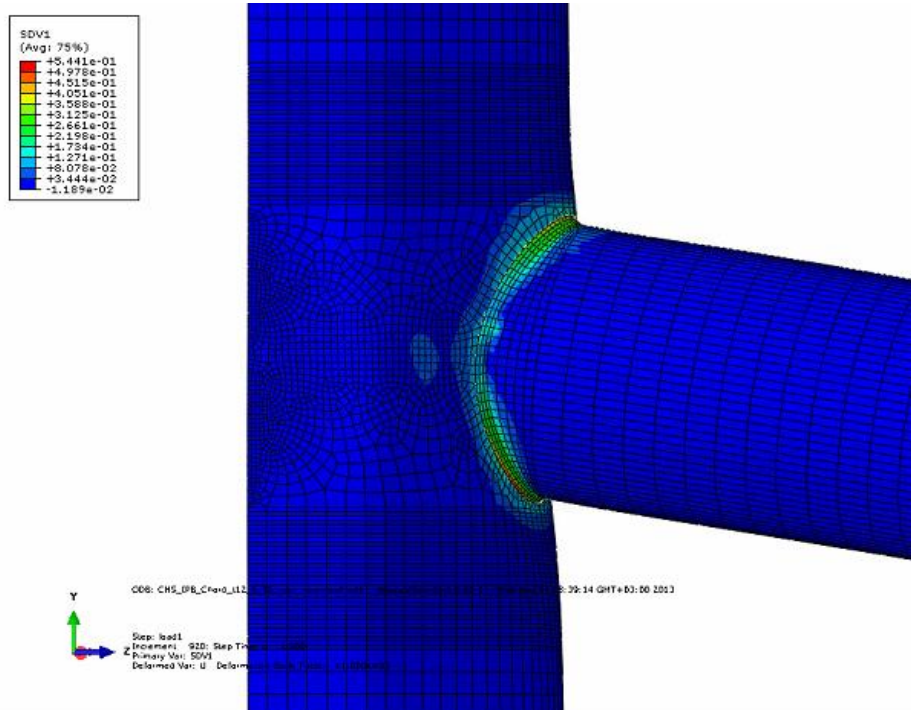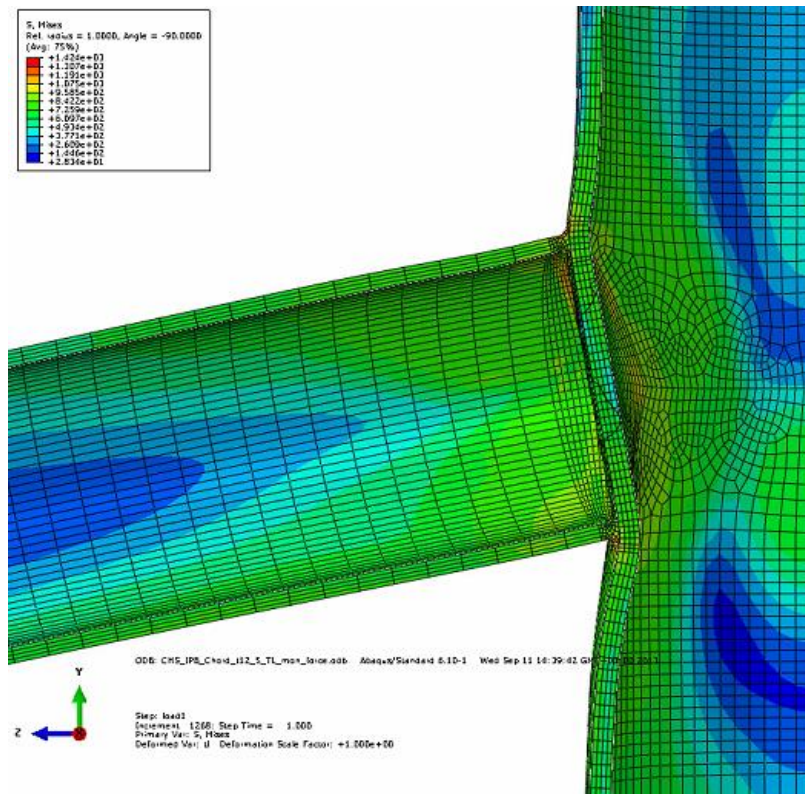
(b)

Figure 5.9: In-plane bending test simulation. (a) Distribution of equivalent plastic strain at the weld-toe area, (b) Deformed chord geometry at mid-span section.

5.5.2 Simulation of OPB tests

For the simulation of the OPB tests, similar models with the IPB case have been employed. As displayed in Figure 5.10, the experimental measurements in terms of the moment-displacement diagram can be numerically reproduced quite accurately for monotonic and cyclic loading conditions.

The numerical results indicate that joint behavior is sensitive to rather small variations of the chord thickness value, especially for higher applied load-point displacement values. This is attributed to the reduced joint resistance when chord thickness is reduced. The results show that the numerical model is capable of simulating accurately the experimental procedure and representing the experimental results.

The distribution of the hot spot strains along the weld toe path on the joint chord ε_r, are plotted in Figure 5.11 at several loading levels, normalized by the yield strain ε_y. The chord saddle is positioned at zero degrees. In the OPB case, there is a dominant concentration of local strains at the chord saddle weld to area where the test specimens failed, which is reduced towards the chord crowns. The deformed geometry of the joint chord presented in Figure 5.12(a) indicates the severe chord wall local bending and the localization of the

131

developing plastic strains at the chord saddle weld toe [Figure 5.12(b)]. The numerical model is able to verify the fracture locus observed experimentally.

The *SNCF* and *SCF* values have been also evaluated numerically, using the extrapolation method described in the previous section. Based on experimental measurements, the estimated *SNCF* value ranges between 5.06 and 5.51 for the specimens T5 to T8 (Table 5.4). The numerical prediction for the *SNCF* is equal to 6.81, higher than the experimentally evaluated values. According to CIDECT No. 8 guidelines, the corresponding *SCF* for the joint under consideration is equal to 8.94, the (W/S) prediction is equal to 8.26, whereas the numerical model results to a *SCF* value equal to 8.19. The above differences are attributed to the sensitivity of the strain/stress field near the weld toe due to the local geometric conditions (notch effect). Finally, the corresponding hot spot strain values at the chord crown weld toe position measured at the load-point displacements where failure of the specimens was observed are equal to 10.74% and 8.14% for the weld A and weld B specimens respectively. These values are different than the corresponding values predicted for the IPB tests.
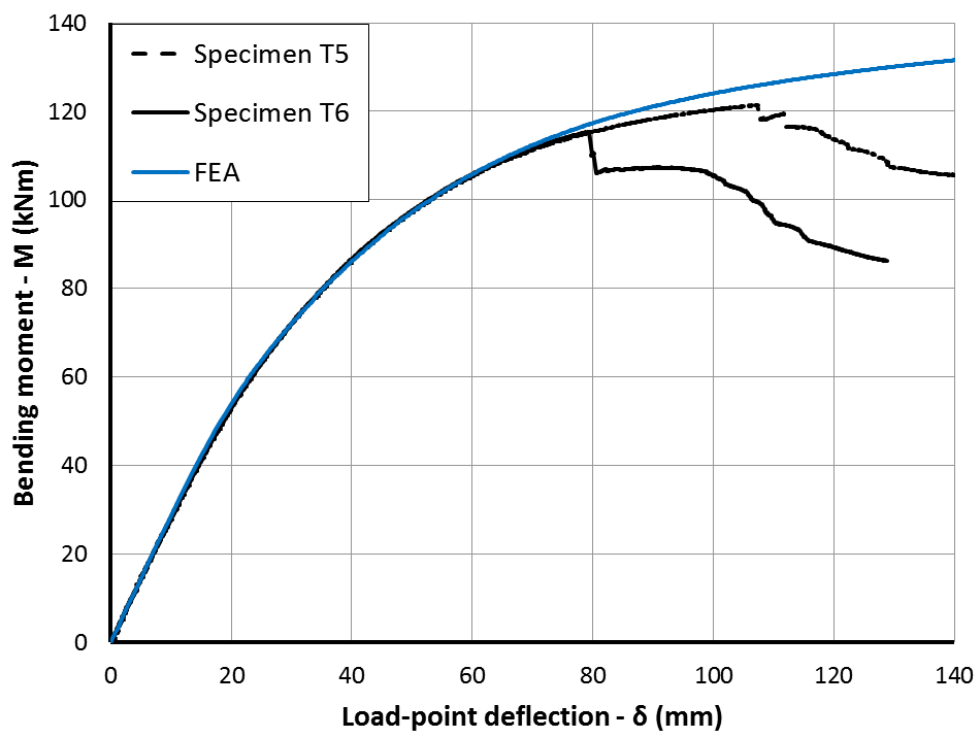
(a)
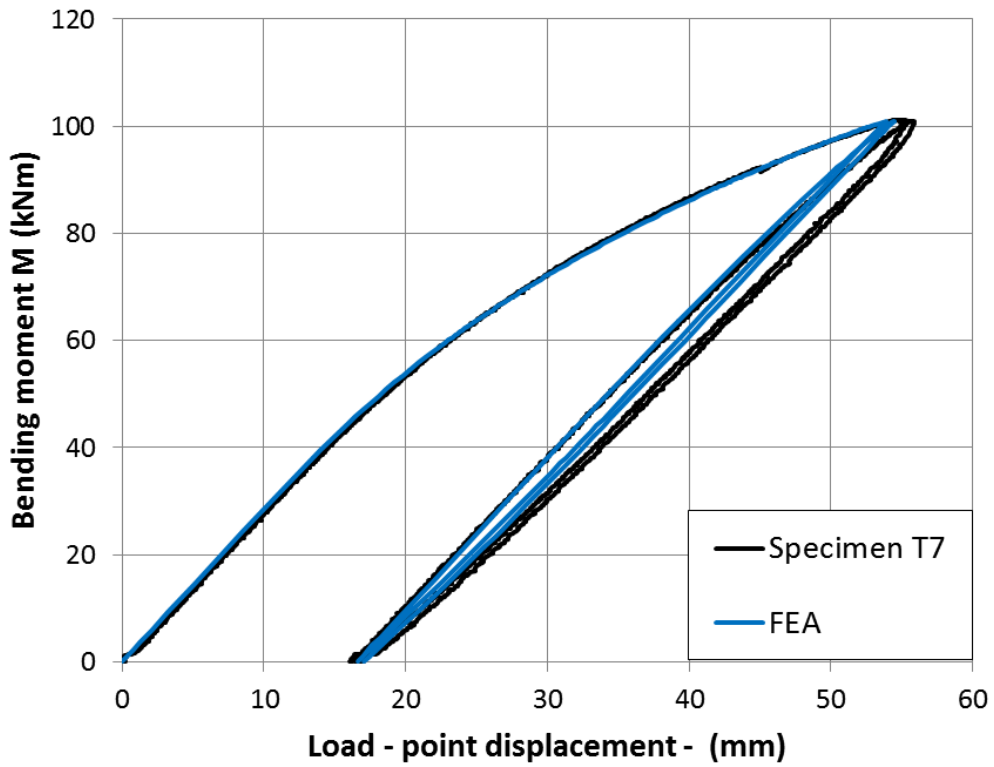
(b)

Figure 5.10: Comparison of the numerical and experimental load vs. displacement curves: (a) Monotonic, (b) Cyclic loading.

Figure 5.11: Distribution of the hot spot strains on the joint chord along the weld toe (chord saddle at 0 degrees, chord crown at ±90 degrees).

133
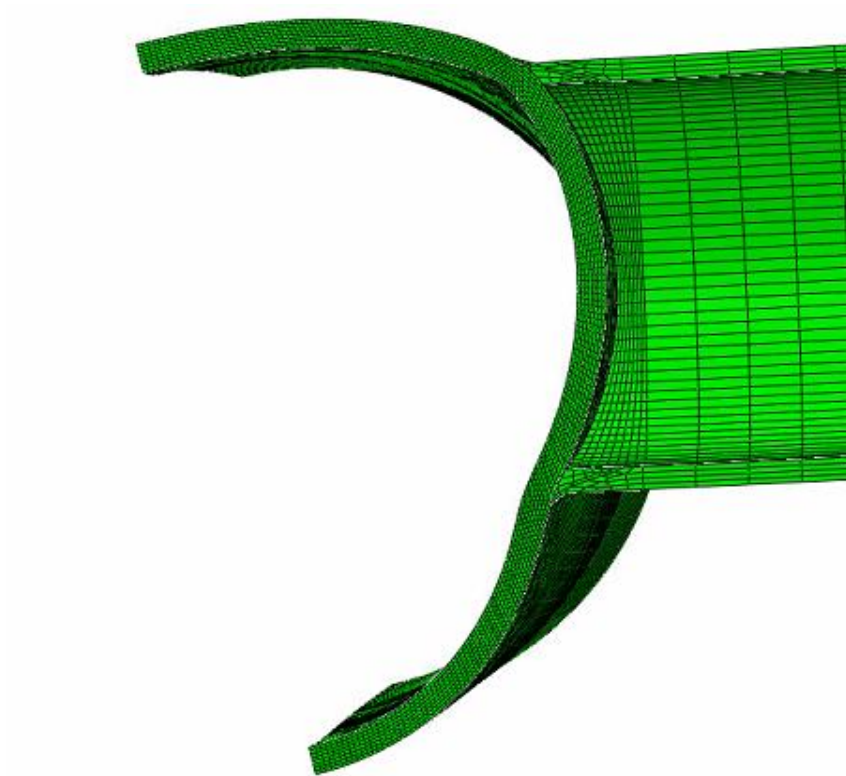
(a)
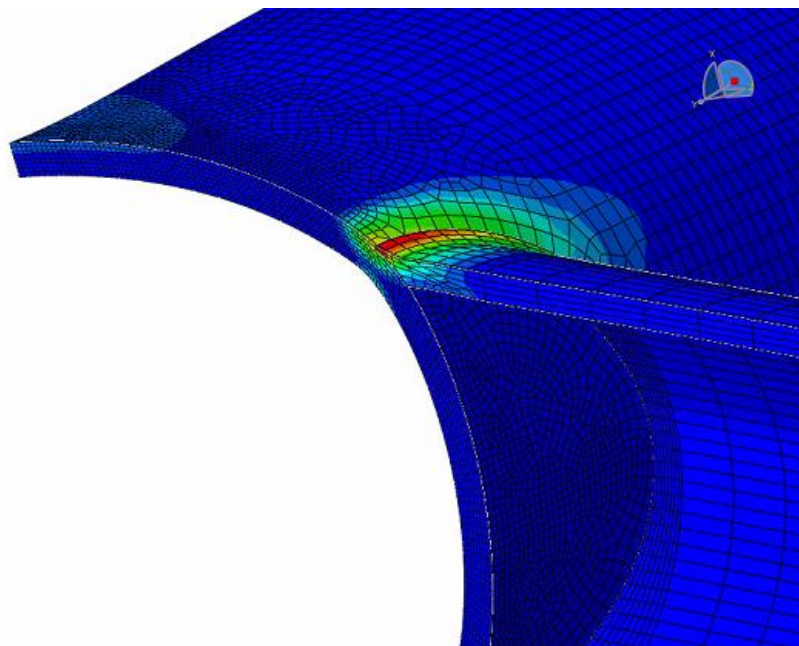
(b)

Figure 5.12: Mid-span section (a) Deformed chord geometry (b) Equivalent plastic strain distribution at the weld-toe area

134

5.5.3 Simulation of the AX loading tests

The axial cyclic loading tests have been also simulated using the developed numerical model. The simulation results are presented in Figure 5.13 and are in good agreement with the experimental measurements in terms of the load-displacement curve. In addition, the joint behavior under monotonic compressive and tensile loading is significantly different. In Figure 5.16, the deformed geometry configurations are depicted.

In addition, the distribution of the local strains ε_r along the weld toe on the chord side of the weld, are plotted in Figure 5.11 at several loading levels for the joint under tension loads, normalized by the yield strain ε_y. Following the pattern used in the OPB case, the two chord crowns are positioned at 0 and 180 degrees, while the chord saddle is positioned at 90 degrees. A significant concentration of local strains occurs at the chord saddle weld toe area, where the test specimens failed, which is reduced towards the chord crowns.

The analysis also computed the *SNCF* and the *SCF* values. The *SNCF* value is measured equal to 5.68 and 6.34 for the specimens T9 and T10 respectively, as presented in Table 5.4. The numerical model prediction for the strain concentration factor is equal to 8.78. The stress concentration factor has been evaluated according to the provisions of CIDECT No. 8 equal to 18.35, and equal to 17.15 according to the W/S formula. The numerical model predicts a stress concentration factor equal to 13.31. Similarly to the case of OPB, the difference between the aforementioned values can be attributed to the sensitivity of the numerical predictions on the local weld effects, which can affect the predictions drastically especially where the stress/strain local risers are very high, as in the current case. Besides these differences, plastic strain concentration coincides with the crack location observed experimentally. It should be also noted that joint behavior under compressive and tensile axial loading may not be the same.

To illustrate this observation, the monotonic compressive and tensile load-displacement curves are reported in Figure 5.14, while the resulting deformed shapes are presented in Figure 5.16. Under tensile loads, the joint presents increase load resistance associated with severe deformation of its chord, as presented in Figure 5.16(a) and eventually membrane action effects that result to a further increase of its stiffness (Figure 5.14). On the contrary, the application of compressive loads may result in flattening and crushing of the chord, as shown in Figure 5.16(b), and thus the overall load-displacement curve exhibits a limit point and a descending branch after that point.

135
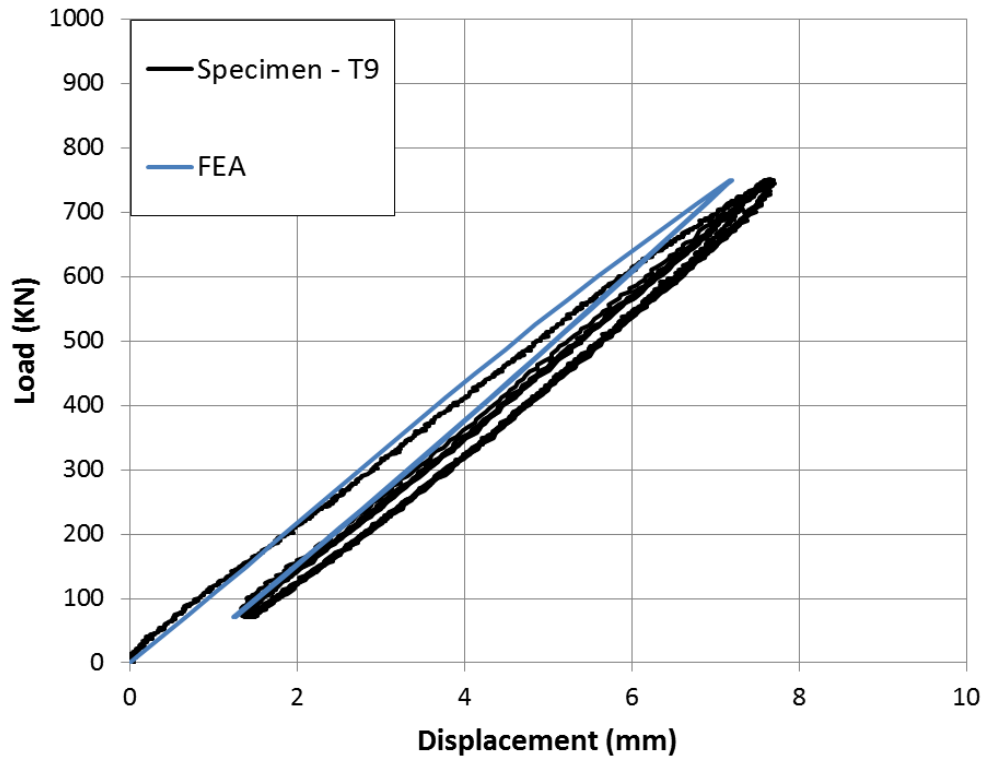
Figure 5.13: Numerical simulation of high-strength steel X-joint subjected to cyclic axial loading; load-displacement curves.
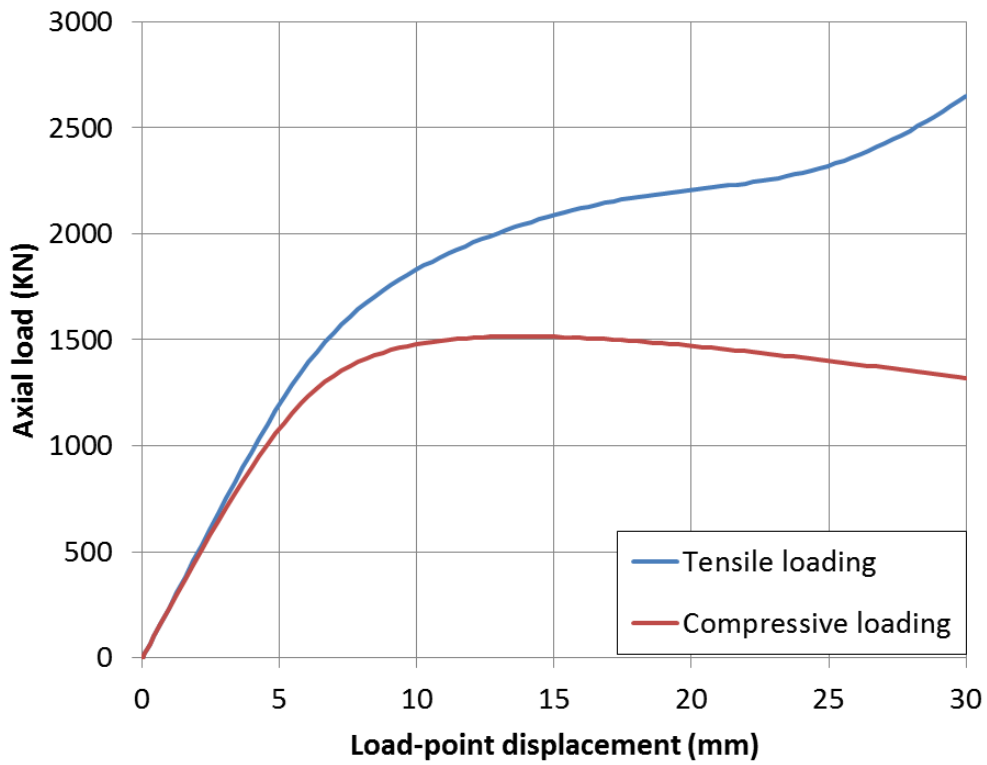
Figure 5.14: Numerical simulation of an X-joint subjected to monotonic tensile and compressive axial loading; load-displacement curves.
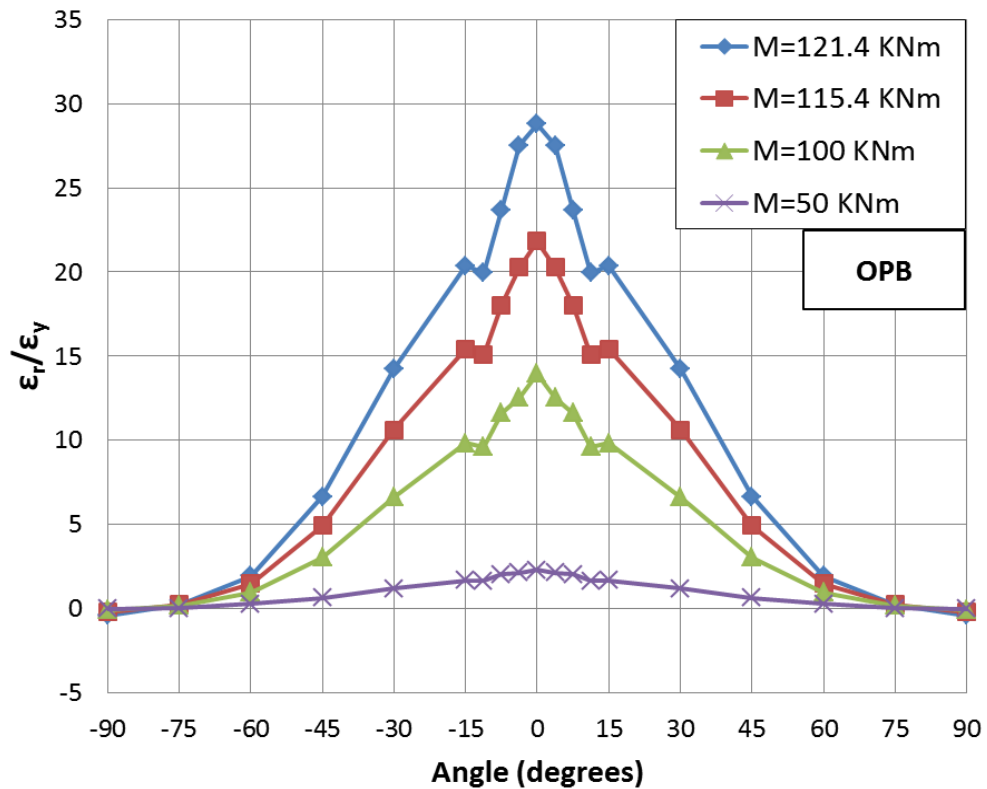
136
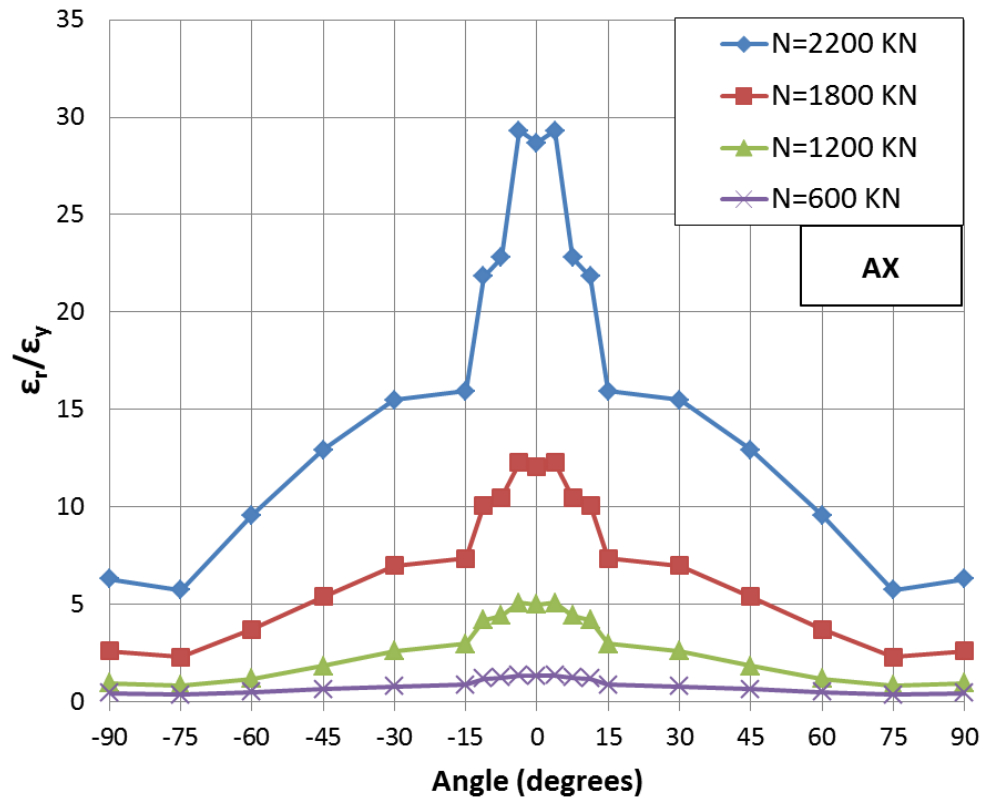
Figure 5.15: Distribution of the hot spot strains on the joint chord along the weld toe (chord saddle at 0 and 180 degrees, chord crown at ±90 degrees).

(a)

137
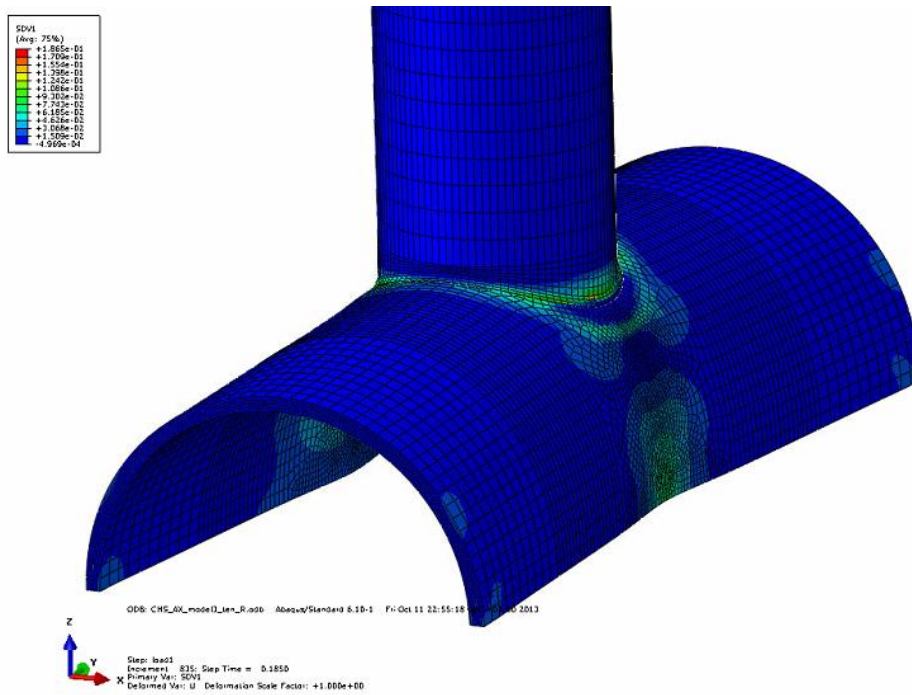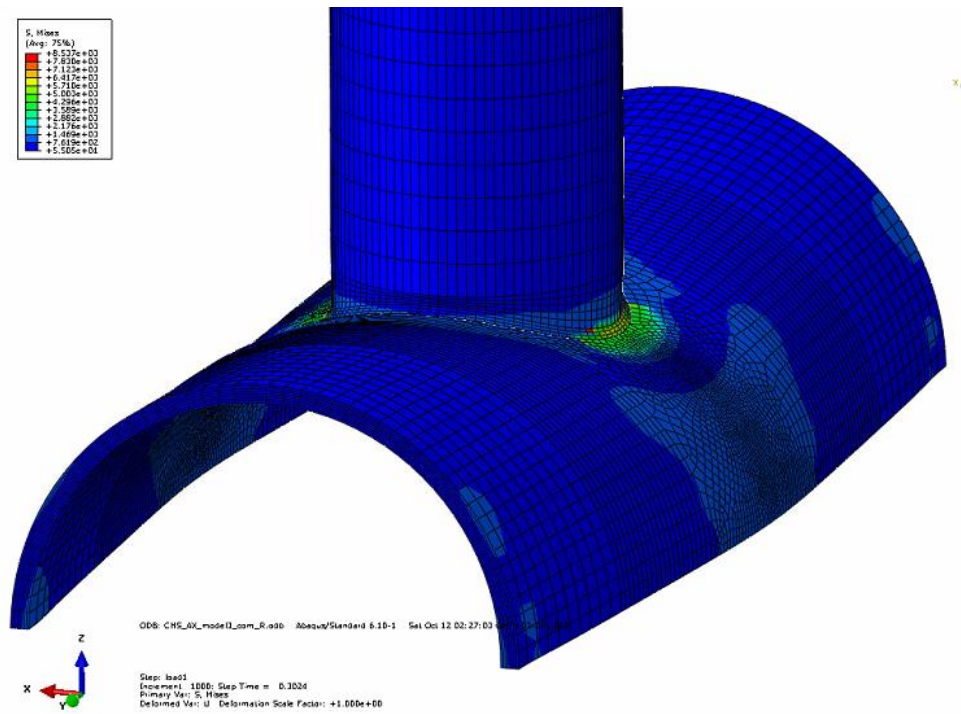
(b)

Figure 5.16: Deformed joint geometry under axial loading: (a) tensile forces, (b) compressive forces.

Table 5.4: Experimental and numerical *SNCF*.

Test No.	Type of specimen and loading type	*SNCF* exp	*SNCF* FEA
1	IPB	2.82	2.51
2		2.91	
3		2.70	
4		3.68	
5	OPB	5.34	6.81
6		5.06	
7		5.31	
8		5.51	
9	AX	5.68	8.78
10		6.34	

138

5.6 Fatigue design

5.6.1 Fatigue design based on elastic hot spot stresses

The fatigue design of welded tubular connections can be conducted either with the "classification of details" method, adopted in EN 1993-1-9, section 8 (referring to a limited number of joint geometries), or through the "hot spot stress" method. It has been widely recognized that the use of the classification method is rather inappropriate for the fatigue design of welded tubular connections. It is also noticed that EN 1993-1-9 covers only a small range of possible joint geometries, not including the X-joints under consideration. On the other hand, the hot spot stress method is the most efficient method for the fatigue design of such joints, also adopted by CIDECT No.8 Guidelines. There is no special provision in EN 1993-1-12 for the fatigue design of welded tubular connections made of high-strength steel.

The hot spot method requires the calculation of the hot spot stress, which is the maximum geometric elastic stress at the vicinity of the weld. Subsequently, the fatigue design life is calculated though an appropriate fatigue S-N curve. The CIDECT guidelines present a complete procedure for hot spot stress fatigue design, and propose a concise methodology for the calculation of the hot spot stress at a specific welded tubular joint, either through special-purpose parametric equations for stress concentration factors or an elastic finite element analysis and appropriate extrapolation of the computed stress to the weld toe. Upon calculation of the hot spot stress, a fatigue curve is used to estimate the fatigue life of the connection, expressed as follows:

For $10^3 < N_f < 5 \cdot 10^6$

$$\log\left(N_f\right) = \frac{12.476 - 3 \cdot \log\left(S_{hs}\right)}{1 - 0.18 \cdot \log\left(\dfrac{16}{t}\right)} \tag{5.5}$$

For $5 \cdot 10^6 < N_f < 10^8$

$$\log\left(N_f\right) = 16.327 - 5 \cdot \log\left(S_{hs}\right) + 2.01 \cdot \log\left(\frac{16}{t}\right), \tag{5.6}$$

The above fatigue curve is applicable for high-cycle fatigue, i.e. for number of cycles greater than 10^3.

The DNV–RP–C203 standard for the fatigue design of offshore steel structures also contains a fatigue design methodology for welded tubular joints. According to this standard, the basic fatigue design equation is given as follows:

For $10^4 < N_f < 10^7$

139

$$\log(N_f) = 12.164 - 3\log S_{hs} \tag{5.7}$$

For $N_f > 10^7$

$$\log(N_f) = 15.606 - 5 \cdot \log S_{hs} \tag{5.8}$$

The applicability of this design curve is intended for fatigue loading that exceeds 10^4 cycles. Fo2r low-cycle fatigue assessment, a linear extrapolation of the curve can be adopted, as suggested in Appendix D of the standard. The linear extrapolation of the high-cycle fatigue curve into the low-cycle fatigue regime has also been proposed by Ballio & Castiglioni (1995), following extensive fatigue experiments of plated connections.

Apart from the aforementioned fatigue design curves, Hochman et al. (2010) proposed a fatigue design curve covering both high-cycle and low-cycle fatigue ranges as well. This curve is based on a series of tests including low-cycle fatigue tests, as well as an extensive test database on tubular joints made of steel material of ordinary grade (ultimate stress not exceeding 580 MPa). The fatigue design curve proposed by Hochman et al. (2010) is given in the following equation:

For $1 < N_f < 10^3$

$$\log(N_f) = 13.386 - 3.336 \cdot \log S_{hs} \tag{5.9}$$

For $10^3 < N_f < 10^7$

$$\log(N_f) = 12.476 - 3 \cdot \log S_{hs} \tag{5.10}$$

For $N_f > 10^7$

$$\log(N_f) = 16.127 - 5 \cdot \log S_{hs} \tag{5.11}$$

The methodology of using the elastic hot spot stress together with a linear extrapolation of a fatigue curve in the low-cycle fatigue regime is applied in the following. The CIDECT and DNV design curves are extended in the low-cycle fatigue range, plotted with dashed lines as presented in Figure 5.17. In this figure, the results from the tests on the tubular joints in terms of the developing hot spot stresses are also plotted. These hot spot stresses are derived by multiplying the nominal stress ranges by the *SCF* as given in the CIDECT specifications. No correction for local plastic deformation in the ultra-low cycle fatigue range is considered at this stage. The value of this elastic hot spot stress is very high, significantly higher than the yield stress of the material and, therefore, it is not a real stress, but a conventional stress only for design purposes.

140

From the comparison of the design curves with the experimental data, it can be observed that near the high-cycle fatigue range, all the curves can provide safe fatigue life predictions. In the low-cycle fatigue range, the linearly extrapolated CIDECT and DNV curves can provide safe predictions but only for a number of cycles in the range of 100. The fatigue design curve proposed by Hochman et al. (2010) is very close to the CIDECT/DNV curve both in the high-cycle regime, as well as in the low-cycle fatigue regime. Nevertheless, all of the aforementioned curves fail to cover the hot spot stress evaluated for the monotonic loading cases.

Table 5.5: Fatigue design results

Test No.	Loading cycles to failure N_f	ΔM (KNm) or ΔN (KN)	$\Delta\sigma_{nom}$	SCF (CIDECT)	$\Delta\sigma_{HS}$ (MPa)
1	0.5 *	267.8	813.90	3.48	2832.36
2	0.5 *	251.5	764.36	3.48	2659.97
3	976	191.8	582.92	3.48	2028.56
4	669	191.8	582.92	3.48	2028.56
5	0.5 *	121.4	482.41	8.94	4312.78
6	0.5 *	115.4	458.57	8.94	4099.63
7	240	84.1	334.19	8.94	2987.68
8	200	84.1	334.19	8.94	2987.68
9	1,000	675	116.96	18.35	2146.25
10	750	675	116.96	18.35	2146.25

(*): monotonic test.
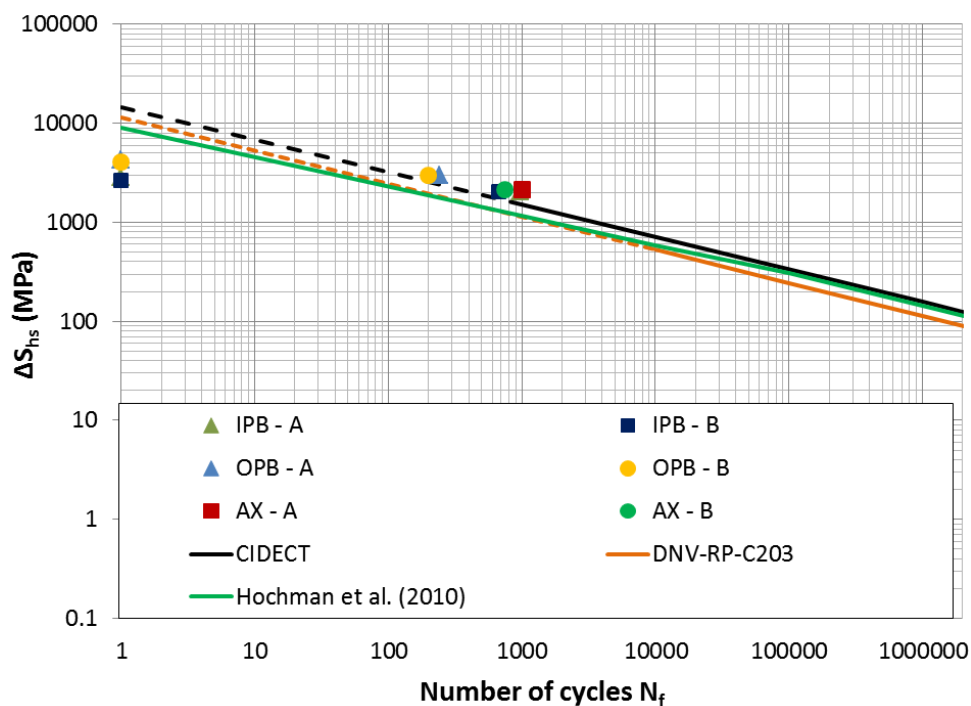
Figure 5.17: Hot spot-stress method fatigue curve and experimental data.

141

5.6.2 Fatigue design considering elastic-plastic material behavior.

To predict the fatigue life of cyclically loaded tubular welded joints under low-cycle fatigue conditions, it is necessary to estimate the local strain at the critical location. The fatigue design curves proposed by the CIDECT Guidelines No.8 and DNV-RP-C203 standards, as well as the curve proposed by Hochman et al. (2010) presented in the previous section, can be used to estimate the fatigue life of a tubular connection using an "elastic hot spot stress", calculated from a linear elastic analysis of the joint under consideration. Moreover, the fatigue curves of CIDECT and DNV are proposed for number of cycles higher than 10^3 or 10^4 cycles respectively, and therefore, an extrapolation is necessary into the low-cycle fatigue regime.

On the other hand, the above fatigue methodology does not take into account the real material behavior at the hot spot. Under severe cyclic loading, this behavior is not elastic, and the inelastic cyclic behavior of steel material needs to be accounted for.

The NORSOK N-006 standard for the assessment of the load-bearing capacity of offshore structures, provides a complete fatigue design curve covering both high-cycle and low-cycle fatigue ranges. In particular, the NORSOK N-006 fatigue curve has the following form:

For $1 < N_f < 10^5$

$$\log\left(N_f\right) = 19.405 - 5.834 \log S_{hs} \tag{5.12}$$

For $N_f > 10^5$

$$\log\left(N_f\right) = 12.164 - 3 \cdot \log S_{hs} \tag{5.13}$$

It is interesting to note that the NORSOK N-006 standard uses the same equation for the fatigue life curve for number of cycles more than 10^5 as the DNV–RP–C203 standard.

The key difference between NORSOK N-006 and the other standards presented in the previous section refers to the definition of the hot spot stress. According to NORSOK N-006 the evaluation of the hot spot stress range should consider the actual elastic-plastic behavior of the material. This can be achieved either by using appropriate finite element models that account for geometric and material nonlinearities, or alternatively using simplified methodologies such as Neuber's equation [Neuber (1961)], as presented in Chapter 4 for the design of elbows. The main issue in Neuber's methodology is the relation between the elastic *SCF* value with the inelastic stress and strain concentration factors.

In addition, to employ the Neuber's methodology and compute the local strain range, the knowledge of the so-called "cyclic stress-strain curve" is necessary. Based on material testing data on the high-strength steel grade under

142

consideration, as presented in Figure 5.18 [Bursi (2012)], an analytical expression for the cyclic material curve can be considered in the form:

$$\frac{\Delta \varepsilon}{2} = \frac{\Delta \sigma}{2E} + \left(\frac{\Delta \sigma}{2K} \right)^{1/n} \tag{5.14}$$

where K, n are the cyclic stress coefficient and cyclic strain hardening exponent respectively, which can be readily computed equal to 778.94 MPa and 0.146 respectively, using a fitting procedure.

Under cyclic bending with moment range ΔM, the nominal stress and strain ranges (ΔS, Δe) are calculated from simple mechanics equations, whereas the hot spot strain range according to this methodology, denoted as $\Delta \varepsilon_N$, is defined by the intersection of the cyclic material curve with Neuber's hyperbola. Subsequently, according to NORSOK provisions, the local strain range $\Delta \varepsilon_N$ is multiplied by Young's modulus, in order to define a pseudo-elastic hot spot stress $\Delta \sigma_{\text{pseudo}}$, which can be compared directly with the available fatigue design curve.
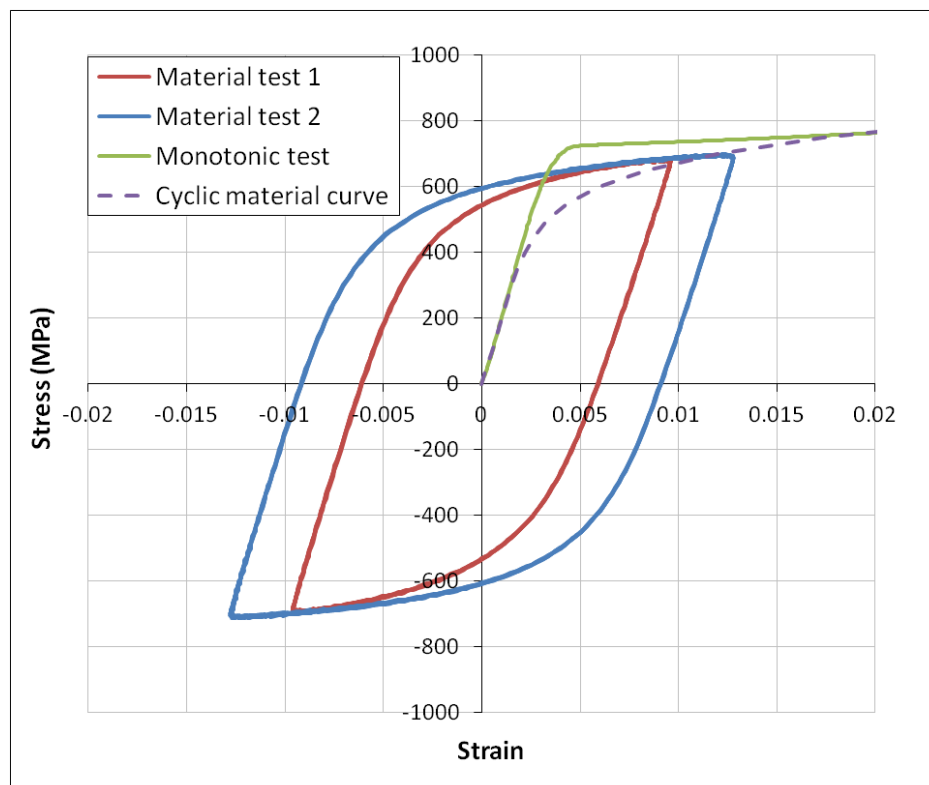
Figure 5.18: Cyclic material stress-strain curve.

Calculation of the SCF value, can be performed either numerically, as presented in the previous paragraphs using a finite element model or, in lieu of detailed finite element analysis, through available SCF formulae, such as the ones suggested in CIDECT No.8 Guidelines.

143

This simplified fatigue methodology has been applied for the fatigue analysis of the tested specimens. For each test conducted, the values of the predicted strain range are presented in Table 5.6. In the same table, the corresponding strain-range values predicted by the numerical models, denoted as $\Delta\varepsilon_{HS, FEA}$, are also presented. By comparing the two sets of strain ranges, it is observed that apart from the monotonic tests, in all the rest cases under examination the adoption of the Neuber's rule results to an overestimation of the locally developing strain range.

Subsequently, the above strain ranges, which account for inelastic material behavior, are multiplied by Young's modulus to define the pseudo-elastic stress ranges, denoted as $\Delta\sigma_{pseudo}$ and $\Delta\sigma_{pseudo-FE}$ respectively (Table 5.6). These stress values are plotted in Figure 5.19 along with he NORSOK design curve. Comparison of the these two hot spot stress ranges shows that, except for the monotonic loading cases, in all other cases the application of the Neuber's rule results to an overestimation of the hot spot stress range. It can be also observed that the comparison between the resulting stress ranges and the NORSOK fatigue design curve implies a conservative design. The over-conservatism of the specific deign curve would result in a prediction of zero load cycles for all the tests conducted
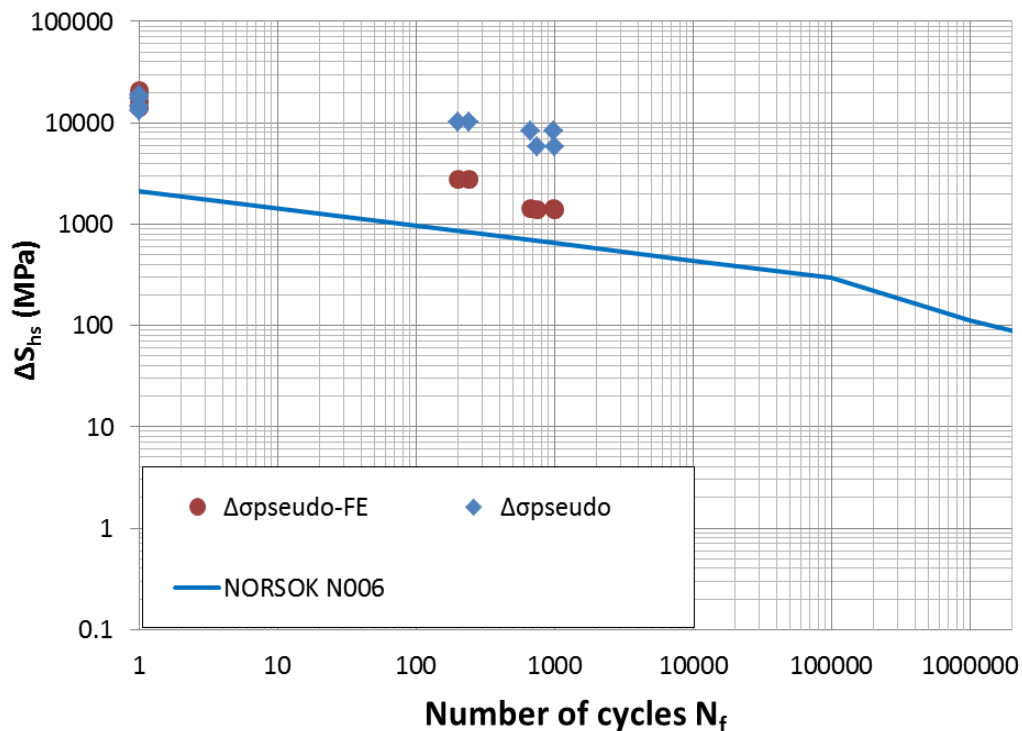
Figure 5.19: Application of the Neuber's equation for the fatigue design of the joints.

144

Table 5.6: Hot spot stress and strain ranges using the Neuber's rule and FE data

Test No.	Loading cycles to failure N_f	$\Delta\varepsilon_{HS, FEA}$ (%)	$\Delta\varepsilon_N$ (%)	$\Delta\sigma_{pseudo-FE}$ [MPa]	$\Delta\sigma_{pseudo}$ [MPa]
1	0.5 *	9.50	7.20	19000	14400
2	0.5 *	7.01	6.60	14020	13200
3	976	0.72	4.10	1440	8200
4	669	0.72	4.10	1440	8200
5	0.5 *	10.40	9.5	20800	19000
6	0.5 *	8.10	8.60	16200	17200
7	240	1.37	5.10	2740	10200
8	200	1.37	5.10	2740	10200
9	1,000	0.69	2.90	13180	5800
10	750	0.69	2.90	13180	5800

(*): monotonic test.

5.7 Parametric analysis

The effects of geometrical parameters on the structural behavior of the X joint have been examined through a parametric analysis of seven models. Loading is considered in a set-up identical to the one used in the experiments. The tube material is high-strength steel (746 MPa), same to the one of the tubular specimens. The numerical models developed for the parametric analysis are similar to those used for the simulation of the experiments, with the same mesh configuration presented in Figure 5.5 has been adopted. In addition, the material behavior is described adopting the bounding surface plasticity model calibrated through appropriate test results, as reported in Table 5.3. In Table 5.7, a summary of the joint geometries examined in the present parametric study is presented.

Table 5.7: Parametric analysis geometries

Model No.	D_0	t_0	D_1	t_1	β	γ	τ
1	355.6	10	193.7	10	0.545	17.78	1
2	355.6	12.5	193.7	10	0.545	14.224	0.8
3	355.6	16	193.7	10	0.545	11.113	0.625
4	355.6	12.5	193.7	6.3	0.545	14.224	0.504
5	355.6	12.5	193.7	14.2	0.545	14.224	1.136
6	355.6	12.5	139.7	10	0.393	14.224	0.8
7	355.6	12.5	244.5	10	0.688	14.224	0.8

5.7.1 Numerical results for ultimate loading

At each model, monotonic IPB, OPB and AX (tensile) loading schemes have been applied. A summary of the load – deflection curves obtained from the finite element models is presented for all three loading conditions.

145

Numerically, it is possible to extend those curves up to large deformation of the joint. However, from experimental observations, those curves are interrupted due to weld failure. The exact point on each curve corresponding to weld failure, requires a different analysis than the one presented herein, with a refined description of the crack opening area. Nevertheless, it is possible to consider an estimate the location of this point, assuming that the weld will fail when the local geometric strain reaches the corresponding value calculated when test specimens fail. This consideration may provide a rough approximation of the ultimate capacity and the deformation capacity of each tubular joint.

In each curve depicted in Figure 5.22 for IPB and OPB, the joint deformation corresponding to the stage where local maximum strain at the weld toe reaches the critical value for weld failure is depicted. Two points on each curve are identified, corresponding to failure of weld A and weld B respectively. For the case of axial loading, the corresponding points are obtained using the local strain limit values for the OPB case, based on the fact that both loading types are associated with failure at the chord saddle location.

In all graphs of Figure 5.22, the prediction for the ultimate load/moment of each joint calculated from CIDECT Guidelines No.1 (identical to EN 1993-1-8 provisions), is also indicated, as "EC3 limit" and compared with the corresponding load/moment corresponding to the weld A and weld B failure.

Yura et al. (1980) also proposed a formula for the deformation capacity of tubular X joints under bending loads. The formula proposed by Yura (1980) is based on the evaluation of the so-called "useful rotation" of the joint:

$$\theta_u = 4\theta_y = \frac{8\sigma_y}{3E}\left(\frac{L}{D}\right) \tag{5.15}$$

and is based on the assumption that the joint configuration can be approximated by a simply supported tubular beam with the geometrical characteristics of the brace member, subjected to uniformly-distributed load. The joint configuration considered in the present analysis has an L/D ratio equal to 6.75. Consequently, Eq.(5.15) reduces to:

$$\theta_u = 18\frac{\sigma_y}{E} \tag{5.16}$$

Finally, the deformation capacity of those joints can be evaluated in terms of the ductility μ of the joint, defined as the ratio of the ultimate displacement δ_u over the yield displacement δ_y:

$$\mu = \frac{\delta_u}{\delta_y} \tag{5.17}$$

146

To define the yield displacement δ_y of the load-displacement curve, the ECCS No.45 publication is employed. In particular, δ_y is defined at the intersection point of the elastic slope with the slope equal to 1/10 of the initial elastic slope, as shown graphically in Figure 5.20. Motivated by Yura's assumption, a representative value μ is equal to 4, so that:

$$\delta_u = 4\delta_y \qquad\qquad (5.18)$$
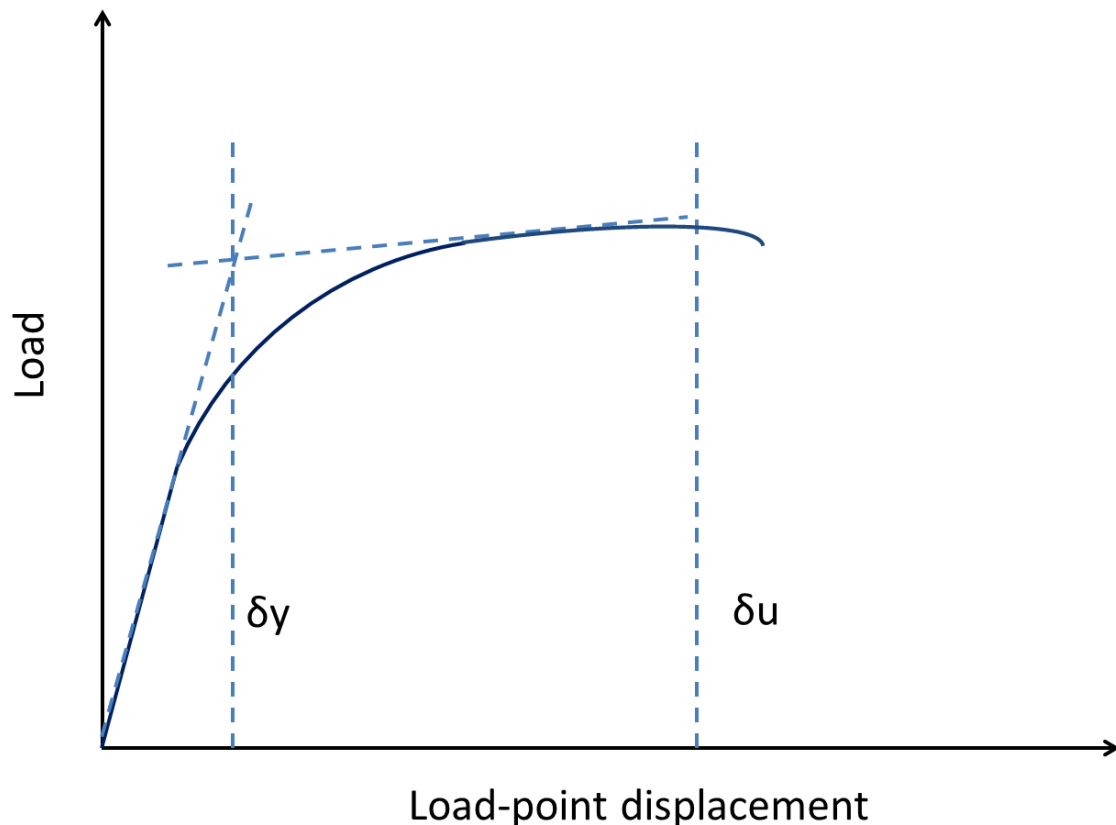
Figure 5.20: Graphical representation of the ductility limit.

In Table 5.8 the predicted deformation capacity using the above methodologies is summarized. The specific case of model No.2 corresponds to the nominal geometry of the joints used in the experiments. The deformation predictions from Yura's criterion, as well as from Eq.(5.18) are in fairly good agreement with the deformation limits corresponding to failure of the welds. Moreover, for model No. 4 geometry and both IPB and OPB loading conditions, no deformation values for weld A and B strain limits are reported. In this case, due to the small thickness of the brace, local buckling occurs at the brace prior to the development of high local strains at the weld toe and weld fracture. The resulting deformation modes for IPB and OPB are presented in Figure 5.22.

147
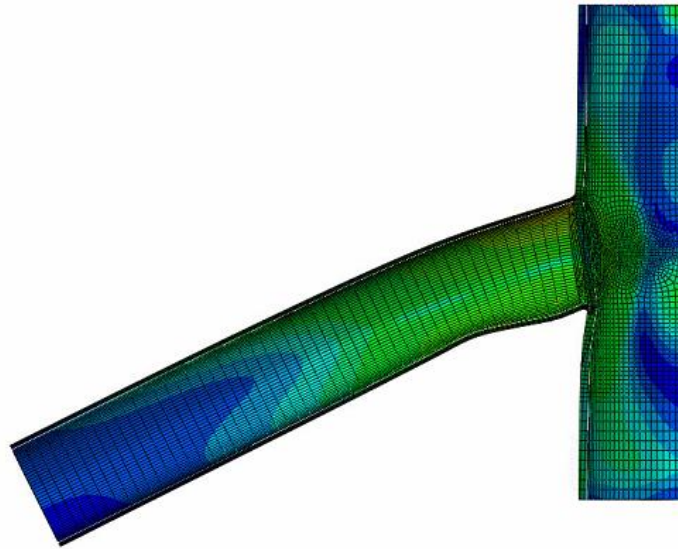
(a)
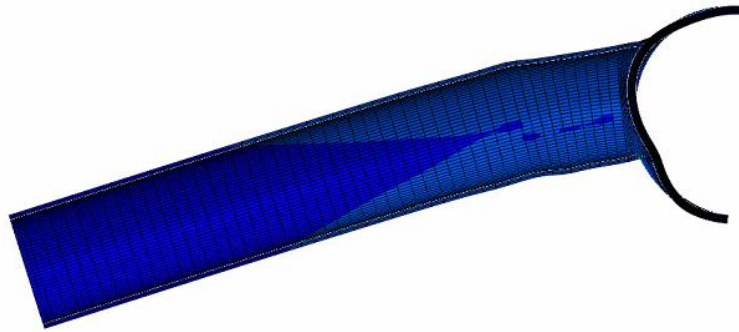
(b)

Figure 5.21: Model No.4 deformation modes: (a) IPB, (b) OPB.
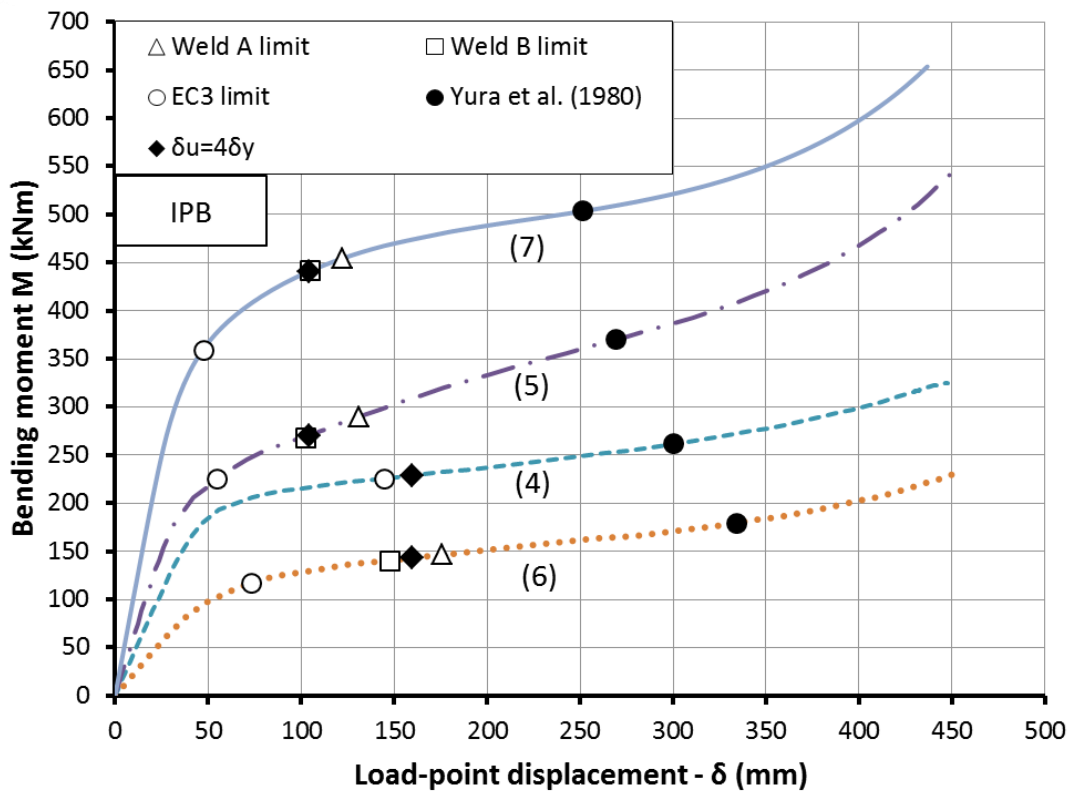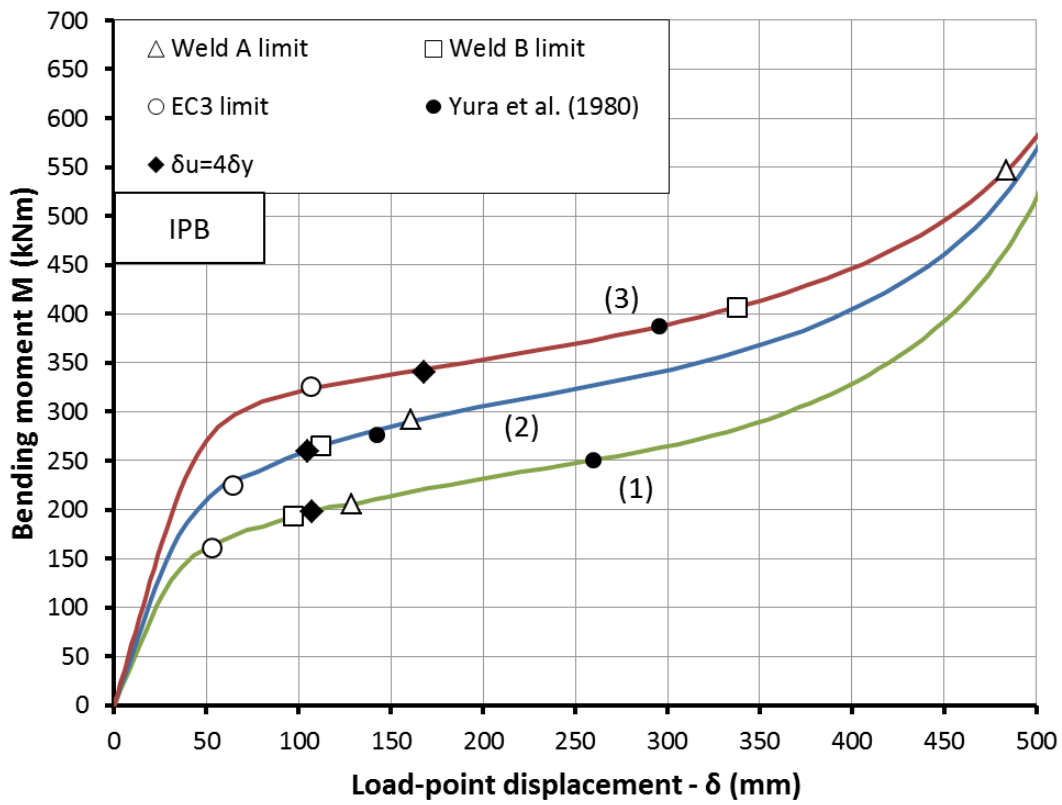
(a)
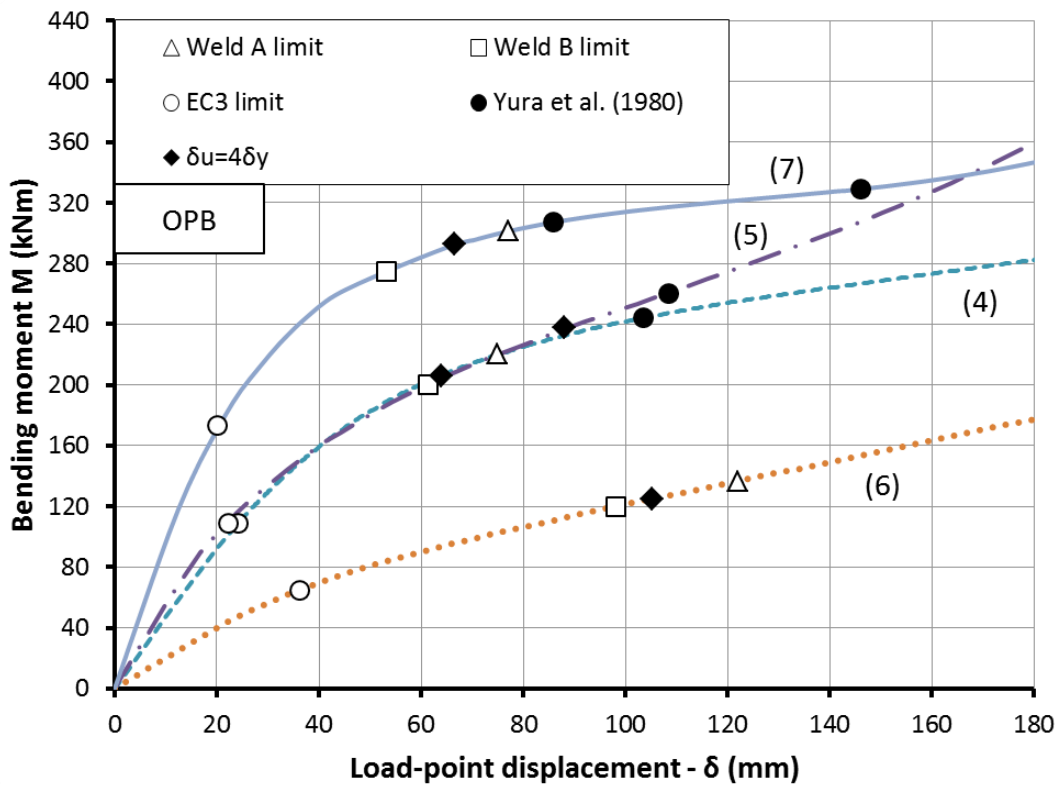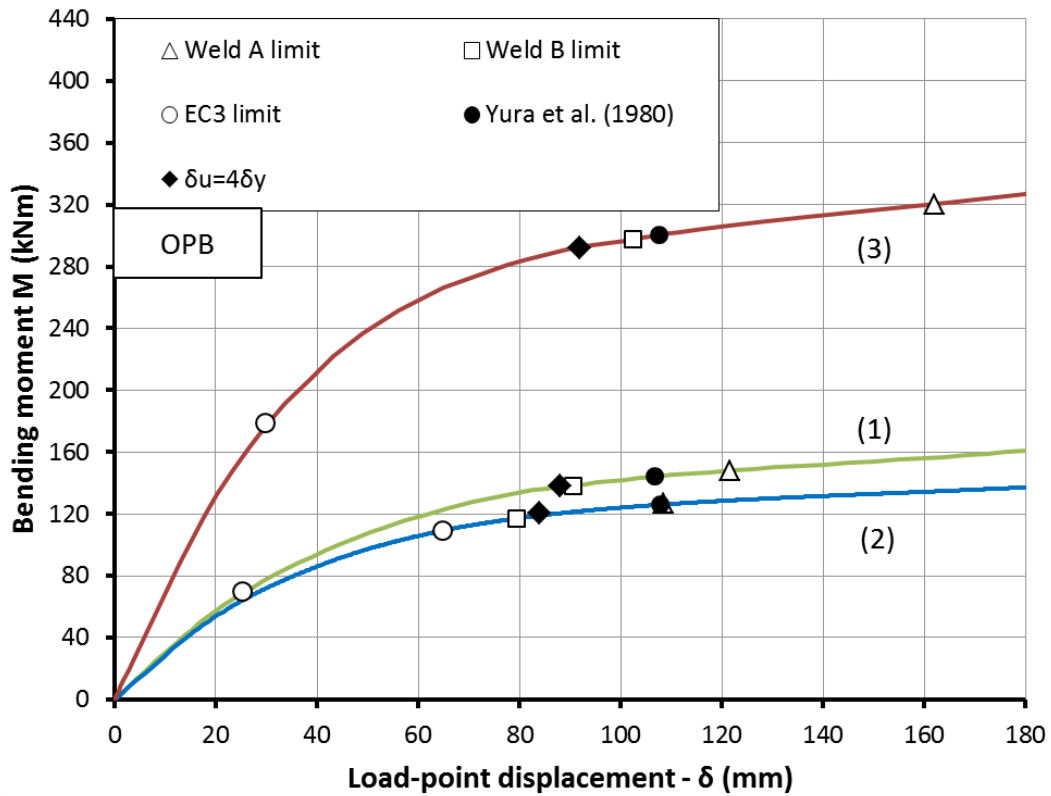
(b)
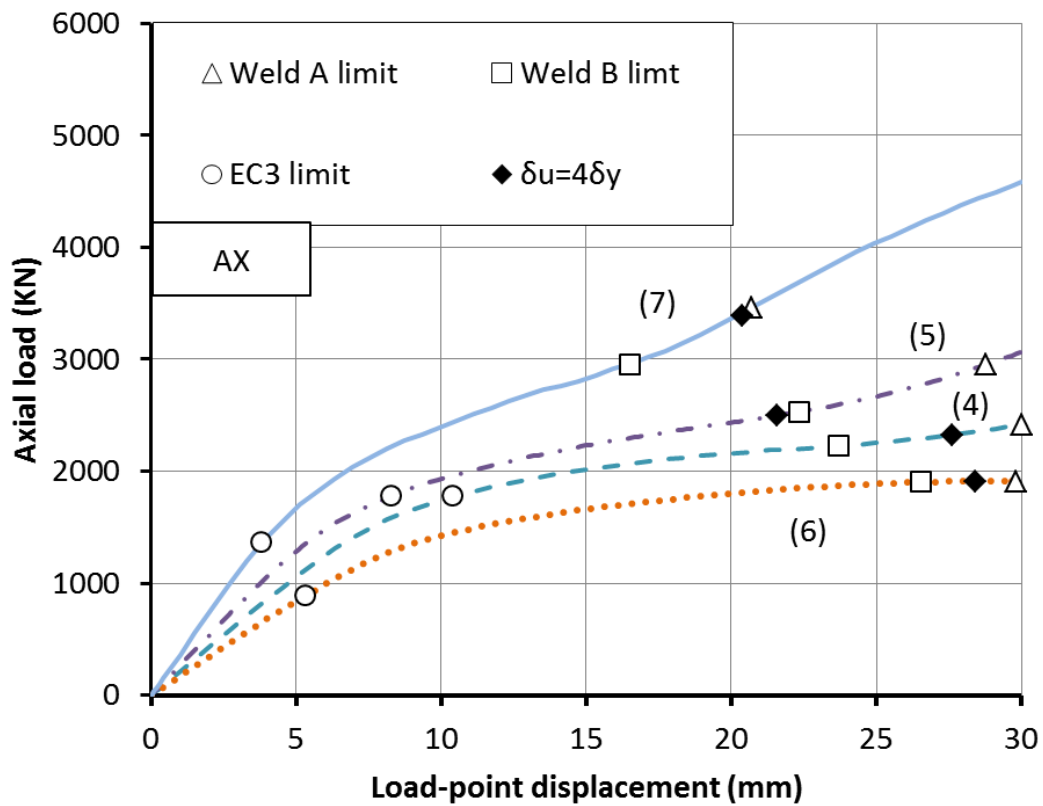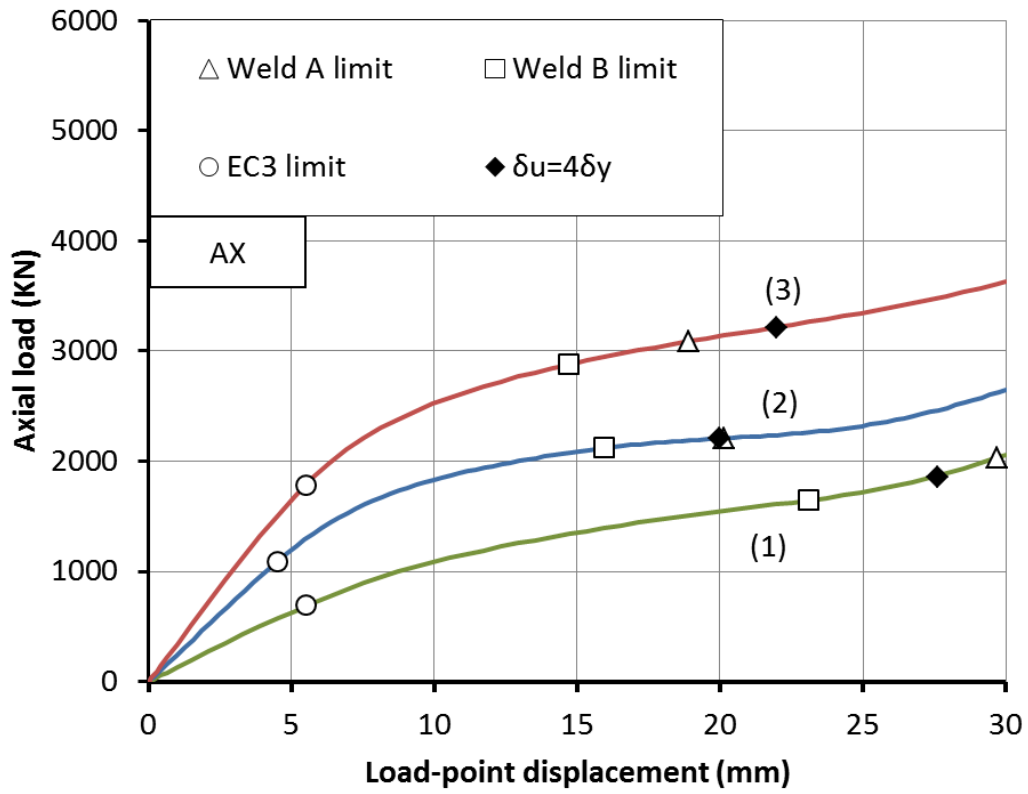
(c)

Figure 5.22: Parametric analysis – monotonic loading: (a) IPB, (b) OPB, (c) AX.

151

Table 5.8: Deformation capacity of the joints: (a) IPB, (b) OPB, (c) AX.

Model No.	IPB - Deformation capacity (mm)				
	Weld A limit	Weld B limit	EC 3 limit	Yura et al. (1980)	$\delta_u = 4\delta_y$
1	128.59	97.0	53.0	260.0	107.2
2	161.00	112.4	64.4	142.5	105.2
3	483.71	337.8	107.0	295.7	168.2
4	-	-	145.0	300.5	160.0
5	131.44	102.5	55.0	269.5	104.2
6	175.88	148.1	73.7	334.3	160.0
7	122.26	104.8	48.0	251.3	104.4

(a)

Model No.	OPB - Deformation capacity (mm)				
	Weld A limit	Weld B limit	EC 3 limit	Yura et al. (1980)	$\delta_u = 4\delta_y$
1	121.6	90.6	69.8	106.8	88.0
2	108.5	79.5	109.1	107.9	84.0
3	162.0	102.4	178.7	107.7	92.0
4	-	-	109.1	103.6	88.0
5	75.0	61.3	109.1	108.4	64.0
6	122.1	98.1	64.5	146.1	105.2
7	77.1	53.2	173.7	85.9	66.6

(b)

Model No.	AX - Deformation capacity (mm)			
	Weld A limit	Weld B limit	EC 3 limit	$\delta_u = 4\delta_y$
1	29.7	23.1	5.5	27.6
2	20.2	16.0	4.5	20.0
3	18.9	14.7	5.5	22.0
4	30.0	23.7	10.4	27.6
5	28.8	22.3	8.3	21.6
6	29.8	26.5	5.3	28.4
7	20.7	16.5	3.8	20.4

(c)

A review of the results presented in Table 5.8 shows that the predicted deformation capacity of the joint accounting for weld A and B local strain limits is higher than the deformation capacity corresponding to EC3 limits for all the loading types considered. Yura's criterion results in similar predictions for the case of OPB, while it provides unreasonably high deformation capacity for the case of IPB. On the contrary, the ductility criterion in Eq.(5.18) provides more reasonable results.

Apart from the overall behavior of the joints, for each model the corresponding *SCF* has been evaluated at the chord saddle weld toe area and the numerically predicted value is compared with the corresponding values derived using the CIDECT and W/S formulae. The results are presented in Table 5.9 and show that the numerical *SCF* predictions are in good agreement with the corresponding predictions adopting the CIDECT Guidelines No. 8 and Wordsworth & Smedley (1978) formulae (W/S). It should be noted that the geometrical characteristics of model No.5 are outside application range of CIDECT and W/S are valid. Nevertheless, their predictions are generally in reasonable accordance with the numerical findings.

Table 5.9: Parametric analysis results - *SCF*

Model	*SCF* - FEA			*SCF* – W/S			*SCF* - CIDECT		
No.	IPB	OPB	AX[a]	IPB	OPB	AX[a]	IPB	OPB	AX[a]
1	5.53	16.71	26.28	4.30	12.61	26.19	4.84	13.97	28.67
2	3.57	8.19	13.31	3.22	8.26	17.15	3.48	8.94	18.35
3	2.34	5.30	8.00	2.33	5.15	10.70	2.41	5.46	11.20
4	2.86	4.60	6.81	2.23	5.20	10.81	2.60	5.63	11.56
5	3.82	7.91	18.64	4.26*	11.72*	24.36*	4.68*	12.69*	26.06*
6	3.04	4.28	11.14	3.20	6.18	14.45	3.30	6.83	15.81
7	3.22	5.35	14.59	3.10	9.34	16.89	3.39	9.86	17.88

*: Out of dimensional application limits, [a]: Chord saddle location

In addition to the *SCF* values, the elastic strain concentration factor *SNCF* has been evaluated for each model for the three loading actions (IPB, OPB, AX) and the results are reported in Table 5.10. The comparison with the corresponding *SCF* shows some differences in the resulting values which can be attributed to the extrapolation method followed for each parameter. More specifically, as suggested by CIDECT Guidelines No.8, a linear extrapolation method has been adopted for the evaluation of the *SNCF* values, while quadratic extrapolation curve has been used for the evaluation of the *SCF* .

Table 5.10: Evaluation of the $SNCF$ for the parametric analysis models

Model No.	$SNCF$ - FEA		
	IPB	OPB	AX[a]
1	3.65	14.45	10.55
2	2.51	6.81	8.78
3	1.69	2.85	6.37
4	2.39	3.73	5.52
5	3.14	3.14	14.81
6	2.34	3.77	9.31
7	2.45	4.55	11.13

[a]: Chord saddle location

An overview of the numerical results in terms of the evaluated SCF and $SNCF$ shows that for joints with the same brace geometry and chord diameter, but with different chord thickness (models No. 1, 2, 3), the increase of the chord thickness results to a decrease of both SCF and $SNCF$. In addition, for joints with the same chord geometrical characteristics and same brace diameter, but with different brace thickness (models No. 2, 4, 5), the increase of the brace thickness results to a decrease of the resulting SCF and $SNCF$. Finally, the comparison of models No. 2, 6 and 7 shows that for joints with the same chord geometry and brace thickness, but with different brace diameter, the increase of the brace diameter within the considered range, does not have a significant effect on the resulting SCF and $SNCF$ values under IPB, while it results to an increase of the resulting values under OPB and AX loading.

5.7.2 Numerical results for cyclic loading

The set of geometries depicted in Table 5.7 adopted for the parametric analysis has also been subjected to cyclic bending loads (IPB and OPB). Following the provisions of Eurocode 3, part 1-8 (EN 1993-1-8), the design resistance for each joint geometry has been evaluated using the actual yield stress of the TS590 grade (746 MPa).

The joints where subjected to cyclic IPB and OPB loading with a maximum loading moment equal to 80% of the ultimate joint resistance under monotonic loading. This loading scheme is similar to the one followed during the cyclic experiments. Two loading ratios were adopted, namely R=0.1 and R=-1, resulting to two different minimum loading values for each joint. Characteristic bending moment – load-point deflections curves are presented in Figure 5.23 for Model 3. It can be observed that for the same maximum loading level (80% of the geometry capacity) the OPB loading results to a more pronounced nonlinear overall behavior of the joint, indicating increased plastic deformations at the critical regions. In particular, for the case of R=-1, the resulting hysteresis loop is

154

quite substantial, indicating presenting higher energy dissipation through plastic deformations, during cyclic loading.

For all loading schemes and load ratios examined for cyclic loading, the local strain range for the critical location was recorded or each joint configuration. The resulting ranges are reported in Table 5. 11. The results show that the local strain ranges for the joints subjected to OPB loads are higher than the corresponding ranges for the same joints subjected to IPB loads at the maximum load levels equal to 80% of their predicted capacity. As a result, the expected fatigue life of these joints under OPB would be lower than their fatigue life for IPB, which is in accordance with the corresponding experimental findings as well.
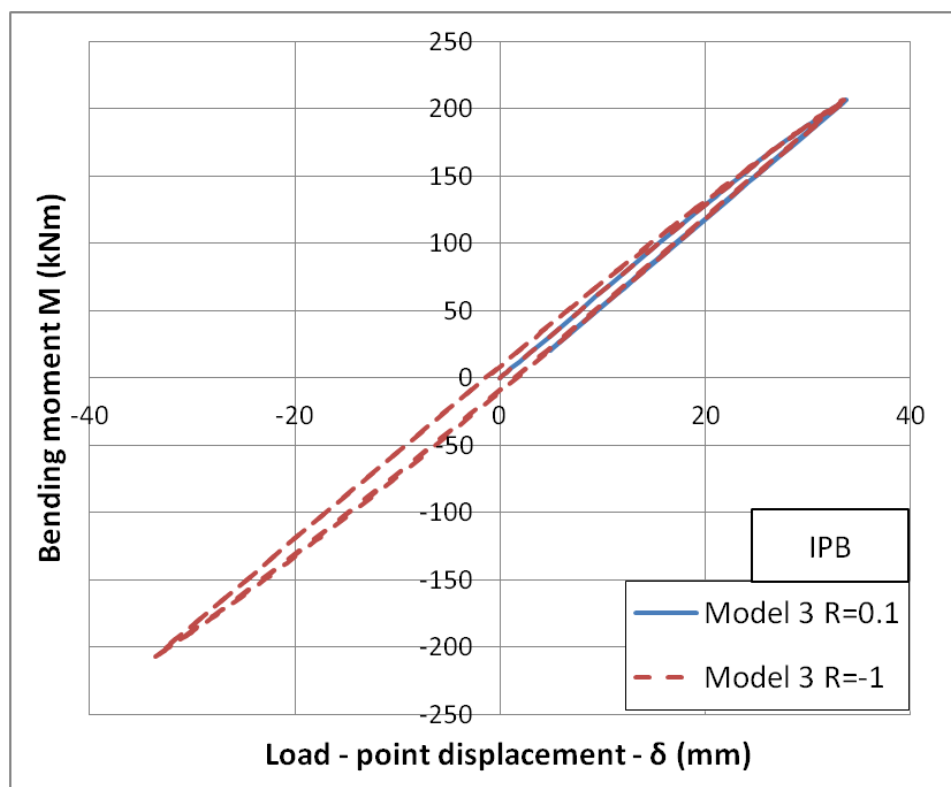
(a)
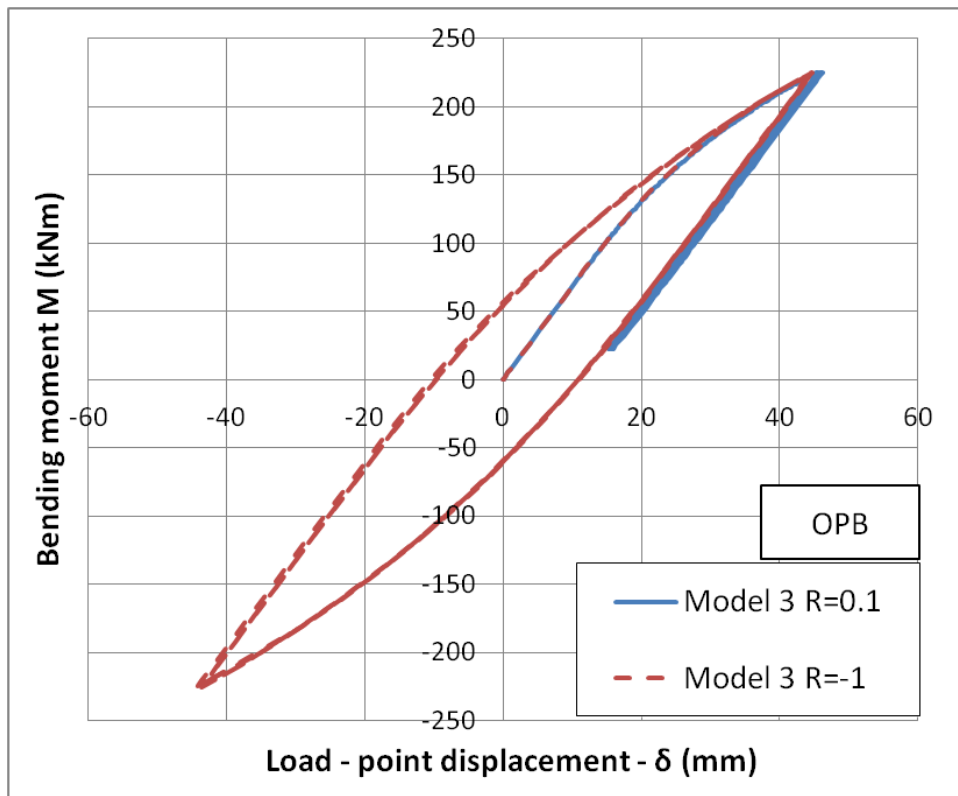
(b)

Figure 5.23: Model 3 – cyclic loading: (a) IPB, (b) OPB.

Based on the local strain range values and following the fatigue design methodology presented in the previous paragraph, the pseudo-elastic hot spot stress range was evaluated. Subsequently, the fatigue design equation proposed by Hochman et al. (2010) and presented in Eq. (5.9) was adopted in order to estimate the fatigue life of each joint, i.e. the number of cycles that the joint can sustain. A summary of the results is presented in Table 5. 11. The increase of loading ratio from R=0.1 to R=-1 results to a substantial reduction of the fatigue life of the joint due to the fully alternating loading moments and the increased resulting local strain range values. It should be also noted that for the specific case of model No. 4, the fatigue life is governed by the expected cracking at the brace side of the saddle weld toe area where the strain ranges are significantly higher than the corresponding ranges at the chord saddle weld toe.

156

Table 5. 11: Evaluation of hot-spot strain range $\Delta \varepsilon$ for the parametric analysis models

Model No.	$\Delta \varepsilon$ (%) - FEA				N_f [a]			
	IPB		OPB		IPB		OPB	
	R=0.1	R=-1	R=0.1	R=-1	R=0.1	R=-1	R=0.1	R=-1
1	0.53	1.88	0.95	4.45	2512	28	280	1
2	0.54	1.77	1.37	7.32	2375	35	82	0
3	0.45	1.36	1.27	8.17	4104	84	106	0
4	0.47/ 0.89*	1.56/ 3.59*	0.83	2.73	348*	3*	440	8
5	0.51	1.54	0.44	3.94	2819	56	4390	2
6	0.55	4.1	1.21	4.57	2248	2	125	1
7	0.48	1.54	1.13	3.22	3382	56	157	4

*: values refer to the weld toe on the joint brace location,

[a]: Fatigue life predictions according to Hochman et al. (2010)

5.8 Conclusions

The behavior of high-strength steel tubular joints subjected to extreme loading conditions has been presented in the previous paragraphs. The experimental results of tests on 10 tubular X-joints conducted in the University of Thessaly, as reported in Bursi (2012), have been presented. The joints were subjected to in-plane bending, out-of-plane bending as well as axial loading schemes. Their behavior under both monotonic and strong cyclic loads was examined. In the case of strong cyclic loading, due to the high magnitude of the applied loads, failures occurred in the low-cycle fatigue regime.

The main part of the present analysis is numerical and consists of the development of detailed numerical finite element models used for the verification of the experimental results. The nonlinear material behavior is described through the use of the material plasticity model, presented in Chapter 2. A very good agreement between the test results and the numerical predictions has been achieved in terms of the description of the overall load-displacement behavior of the joints, as well as in the estimation of the local strain fields at the critical locations. Moreover, an insight in the behavior of these joints under various loading types has been provided by monitoring the development of the local strains along the weld toe circumference. The similarities of out-of-plane bending and axial loading effects on the development of local strains are addressed, in contradiction to the more acute strain field at hot spot location resulting from in-plane bending loads.

Based on the experimental observations and the numerical results, design issues are discussed both for monotonic and cyclic loading conditions. It is found that the available design provisions of CIDECT Guidelines No.1 (similar to EN 1993-1-8 provisions) and those of API RP 2A for ultimate load capacity,

originally developed for tubular joints made of ordinary steel grades, can be applied for the design of high-strength steel joints as well.

Two methodologies for fatigue design of tubular joints into the low-cycle fatigue range have also been presented, and their capability of predicting the experimental data has been examined. The first methodology refers to the elastic hot spot stress, whereas the second methodology accounts for the inelastic behavior of the material at the hot spot location. The two methodologies are presented in terms of the available provisions of various standards and recommendations (e.g. CIDECT Guidelines No. 8, DNV–RP–C203 NORSOK N-006).

A parametric analysis has been conducted on various geometries of steel joints. Special attention has been given on the effects of the joint geometrical characteristics on the overall predicted behavior as well as the predicted local stress and strain fields at the hot spot locations for each loading type. Using various deformation criteria, the deformation capacity of the joints has been also estimated.

The maximum capacity of each joint configuration under in-plane and out-of-plane loading has been compared with available design equations. It was found that the 0.8 reduction factor proposed by EN1993-1-12 penalizes significantly the predicted ultimate capacity of the joints under consideration. Subsequently, the joints are analyzed under cyclic loading schemes at a maximum loading level equal to 80% of their capacity and two different loading ratios R equal to 0.1 and -1. For each case, the local strain range has been evaluated and correlated to a predicted fatigue life using available design equations.

Chapter 6

Conclusions

The present dissertation is aimed at detailed investigation of the performance of steel members subjected to strong cyclic loading associated with severe plastic deformations, leading to failure in the form of low-cycle fatigue or local buckling. In particular, steel tubular members are examined and characteristic engineering applications are presented, showing the correlation of cyclic plasticity with low-cycle fatigue phenomena. Despite the fact that the study concerns tubular members and pipes, as well as on tubular joints, the developed methodologies can also be applicable to steel members of any cross-sectional geometry.

For the accurate description of steel members under severe cyclic loading using the finite element method, proper simulation of cyclic plasticity related phenomena, such us the Bauschinger effect and the accumulation of plastic deformations, is necessary. Towards this purpose, advanced constitutive material models need to be employed. A key feature of the present study is the adoption and enhancement of cyclic-plasticity constitutive material model, which follows the "bounding surface" concept. The theoretical formulation and the numerical integration scheme of the model are described in detail in Chapter 2. In the same chapter, the capabilities of this model are also presented through the use of illustrative examples. Enhancements and modifications of the model that improve its predicting capabilities are also presented. The proposed model formulation is able to describe accurately the behavior of steels in terms of their stress-strains curve under monotonic or cyclic loading conditions. More specifically, under monotonically increasing plastic deformations, smooth elastic-plastic stress-strain curves or curves containing a yield plateau after the initial yielding point and a strain hardening region can be accurately described. In addition, under cyclic loading in the plastic range, the Bauschinger effect and the accumulation of plastic deformations can be represented. The plasticity model is implemented in ABAQUS, in a user-material subroutine UMAT, and it is employed for the analysis of several engineering problems related to severe cyclic loading, presented in Chapters 3 to 5.

The numerical investigation of the mechanical behavior of high-strength steel tubular members subjected to cyclic bending conditions beyond the elastic behavior limit is presented in Chapter 3. The investigation is motivated by relevant experimental evidence conducted at Centro Sviluppo Materiali SpA (CSM) in the framework of European research project HITUBES, and employs rigorous finite element simulation tools, which adopt the bounding-surface constitutive cyclic plasticity model, presented in Chapter 2.

159

A set of numerical models has been developed for the simulation of cyclic bending experiments on the tubular members. The numerical models account for diameter and thickness measurements of the specimens, obtained prior the test execution, and for the actual test loading conditions. The numerical findings compare very well with the experimental results both in terms of the resulting moment-rotation behavior, as well as in the prediction of the number of cycles to buckling, referred to a "buckling life" (i.e. the number of loading cycles to buckling).

A parametric analysis is also conducted focusing on the effect of the geometrical imperfections on the "buckling life" of the tubes under consideration. The results demonstrate that under rotation-controlled cyclic bending conditions, tubular members are susceptible to buckling, even for rotation amplitudes well below the rotation limits imposed by monotonic loading conditions. The results also show significant imperfection sensitivity on the "buckling life" of these members, especially for relatively small rotation amplitudes; for initial wrinkling values greater than 2% of the tube thickness, the corresponding number of cycles to buckling for a given value of imposed rotation is quite small, but not significantly affected by the amplitude of the initial wrinkles. Under both symmetric and non-symmetric cyclic loading conditions, the evolution of the cross-sectional ovalization contributes to the formation of local buckling of the cylindrical member. It is interesting to note that buckling under cyclic loading conditions occurs at an ovalization value very close to the ovalization value that corresponds to buckling under monotonic loading conditions.

The behavior of steel elbows subjected to strong cyclic in-plane bending in the presence of internal pressure is examined thoroughly in Chapter 4. The analysis is supported by experimental results from two different set of tests conducted at TU Delft and CSM laboratories, within European research project INDUSE. The tests were conducted in a constant amplitude displacement-controlled mode resulting to failures in the low-cycle fatigue range. Different internal pressure levels were used in order to examine their effect on the fatigue life of the specimens, up to 45% of yield pressure.

The work presented in Chapter 4 mainly focuses on the development of rigorous finite element models for the support of the above experimental investigation. Using detailed dimensional measurements and material testing obtained prior to specimen testing, detailed numerical models have been developed to simulate the conducted experiments. The advanced cyclic plasticity material model presented in Chapter 2 has been employed for simulation of the tests. Emphasis is given on the local strain development at the critical part of the elbow where cracking occurs. The numerical results are reported in the form of load-displacement and flattening-displacement curves, and also refer to the evolution of local strain at the critical elbow location, showing good agreement with the test data.

An alternative and efficient methodology for estimating local strain ranges of cyclically loaded elbows developed at the critical location is also presented. This method is based on Neuber's equation and the cyclic stress-strain curve of the material and allows for safe strain-range estimations without requiring the use of finite element analyses. In addition, a numerical study is conducted examining the effects of the variation of geometrical characteristics of the elbow on its mechanical behavior and the local strains at critical locations.

The currently available design provisions of the EN 13480 and ASME B31.3 standards for the estimation of the ultimate capacity of steel pipe elbows and their fatigue life are discussed in detailed. The lack of adequate design provisions of these standards for the low-cycle fatigue design of piping components is highlighted. The ASME BPVC standard for nuclear piping components is the only standard that covers the low-cycle fatigue regime. The aforementioned design provisions are critically assessed.

Based on the available experimental and the numerical results of the proposed model, an efficient fatigue design methodology is presented. The local strain-ranges measured at the elbow critical location are correlated with the fatigue life of the elbow, also accounting for the presence of internal pressure in a rigorous manner.

In Chapter 5 the behavior of high-strength steel tubular joints subjected to extreme loading conditions is presented. As part of European research project HITUBES, ten tubular X-joints were tested at the laboratory facilities of the Civil Engineering Department of the University of Thessaly under in-plane bending, out-of-plane bending and axial loading schemes. Those tests constitute the motivation of the present investigation.

The behavior of high-strength steel tubular joints under both monotonic and cyclic loading schemes were examined and emphasis was given on their low-cycle fatigue performance. A set of detailed numerical finite element models have been developed for the simulation of the full scale tests. The nonlinear material model that uses the bounding surface concept (presented in Chapter 2) is used to describe material behavior. A very good agreement between the test results and the numerical predictions has been achieved in terms of the description of the overall load-displacement behavior of the joints, and a fairly good agreement has been obtained in terms of local strain at the critical locations. Furthermore, based on the available experimental and the numerical results of the proposed model, design implications are discussed both for monotonic and cyclic loading conditions. It is found that the currently available design provisions of EN 1993-1-8/ CIDECT No.1 for the joint ultimate load capacity, originally developed for tubular joints of ordinary steel grades, can be applied for the design of high-strength steel joints as well, without the reduction factor suggested by EN 1993-1-12. For fatigue loading, the NORSOK design code provisions, are the only available provisions for the low-cycle fatigue range, and can be rather conservative in the low-cycle fatigue range. A linear extrapolation of the CIDECT

161

No8 and DNV-RP-C203 design equations, originally issued for the description of high-cycle fatigue phenomena, in the low-cycle fatigue range has been attempted based on the concept of pseudo-elastic stresses. This approach is found to result in safe and reasonable estimates of the fatigue life of welded tubular joints in the low-cycle fatigue region. Furthermore, a very similar equation proposed by Hochman et al. (2010) is found to be in good agreement with the present analysis results.

The numerical results are also compared with the predictions obtained from Neuber's criterion in terms of local strain range. The predicted strain values are found in good agreement with the corresponding values derived numerically for the monotonic loading cases. Nevertheless, for the cyclic loading cases examined, Neuber's approach results to overestimation of local strains, thus penalizing the fatigue design of the joints under consideration.

Numerical models of tubular X-joints with varying geometrical characteristics have also been developed and a parametric numerical analysis has been conducted. Special attention has been given on the effects of joints geometrical characteristics on the overall joint performance under consideration when subjected to monotonic and cyclic loading. The resulting local strain fields have been examined in detail and an attempt to estimate the deformation capacity of each joint based on different limit criteria has been conducted. Finally, under cyclic loading conditions, the resulting local strain ranges at the critical regions were correlated to the expected fatigue life of the joints under consideration.

References

[1]   American Petroleum Institute, API, 2000. Recommended Practice for Planning, Designing and Constructing Fixed Offshore Platforms – Working Stress Design. API RP 2A-WSD, Edition 22.

[2]   American Society of Mechanical Engineers, 2006. Process Piping, B31.3, ASME Code for Pressure Piping, New York, NY.

[3]   American Society of Mechanical Engineers, 2010. Boiler and Pressure Vessel Code Section III: Rules for Construction of Nuclear Facility Components, Mandatory Appendix I.

[4]   Armstrong, P.J., Frederick, C.O., 1966. A mathematical representation of the multiaxial Bauscinger effect, CEGB Report No. RD/B/N 731.

[5]   ASTM E466-07, 2007. Standard practice for conducting force controlled constant amplitude axial fatigue tests of metallic materials, ASTM International, USA.

[6]   AWS D1.1/D1.1M:2004, Structural Welding Code – Steel.

[7]   Baba, S., Arizumi, Y., Naruoka, M., 1981. Low-Cycle Fatigue Test of Welded Tubular joints, *Journal of the Structural Division*, ASCE, Vol. 107, Issue 3, pp. 487-505.

[8]   Balan, C. and Redektop, D., 2004. The effect of bidirectional loading on fatigue assessment of pressurized piping elbows with local thinned areas, *Int. J. Pressure Vessels and Piping,* Vol. 81, pp. 235-242.

[9]   Ballio, G., Castiglioni, C.A., 1995. A Unified Approach for the Design of Steel Structures under Low and/or High cycle Fatigue, *Journal of Construction Steel Research*, Vol. 34, pp. 75-101.

[10]   Bari, S., Hassan, T., 2001. Kinematic hardening rules in uncoupled modeling for multiaxial ratcheting simulation, *International Journal of Plasticity,* Vol. 17, pp. 885-905.

[11]   Bari, S., Hassan, T., 2000. Anatomy of coupled constitutive models for ratcheting simulation, *International Journal of Plasticity,* Vol. 16, pp. 381-409.

[12]   Bauschinger, J., 1881. Ueber die veraenderung der elasticitaetgenze und des elasticitaetmodulus verschiedener metalle, *Civilingeneur*, Vol. 27, pp. 289–348.

[13]   Bea, R.G., Young, C.N., 1993. Loading and Capacity Effects on Platform Performance in Extreme Storm Waves and Earthquakes, *Proc. Offshore Technology Conference OTC,* 7140.

[14] Beale, L.A. and Toprac, A.A., 1967, Analysis of In-Plane T, Y and K Welded Tubular Connections, Welding Research Council bulletin, No. 125.

[15] Bijlaard, P., 1955. Stresses form Local Loadings in Cylindrical Pressure Vessels, *Journal of Applied Mechanics*, ASME, Vol. 22.

[16] Billington, C.J., Lalani, M., Tebbet, I.E., 1982. Backround to new Formulae for the Ultimate Limit State of Tubular Joints, *Offshore Technology Conference*, Paper 4189, Houston, Texas.

[17] Boge, F., Helland, T.K., Berge, S., 2007. Low cycle fatigue of T-tubular joints with out-of-plane bending loading, *Proceedings of the International Conference on Offshore Mechanics and Arctic Engineering- OMAE,* 4, pp. 107-115.

[18] Bursi, O. S., 2012, Design and Integrity Assessment of High-Strength Tubular Structures for Extreme Loading Conditions, Final report of HITUBES RFCS project, Trento, Italy (Available in http://bookshop.europa.eu).

[19] Centro Sviluppo Materiali (CSM), 2011. Cyclic loading on P355N steel grade material coupons; CSM Internal Report, INDUSE RFCS project.

[20] Chaboche, J.L., 1986. Time-independent constitutive theories for cyclic plasticity, *International Journal of Plasticity,* 2, 149-188.

[21] Chaboche, J.L., Dang-Van, K., Cordier, G.,1979. Modelization of the strain memory effect on the cyclic hardening of 316 stainless steel, *Proceedings of the 5th International Conference on SMiRT*, Div. L, Berlin, Germany.

[22] Chang, K. H. and Pan, W. F., 2009. Buckling life estimation of circular tubes under cyclic bending, *International Journal of Solids and Structures,* Vol. 46 (2), pp. 254–270.

[23] Chattopadhyay J., Nathani, D. K., Dutta, B. K. and Kushwaha, H. S., 2000. Closed-Form Collapse Moment Equations of Elbows Under Combined Internal Pressure and In-plane Bending Moment, *J. Pressure Vessel Technology*, ASME, Vol. 122, pp. 431-436.

[24] CIDECT No. 1. 1991. Design Guide for Circular hollow Sections (CHS) under Predominantly Static Loading

[25] CIDECT No. 8. 2001. Design Guide for Circular and Rectangular Hollow Section Welded Joints under Fatigue Loading

[26] Comité Européen de Normalisation, 2002. Metallic Industrial Piping – Part 3: Design and calculation, EN13480-3, Brussels.

[27] Corona, E., Hassan, T., Kyriakides, S., 1996. On the Performance of Kinematic Hardening Rules in Predicting a Class of Biaxial Ratcheting Histories, *International Journal of Plasticity*, Vol. 12, pp. 117-145.

164

[28] Corona, E., Kyriakides, S., 1988. On the collapse of inelastic tubes under combined bending and pressure, *International Journal of Solids and Structures,* Vol. 24 (5), pp. 505–535.

[29] Corona, E., Kyriakides, S., 1991. An experimental investigation of the degradation and buckling of circular tubes under cyclic bending and external pressure, *Thin-Walled Structures,* Vol. 12, pp. 229–263.

[30] Dafalias, Y.F., Popov, E.P., 1976. Plastic internal variables formalism of cyclic plasticity, *Journal of Applied Mechanics*, Vol. 43, pp. 645-650.

[31] Dama E., Karamanos, S. A., and Gresnigt, A. M., 2007. Failure of Locally Buckled Pipelines, *Journal of Pressure Vessel Technology*, ASME, Vol. 129, No. 2, pp. 272-279.

[32] DeGrassi, G., Hofmayer, C., Murphy, A., Suzuki, K., and Namita, Y., 2003. BNL nonlinear pre-test seismic analysis for the NUPEC ultimate strength piping test program, *Transaction of SMiRT 17 Conference*.

[33] Dhalla, A. K., 1987. Collapse Characteristics of a Thin-Walled Elbow, *J. Pressure Vessel Technology*, ASME, Vol. 109, pp. 394-401.

[34] DNV–RP–C203. Fatigue Design for Offshore Steel Structures. Det Norske Veritas, 2011.

[35] Drucker, D.C., Palgen, L., 1981. On stress-strain relations suitable for cyclic and other loadings, *Journal of Applied Mechanics,* Vol. 48, pp. 479-485.

[36] Dunne F., Petrinic N., Introduction to computational plasticity, Oxford University Press, 2005.

[37] Elchalakani M, Zhao XL, Grzebieta RH., 2004. Cyclic bending tests to determine fully ductile slenderness limits for cold-formed circular hollow sections, *J Struct Engrg ASCE*, 130(7):1001–10.

[38] EN 10216 (2006). Seamless steel tubes for pressure purposes – Technical delivery conditions, European Committee for Standardization, Brussels.

[39] EN 1993-1-12. 2009. Eurocode 3: Design of steel structures – Part 1-12: Additional rules for the extension of EN 1993 up to steel grades S 700, European Committee for Standardization

[40] EN 1993-1-8. 2002. Eurocode 3: Design of steel structures – Part 1-8: Design of joints, European Committee for Standardization.

[41] EN 1993-1-9. 2002. Eurocode 3: Design of steel structures – Part 1-9: Fatigue strength of steel structures, European Committee for Standardization.

[42] EN ISO 15609-1.2004. Specification and qualification of welding procedures for metallic materials — Welding procedure specification.

[43] European Convention for Constructional Steelwork - (1986). Recommended Testing Procedure for Assessing the Behavior of Structural Steel Elements under Cyclic Loads, ECCS Publication No 45.

[44] Fujiwaka, T. Endou, R., Furukawa, S., Ono, S., Oketani, K., 1999. Study on strength of piping components under elastic-plastic behavior due to seismic loading, *PVP Conference*, Seismic engineering, PVP-Vol 137.

[45] Gao, S. B., Usami, T., Ge, H. B., 1998. Ductility evaluation of steel bridge piers with pipe sections, *J Engrg Mech*, ASCE, 124(3):260–7.

[46] Graff, W.J., et al. 1981. Review of Design considerations for Tubular Joints, ASCE International Conventions, New York.

[47] Greenstreet, W. L., 1978. Experimental Study of Plastic Responses of Pipe Elbows, ORNL/NUREG-24 report, Contract No. W-7405-eng-26.

[48] Gresnigt, A. M. and Van Foeken, R., 1995. Strength and Deformation Capacity of Bends in Pipelines, *Int. J. Offshore and Polar Engineering*, Vol. 5, No. 4, pp. 294-307.

[49] Gresnigt, A. M., 1986. Plastic Design of Buried Steel Pipelines in Settlement Areas, Heron, Vol. 31, No. 4

[50] Guionnet, C., 1992. Modeling of ratcheting in biaxial experiments, *Journal of Engineering Materials and Technology*, Vol. 114, pp. 56-62.

[51] Hassan, T., Kyriakides, S., 1992. Ratcheting in Cyclic Plasticity, Part I: Uniaxial Behavior, *Int. Journal of Plasticity*, Vol. 8, pp.91-116.

[52] Hassan, T., Kyriakides, S., 1994. Ratcheting of Cyclically Hardening and Softening Materials: II. Multiaxial Behavior, *Int. Journal of Plasticity*, Vol. 10, No. 2, pp. 185-212.

[53] Herynk, M.D., Kyriakides, S., Onoufriou, A., Yun, H.D., 2007. Effects of the UOE /UOC pipe manufacturing processes on pipe collapse pressure, *International Journal of Mechanical Sciences*, Vol. 49, pp. 533–553.

[54] Hilsenkopf, P., Boneh, B. and Sollogoub, P., 1988. Experimental Study of Behavior and Functional Capability of Ferritic Steel Elbows and Austenitic Stainless Steel Thin-Walled Elbows. *Int. J. Pressure Vessels and Piping*, Vol. 33, pp. 111-128.

[55] Hoadley, P.W., and Yura, J.A., 1983. Ultimate Strength of Tubular Joints Subjected to Combined Loads, Ph.D. Dissertation, Dept. of Civil Engineering, University of Texas at Austin.

[56] Hochman, M., Madshus, M., Berge, S., 2010. Low Cycle Fatigue of T-tubular Joints under Axial Loading, *Proceedings of the Twentieth International Offshore and Polar Engineering (ISOPE)*, Beijing, China.

166

[57] Houliara, S. and Karamanos, S. A., 2011. Buckling of Thin-Walled Long Steel Cylinders under Bending, *Journal of Pressure Vessel Technology*, ASME, Vol. 133, No.1, Article Number: 011201.

[58] HSE 2004. Review of low cycle fatigue resistance. Research report 207 by Failure Control Limited.

[59] International Institute of Welding, 1981. Design Recommendations for Hollow Section joints in Predominately Statically Loaded Joints, IIW Doc. XV-491-82, Annual Assembly, Portugal.

[60] Jiao, R. and Kyriakides, S., 2009. Ratcheting, wrinkling and collapse of tubes under axial cycling, *International Journal of Solids and Structures*, Vol. 46, pp. 2856–2870.

[61] Jiao, R. and Kyriakides, S., 2010. Wrinkling of Tubes by Axial Cycling, ASME, *Journal of Applied Mechanics*, Vol. 77, paper No. 031012-1.

[62] Jiao, R. and Kyriakides, S. 2011a. Ratcheting and wrinkling of tubes due to axial cycling under internal pressure: Part I experiments, *International Journal of Solids and Structures*, Vol. 48, 2814–2826.

[63] Jiao, R. and Kyriakides, S. 2011b. Ratcheting and wrinkling of tubes due to axial cycling under internal pressure: Part II analysis, *International Journal of Solids and Structures*, Vol. 48, pp. 2827–2836.

[64] Ju, G.-T. and Kyriakides, S., 1992. Bifurcation and localization instabilities in cylindrical shells under bending. Part II. Predictions, *Int. J. Solid. Struct.* Vol. 29, pp. 1143–1171.

[65] Karamanos, S. A. and Tassoulas, J. L. 1991. Stability of Inelastic Tubes Under External Pressure and Bending, *Journal of Engineering Mechanics*, ASCE, Vol. 117, No. 12, pp. 2845-2861.

[66] Karamanos, S. A. and Tassoulas, J. L. 1996. Tubular Members I: Stability Analysis and Preliminary Results; II: Local Buckling and Experimental Verification, *Journal of Engineering Mechanics*, ASCE, Vol. 122, No. 1, pp.64-71 and 72-78.

[67] Karamanos, S. A., Giakoumatos, E. and Gresnigt, A. M., 2003. Nonlinear Response and Failure of Steel Elbows Under In-Plane Bending and Pressure, *J. Pressure Vessel Technology*, ASME, Vol. 125, No. 4, pp. 393-402.

[68] Karamanos, S. A., Tsouvalas, D. and Gresnigt, A. M., 2006. Ultimate Bending Capacity and Buckling of Pressurized 90 deg Steel Elbows, *J. Pressure Vessel Technology*, ASME, Vol. 128, No. 3, pp. 348-356.

[69] Karamanos, S.A., 2013. Structural Safety of Industrial Steel Tanks, Pressure Vessels and Piping Systems under Seismic loading, INDUSE RFCS project, Volos, Greece (Available in http://bookshop.europa.eu).

167

[70] Khan, A.S., Huang, S., Continuum Theory of Plasticity. John Wiley & Sons, Inc., NY, USA. 1995.

[71] Klever, F.J., Palmer, A.C., Kyriakides, S., 1994. Limit-state design of high-temperature pipelines, *Proc. of 13th International conference on Offshore Mechanics and Arctic Engineering*, Houston, Vol. V, pp.77-92.

[72] Kyriakides, S. and Corona, E., Mechanics of offshore pipelines, Vol. I Buckling and Collapse. Elsevier, 2007.

[73] Kyriakides, S. and Ju, G.-T., 1992. Bifurcation and localization instabilities in cylindrical shells under bending. Part I. Experiments, *Int. J. Solid. Struct.* Vol. 29, pp. 1117–1142.

[74] Kyriakides, S., and Corona, E., 2007. Mechanics of Offshore Pipelines. Buckling and Collapse, Vol. 1. Elsevier, Amsterdam (Chapters 8 and 9).

[75] Kyriakides, S., Shaw, P.K., 1987. Inelastic buckling of tubes under cyclic loads, *Journal of Pressure Vessel Technology*, ASME, Vol. 109, pp. 169–178.

[76] Lee, K. L., Pan, W. F., Kuo, J. N., 2001. The influence of the diameter-to-thickness ratio on the stability of circular tubes under cyclic bending, *International Journal of Solids and Structures,* Vol. 38, pp. 2401–2413.

[77] Lee, M-G, Kim, D., Kim, Ch., Wenner, M.L., Wagoner, R.H, Chung, K., 2007. A practical two-surface plasticity model and its application to spring-back prediction, *Int. Journal of Plasticity*, Vol. 23, pp. 1189-1212.

[78] Marshall, P.W., 1974, Basic Considerations for Tubular Joint Design in Offshore Construction. Welding Research Council Bulletin, No. 193.

[79] Moreton, D.N., Yahiaoui, K., Moffat, D.G., 1996. Onset of ratcheting in pressurised piping elbows subjected to in-plane bending moments, *Int. J. Pressure Vessels and Piping*, Vol. 68 (1). pp. 73-79.

[80] Mourad, H. M. and Younan, M. Y. A., 2001. Nonlinear analysis of pipe bends subjected to out-of-plane moment loading and internal pressure, *J. Pressure Vessel Technology*, ASME, Vol. 123, No. 2, pp. 253-258.

[81] Mroz, Z., 1967. On the description of anisotropic work hardening, *Journal of the Mechanics and Physics of Solids,* Vol. 15, pp. 163-175.

[82] Neuber, H., 1961. Theory of Stress Concentration for Shear Strained Prismatical Bodies with Arbitrary Non Linear Stress Strain Law, *Journal of Applied Mechanics*, Vol. 28, pp. 544.

[83] Noordhoek, C., Verheul, A., 1998. Static Strength of High Strength Steel Tubular Joints, CIDECT Research Project Final Report No. 5BD-9/98.

[84] NORSOK N-006. 2009. Assessment of Structural Integrity for Existing Offshore Load-bearing Structures.

[85] Ohno, N., Wang, J.-D., 1993. Kinematic hardening rules with critical state of dynamic recovery, part I: formulations and basic features for ratcheting behavior, *International Journal of Plasticity,* Vol. 9, pp. 375-390.

[86] Pan, P.B., et al, 1976. Ultimate Strength of Tubular Joints, *Offshore Technology Conference*, Paper 2644, Houston, Texas.

[87] Paolacci, F., Reza, M. S., Bursi, O. S., 2011. Seismic design criteria of refinery piping systems*, Conference on Computational Methods in Structural Dynamics and Earthquake Engineering - COMPDYN 2011*, Corfu, Greece.

[88] Pappa, P. and Karamanos, S. A., 2012. Buckling of High-Strength Steel CHS Tubular Members Under Axial Compression and Bending, *14th International Symposium on Tubular Structures (ISTS 14)*, Paper No. 104, London, UK.

[89] Pappa, P., Tsouvalas, D., Karamanos, S. A. and Houliara, S., 2008. Bending Behavior of Pressurized Induction Bends, *Offshore Mechanics and Arctic Engineering Conference*, ASME, OMAE2008-57358, Lisbon, Portugal.

[90] Pournara, A. E., Karamanos, S. A., Ferino, J., and Lucci, A. 2012. Strength and stability of high-strength steel tubular beam-columns under compressive loading, *14th International Symposium on Tubular Structures (ISTS 14)*, Paper No. 103, London, UK.

[91] Prager, W., 1956. A new method of analyzing stresses and strains in work hardening plastic solids, *Journal of Applied Mechanics*, Vol. 23, pp. 493–496.

[92] Rahman, S. M. and Hassan, T., (2009). Simulation of ratcheting responses of elbow piping components, *ASME Pressure Vessels and Piping Division Conference, PVP2009-77819*, Prague, Czech Republic.

[93] Reber, J.B., 1972. Ultimate Strength Design for Tubular Joints, *Offshore Technology Conference*, Paper 1664, Houston, Texas.

[94] Romeijn, A., 1994. Stress and strain concentration factors of welded multiplanar tubular joints, PhD Thesis, Delft, The Netherlands.

[95] Schmucker, D.G., Cornell, C.A., 1994. Dynamic Behavior of Semi-Ductile Jackets under Extreme Wave and Wave-in-Deck Forces, *Proc. Of BOSS'94 Conference*.

[96] Shalaby, M. A. and Younan, M. Y. A., 1998. Limit Loads for Pipe Elbows with Internal Pressure Under In-plane Closing Bending Moments, *J. Pressure Vessel Technology*, ASME, Vol. 120, pp. 35-42.

169

[97] Shaw, P. K., Kyriakides, S., 1985. Inelastic analysis of thin-walled tubes under cyclic bending, *International Journal of Solids and Structures*, Vol. 21, No. 11, pp. 1073–1110.

[98] Shen, C., Tanaka, Y., Mizuno, E., Usami, T., 1992. A Two-Surface Model for Steels with Yield Plateau, *Structural Eng./Earthquake Eng.*, Vol. 8, No.4, pp. 179-188.

[99] Shimomura, K., Ishitoku, H., Sakurai, S. and Hirose, F., 2002. Advanced Technologies of Preventive Maintenance for Thermal Power Plants., *Hitachi Review*, Vol. 51, No. 5, pp. 137-142.

[100] Slagis, G.C., 1998. Experimental Data on Seismic Response of Piping Components, *J. Pressure Vessel Technology*, ASME, Vol. 120, pp.449-455.

[101] Sobel, L. H. and Newman, S. Z., 1980. Comparison of Experimental and Simplified Analytical Results for the In-Plane Plastic Bending and Buckling of an Elbow, *J. Pressure Vessel Technology*, ASME, 102, pp. 400-409.

[102] Sobel, L. H. and Newman, S. Z., 1986. Simplified, Detailed and Isochronous Analysis and Test Results for the In-Plane Elastic-Plastic and Creep Behavior of an Elbow, *J. Pressure Vessel Technology*, ASME, Vol. 108, pp. 297-304.

[103] Suzuki, K., 2006. Earthquake Damage to Industrial Facilities and Development of Seismic Vibration Control Technology – Based on Experience from the 1995 Kobe Earthquake, *J. Disaster Research*, Vol. 1, No.2.

[104] Suzuki, N., Nasu, M., 1989. On-linear Analysis of Welded Elbows Subjected to In-Plane Bending, *Computers & Structures*, Vol. 32, No.3/4,pp.871-881.

[105] Swensson , K.D., Yura, J.A., 1987. Ultimate strength of double-tee tubular joints: Interaction effects. PMFSEK report No. 87-9.

[106] Tan, Y., Matzen, V. C. and Yu, L. X., 2002. Correlation of test and FEA results for the nonlinear behavior of straight pipes and elbows, *J. Pressure Vessel Technology*, ASME, Vol. 124, pp.465-475.

[107] Tseng, N. T., Lee, G. C., 1983. Simple plasticity model of the two-surface type. ASCE, *J. of Engineering Mechanics,* Vol. 109, pp. 795-810.

[108] Ucak, A. Tsopelas, P., 2011. Constitutive Model for Cyclic Response of Structural Steels with Yield Plateau, *Journal of Structural Engineering*, ASCE, pp. 195-206.

[109] Underwater Engineering Group, 1985. Design of Tubular Joints for Offshore Structures Vol.2, Page Bros (Norwich) Limited.

[110] Usami, T., Gao, Sh., Ge, H., 2000. Elastoplastic analysis of Steel Members and Frames Subjected to Cyclic Loading, *Journal of Engineering Structures*, Vol. 22, pp. 135-145.

[111] V.d. Vegte, G.J., de Back, J., Wardenier, J., 1989. Low Cycle Fatigue of Welded Structures, Stevin Report 25.6.89.09/A1, Delft University of Technology.

[112] van der Vegte, G.J., de Back, J., Wardenier, J., 1989. Low cycle fatigue of welded structures. Analysis of low cycle fatigue on tubular T-and X-joints. Stevin report 15.6.89.11/A1, CIDECT report 7H-89/2-E.

[113] Varelis, G. E., Karamanos, S. A., and Gresnigt, A. M., 2013a. Steel Elbow Response Under Strong Cyclic Loading, *Journal of Pressure Vessel Technology*, ASME, Vol. 135, No.1, Article Number: 011207.

[114] Varelis, G. E., Pappa, P., Karamanos, S. A., 2011. Finite element analysis of industrial steel elbows under strong cyclic loading, *Pressure Vessel and Piping Conference,* ASME, PVP2011-57260, Baltimore, Maryland, USA.

[115] Varelis, G. E., Vathi, M., Houliara, S., and Karamanos, S. A., 2009. Effect of UOE Manufacturing Process on Pressure Buckling of Thick-walled Pipes, *10th International Conference on Computational Plasticity - COMPLAS X*, Barcelona, Spain.

[116] Varelis, G.E., 2010. Application of the Armstrong - Frederick Cyclic Plasticity Model for Simulating Structural Steel Member Behavior, Graduate Diploma (M.Sc.) Thesis, Department of Mechanical Engineering, University of Thessaly.

[117] Varelis, G.E., Ferino, J., Karamanos, S.A., Lucci, A., Demofonti, G., 2013b. Experimental and Numerical Investigation of Pressurized Pipe Elbows under Strong Cyclic Loading, *Pressure Vessel and Piping Conference*, ASME, PVP2013-97977, Paris, France.

[118] Waalen, J., Berge, S., 2005. Low cycle fatigue of T-tubular joints with in-plane bending loading. *Proceedings of the International Conference on Offshore Mechanics and Arctic Engineering- OMAE*, 3, art. no. OMAE2005-67468, pp. 211-219.

[119] Wordsworth, A.C., and Smedley, G.B., 1978. Stress concentrations at unstiffened tubular joints, Loyd's Register of Shipping, Paper 31.

[120] Yahiaoui, K., Moffat, D.G., Moreton, D.N., 1996a. Response and cyclic strain accumulation of pressurized piping elbows under dynamic in-plane bending, *J. Strain Analysis for Engrg Design*, Vol. 31 (2), pp. 135-151.

[121] Yahiaoui, K., Moreton, D.N., Moffat, D.G., 1996b. Response and cyclic strain accumulation of pressurized piping elbows under dynamic out-of-plane bending, *J. Strain Analysis for Engrg Design*, Vol. 31 (2), pp. 153-166.

[122] Yura, J.A., Zettlemoyer, N., and Edwards, I.F., 1980. Ultimate Capacity Equations for Tubular Joints, *OTC Proceedings*, Vol. 1, No. 3690.

[123] Zayas, V. A., Mahin, S. A. and Popov, E. P., 1982. Ultimate strength of steel offshore structures, *Behavior of Offshore Structures*, *Proc. 3rd International Conf*, ed. C. Chrissostomides and J. J. Connor. Vol 2, MIT, Boston, MA, pp. 34-58.